MF RADAR OBSERVATIONS OF D-REGION ELECTRON DENSITIES AT ADELAIDE

By

Rupa Vuthaluru, M. Sc, M.phil

Thesis
submitted for the degree of
DOCTOR OF PHILOSOPHY
at the
UNIVERSITY OF ADELAIDE
(Department of Physics and Math Physics)

July, 2003

Contents

Abstract

This thesis focuses on the study of lower ionospheric ionization by means of data obtained with MF radar located at Adelaide (35°S, 138°E). Observations from this radar covering 60-80 km during day light hours and 80 - 100 km during night hours are used to analyze the electron density profiles and hence the physics of the $D-$region. Sen and Wyller magneto-ionic theory is used to estimate the electron densities from ordinary and extra-ordinary mode amplitudes of the signals returned from the ionospheric $D-$region.

The thesis begins with an introduction (Chapter 1) to highlight the general understanding of the atmosphere and ionosphere. A detailed description of the Buckland Park MF radar facility, for collecting the data along with the necessary assumptions and rejection criteria are also presented in this chapter.

In Chapter 2, the basis of the technique for implementing the Differential Absorption Experiment (DAE) and collision frequencies derived are presented. It is found that the derived collision frequencies are in good agreement with the latest laboratory measurements of the momentum transfer collision frequencies and these laboratory collision frequencies are adopted as a new standard for our work.

In Chapter 3, daytime radar observations are used to study mid-latitude lower $D-$region (60-80 km region) characteristics. Solar control is found to be the dominant influence in determining the seasonal and diurnal variation of noon electron densities and in general, as the zenith angle increased the electron density decreased. However, at constant solar zenith angle, mean electron densities are found to be enhanced in autumn months and reduced in spring months, in contrast to the predicted behaviour of a static atmosphere. IRI and FIRI model results and MF radar electron densities at Wakkanai (45°N) are compared with our observations.

In Chapter 4, new and unique MF radar observations at night are investigated to look at the general characteristics of mid-latitude nighttime ionization in $80 - 100$ km region. Different mechanisms required to maintain the nighttime ionization and structure are investigated. Comparisons between NO density variations and our observations are found to be in good agreement. Average recombination rates are estimated and these estimated values compare well with the earlier studies. Diurnal variation of electron density generally exhibited decay after sunset. For the sunspot minimum period, in the equinoctial months, the electron density decay is more prominent than in other months.

Seasonal variation of nighttime electron densities at Adelaide showed moderate increase of N_e values in winter and spring than in summer values, especially in the height range of $88 - 96$ km. This is found to be in correlation with the two dimensional model calculations of NO transport in the middle atmosphere by Siskind et al. (1997). Also, monthly mean vertical profiles of electron density in the nighttime $D-$region are in correlation with the corresponding structure in the nitric oxide profiles. Comparison of our results with those of earlier workers and IRI and FIRI model results are used to understand the variation of N_e in the nighttime lower ionosphere.

Influences of solar cycle changes are considered on daytime and nighttime electron densities. Below 80 km the electron density generally decreases with sunspot number (SS). Above 80 km altitude, although the electron density increases with SS, strong influences of seasonal variations appear to persist. Examples of electron density enhancement during solar flare conditions are also addressed.

In Chapter 5, observed asymmetry in the diurnal variation of electron density N_e is investigated. The asymmetry is larger in summer than in winter and mostly morning electron densities are larger than the corresponding afternoon values. An explanation of this asymmetry is given in terms of diurnal asymmetry in the variation of NO which was reported to be consistent with a perturbation induced by the migrating diurnal tide (Marsh et al., 2000). Also, effect of temperature and density tidal oscillations are considered. The ratio of prenoon to postnoon recombination coefficient due to temperature oscillations (α_1/α_2) is found to be around 1.12 in comparison to the ratio due to diurnal tidal wind variations of 2.37, indicating that the dominant perturbing mechanism is direct tidal advection.

In summary, the thesis work has endeavoured to understand the lower ionospheric ionization with help of estimated electron densities from MF radar sited at Adelaide. This work supports the fact that NO densities play a major role in the formation of lower ionospheric ionization and complements the efforts in forming the NO climatology with the use of global measurements of nitric oxide in the Earth's upper atmosphere by satellite experiments. In particular, the work can contribute to the understanding of transport of thermospheric NO into the middle atmosphere (due to vertical and horizontal mixing) where it could react with ozone.

Observations due to our improved MF radar are proved to be very useful in understanding the nighttime $D-$region characteristics. Investigations for the cause of diurnal and seasonal asymmetry observed, demonstrated the effect of planetary waves on the electron density rearrangement. The observational results are consistent with the theoretical studies indicating that the Ly-α radiation has the strongest influence in the formation of both daytime and nighttime $D-$region.

Originality declaration

This work contains no material which has been accepted for the award of any other degree or diploma in any university or other tertiary institution and, to the best of my knowledge and belief, contains no material previously published or written by another person, except where due reference has been made in the text.

I give consent to this copy of my thesis, when deposited in the University Library, being available for loan and photocopying.

Signed: .... dated: 04/07/2003

Rupa Vuthaluru, M. Sc, M.phil

Acknowledgements

I take this opportunity to thank my supervisor Professor R. A. Vincent for his profound guidance, constructive criticism and enthusiastic support throughout the course of this work. I also wish to express my sincere gratitude to Dr. D. A. Holdsworth for his support and for many invaluable discussions regarding the experimental procedure during the course of this investigation. Special thanks must go to Dr. Iain Reid for many helpful suggestions and support.

I also wish to express my regards and sincere gratitude to Prof. G. Elford, whose timely input in bringing the laboratory measurements of collision frequencies led to a valuable comparison and new findings. Special thanks to Dr. D. R. Marsh[1] for his timely communications and useful suggestions of tidal effects on electron densities. Sincere thanks to Prof. Merve Lynch[2] for his help in undertaking my thesis work as a remote candidate, at Curtin University of Technology.

I would like to thank my past and present colleagues of Atmospheric group, Andrew Mackinnon, Daniel Badger, Jonathan Woithe, Sujatha Kovalam, Stephen Grant, Chris Lucas, Florian Zink, Alireza Kazempour, Bridget Hobbs, Karen Berkfield, Scott Dullaway, Andrew Taylor, Dorothy Gibson-Wilde, and Lawrence Campbell for their help and cooperation in various stages of the work. Special thanks to Jonathan Woithe for his constant support regarding computing systems even while I was working away from the Department as a remote candidate. Thanks also to Dallas Kirby for her support in administrative and all other matters.

---

[1] National Center for Atmospheric Research, Boulder, Colorado

[2] Department of Physics, Curtin University of Technology, Perth

Finally, my deepest praise is for my husband, Hari, and our daughter Priya (Huppy) whose love, patience, support, sacrifice and constant encouragement made this work possible. I want to thank the rest of my family. I am specially indebted to my parents for their advice, support and inspiration over many years of my education. The completion of my PhD is as much a joyous event for all of them as it is for me.

I would like to acknowledge the University of Adelaide for providing the financial assistance in the form of a Scholarship during the tenure of my research work.

List of Figures

List of Tables

Chapter 1

General Introduction

1.1 Theme

In recent years it has become more widely recognized that the Earth's biosphere is a highly coupled system. Changes in the state of one component can have broad implications to the whole atmosphere. The atmosphere is but a part of this chain, due to its nature though, it is a key factor in the dissemination of global changes. The uneven heating of the Earth causes circulation within the atmosphere in an attempt to transfer the heat from warmer to cooler regions. The circulation in turn transports minor constituents around the globe. Sometimes the nature of the global circulation can cause the accumulation of minor constituents, which in term can cause changes in the local chemistry. This effect is evident in some of the results presented in this work.

This work is concerned with the free electrons that are produced in the lower ionosphere by the ionizing action of Sun's radiation on the Earth's atmosphere. Before embarking on the main research topics it is instructive, and to some extent vital (e.g. description of experimental setup), to consider some of the background theory. The nature of ionosphere as well as neutral atmosphere are considered first. Brief review of theoretical models used for comparison, description of experimental facility at Adelaide along with the assumptions and rejection criteria used are presented next.

The part of the atmosphere above 50 km, where free electrons exist in numbers sufficient to influence the propagation of radio waves, is called the *ionosphere*. The Earth's magnetic field affects the motion of electrons at all heights, but with increasing importance at heights greater than $\sim$ 100 km. That part of the ionosphere is called the *magnetosphere*. Although there is no clear height at which the magnetosphere can be said to start, it is suggested that its base might be taken to be at the plasmapause. To show how the electrons in the ionosphere are produced by the solar radiation and how they are affected by the motion of different atmospheric waves, it is first necessary to discuss the nature of the neutral atmosphere.

1.2 The Atmosphere

Although the atmosphere is in reality a single fluid body, with a fixed lower boundary at the surface of the Earth, and a tenuous upper boundary extending into solar-terrestrial space, it is often segmented into altitude regions for the purposes of closer study. The segmentation or classification of the regions varies with the physical process under consideration. Due to the gravitational attraction of the Earth, the bulk of the atmosphere (by mass) remains at lower altitudes; the atmospheric density decreasing exponentially from the surface. This, combined with the fact that solar radiation enters from the 'top' of the atmosphere, means that the recombination rate for ionized species decreases with altitude, while the dissociation rate increases. Thus the outer regions of the atmosphere are substantially ionized (although the number density of the neutral species is higher than that of the charged particles out to altitudes of the order of 1000 km). The atmosphere can therefore be classified *via* the properties of the neutral gases or *via* the ionisation (see Figure 1.1).

1.2.1 The neutral atmosphere

The vertical temperature profile of the atmosphere also allows the distinction of a number of regions. These, like the ionospheric regions, are formed by the changing

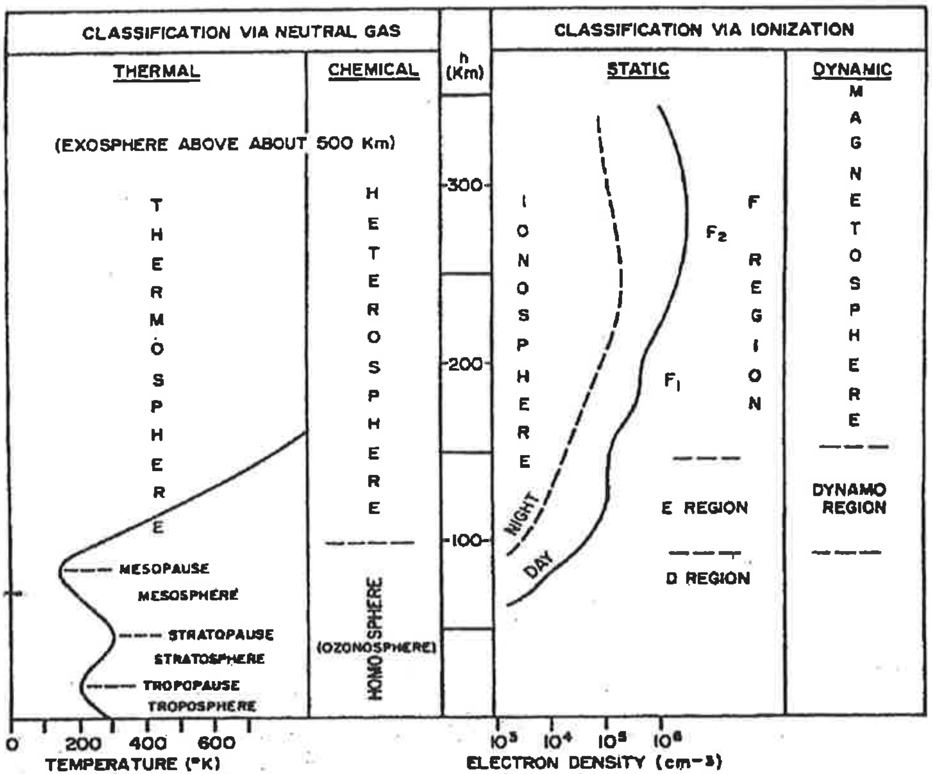

Figure 1.1: Various schemes for the classification of the atmosphere [Figure 1.1 of Hines (1965)]

physics with increasing altitude. Figure 1.1 shows a typical height profile of temperature at 40°S in the mid latitude region. The thermosphere is the uppermost layer and extends from about 90 km above the surface to the outer limits of the atmosphere. Gases in this layer exist in such a very low concentration that they make up a mere .001 percent of the total mass of the atmosphere. The density of the gases in the thermosphere is so low that it approaches a vacuum, and the gases may become very hot. With temperatures ranging from 200°K to 1400°K throughout the year (hence the name thermosphere), very little heat can actually be held or conducted by gases of such low density.

At some level, commonly between 90 and 120 km, is the turbopause, below which the atmosphere is reasonably well mixed, the mixing being dominated by eddy or turbulent processes. Above 120 km molecular diffusion dominates, so that molecular species are separated according to their respective masses. Above these levels also, the action of the electric and magnetic fields on the ionized component of the atmosphere is important in determining the motion. Extreme ultraviolet (EUV) radiation emitted from the sun is absorbed by atomic oxygen throughout the region, and solar variability in EUV forcing largely accounts for the broad range of upper thermospheric temperatures.

Immediately beneath the thermosphere is the mesosphere (middle sphere). This layer lies between 50 km and 90 km above the earth's surface and, unlike the thermosphere, has decreasing temperatures which reach a minimum at $\sim$ 90 km. The upper boundary of mesosphere is mesopause which can vary between above 85 and $\sim$ 100 km altitude for a global minima. The existence of strong turbulence is a characteristic feature of mesosphere, which seems to be generated by the breaking of gravity waves.

The heat source of the high temperature around the stratopause is the absorption of ultraviolet wavelengths of solar radiation by the ozone layer. Hard solar X-rays ($\sim$ 0.1 to 2 nm) and UV-radiation ($\sim$ 170 to 200 nm) are absorbed in the mesosphere between 60–90 km altitude (see Figure 1.2). In the EUV, the Lyman-α line (121.6 nm) represents an important source of ionization and dissociation at the ionospheric D-layer (60–100 km) heights. The mesosphere is the primary region of interest in this dissertation.

Below the mesosphere lies the stratosphere. The temperature increases due to the absorption of ultraviolet (UV) radiation in the $\sim$ 200–300 nm range (see Figure 1.2) by ozone (O_3). The heating which results from this absorption is greatest at about 50 km, the upper limit of the stratosphere, where the temperature is 270°K. Between about 10 and 20 km above the earth's surface the stratosphere reaches its lowest temperatures, about 210°K. The increase of temperature with height makes the atmosphere in this region highly stratified and very stable, hence the name stratosphere.

The region from the ground to approximately 15 km is called troposphere. This layer contains most of the total mass of the atmosphere. It is most important to us since it is the layer in which the 'weather' occurs. Unsaturated air in the troposphere consists of 78 percent nitrogen and 11 percent oxygen. However, it is the minor gases of the troposphere, such as water vapor, which are important in meteorology. Temperatures usually decrease with height in the troposphere with a lapse rate of about 6.5°K km^{-1}.

1.2.2 The ionosphere

The regions where ionisation is important have been called the ionosphere since the primary work of Appleton in 1924. The term ionosphere was introduced by R. A. Watson-Watt in a letter to the United Kingdom Radio Research Board, in 1926 (Rishbeth and Garriott, 1969). The vertical electron density profile causes three regions to be distinguished.

In the D-region (60 $\sim$ 90 km) the electron density increases with altitude during the day. Daytime electron densities tend to peak at about $\sim$ 100 km, which marks the E-region (90-150 km). Above the E-region electron densities begin to increase again; this is the F-region (150-1000 km). Sometimes a minor peak or plateau in electron density is observed near 200 km, which is referred to as the F1-layer. A broader but more consistent peak around 300 km is referred to as the F2-layer. The F-region is 'partially' ionized with much of its structure being determined by the differential diffusion of the electrons and ions. Transport is therefore an important mechanism. The boundaries between all these regions are not well defined (Figure 1.1).

Ionisation is mainly produced by the incoming solar UV and EUV radiation[1] and soft X-rays. The EUV (17-80 nm) radiation is generally absorbed by the F-region and is largely responsible for the F1 layer. Hard UV (80-100 nm) penetrates to the E-region where it too is absorbed. Soft X-rays (0.8-14 nm) are absorbed in the D- and E-regions. The absorption of X-rays from 0.1-1.6 nm and UV from 100-180 nm help maintain the D-region. The height at which most of the solar radiation has been absorbed is shown in Figure 1.2. Note that in these figures units of Angstrom, $A°$, are used ($1A° = 0.1nm$).

As a note of historical interest, the notation of D, E and F came about from the way

---

[1] Ultra-Violet (UV),Extreme-Ultra-Violet(EUV)

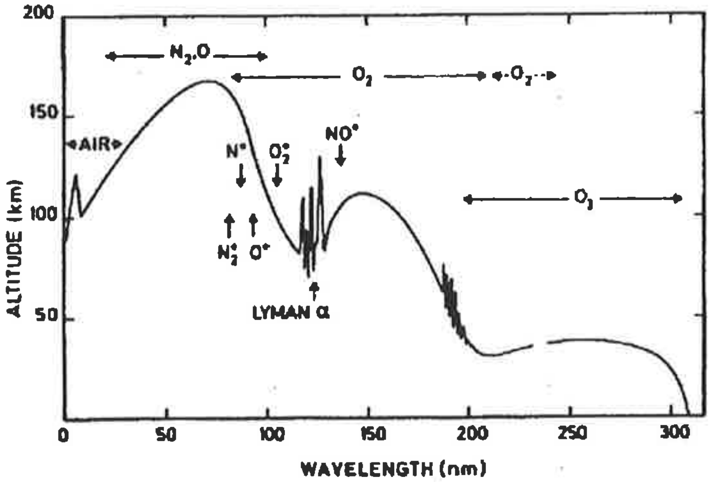

Figure 1.2: Penetration depth of a solar radiation as function of wavelength. Altitudes correspond to attenuation of $1/e$. The principle absorber and ionization are indicated [After Volland (1988)].

the ionosphere was discovered. It was found that the E-mode (i.e. left-hand circularly polarized) radio signal was reflected from a layer in the atmosphere, naturally named the 'E-layer'. When reflecting layers were discovered below and above this layer they were naturally named the D- and F-layers. These distinct ionospheric regions exist due to:-

- the different absorption characteristics of the atmosphere at different altitudes, causing differing solar energy deposition.
- recombination physics depending on the atmospheric density; again a function of altitude.
- the atmospheric composition changing with altitude.

The electron density profile varies with (amongst other things) latitude, season, and solar cycle. The differing physics of these regions are the real bases for their differentiation.

Electron density in the D- and the lower E-regions can be conveniently classified into four regions as shown in Figure 1.3. Region I is the one above the sharp gradient in electron density ledge (Region II) occurring usually between 82 and 85km and

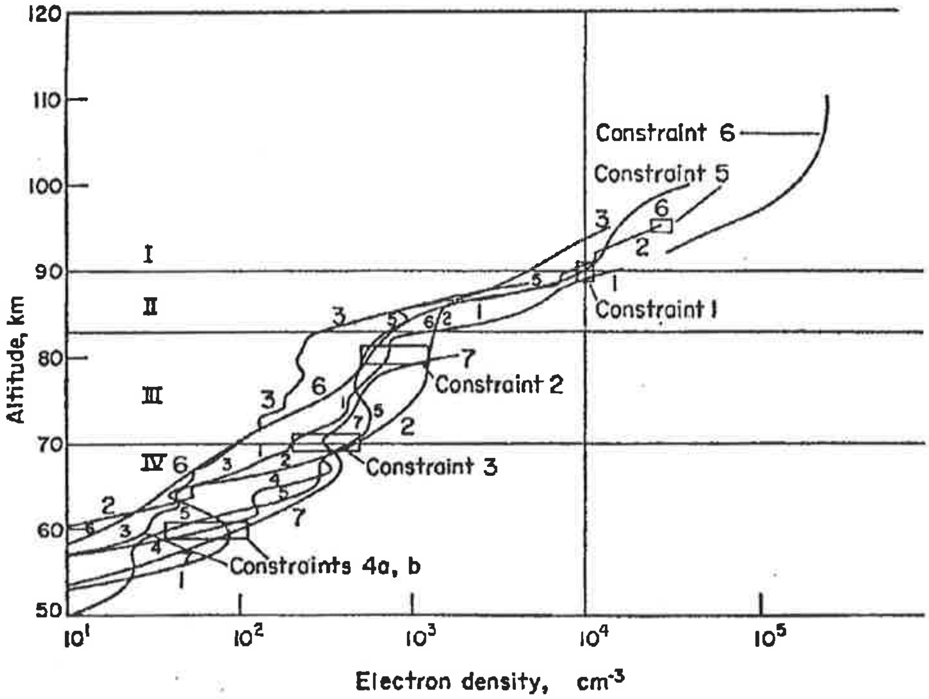

Figure 1.3: Lower ionosphere classification into four regions I, II, III and IV, see text for more explanation [After Mitra and Rowe (1974)]

coinciding with height with the level where water cluster ions suddenly disappear. Region III includes the region between this ledge and around 68km, is controlled almost entirely by the photo-ionization of NO by L_α, and during daytime is not influenced by negative ions except at and near the lower limit. This is also the region where electron density measurements by different authors and by different techniques (both ground based and rocket-borne) agree to a surprising degree. Region IV is the negative ion dominated region below 68km; this is also the region where there is no general agreement on the nature and magnitude of N_e values, although there is some evidence that there is a residual bank of ionization in excess of $10cm^{-3}$ at 60km.

Figure 1.3 shows different regions classified above (I, II, III, and IV) and different numbers on each curve refer to the experimental electron densities measured by previous workers as mentioned below. 1)summer noon Bain and Harrison (1973), 2) Illinois active sun ($\chi = 60°$) Mechtly et al. (1972) 3) Illinois quiet sun ($\chi = 60°$) Mechtly et al. (1972), 4) VLF, 5) Partial reflection (corrected) ($F_{10.7} = 100$), Belrose and Segal

(1973), 6) Bremer et al. (1973) ($\chi = 60°$), 7) Penn. State cross-modulation ($\chi = 60°$) solar activity reversal region. Various ionospheric constraints of mesospheric nitric oxide (as indicated in the figure) are detailed in the paper by Mitra and Rowe (1974).

The ionospheric daytime data obtained using Buckland Park (BP) partial reflection facility fall into the regions III and IV, making these measurements very useful in investigating the nature of variations of electron density. Similarly, nighttime results fall into the region II and partly into region I and the variation of these nighttime electron densities are discussed in Chapter 4 in this thesis. However, relevant information regarding sources of radiant energy in the night sky is given below, as the study of these nighttime observations is one of the key features of this dissertation as a consequence of improved DAE setup.

1.2.2.1 Nighttime sources

Hydrogen and helium atoms comprise the outermost regions of the earths atmosphere because of their low atomic weight. Typical scale heights for these constituents are approximately 100 to 300 km and therefore the hydrogen and helium extend out to a few earth radii in significant quantities. Because of these great distances, the solar ultra violet emissions in the main absorption bands of H and He are able to re-radiate (resonance scattering) into the nighttime ionosphere. This vast extension of hydrogen and helium above the earth with its ability to scatter solar radiation is called geocorona. Ultraviolet radiation at night from the geocorona and extraterrestrial origin can excite and ionize the atmospheric constituents in the region above 80 km.

Theoretical models of the geocorona (Meier and Mange, 1973) are used by Strobel et al. (1974) to obtain Ly$-\alpha$, Ly$-\beta$, He-I and He-II flux variations with altitude for different solar zenith angles. Average Ly$-\alpha$ intensities compiled by Ogawa and Tohmatsu (1966) for a number of experimental observations gave an intensity of 1.9 kR (kilorayleighs). Weller and Carruthers (1972) have observed a nighttime intensity of 1.6 kR at Wallops Island. These measurements suggests that in addition to geocorona Ly$-\alpha$ scattered from interplanetary hydrogen. Since Ly-α ionizes only NO the maximum absorption takes place below 120 km where NO is greatest and coincides with the region of our interest.

Ly-β (102.6nm) intensities were first estimated from hydrogen night-glow radiation(656.3nm) and from Ly-α emissions(121.6nm) by Ogawa and Tohmatsu (1966). Ly-β predominantly ionizes molecular oxygen with a cross section of absorption and ionization which is very small(1.52 and $0.97 \times 10^{-18} cm^2$, respectively) relative to Helium emissions. Additional measurements of Ly-β show that the mid-latitude intensities may vary by a factor of 5 (Swider, 1972) and (Weller and Carruthers, 1972). It is also believed that approximately half of the Ly-β radiation is of extraterrestrial origin (Gough, 1975) and there would remain nearly constant in time. The similar temporal variation for Ly-β and Ly-α are expected since both originate from hydrogen emission.

Theoretical calculations by Poppoff and Whitten (1969) with observed $X-$ray spectrum of Scorpio (SCO) XR-1 (Cosmic X-ray source) have shown that the ionization rate profile due to this source is much smaller than the total rate from galactic cosmic rays and from scattered Ly$-\alpha$ at all altitudes below 90 km. It was shown by Mitra and Ramanamurthy (1972) that a marginal effect is, in fact, possible if certain conditions are full-filled. Hence, the average ionization rates estimated using Buckland Park MF radar measurements are compared with the contribution of these cosmic X-rays in the production of ionization in the nighttime $D-$region along with above mentioned ultraviolet sources in Chapter 4.

1.3 Sun‘s Radiation

1.3.1 Sunspot number and solar cycle

Patches of comparative darkness are frequently visible on the sun: they are called *sun spots*. A *sunspot number*, R, based on measurements made by several observatories, is used to represent, in a composite way, the number and area of the spots. The magnitude of R varies between about zero and 200 with quasi period of about 11

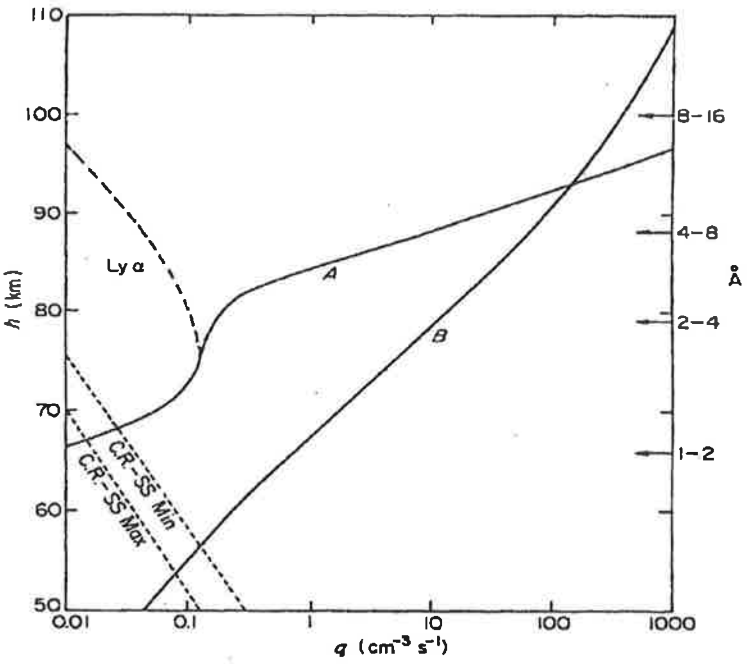

Figure 1.4: The rates at which electrons are produced in the atmosphere below 110 km. *A*) X-rays quiet sun, *B*) X-rays solar flares [After Rishbeth and Garriott (1969)]

years. This cyclical variation is called the *solar cycle*. The observation period of the present study falls into the Cycle number 23.

Throughout the solar cycle the energy flux in the ultraviolet part of the spectrum is approximately proportional to $(1 + 0.01R)$; it thus increases by a factor of about 2 as R increases from 0 to 100. In the part of the spectrum with wavelength less than 10 nm (the X-radiation), the changes throughout the cycle are greater; thus as R changes from 0 to 100 the power with wavelengths between 5 and 10nm increases by a factor of about 30. By contrast the power in the Ly-α of hydrogen changes by only 50 percent through the solar cycle, and that in the visible part of the spectrum hardly at all.

In contrast, the galactic cosmic radiation is weaker at solar maximum than at solar minimum by a factor of about 0.5. This change is attributed to its being partially directed away from the neighborhood of the earth by the solar magnetic field, which is greater at solar maximum. These differences in the rates of ionization (Figure 1.4) cause different parts of the D region to vary throughout the solar cycle in different ways.

1.3.2 Solar disturbances

Disturbances occur on the sun accompanied by the emission of one or more of the following radiations each of which can produce its own type of disturbance in the ionosphere (Ratcliffe, 1972).

1. A sudden increase in the strength of the visible H_α line. The phenomenon is known as a *solar flare.*

2. A sudden increase in the strength of the X-radiation is known as an $X - ray\ flare$.

3. The emission of a group of protons and electrons so dense that interaction between the particles gives it the characteristics of a plasma cloud. It forms an enhancement of the normal solar wind and reaches the earth after about 36 hours. It is convenient to call it a *solar plasma event.*

4. The emission of energetic protons and electrons with such small concentrations that they travel like independent charged particles. They reach the earth in a few hours. It is called a *solar proton event.*

During a solar flare the X-ray flux may rise by a factor of as much as 10 at shorter wavelengths. For example, during a flare of importance 2 (on a scale 1 to 3), at an epoch in the solar cycle when $R = 100$, the energy flux in the wavelength range $1 - 2$ nm exceeds the normal flux by a factor of 10 roughly. Under such circumstances X-rays are the major source of D-region ionization and the electron density of the layer is enhanced greatly. These events, which are of 10 to 15 minutes duration, are termed sudden ionospheric disturbances, or SID. Only a limited amount of information is available on variations of other portions of the solar spectrum during flares. However, available evidence seems to indicate that the solar flux at wavelengths greater than 10 nm varies by less than a factor of 2 during solar flares. Thus, while some modification of the electron density distribution occurs above 100 km the major effect of solar flare photon radiation is in the D region. Some examples of these flare effects are provided in Chapter 3, using the observations made at Adelaide. Classification and meaning of different types of flares are given in Table 1.1.

Table 1.1: Solar X-ray flux classification

Level	Flux (watts/sq meter)	Description
A	less than 10^{-8}	Very Low Background
A	between 10^{-8} and 10^{-7}	Low Background
B	between 10^{-7} and 10^{-6}	Moderate Background
C	between 10^{-6} and 10^{-5}	High Background/Low Flare
M	between 10^{-5} and 10^{-4}	Moderate Flare
X	between 10^{-4} and 10^{-3}	High Flare
Y	greater than 10^{-3}	Extreme Flare

As an example a value M3.2 indicates that the flux is 3.2×10^{-5} watts m^{-1}. The Y classification of flares is new, and these extremely large flares are often still classed as X flares with a qualifying number greater than 10. Hence a Y1.6 flare is exactly the same as an X16 one. The above information can also be found on the ionospheric prediction services web site (www.ips.gov.au).

1.4 Observational Techniques

It has already been described how the atmosphere is a complex fluid, whose physics changes with altitude. This is not to say that different fundamental physical laws are obeyed in different regions, rather, that the relative importance of various terms change as the state of the atmosphere changes. Due to this, no single technique can be used to define the atmosphere throughout its entire depth. Different techniques exploit different properties of the atmosphere, making them useful over certain altitude ranges.

Information can be gained about the atmosphere in three basic ways. The first, and most obvious way, is to place a probe in the medium and take measurements, hence these techniques are called *insitu*. A less intrusive technique is to measure some phenomenon whose source of variation is in the atmosphere, then infer atmospheric properties. These techniques are called passive remote sensing. In the last group of techniques, some property of the atmosphere is exploited by actively stimulating it. These techniques are called active remote sensing. More detailed information can be found in Volume 13 of the MAP Handbook (Vincent, 1984). Appendix A of Kelley (1989), and Chapter 2 of Rishbeth and Garriott (1969) also contain more information than that provided here.

The ground based remote sensing systems, such as radar and lidar are characterized by the continuous monitoring of the atmosphere, and height and time resolution of 100–5 km and 1–10 min. The first form of the ground based radar was the ionosonde which sweeps the entire high frequency (HF) region of the electromagnetic spectrum. The total reflection occurs for the ionospheric electron densities in the HF region and the ionosonde obtain reflections from different altitudes at different frequencies, as the atmospheric electron density changes. The ionograms are then used to determine the vertical profile of electron densities.

In the very high frequency (VHF[2] and UHF[3]) region, MST[4] radars can detect weak backscattering arising by refractive index fluctuations in the mesosphere, stratosphere and lower thermosphere (Balsley and Gage, 1980). The MST radar technique was developed from the incoherent radar scatter, which is used to obtain the weak partial reflections due to incoherent scatter from free electrons in the ionosphere. The MST radar technique is capable of obtaining strong and useful echo returns over the height range of 1–100 km. Figure 1.5 illustrates a good example of relative echo powers for various MST radar facilities (Gage and Balsley, 1984). Below $\sim$ 50 km, echoes arise primarily from the fluctuations in the refractive index due to small scale turbulence. In the lower troposphere, water vapor becomes the most important factor and atmospheric density dominates up to the stratopause. In the mesosphere, the echoes arise from the neutral turbulence fluctuations which are enhanced by free electrons.

---

[2] Very-High-Frequency, 30–300MHz

[3] Ultra-High-Frequency, 300–3000MHz

[4] Mesosphere-Stratosphere-Thermosphere

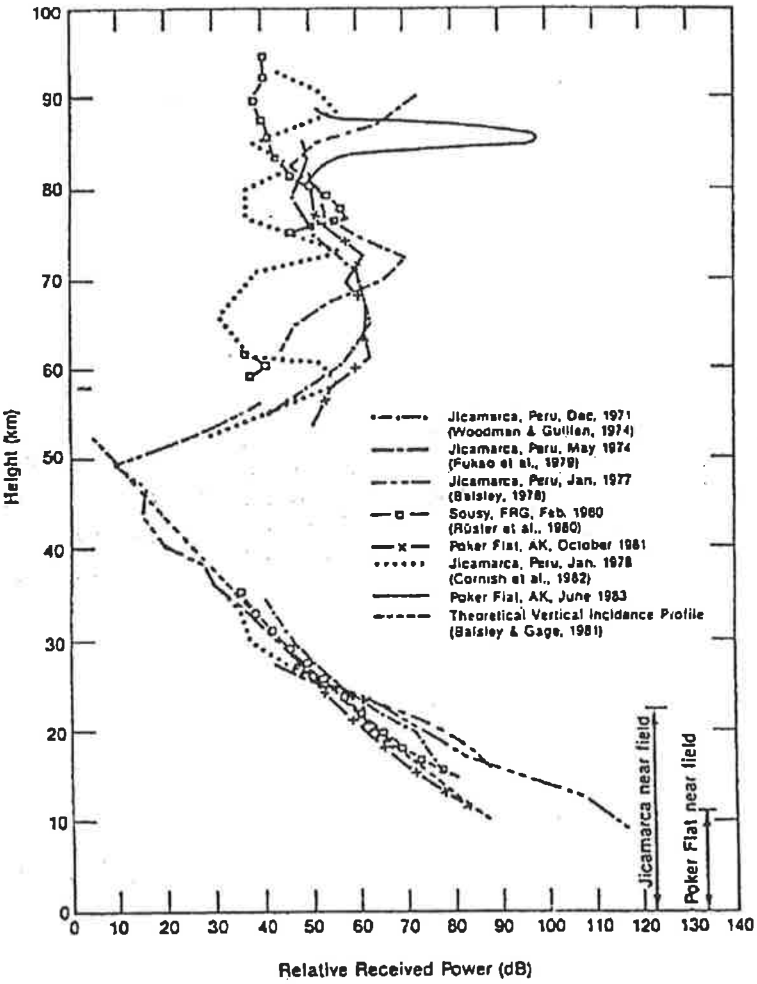

Figure 1.5: Relative echo power profiles for various MST radar facilities [After Gage and Balsley (1984)].

At heights above ~ 80 km, HF and VHF radars can obtain reflections from incoming meteors. The MST radar operating in this mode is called Meteor radar. When the meteors traverse the atmosphere, intense ionisation columns are formed at the heights of the mesosphere and lower thermosphere. These ionized meteor trails scatter radio waves, before they diffuse.

The MF radars can be used to study the partial reflections in the D-region. In this case the radio waves are coherently backscattered from refractive index variations caused by a mixture of changes in the ionization, turbulence and wave motions. As the ionisation is strongly coupled to the neutral air, measurements of scatter motions can be associated with motion of the neutrals. Thus neutral winds and electron densities can be estimated by using such partial reflections.

Although, the ground based electron density measurements depend strongly on the underlying assumptions about the collision frequencies, they provide valuable indirect evidence for the state of the Ionosphere. The use of MF radars to obtain electron density profiles from ~ 60 - 100 km, using differential absorption experiment (DAE) method is an extremely valuable and economical technique. Apart from studying a great deal of lower ionospheric physics, the long record of electron density measurements, can be of assistance in finding the optimal empirical representation of all available experimental evidence, and can be used for exploring the role of various chemical reactions and neutral constituents, e.g. the role of the minor constituent nitric oxide. The following section provides the details of the MF radar used to collect the data for the present work.

1.5 Buckland Park Experimental Arrangements

The Buckland Park MF radar is located 35 km North of Adelaide (34° 38′ S, 138° 29′ E, dip angle −67°), and operates at a frequency of 1.98 MHz. Full details of the radar site and radar installation can be found in Briggs et al. (1969) and Holdsworth and Reid (2003), in brief its description follows.

The radar was constructed in the mid-sixties (Briggs et al., 1969) to enable the investigation of upper atmospheric dynamics, scattering processes, and turbulence. The radar used a 4-element array consisting of two parallel pairs of folded dipoles forming a square for transmission, and a large 1-km diameter array of 89 pairs of individually accessible North-South and East-West aligned half wave dipoles for reception. The radar was upgraded between 1993 and 1995 (Reid et al., 1995), involving the refurbishment of the entire antenna array and the commissioning of new transmission and radar data acquisition systems. The receiving antenna array (hereafter the "antenna array") can now also be used for transmission, enabling the BPMF to operate as a true Doppler radar (Vandepeer and Reid, 1995). The flexibility of the radar allows it's use for specialized experimental campaigns. On-line spaced antenna observations are performed outside campaigns and maintenance periods (D. A. Holdsworth, private communication, 2003).

The transmitting system consists of three 10-channel solid- state modules, each of which can be employed as an individual transmitter. Each transmitter channel consists of a power-amplification (PA) module, a phase control module (PCM), and a transmit-receive (T/R) switch. The PA modules for transmitters 1 and 2 each produce 2.5 kW nominal power, while those for transmitter 3 each produce 5 kW nominal power. The maximum total RMS peak envelope power for the system is therefore 100 kW. Each transmitter channel is connected to three dipoles of the antenna array, and these dipoles can also be used for reception via the T/R switches. The PCMs allow the phase of the transmitted signal for each channel to be adjusted in 8.5° increments, allowing the transmitter polar diagram to be steered off-zenith in any direction. Each transmitter produces length adjustable Gaussian shaped pulses whose optimal pulse length (half-power half-width) is approximately 25μs, producing a range resolution of approximately 4 km. The duty cycle of each transmitter is approximately 0.2%.

The radar data acquisition system (RDAS) consists of 16 receiving channels, each comprising of a receiver and signal processor. Each channel can be connected to individual dipoles or to groups of three dipoles, including those employed for transmission via the T/R switches. The signal processors use 12-bit digitization, which is increased to 16-bit upon coherent integration. The receiver bandwidths corresponds to a range resolution of 1 km, which is half the transmit pulse duration. This bandwidth was chosen with the use of narrower transmit pulse widths and pulse coding in mind, and is not optimal for the 4000 m pulse length currently used. The signal returns can be sampled at range resolutions of 1 or 2 km (see Figure 1.6).

The DAE was incorporated into the on-line BPMF observations on 10th September 1996. The relevant radar parameters for on-line analysis are shown in Table 1.2. Transmission was performed using the North-South aligned antennas, producing a linearly polarized transmitted signal. The transmit beam half-power half-widths used

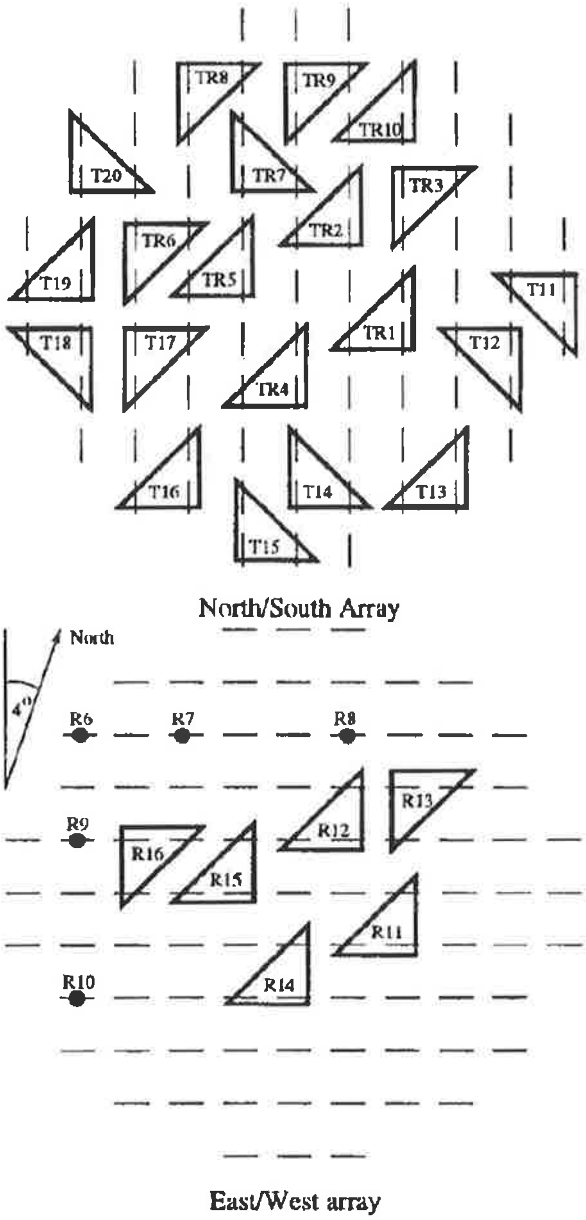

Figure 1.6: Antenna configuration employed for initial routine observations using the Buckland Park MF radar. Each North-South line on the North/South array (left) represents a single North-South aligned antenna, while each East-West line on the East/West array (right) represents a single North-South aligned antenna. The triangles denote the antennas used for observations, and the appropriate transmit channel. Antenna groups denoted TR_i and T_i were connected to transmitter i. Antenna groups denoted TR_i were connected to receiver i via T/R switch i. Antenna groups denoted R_i were connected directly to receiver i. The filled circles denoted R_i were connected to receiver i for meteor observations from March 2000. [After Holdsworth and Reid (2003)].

Table 1.2: Experimental parameters used for routine spaced antenna (SA) analysis for the Buckland Park MF radar.

Parameter	Day Value	Night Value
Height resolution	2 km	2 km
Number of heights	25	15
Start height, km	50	70
Polarization	linear	linear
PRF, Hz	100	20
Coherent integrations	40	8
Effective sampling time, s	0.4	0.4
Number of samples	280	280
Record length, s	112	112

throughout observations are shown in Table 1.3. Reception for DAE is performed using 10 groups of three antennas, using five of the North-South aligned antenna groups used for transmission, connected via transmit-receive (TR) switches to receivers 1 to 5, and the corresponding five East-West aligned groups connected directly to receivers 11 to 15. The 10 linearly polarized received signals are decomposed into five pairs of O- and X-mode polarized components in software, and the resulting 5 pairs of O- and X-mode signals are combined to produce individual 2-min O- and X-mode time-series used for DAE analysis.

Because each of the 10 receiving channels used for DAE reception may have complex gain offsets introduced through the antennas, feeder cables, TR switches and receivers, it is necessary to estimate and correct for any complex gain differences between receiving channels prior to decomposing linearly polarized received signals into the circular components. The technique applied for estimation and correction of complex gain differences is described in the paper published by Holdsworth et al. (2002) (see Appendix B). The consequences of complex gain differences upon the DAE are also described in the same paper, illustrating that small amplitude and phase differences can have significant effects upon the DAE analysis.

The on-line analysis software forms part of a commercially available software suite supplied by Atmospheric Radar Systems (ATRAD). Identical DAE software is also used at the Wakkanai and Yamagawa MF radars in Japan, the Poker Flat MF radar

Table 1.3: Observation periods for routine spaced antenna (SA) analysis for the Buckland Park MF radar.

Observation period	Number of antennas	Transmit HPHW (deg)	Peak Power (kw)
10/9/1996 to 16/7/1997	30	10	25
16/7/1997 to 4/1/1998	60	5	75
23/3/1998 to 23/4/1998	30	10	25
24/3/1998 to 29/6/1998	60	5	50
2/3/1999 to 31/7/1999	75	4.5	82.5
1/8/1999 to present	60	5	50

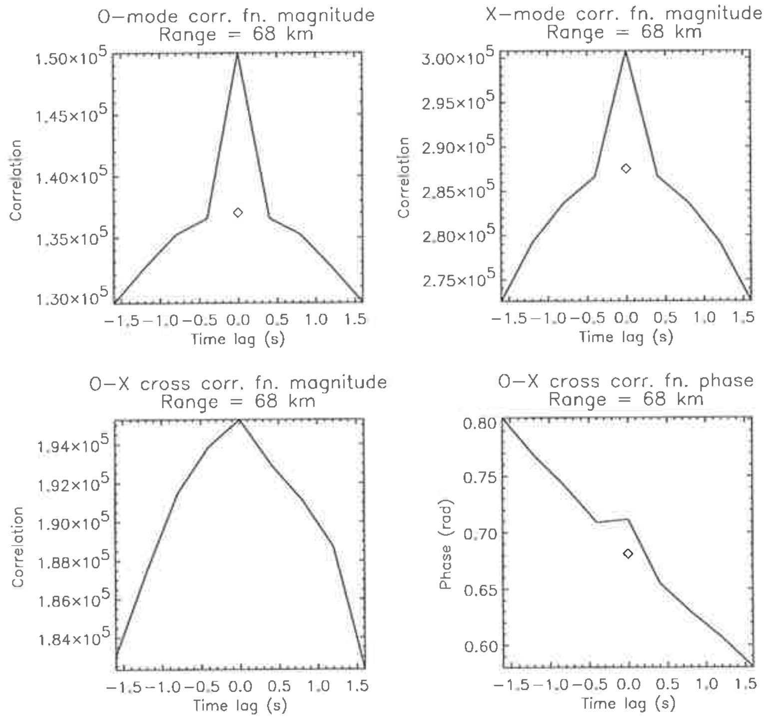

Figure 1.7: Example of zero-lag auto-covariance and cross-covariance functions utilized to calculated amplitude ratios and phase differences.[After (private communication, D.A. Holdsworth, 2003)].

in Alaska (Igarashi et al., 1999), and the Andenes MF radar in Norway (W. Singer, private communication). These MF radars differ from the BPMF radar in that wider transmitter polar diagrams are used, and that transmission and reception is alternated between O- and X- mode polarisation after every set of coherent integrations.

The amplitudes of the O- and X-mode returns are calculated using the square root of the zero-lag auto-covariance function magnitudes obtained after interpolating over zero-lag to remove the effects of noise. These amplitudes are then used to determine

Table 1.4: Rejection criteria for DAE analysis.

Error code	Criteria
1	Saturation level in either mode exceeds 5 %
2	SNR in either mode $<$ -6 dB
3	Amplitude ratio less than 0.25
4	Electron density $< 10\text{cm}^{-3}$

A_{xo} (ratio of O- and X- mode amplitudes). The phase difference ϕ_{xo} is estimated using the zero-lag cross-covariance phase (Figure 1.7).

The analysis rejection criteria are shown in Table 1.4. Criterion 1 is applied because reliable amplitude ratios cannot be obtained from saturated data (when the signal goes beyond the voltage limit while digitizing the signal). Criterion 2 is applied because the zero-lag auto-covariance function interpolation used to determine the signal amplitudes cannot provide accurate estimates of the signal amplitude for SNRs below -6 dB. Criterion 3 is introduced as a consequence of the assumption of circular polarisation used in the analysis. Unless observations are conducted at the magnetic dip-poles of the world, the actual polarisation of O- and X-mode components are conjugate ellipses. Assuming O- and X-modes to be circular components therefore causes some X-mode signal to be present in the assumed O-mode signal, and some O-mode signal to be present in the assumed X-mode signal. Consequently, the strong O-mode returns obtained during daytime observations above 80 km can result in the assumed X-mode returns containing only O-mode signal, producing an erroneous amplitude ratio. Criterion 3 is therefore used to reject data indicative of such "leakage" from the analysis. Criterion 4 is used to reject negative and small positive values of electron densities that can occur due to statistical errors in the A_{xo} profiles.

It should be noted that the 2-min record lengths used for A_{xo} and ϕ_{xo} estimation may be considered short, given the accepted belief that record lengths of approximately 50 times the fading time are required for accurate parameter estimation using correlation functions (e.g. May, 1988). Typical fading times for the BPMF radar range from 1 to 6 seconds, suggesting a minimum acceptable acquisition period of 5-min. However, we note that the BPMF radar has used 2-min observations for on-line spaced antenna wind observations for over 20 years, and has produced many years of valuable dynamical information (e.g. Vincent et al, 1998). On implementing the DAE analysis on the BPMF radar, there was no reason to believe that this could not be translated into successful 2-min DAE observations.

1.6 IRI95 Overview

The International Reference Ionosphere (IRI) provides a representation of electron density and the ion composition in the E and D region (from 60 km upward) based on measurements from the ground (ionosonde, incoherent scatter radar) and from rockets (Bilitza, 1998). In IRI, the D region profiles described in terms of sunspot number and solar zenith angle are based on a survey of the most reliable rocket measurements by Mechtly (1974).

As a new option IRI will now include the $D-$region model of Friedrich and Torkar (2001) called FIRI and a brief description of this model is provided in the following section. They use the full set of available and reliable rocket measurements, whereas the standard IRI $D-$region model (Bilitza, 1990) is based on a limited selection of these profiles. Also included in IRI as a new option will be the $D-$region model by (Danilov, 1998) which is based on a large number of rocket data mostly from mid-latitudes. Different from the other two IRI options this assumes that there is no variation with solar activity. As a new feature the model specifies the effect of meteorological influences: quiet(Q), stratospheric warming(SW), weak winter anomaly(WA), strong WA. IRI model results can be found on the IRI $http://www.iri95.html$, the web pages of "NASA's National Space Science Data Center". A good overall description of the IRI model is provided in the IRI-90 report (Bilitza, 1990).

1.7 FIRI Overview

The most common of the methods for partially in situ radio wave propagation methods makes use of the fact that the plane of the polarization rotates as a function of total electron content (TEC), this effect is called Faraday rotation. The name FIRI implies that the data contributed to IRI using electron density data based on Faraday rotation experiment (Friedrich and Torkar, 2001). The data used for establishment of FIRI are restricted to the results from rocket-born soundings with a radio wave propagation experiment. As indicated above, the $D-$region is covered by the general empirical ionospheric model IRI. The latest version of model FIRI-05 is the result of several precursor attempts and details of each version can be found in Friedrich and Torkar (2001). All the versions were reported to have three features in common: (i) Only "appropriate" data, that is, all based on rocket borne wave propagation experiments are used. (ii) All altitudes are treated independently from each other and (iii) in general, analytical descriptions are established for neutral density levels (or pressure surfaces) rather than for geometric altitudes.

For our comparisons FIRI model data are obtained from the web pages of $ftp : //nssdcftp.gsfc.nasa.gov/models/ionospheric/iri/iri2001/fortran_code/iridreg.for$. Both IRI and FIRI model comparisons with our observations are presented in this thesis. Since the FIRI model results were available almost at the end of this thesis work, only limited comparisons are made.

1.8 Thesis Overview

The structure of the thesis is as follows: Detailed description of MF radar facility at Adelaide is presented in this chapter (Chapter 1) along with the basic structure of Ionopshere. Chapter 2 details the differential absorption experiment (DAE) used for the present study along with collision frequencies used for the calculation of electron densities. In Chapter 3, we study mid-latitude, lower ionospheric (D region) characteristics using data from daytime radar observations. Chapter 4 details the nighttime ionization, using seasonal, diurnal and spatial variation of the data at Adelaide. Theoretical ionization sources and the findings of previous workers are compared with the present findings. Finally, Chapter 5 discusses the role of dynamics on the electron density profiles. Partial reflection winds data are used to study the effects of tides and other atmospheric waves on the lower ionosphere.

Chapter 2

Essentials of the DAE

2.1 Introduction

When an electromagnetic wave travels through a plasma, the electrons are set in motion by the electric vector of the wave. If there are no collisions, the oscillating electron (or ion) will reradiate all of its energy, which will be restored to the wave. The process of absorption and reradiation of the energy is accomplished with a change of phase which brings about the change in phase velocity and, hence, of refractive index.

The presence of the geomagnetic field makes the plasma (ionosphere) dually refractive, that is there exits two modes of propagation. If a linearly polarized radio wave is transmitted, the signal is decomposed into two circularly polarized waves rotating in opposite direction. If the geomagnetic field has a component in the propagation direction, the two partial waves experience different refractive indices. The composition at the receiver will maximize at an angle with respect to original linear polarization (Faraday rotation). The imaginary parts of the refractive indices are generally different (differential absorption). The received polarization pattern is therefore in general elliptical. The two amplitudes measured at the receiver are used to calculate electron densities.

To derive electron densities for a given geometry, signal frequency, geomagnetic field and collision frequency, it requires the use of magneto-ionic theory. The generally accepted magneto-ionic theory is the one formulated by Sen and Wyller (1960) in which collision frequency is proportional to pressure. Using these basic principles partial reflection differential absorption experiment (DAE) has been implemented at Buckland Park. This chapter describes the implementation of the DAE using the Buckland Park MF (BPMF) radar. Section 2.2 describes the basis of the technique, the assumptions used, and their validity. A rigorous treatment of collision frequency is provided in Section 2.3. In Section 2.4 the height structure and seasonal variation of amplitude ratios are presented. Finally Section 2.5 deals with the electron density estimation. This chapter complements and extends the work presented in Appendix A and Appendix B.

2.2 The Differential Absorption Experiment (DAE)

The differential absorption experiment proposed by Gardner and Pawsey (1953) estimates the electron density using the ratio [illegible] of the extraordinary (E or X) to ordinary (O) mode amplitudes (A_{xo}) of the signals returned from the ionospheric D-region. The amplitude ratio at range h is assumed to be given by

$$A_{xo}(h) = R_{xo}(h)\ \exp[-2\int_0^h (k_x(h) - k_o(h))dh] \tag{2.1}$$

where $R_{xo}(h)$ is the ratio of X- to O-mode reflection coefficients at range h, and $k_x(h)$ and $k_o(h)$ are the absorption coefficients for X- and O-mode radiation, respectively. If A_{xo} is measured at two ranges h_1 and h_2 with small separation $\triangle h$, such that k_x and k_o can be considered constant, (2.1) may be rewritten as

$$\ln\left(\frac{A_{xo2}}{A_{xo1}}\right) = \ln\left(\frac{R_{xo2}}{R_{xo1}}\right) - 2(k_x - k_o)\triangle h \tag{2.2}$$

where A_{xoi} and $R_{xoi}, i = 1, 2$, are the amplitude and reflection coefficient ratios, respectively, at ranges h_i. Using the assumption of Fresnel reflection from perturbations in electron density (i.e. $\triangle N/N$), $R_{xo}(h)$ can be computed using an assumed electron density N and electron-neutral collision frequency $\nu(h)$. The electron density $N(h)$

can be expressed in terms of $R_{xo}(h)$ and $k_{o,x}$ via (2.2) using the Appleton-Hartree magneto-ionic equations (Budden, 1985). In formulating these equations (constitutive relations of the medium for radio waves of small amplitudes), it was assumed that the collision frequency is independent of electron energy and therefore the distribution of electron speeds were neglected.

However, for the propagation of medium frequencies in the D and lower E regions, where the collision frequency is comparable with the angular wave frequency, the above assumption is no longer valid. Hence, the DAE has subsequently been enhanced by the use of the generalized magneto-ionic equations (Sen and Wyller, 1960). The Sen-Wyller equations were adopted by subsequent investigators, either in the quasi-longitudinal (Belrose and Burke, 1964) or "full" form. The solution for electron density N_e at a particular height h_i requires the derivatives of equation 2.2.

$$\frac{d}{dh}\left(ln\frac{A_{xo2}}{A_{xo1}}\right) = \frac{d}{dh}\left(ln\frac{R_{xo2}}{R_{xo1}}\right) - \frac{2(k_x - k_o)}{N_e}N_e \tag{2.3}$$

where all quantities are evaluated at h_i, $i = 1, 2,$. Thus for the DAE:

$$N_e = \left(\frac{\frac{d}{dh}\left(ln\frac{R_{xo2}}{R_{xo1}}\right) - \frac{d}{dh}\left(ln\frac{A_{xo2}}{A_{xo1}}\right)}{\frac{2(k_x - k_o)}{N_e}}\right) \tag{2.4}$$

In practice, the experimental derivatives are found by comparing measurements at finite height differences, and those for the reflection coefficients are estimated from models of the collision frequency profile and irregularity structure. Theoretically, in the situation where differential absorption is small k_x and k_o tend to zero, and (2.2) becomes

$$A_{xo} \approx R_{xo}. \tag{2.5}$$

This equation can be used to determine the collision frequency at the base of the D-region. In section 2.3, a detailed explanation of collision frequency estimation and use in calculating electron density for our location is given.

A number of authors have investigated the assumptions and applicability of the DAE. The assumption of reflection from electron density perturbations was investigated by Piggott and Thrane (1966), Belrose et al. (1972) and Meek and Manson (1981), who also considered reflection from perturbations in collision frequency (i.e. $\triangle\nu/\nu$). The relative importance of the two mechanisms is often parameterized as

$$\alpha = \frac{\triangle\nu/\nu}{\triangle N/N}, \tag{2.6}$$

where $\alpha = 0$ indicates reflections from perturbations in electron density (Piggott and Thrane, 1966). Their investigations suggested reflection from electron density perturbations was the dominant mechanism. The Fresnel reflection assumption was investigated by Flood (1968), who proposed a volume scatter technique to account for scatter from multiple reflectors and variability of differential absorption within the radar volume. This model was extended by Cohen and Ferraro (1973) by including variability of the reflection coefficients throughout the radar volume. These authors illustrated that significant errors could result from using (2.2) in the multiple reflection situation for transmit pulses with lengths exceeding 25 μsec. Deconvolution techniques have also been proposed to account for the finite transmitter pulse length (Coyne and Belrose, 1974).

The DAE has also been complemented by the use of the differential phase experiment (DPE), which uses the phase difference ϕ_{xo} between the X- and O- mode signals to provide a computationally independent estimate of the electron density (VonBiel and Flood, 1970). An analogous expression to (2.2) applies to the differential phase $\phi_{xo} = \phi_x - \phi_o$, given by

$$\Delta\phi_{xo} = \Delta\Phi_{Rxo} + \frac{2\omega}{c}\int_0^h (\mu_x - \mu_o)dh. \tag{2.7}$$

Here Φ_{Rxo} is the phase difference that occurs on reflection and μ_x, μ_o are the real parts of the respective refractive indices. In analogy with the DAE, when differential absorption is small

$$\phi_{xo} \approx \Phi_{Rxo}, \tag{2.8}$$

where Φ_{Rxo} is the difference in the phase of the extraordinary and ordinary mode reflection coefficients. Use of (2.5) and (2.8) allows DAE and DPE to be combined to provide estimates of the collision frequency for comparison with the input model estimates.

Despite the alternative techniques described above, the implementation of the original DAE technique incorporating the Sen-Wyller equations is generally considered adequate (Manson and Meek, 1984), in part due to it's simplicity and the fact that the volume scatter and deconvolution techniques are unsuitable for on-line use.

2.3 Collision Frequency Profiles $\nu(h)$

Since one of the main objectives of the investigations is the determination of seasonal variations of N_e, it is necessary and important to estimate the seasonal variations of ν(h) as this is used in the computation of N_e.

Various expressions for the collision frequency have been used. One commonly used expression gives the profile in terms of atmospheric pressure p,

$$\nu(h) = 6.4 \times 10^7 p \text{ s}^{-1} \tag{2.9}$$

where p is in hPa (Gregory et al., 1967). Equation (2.9) is an empirical expression deduced from the then best available laboratory measurements of momentum transfer cross-sections involving collisions between electrons and neutral gas molecules, such as nitrogen and molecular and atomic oxygen.

Recently, however, new laboratory studies of the mobility of electrons in atmospheric gases have resulted in a significant revision of the collision cross sections for nitrogen (Robertson et al., 1997). Using values of atmospheric temperature and number density (or pressure) from the CIRA-86 it is possible to compute the mean momentum transfer collision frequency of electrons with neutral gas molecules in a weak plasma (Robertson et al., 1997) using the following expression

$$\nu = \left(\frac{8kT}{\pi m}\right)^{1/2} \frac{N}{N_o} \int_0^\infty \frac{\sigma}{\sigma_o} \left(\frac{E}{kT}\right) exp\left(-\frac{E}{kT}\right) d\left(\frac{E}{kT}\right) \tag{2.10}$$

where k is the Boltzmann constant, N is the gas number density in units of m^{-3}, E is the electron energy (Joules), T is the temperature of the gas, σ is the momentum transfer collision cross section of the gas molecules, and m is the electron mass. N_o and σ_o are normalizing constants chosen so that $N_o\sigma_o = 1$. Equation (2.10) is used to compute the collision frequencies using the latest laboratory measurements of momentum transfer collision cross sections for N_2 (Robertson et al., 1997), together with earlier values for O_2 and O (Phelps and Pack, 1959); (Neyaber et al., 1961).

Unless otherwise stated, all the electron density values are estimated from collision frequencies computed using equation (2.10). Comparison of experimentally and laboratory derived $\nu(h)$ curves and other details of how the electron densities are estimated for the present study are discussed below.

Although a collision frequency profile is assumed in the calculations it is important to note that it is possible to estimate ν directly under certain circumstances. For example, in the lowest part of the ionosphere, where the differential absorption and differential phase are negligible, use of (2.5) and (2.8) allows DAE and DPE to be combined to provide estimates of the collision frequency.

This allows for the correction of any discrepancies in the assumed pressure profile by moving the $\nu(h)$ profile up or down in height and recomputing R_{xo} until the R_{xo} and A_{xo} curves match (Belrose and Burke, 1964; Belrose et al., 1972). Extrapolation of these measurements to higher heights by means of atmospheric pressure data provides a collision-frequency profile for use with (2.1). Therefore, the measured echo amplitude ratios and phase variations at low heights give an estimate of the collision frequency height profile. If an atmospheric scale height is assumed this provides a way of deriving for the collision frequency height curve.

Figures 2.1, 2.2, 2.3 and 2.4 provide examples of amplitude ratio and phase difference distributions at different heights. The distributions were constructed using 2-min

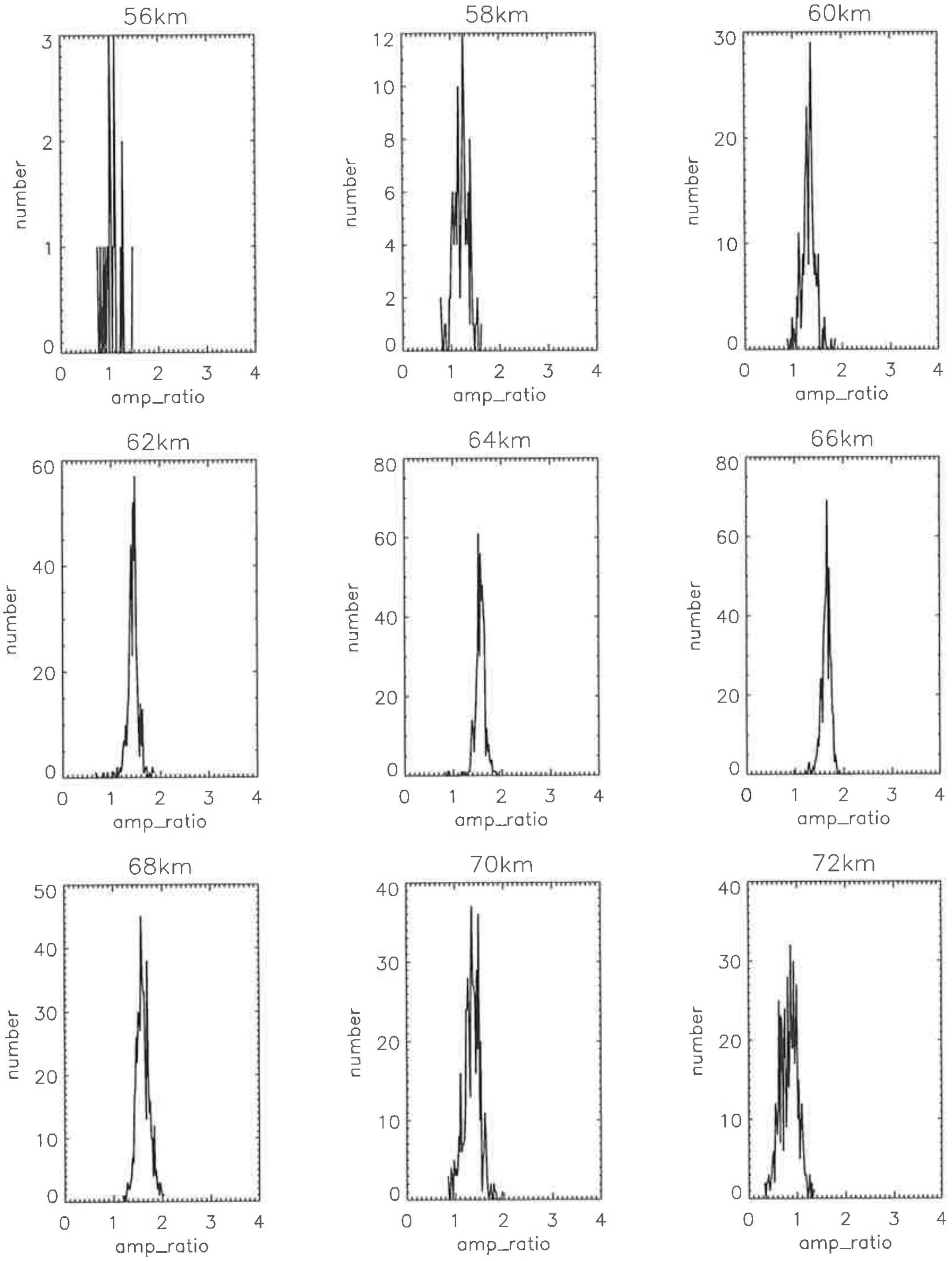

Figure 2.1: Amplitude ratio distributions in November 1997, for the 56-70 km height range at noon.

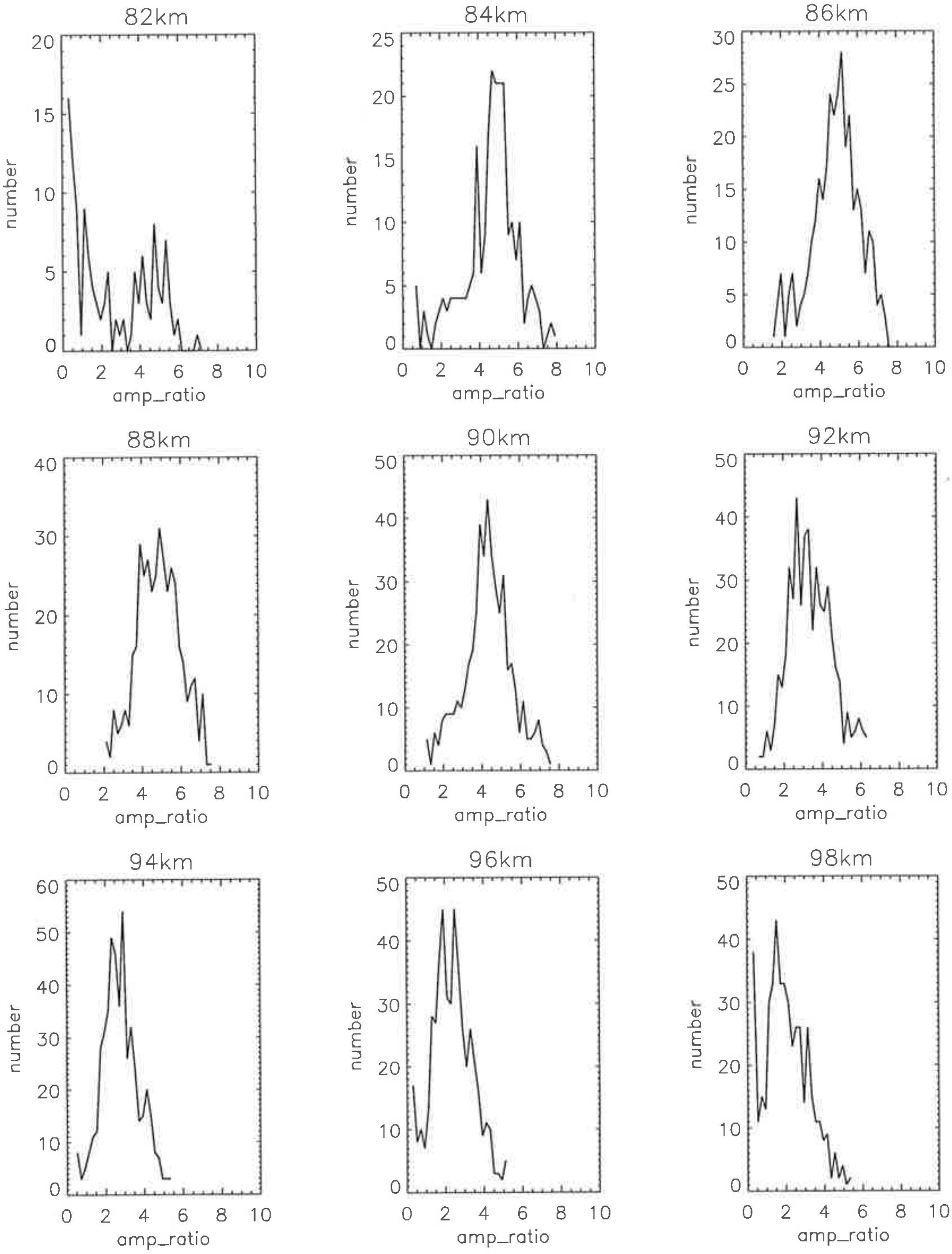

Figure 2.2: Amplitude ratio distributions in November 1997, for the 82-98 km range at nighttime

data samples during November 1999. It is evident the distributions are approximately Gaussian in shape and the peak values clearly defined. However, the scatter increases and the distributions become broader with increasing height.

Monthly-mean values for A_{xo} and ϕ_{xo} were calculated using an iterative procedure to remove all points (for the histograms) more than two standard deviations from the mean. The standard deviations of the resulting cleaned distributions were used to indicate the reliability of the echo amplitudes and phases. The method of obtaining a collision frequency profile from partial reflection data by the use of (2.5) and (2.8) and atmospheric pressure data is as follows.

Initial collision frequency profiles for each month were deduced by using (2.9) and the CIRA-86 pressure data for a latitude of 35°S. Corrections to the $\nu(h)$ profile for each month were estimated by iteratively shifting the initial profile bodily up or down in height and performing χ^2-tests to find the best match between the A_{xo} and R_{xo} height curves at lowest heights (Belrose and Burke, 1964). Similar procedures are followed for comparing the ϕ_{xo} and Φ_{xo} curves.

Values of p obtained from a suitable model, such as CIRA-86, the COSPAR International Reference Atmosphere (e.g. Fleming et al., 1990), gives $\nu(h)$ at any desired latitude and season. Similarly, the input vertical profiles of magnetic field strength $B(h)$ and inclination angle, $\theta_B(h)$, can be obtained from the International Geomagnetic Reference Field (IGRF) model (e.g. Barton, 1997) for the relevant latitude and longitude. The ν, B, and θ_B profiles are then used to calculate the reflection coefficient ratio R_{xo} and absorption coefficient k_x,k_o profiles.

Examples of the amplitude and phase curve comparisons before and after correcting the $\nu(h)$ profile are shown in Figure 2.5. The horizontal bars show the estimated standard errors. The heights to be matched were chosen where there is negligible absorption, which were assumed to occur at least 4 km below the height of maximum A_{xo}, the so-called turnover height. In most cases the comparison heights for noon data were located between 58 km and 62 km, which are much below the average turnover heights of between 66 km and 68 km.

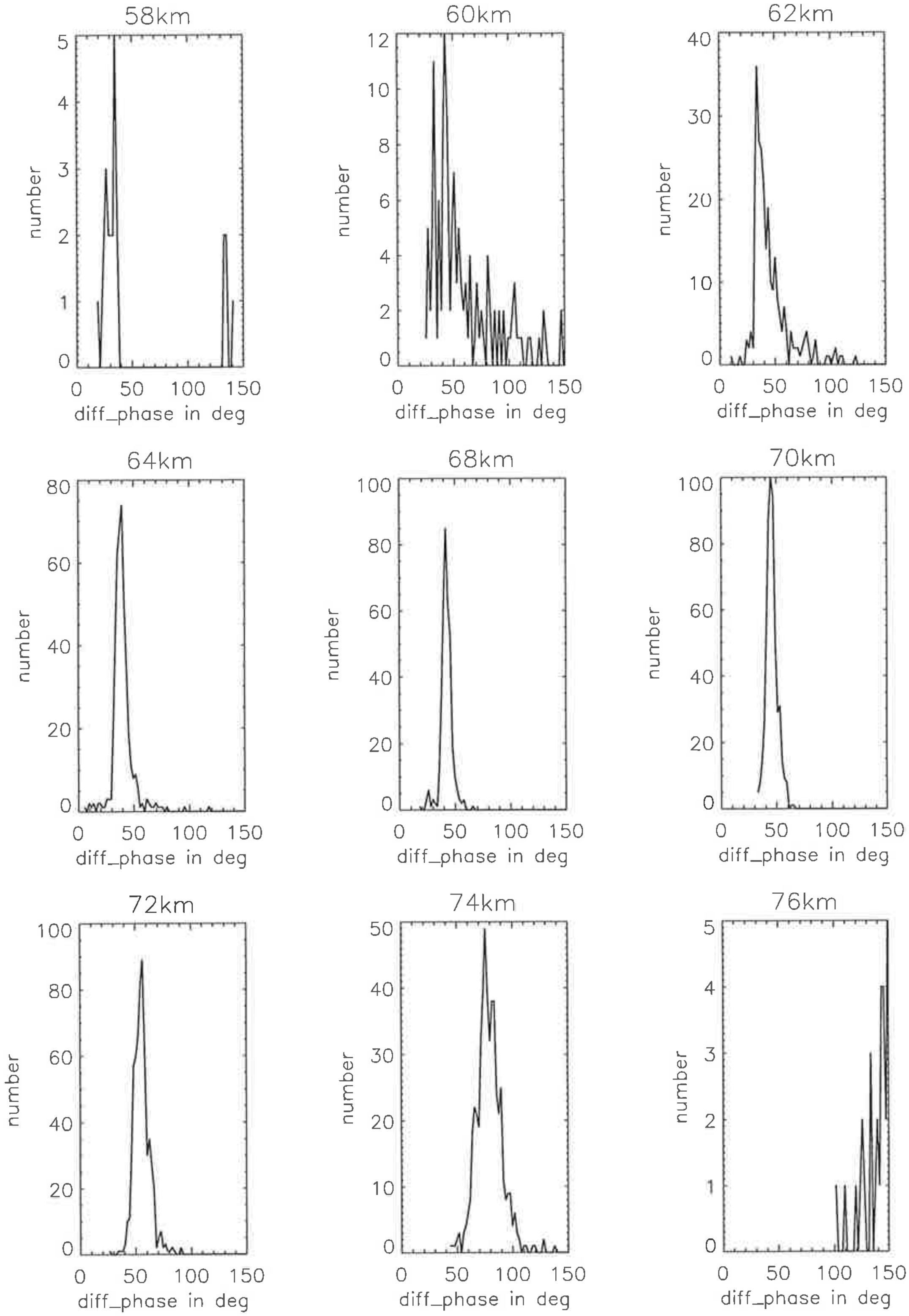

Figure 2.3: As for Figure 2.1, but for phase-difference distributions.

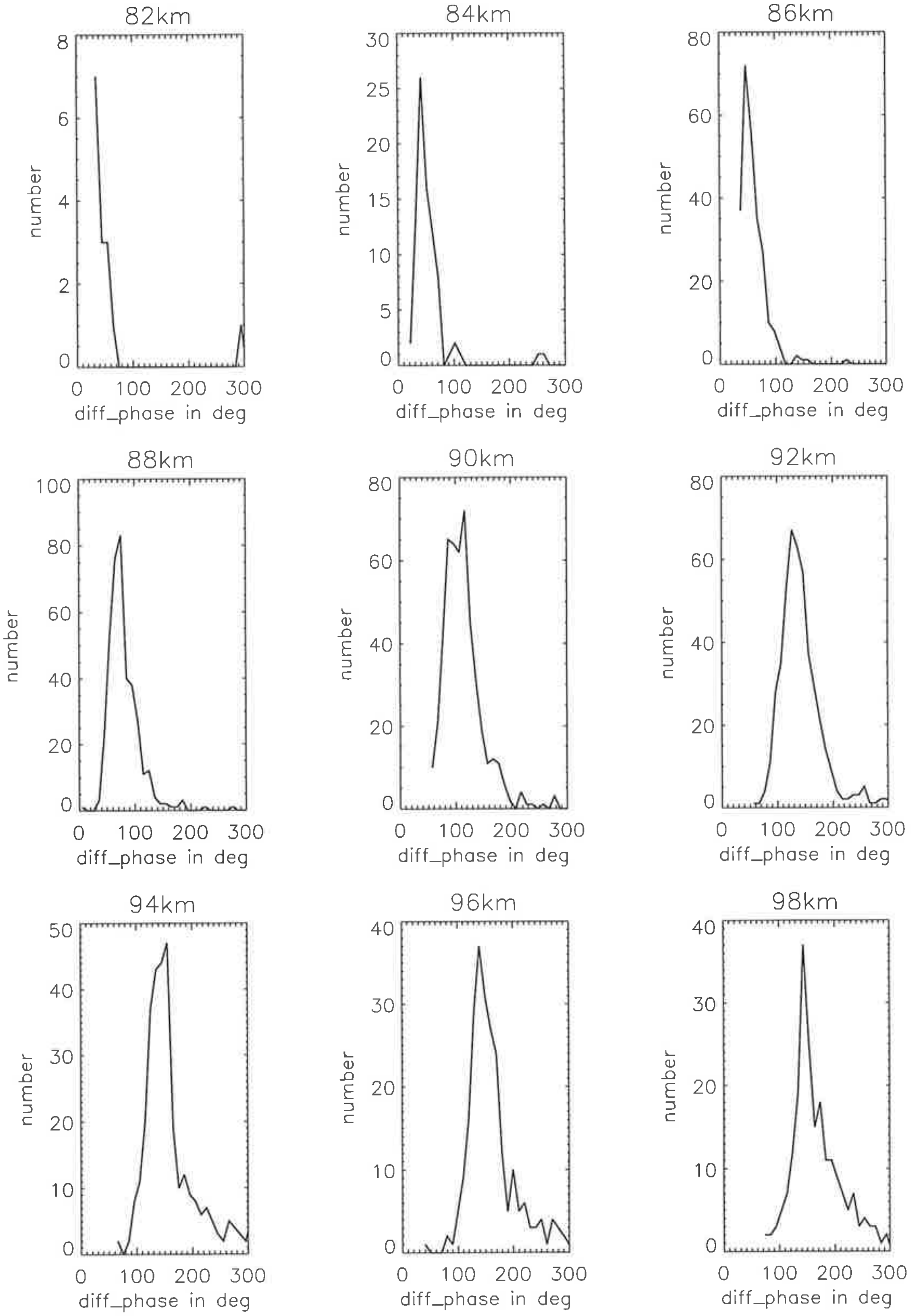

82km

84km

86km

88km

90km

92km

94km

96km

98km

Figure 2.4: As for Figure 2.2, but for phase-difference distributions.

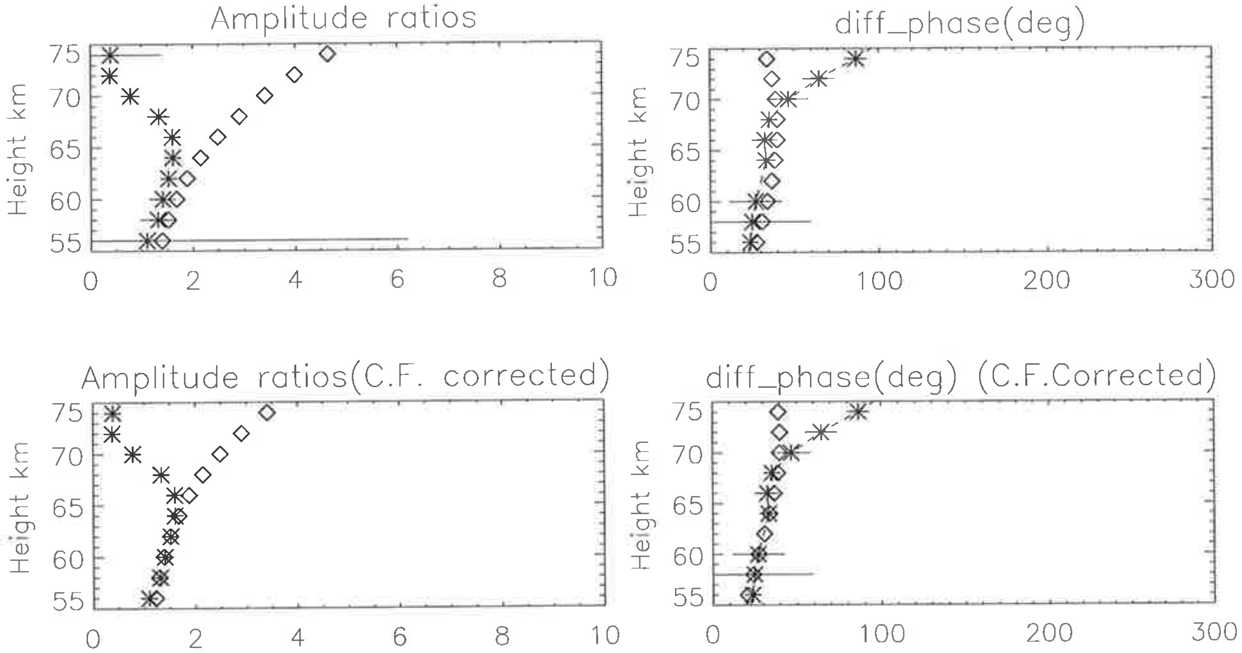

Figure 2.5: Monthly mean amplitude ratios (left) and differential phase (right) shown by (∗), compared with reflection coefficient ratios and phase difference on reflection (◇), before (top) and after (bottom) collision frequency correction. All data are for November 1999.

Table 2.1: Shifts in reference collision frequency profile deduced from amplitude ratios

Month	1996	1997	1998	1999	2000
January	-	-5 km	-	-	-5 km
February	-	-3 km	-	-	-8 km
March	-	-3 km	-3 km	-4 km	-5 km
April	-	-3 km	-	-4 km	-4 km
May	-	-3 km	-3 km	-4 km	-3 km
June	-	-3 km	-4 km	-3 km	-4 km
July	-	-2 km	-	-3 km	-4 km
August	-	-3 km	-	-3 km	-4 km
September	-4 km	-4 km	-	-3 km	-4 km
October	-4 km	-4 km	-	-3 km	-3 km
November	-4 km	-5 km	-	-4 km	-5 km
December	-5 km	-6 km	-	-4 km	-3 km

Table 2.2: As for Table 2.1, but for differential phase.

Month	1996	1997	1998	1999	2000
January	-	-5 km	-	-	-5 km
February	-	-2 km	-	-	-5 km
March	-	-2 km	-	-5 km	-7 km
April	-	-0 km	-	-6 km	-4 km
May	-	-0 km	-	-6 km	-3 km
June	-	-4 km	-	-4 km	-7 km
July	-	-6 km	-	-2 km	-7 km
August	-	-9 km	-	-4 km	-6 km
September	-0 km	-6 km	-	-4 km	-7 km
October	-0 km	-5 km	-	-3 km	-7 km
November	-6 km	-0 km	-	-4 km	-6 km
December	-7 km	-0 km	-	-5 km	-1 km

The corrections are referred to in terms of the height shift to the $\nu(h)$ profile. The estimated shifts for the entire data set due to differential amplitude and differential phase methods are given in Tables 2.1 and 2.2. The shifts shown in Table 2.1 are from the noon data. However, they remained constant for data taken between 0800 and 1600 local solar time. Comparisons between data taken on quiet days and disturbed days show, either that there is no change in the amplitude ratio, or no data below 64 km whereas there is marked difference at heights above this height. This supports the assumption that there is negligible differential absorption below 64 km. The day-to-day variations of the height shifts lie within a ±1km range.

During daytime above 82 km it is difficult to use this technique to estimate corrections to the $\nu(h)$ profile, due to the leakage of the much stronger O-mode signal into the decomposed X-mode signal. In an effort to estimate collision frequencies above 80 km an attempt has been made to make use of the available nighttime data. The height range between about 85 km and 100 km is one in which it is especially difficult either to measure or to deduce atmospheric parameters and collision frequencies with sufficient accuracy to make a useful comparison or to interpret the observed magnitude of the absorption suffered by radio waves. As can be seen from Figures 2.2 and 2.4 the distributions of differential amplitude and phase show considerable spread at the upper heights.

Comparison of the height shifts deduced from amplitude-ratio and differential-phase data reveal that, in most cases, the collision frequency profile that best matches the phase data is also that which gives the best match to the amplitude ratio data (Tables 2.1 and 2.2). In all cases the $\nu(h)$ curve computed using (2.9) had to be moved down in height by values of the order of half a pressure scale height. The recomputed collision frequencies are found to be significantly larger than the initial values. The reliability of the deduced collision frequencies can be best judged by the self-consistency of the results and by comparing with collision frequencies from other experiments.

Equation (2.9) was based on the best laboratory electron-neutral collision cross-sections that were available at the time (Gregory and Manson, 1969). As stated above, however, new laboratory studies of the mobility of electrons in atmospheric gases have resulted in a significant revision of the collision cross sections for nitrogen (Robertson et.al., 1997). Equation (2.10) is used to compute the collision frequencies using the latest laboratory measurements of momentum transfer collision cross sections for N_2 (Robertson et.al., 1997), together with earlier values for O_2 (Hake and Phelps, 1967) and O (Phelps, 1959; Neyaber, 1961).

The comparison of experimentally and laboratory derived $\nu(h)$ curves for conditions in May 1999 are shown in Figure 2.6. This is representative of profiles found for other months and years. The estimated collision frequency profiles are compared with values computed from the latest laboratory measurements data and are found to be in excellent agreement up to about 80 km above which height the laboratory-based values produces a value of ν smaller than the experimental values. This is due to the increasing levels of atomic oxygen in the atmosphere at these levels, whereas the radar estimates are extrapolated from lower heights where N_2 and O_2 predominate. The key finding, however, is the excellent agreement at the heights where the DAE/DPE observations are most accurate.

Although, it is possible to investigate the nature of irregularities with the help of

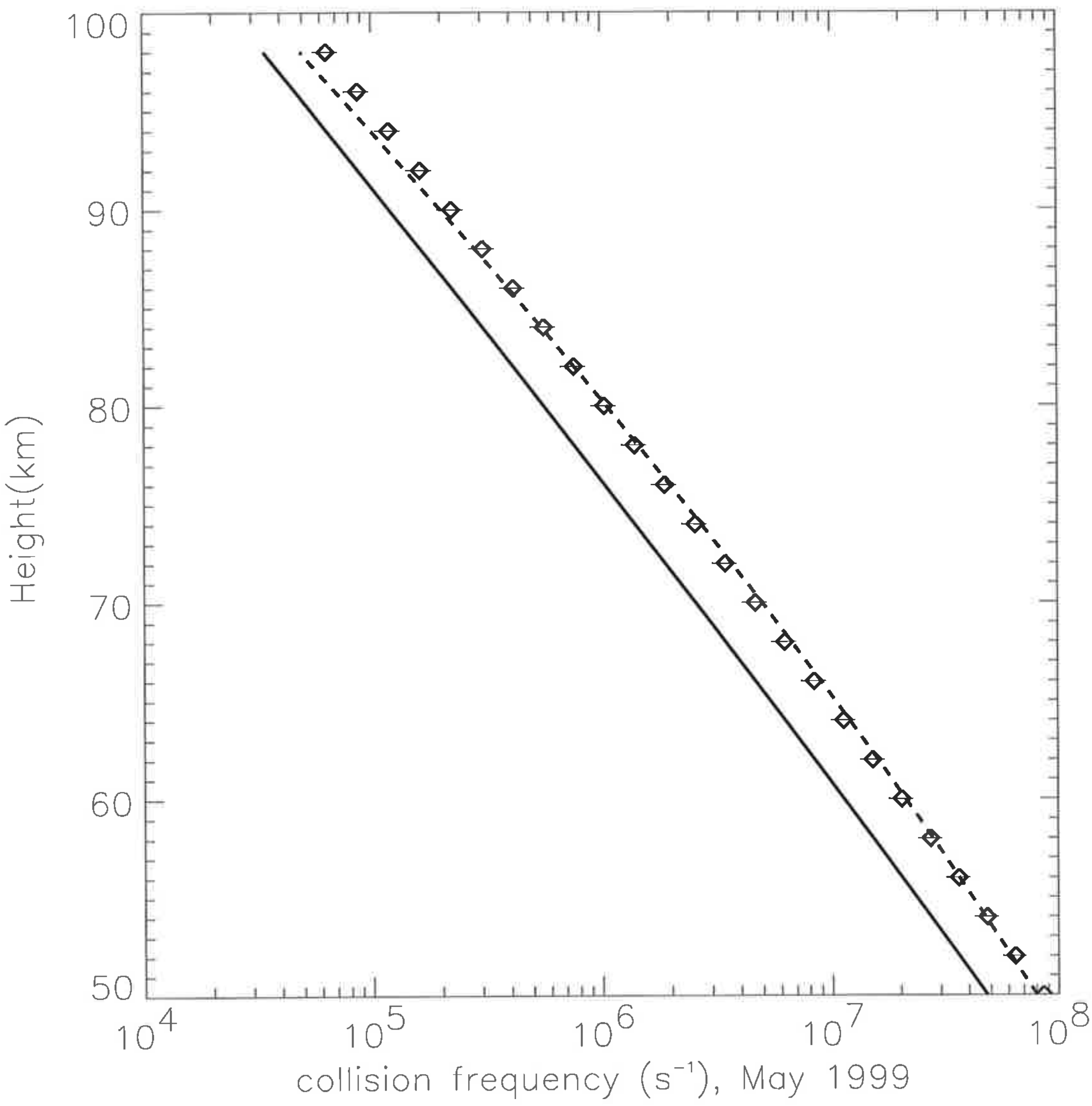

Figure 2.6: Collision frequency profile for May 1999 estimated from ionospheric data (◇) compared with values computed from the latest laboratory collision cross-sections (dashed line) and from equation 2.9 (solid line).

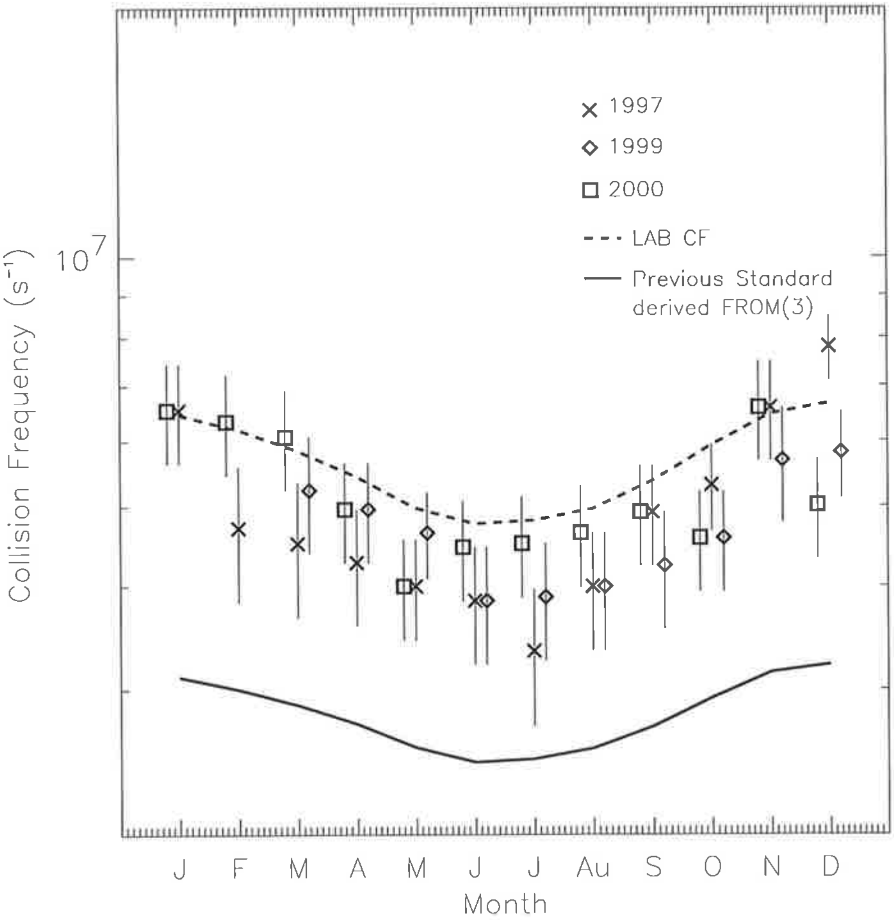

Figure 2.7: Annual variation of collision frequency estimated for a height of 70 km. The dashed line is the collision frequency computed from laboratory cross-sections using (6). The solid line gives the collision frequencies derived using Equation (3).

simultaneous measurements of differential absorption and differential phase data we have taken into the fact that, it has already been established by previous workers like (e.g. Belrose et al., 1972) that electron density irregularities predominate in the region around 60 km. Therefore, the discussion in this study is limited to an interpretation of the data assuming reflections from electron density irregularities. There is little or no evidence of day-to-day variation in either the amplitude ratios or differential phases at the lowest altitudes.

2.3.1 Seasonal and solar cycle variation of $\nu(h)$

Figure 2.7 shows the seasonal variation of collision frequency at 70 km height for different years. It illustrates the degree of month to month and inter-annual variability. The data from September 1996 to Dec 1997 were from a period of low solar activity and the remaining data were during the period of moderate to high solar activity. The 10.7 cm flux during the period 1996–1997 varied from 70 to 100 flux units, whereas during 2000 it varied from 100 to 220 flux units.

From Table 1 the shifts (the change in collision frequency from the reference collision frequency profile) indicate that the collision frequency does not change with solar activity at lower heights. This conclusion differs from that of Belrose and Hewitt(1964) who concluded that at Ottawa the collision frequencies for heights below about 65 km varied with solar activity, but did not vary with season. This conclusion does, however, accord with that of Thrane and Piggott (1966).

Overall, the seasonal changes inferred from the observations are in general agree with variations derived from the calculated values of ν, with a summer to winter ratio of 1.36. However, the values of ν inferred from observations tend to be systematically smaller than the values derived via (6). This may be because the pressures used to compute ν are listed in log-pressure height coordinates in CIRA-86 whereas the radar observations are made in geometric height. Log-pressure heights are usually very close to geometric values in the middle atmosphere, but there are small ($\sim$1 km) differences (e.g. Andrews et al., 1987). The two methods gave results in general agreement, indicating that both laboratory data and partial reflection data are indeed applicable to lower ionospheric conditions. The laboratory data seems to be representative of ideal conditions simulated in the laboratory whereas the ionospheric data are useful in finding the real-time fluctuations in collision frequency. Overall, the collision frequencies are a factor of about 1.6-1.9 larger than values derived from Equation 2.9, (the previous standard). The work presented here suggests a $\nu(h)$ relation as

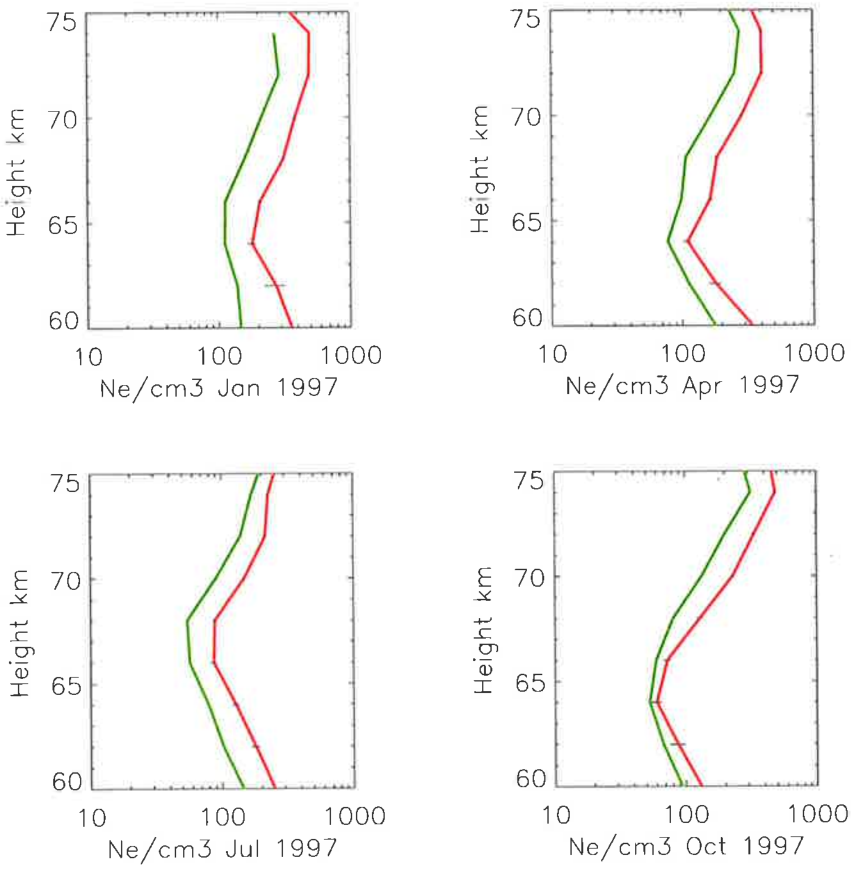

Figure 2.8: Effect of change in collision frequency on the magnitude of electron density, (red) due to latest laboratory collision frequencies and (green) due to old standard collision frequency profile

$$\nu(h) = 1.21 \times 10^8 p \text{ sec}^{-1} \tag{2.11}$$

2.3.2 Effect of collision frequency changes on electron density

Assumptions as to the collision frequency profile underly each calculated value of N_e. We therefore consider how the foregoing results might be affected by the assumption of a collision frequency (the latest laboratory measured collision frequency Equation 2.11) compared to the old standard collision frequency (Equation 2.9). The effect of these changes in computing mean summer and winter N_e profiles is shown in Figures

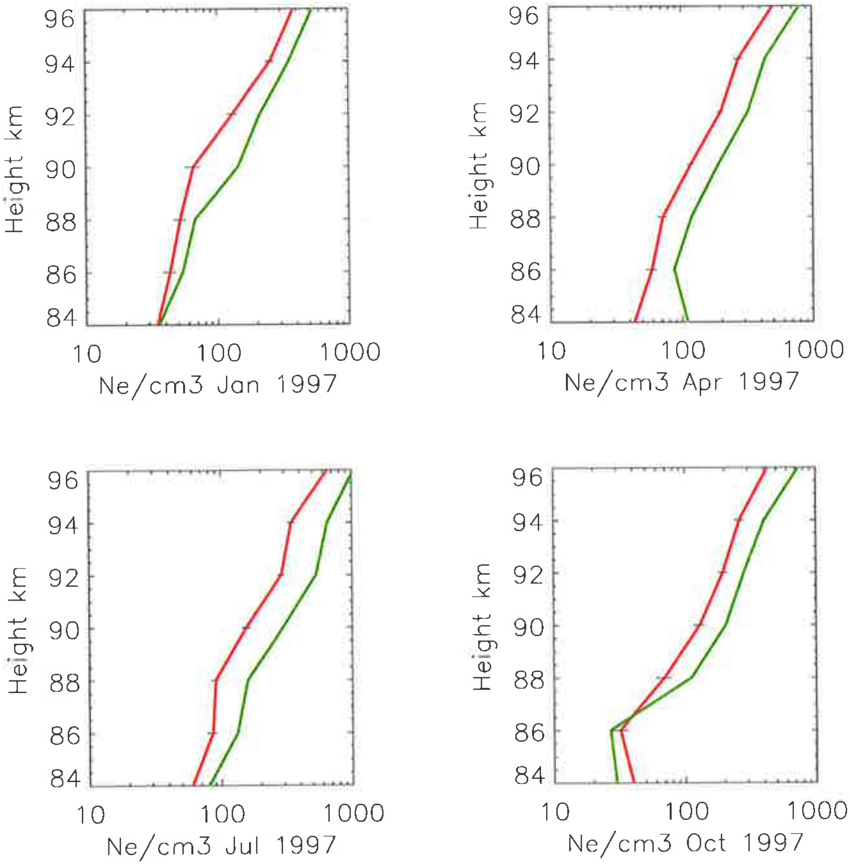

Figure 2.9: As for Figure 2.8, but for nighttime data

2.8 and 2.9.

The changes in computed values due to adoption of an alternative collision frequency profile may be compared with the standard deviation of individual values within each month (Figure 2.8 and 2.9). It is evident that changes in N_e due to collision frequency are in excess of that which might be ascribed to the standard error (horizontal lines) only. However, this latter change is only part of the total uncertainty of each of the data points making up a given mean value. Changes in values of N_e appear with same sign between 60 and 75 km. Electron density estimated using latest laboratory measurements are about 1.2 -2.4 times larger than that due to old standard collision frequencies (Equation 2.9), at these lower heights.

Examination of Figure 2.9 suggests that, above 80 km, the effect of change in

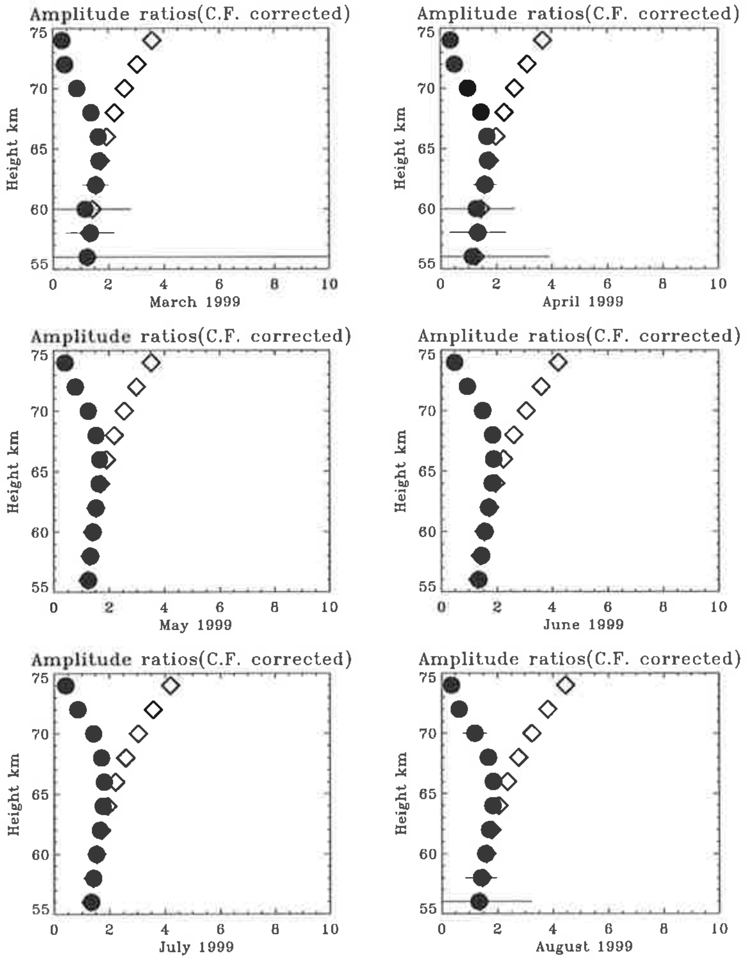

Figure 2.10: Mean amplitude ratio (circles) Ax/Ao and mean reflection coefficient ratio (diamonds) Rx/Ro for March to August in 1999

collision frequency is in the opposite sense. That is, electron density due to latest laboratory collision frequencies (Equation 2.11) are smaller than that due to Equation 2.9, at least by a factor of 0.5 - 0.7, depending on the month and height.

2.4 Mean Amplitude Ratios

The first step in determining the electron densities is the estimation of the monthly mean amplitude ratios $\overline{A}_{xo}$, and the estimation of the appropriate monthly shift in collision frequency. The later has been already discussed above and the variation of amplitude ratios which are of importance in this study are discussed in this section.

If, as is customary, irregularities or fluctuations in electron density are assumed

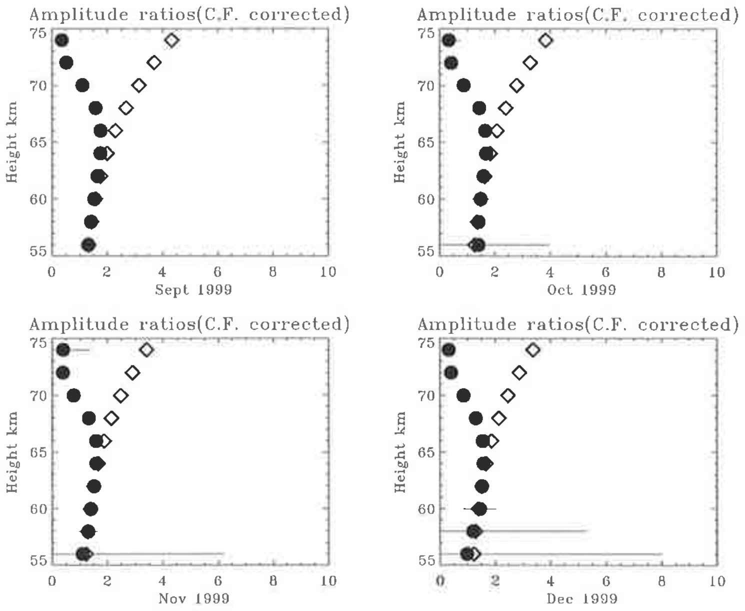

Figure 2.11: As for Figure 2.10 but for September to December

to be responsible for D-region partial reflections, then the R_x/R_o profiles displayed in Figures 2.10 and 2.11 show that 'X' mode polarized waves are generally expected to be reflected more strongly than 'O' polarized waves with this effect increasing with height. In the absence of differential absorption the A_x/A_o profile measured on the ground would be expected to closely follow the R_x/R_o profile and increase with increasing height throughout the $D-$region.

However, in practice, the higher absorption of 'X' waves in the $D-$region opposes this increase and eventually, with increasing height, the integrated differential absorption factor of equation 2.1 becomes dominant and A_x/A_o values rapidly fall. The height at which the resultant peak in A_x/A_o occurs is commonly called the A_x/A_o "turnover" height. The integrated differential absorption factor of equation 2.1 depends on the integrated electron density so that this turnover height is a good general indicator of the level of ionization in the lower $D-$region. Variations of $(k_x - k_o)$ due to collision frequency variations can also contribute to the determination of the turnover height, but this effect is expected to be fairly small with only a small seasonal variation as detailed in Section 2.3.

The monthly mean averaged midday amplitude ratios are shown in Figure 2.12.

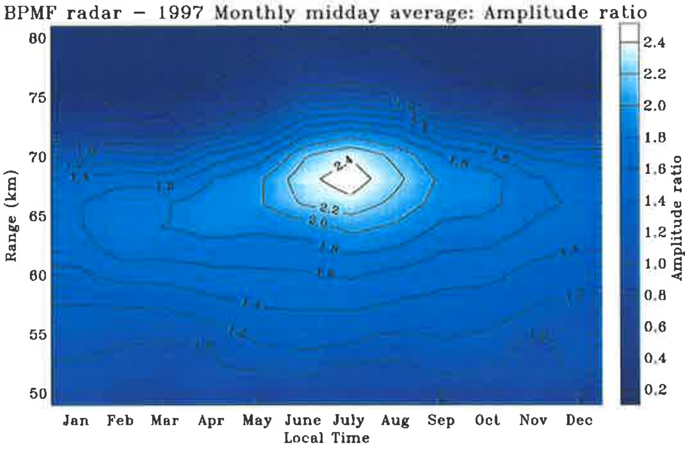

Figure 2.12: Annual variation of 1997 superposed monthly noon amplitude ratio obtained for the BPMF radar.

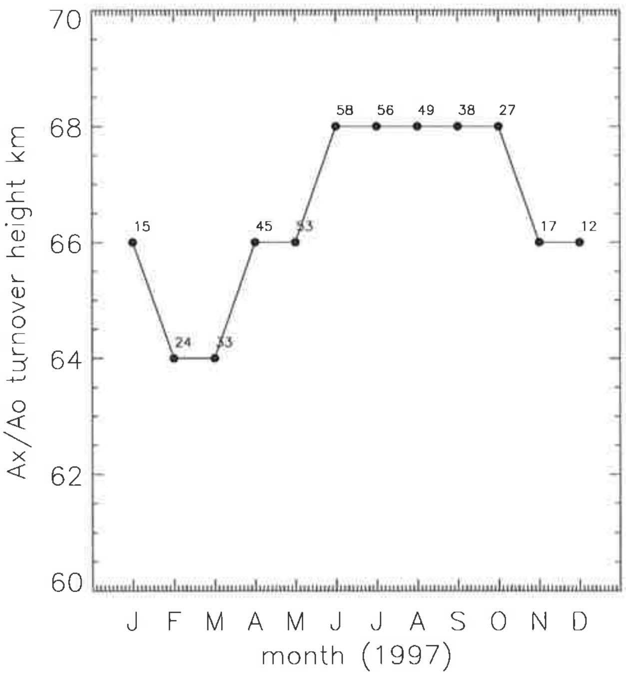

Figure 2.13: Seasonal variation of the noon Ax/Ao 'turnover' height. The numbers at each plotted point indicate the mean solar zenith angle at local noon.

The maximum $\overline{A_{xo}}$ values are largest during winter (June - August), where the turnover heights are also higher. Figure 2.13 shows the experimentally measured seasonal variation of mean noon turnover height. The mean solar zenith angle at which the turnover height was estimated (approaximately local noon) is given beside each plotted point. The seasonal variation from winter to summer is seen to be in excess of the uncertainty. This seasonal variation in turnover height as depicted in the Figure 2.13 is interpreted as demonstrating a distinct solar influence in the production of ionization in the lower $D-$region.

The electron densities presented in this study are calculated using the mean of the 2-minute amplitude ratios $\overline{A_{xo}}$ estimated over an hourly interval using an iterative procedure to remove all estimates more than two standard deviations from the mean. This is preferred to computing the mean of the 2-min electron density estimates, given the accepted belief that a 2-min acquisition may not produce a statistically accurate 2-min A_{xo} (and hence 2-min N_e) estimate. As is evident from Figure 2.14, the 2-minute amplitude ratios can exhibit significant variation.

We have chosen $\overline{A_{xo}}$ in preference to the ratio of mean signal amplitudes (i.e. $\overline{A_x}/\overline{A_o}$) based on results such as those shown in Figure 2.14, which shows the "variation ratio" (the ratio of the standard deviation to mean of the remaining estimates after the iterative procedure) of A_{xo} and the O- and X- mode signal amplitudes for the results shown in Figure 2.15. These results are typical of midday BPMF observations, and suggest the O- and X-mode amplitude variation ratios are significantly larger than A_{xo} variation ratios. It follows that A_{xo} estimated using the mean O- and X-mode signal amplitude will have similarly larger variation ratios. These results suggest that over time-scales of one hour or so A_{xo} is less influenced by variations in the scattering characteristics (and/or electron densities) than the O- and X-mode signal amplitudes, which can vary by up to an order of magnitude over short time-intervals.

Belrose and Burke (1964) claim that the mean A_{xo} estimated by $\overline{A_{xo}}$ and $\overline{A_x}/\overline{A_o}$ are usually quite similar. However, differences by up to 20% in midday hourly averages throughout our dataset are found (for data with reasonable SNRs).

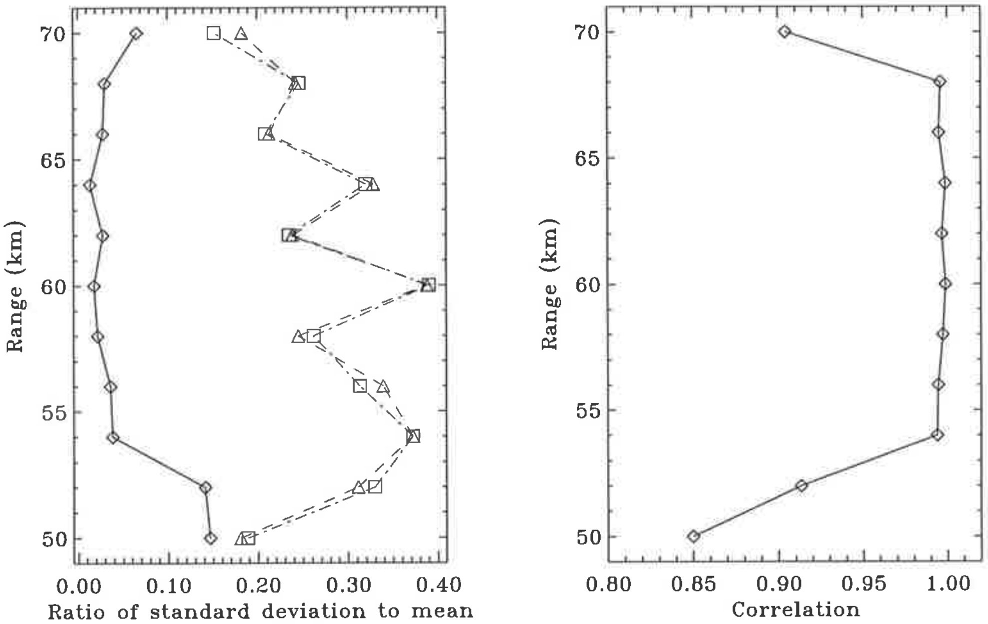

Figure 2.14: left: Ratio of standard deviation to mean of the amplitude ratio (◇, solid line), O-mode amplitude (△, dashed line) and X-mode amplitude (□, dashed-dotted line) obtained between 11:30 and 12:30 local time, 10th September 1996. right: Correlation between O- and X-mode amplitudes obtained between 11:30 and 12:30 local time, 10th September 1996.

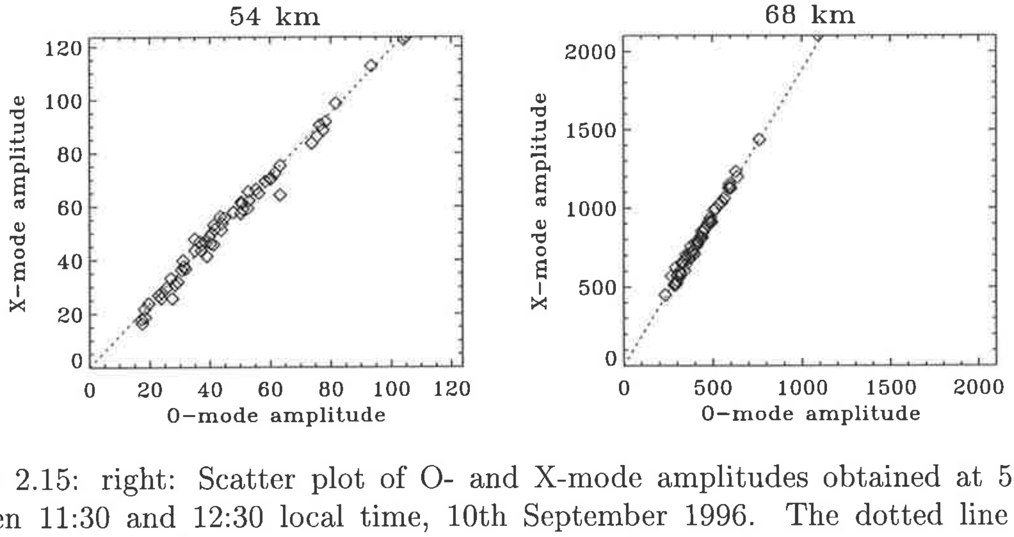

Figure 2.15: right: Scatter plot of O- and X-mode amplitudes obtained at 54 km between 11:30 and 12:30 local time, 10th September 1996. The dotted line indicates $y = A_{xo}x$, where A_{xo} is the estimated amplitude ratio. left: Scatter plot of O- and X-mode amplitudes obtained at 68 km between 11:30 and 12:30 local time, 10th September 1996. The dotted line indicates $y = A_{xo}x$, where A_{xo} is the estimated amplitude ratio.

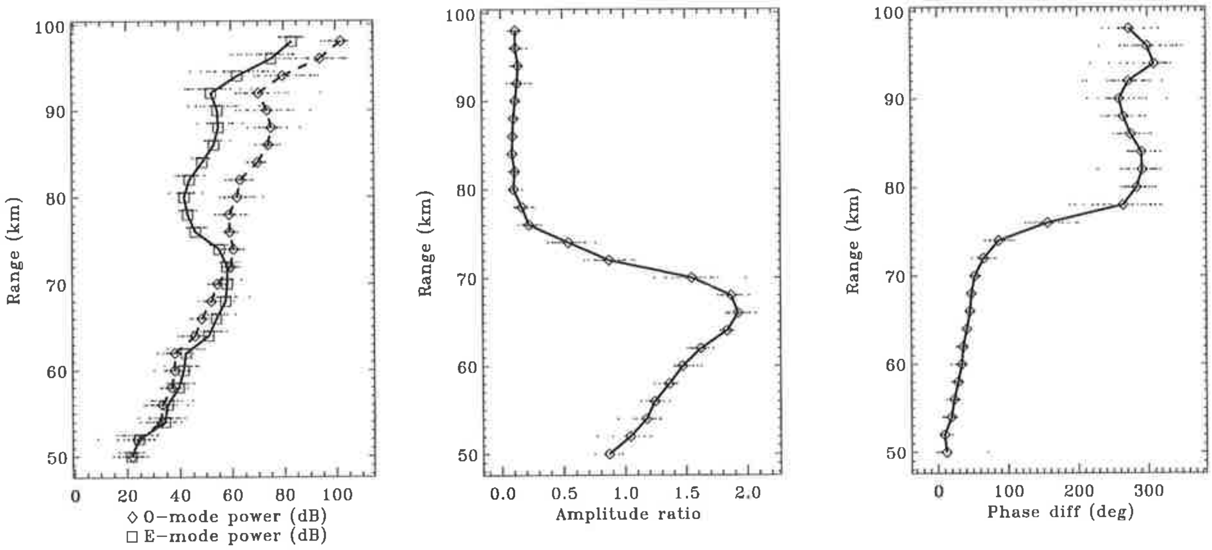

Figure 2.16: Left: Mean Ordinary (◇, dashed line) and Extraordinary (□, solid line) mode powers overlaid upon individual 2-minute estimates (dots) obtained between 11:30 and 12:30 local time on the first day of on-line DAE analysis, 10th September 1996. The individual X-mode powers are raised by 250 m for clarity. Left: Mean (diamonds, solid line) and individual amplitude ratios A_{xo} (dots). Right: Mean (diamonds, solid line) and individual phase differences ϕ_{xo}. [After Holdsworth et al. (2002)]

2.5 Electron Density Estimation

2.5.1 Noon observations

Electron densities are estimated using extraordinay and ordinary radio wave amplitudes as discussed in Section 2.2. The amplitudes of the O- and E-mode returns are calculated using the square root of the zero-lag auto-covariance function magnitudes obtained after interpolating over zero-lag to remove the effects of noise (example Figure 1.7 shown in Chapter 1). These amplitudes are then used to determine the ration A_x/A_o (A_{xo}) (Holdsworth et al., 2002).

The profiles of the O- and X-mode powers, amplitude ratios, and phase differences from 11:30 to 12:30 local time (LT) from the first day of on-line DAE observations, 10th September 1996 (solar zenith angle 39.6°), are shown in Figure 2.16. These results are typical of midday BPMF observations for a "quiet" day (i.e. with low solar activity and low A_p magnetic index). The O- and X- mode power profiles appear "independent" below 82 km. Above this range the X-mode power is offset from the

O-mode power by approximately -20 dB. This is due to the stronger O-mode returns producing O-mode signal in the assumed X-mode signal due to the assumption of circular polarisation.

This leakage provides the upper range limit for DAE electron density calculations. The 20 dB isolation corresponds to an amplitude ratio of ≈ 0.1, as indicated by the amplitude ratio values above 82 km in Figure 2.16. The measured amplitude ratios above this range are not indicative of the actual amplitude ratios. The phase differences above this range are similarly affected. In order to avoid using data indicative of leakage the DAE analysis described in this thesis is applied only at ranges where the amplitude ratios exceed 0.25. The lower limit for electron density estimation depends upon the SNR of the two modes. Although the SNRs are not written to the analyzed data files, a rule-of-thumb relationship based on known receiver gain and receiver characteristics for the BPMF radar can be invoked to relate the power of each mode into an SNR. For the data shown in Figure 2.16, a power of ≈ 35 dB corresponds to an SNR of 0 dB, indicating a power threshold of approximately 29 dB (i.e -6 dB). The lower range limit or the data shown in Figure 2.16 is thus around 50 km, where consequently only a few amplitude ratios have been estimated.

For calculating electron densities at a particular height (h) requires the derivatives of Equation 2.2 as given by Equation 2.4. Electron densities are calculated using the Fresnel reflection implementation at all intermediate ranges $(i+j)/2$ where amplitude ratios have been determined for successive ranges i and j ($i = 1$ and $j = 2$). It is common practice to calculate DAE electron density only at heights above the A_{xo} "turnover" height (i.e. the height where A_{xo} maximizes as detailed in Section 2.4) due to the increasing uncertainty of the amplitude ratios (Belrose et al., 1972) and the increasing possibility of large perturbations in electron density resulting from using A_{xo} below the turnover height (Manson and Meek, 1984). In order to estimate the electron density the appropriate collision frequency is estimated using above method given in section 2.3. As an example, the DAE electron density estimates obtained using Equation 2.11 collision frequency are shown in Figure 2.5, together with the IRI

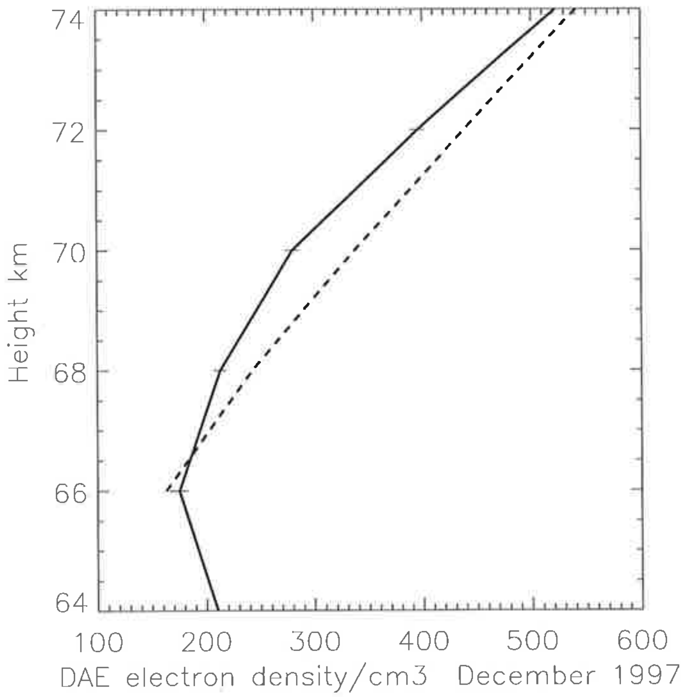

Figure 2.17: Averaged DAE electron densities obtained between 12:00 and 13:00 local time December 1997. The solid line denotes the electron density calculated using the mean amplitude ratio, with error bars. The dashed line indicates the IRI model electron densities.

(International Reference Ionosphere) model estimates.

2.5.2 Night time observations

Despite the widespread application of the DAE to day-time data, there are few published accounts of the application to night-time data such as that of Von Biel (1977). This has generally been due to the higher noise levels and interference observed at night (e.g. Belrose and Burke, 1964). However, there are a few other factors which can contribute to the difficulty in applying the DAE to night time observations. Mid-latitude night-time observations can only be made above 80 km. As explained earlier, at these ranges the effects of group retardation start to become significant, resulting in differences in the propagation speeds of the O- and X-mode signals, and therefore separation of the volumes sampled by the O- and X-mode signals at each range gate.

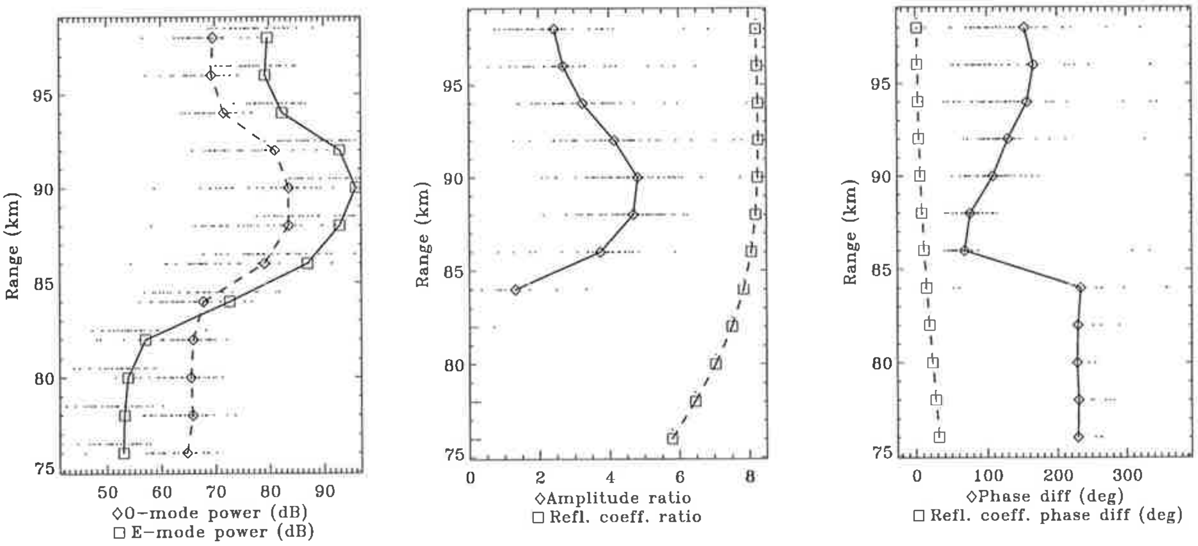

Figure 2.18: Left: Mean Ordinary (diamonds, dashed line) and Extraordinary (squares, solid line) mode powers overlaid upon individual 2-minute estimates (dots) obtained between 2300 and 0100 LT on the first morning of on-line DAE analysis, 10/11th September 1996. The individual X-mode powers are raised by 250 m for clarity. Middle: Mean (◇, solid line) and individual amplitude ratios A_{xo} (dots) with reflection coefficient ratios (□, dashed line). Right: Mean (◇, solid line) and individual phase differences ϕ_{xo} with reflection coefficient phase differences (□, dashed line). [After Holdsworth et al. (2002)]

Another factor is that the relationship between collision frequency and pressure specified by (2.11) is estimated using the latest laboratory measurements of momentum transfer collision cross sections for N_2 (Robertson et al., 1997), however at these heights (especially above 90 km) O_2 and other elements may play major role in producing the ionization. This suggests that a revised relationship between collision frequency and pressure may be used for night-time observations.

A simple procedure has been used to determine the effects of group retardation by estimating the percentage overlap of the O- and X-mode transmitted pulses. This involved using IRI model electron densities to estimate the O- and X- mode refractive index profiles, $n_o(h)$ and $n_x(h)$ using the Sen-Wyller equations, and then using

$$H_{o,x}(h) = \int_0^h n_{o,x}(h)dh \tag{2.12}$$

to estimate the actual heights H of the O- and X-mode pulses as a function of the virtual height h assumed by the radar. This procedure does not consider the horizontal

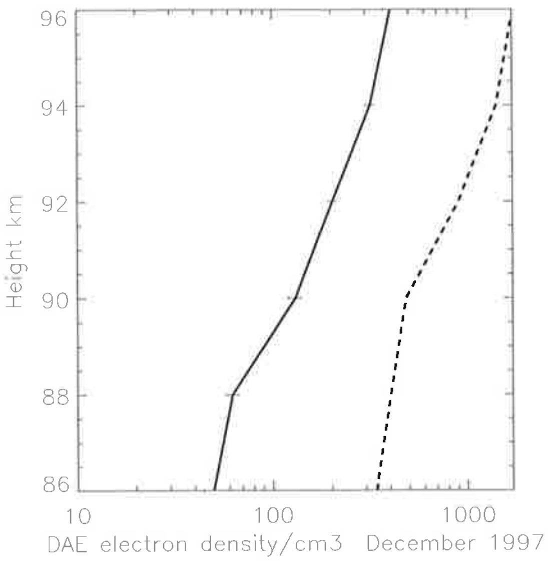

Figure 2.19: Averaged DAE electron densities obtained between 0:00 and 1:00, for March 1997, 2.11 ν profile. The solid line denotes the electron density calculated using the mean averaged amplitude ratio. The dotted line indicates the IRI model electron densities.

separation of the O- and X-mode signals due to ray divergence effects. We are therefore assuming, in effect, that the electron density is horizontally homogeneous, which we feel is a valid assumption for the current purposes. Determination of the horizontal separations requires a ray tracing procedure (e.g. Meek, 1978) which is beyond the scope of this study. The results of applying this procedure suggest the overlap is $\approx$ 88% at 98 km, which is the maximum height used for BPMF DAE observations. We consider this overlap sufficient to produce sensible DAE observations.

Profiles of the O- and X-mode powers, amplitude ratios A_{xo}, and reflection coefficient ratios R_{xo}, and phase differences ϕ_{xo} and reflection coefficient phase differences Φ_{Rxo} from 2300 to 0100 local solar time on the first morning of on-line DAE observations, 10th - 11th September 1996, are shown in 2.18. Unlike the midday results shown in Figure 2.16, there does not appear to be any leakage from one mode into the other, as the O- and X- mode power profiles appear independent at all heights. The power minimum in the O- and X- mode power profiles are in excess of 30 dB higher than the daytime minimum shown in Figure 2.16.

The PRFs used for daytime and nighttime observations are 100Hz and 20Hz, respectively. This suggests the power reduction due to the lower PRF used at night is 7 dB, thereby emphasizing that a larger noise level observed at night. This is further emphasized by the greater spread in the individual power estimates at each height relative to the day-time values shown in Figure 2.16. The O-mode power minimum is approximately 12 dB above the X-mode power minimum, indicating that substantially greater noise is observed in the O-mode signal. This has been observed throughout all night time BPMF DAE observations, and is consistent with the observations of Meek and Manson (1981). The height where the X-mode power maximizes exceeds the height where the O-mode power maximizes. Although this does not necessarily suggest the X-mode signal is being retarded in relation to the O-mode signal, it is likely this is the case.

The larger O-mode noise level provides the lower range limit for electron density calculations. In Figure 2.18, this limit is at about 84 km. It is evident that below this height the amplitude ratio falls off quickly to zero, while the phase difference does not approach the reflection coefficient ratio as it should. The phase difference below 84 km is approximately constant with height, and is similar to the value seen above 80 km in 2.16 where the O-mode signal leaks into the X-mode signal. These observations suggests that the O-mode "noise" may actually be a coherent signal, and that the X-mode noise level is due to leakage of this signal from the O-mode.

The scatter of the nighttime estimates makes hourly averages difficult. However, it is possible to estimate monthly midnight electron densities in the same manner as used to estimate the midday estimates. The resulting electron densities estimated for March 1997 using 2.11 collision frequency (same as daytime estimates) are shown in Figure 2.19. The DAE estimates show the same general behavior as the IRI estimates, but are a factor of 5 times smaller. A similar underestimation factor is also seen in other months.

It is clear that further work is required to improve and interpret the night time DAE results. Despite the limitations discussed here, the DAE may prove useful for determining the influence of factors that may contribute to nighttime ionization. Night time DAE observations will be discussed in Chapter 4.

Chapter 3

Day Time Electron Density

3.1 Introduction

In this chapter and in the reminder of the thesis the deduced electron densities (using the procedure described in the previous chapter) are used to study mid-latitude $D-$region characteristics. This chapter describes the results of measurements of atmospheric electron densities at altitudes below 80 km for three years of low to high solar activity period.

The classical variation of electron densities as described here has been given by several researchers in the past (Manson and Meek, 1984; Meek and Manson, 1981; Coyne and Belrose, 1972; Belrose, 1970; Gregory et al., 1969). However, recently the scope of $D-$region ionospheric studies are extended to inter-compare the dynamic regime of the middle atmosphere and variations of $D-$region parameters (Danilov, 1990). For example an entire issue of the Journal of Atmospheric and Terrestrial Physics (JATP, 1987) is devoted to results of $D-$region studies during the MAP-WINE project. Apart from forming a knowledge base for the mid-latitude $D-$region electron densities, present observations can lead to the possibility of investigating the non-classical behaviour such as diurnal and seasonal asymmetry at different altitudes of the lower ionosphere and increased ionization at the base of the ionosphere.

The self consistence of these results establishes the usefulness of the improved DAE experimental method and may contribute to finding the optimal empirical representation of all available experimental data. Large discrepancies were found between the results of different measurement techniques. Comparison of our results to different theoretical models such as International Reference Ionosphere IRI (Bilitza, 1998) and semi-empirical model FIRI (Friedrich and Torkar, 2001) may contribute in evaluating the reliability of different techniques. An overview of these models is presented in Chapter 1.

Furthermore, comparison of our results with NO variations could yield some implications for models of the ionospheric $D-$region, since mesospheric NO is the major ionizable constituent for the 70-90 km region. In other words, comparisons made between our results (N_e variations) and NO variations observed by the Halogen Occultation Experiment (HALOE) (Siskind et al., 1997; Siskind et al., 1998; Friedrich et al., 1998) may prove to be very useful.

In the following sections variation of electron density (N_e) as a function of solar zenith angle, season, latitude, solar activity and altitude are discussed. The profiles are compared with those derived by other workers, including results at Wakkanai ($45°N$) (Igarashi et al., 1999), IRI and FIRI model results. Back calculated radio wave absorption from the model profiles is compared with measurements at Buckland Park.

3.2 Conditions of Observations

The technique employed was that of differenctial absorption measurements, using partial reflections observed at a frequency of 1.98 MHz. A discussion of theory, assumptions and practice of the experiment is given in the previous chapter. The observations reported here were made between September 1996, and December 2000. Due to equipment modifications some gaps exist in the observed series. However, a significant number of profiles of electron densities were obtained in each season. Data were most consistent throughout the sunspot minimum and maximum years of 1997 and 2000 respectively.

Data which were obtained between 0600 and 1800 local solar time on a given day are considered as representative of daytime. The upper altitude limit of the daytime profiles is around 78 km, and is established by decreasing accuracy of true height determination and by oblique path propagation effects. The lower limit is around 60 km, and is due to lack of any significant differential absorption below this height. The smoothed sunspot number for years 1996-2000 varied from 10 to 180. Data obtained under flare conditions were excluded when estimating monthly and seasonal average profiles.

Mean profiles assembled for each month should be interpreted, as indicated in Chapter 2, as an assemblage of data points, each of which represents an average value over a height interval of 2 km. The horizontal (or vertical) line through each data point show the standard error (at 95% confidence level) obtained at the indicated height and month throughout the period of observations. Examples of amplitude ratio distributions at different heights provided in Figure 2.1showed that the distributions are approximately Gaussian in shape and the peak values clearly defined, indicating negligible standard error. No significant differences between mean and median values were found.

Initially, a detailed study was made of the manner in which collision frequencies are calculated (Section 2.3). This work led to the conclusion that the best available laboratory measurements support the use of 2.11. Unless otherwise stated, all the electron density values are estimated from collision frequencies computed using (2.11).

3.3 Results and Discussion

3.3.1 Diurnal Variations

Figures 3.1 to 3.6 show the diurnal variation of the monthly mean values of electron density at each height and for all the three years. The measurements from all the three years show the same general behaviour throughout the day. Corresponding zenith angles at each hour are shown at the top of the plots. The electron density values between 64 - 74 km ranged approximately from 100 to 500 cm^{-3}.

It is instructive first to compare our findings with the photochemical model of $D-$region processes in a static atmosphere, as proposed by Nicolet and Aiken (1960). Some important points established from the electron density variations are as follows. In general, it can be seen that as the zenith angle increases, the electron density decreases. Solar control is the dominant influence in determining the diurnal variation of the daytime electron densities in the lower ionosphere at mid-latitudes. For an ionized layer described by a Chapman function, the variation of N_e with solar zenith angle should yield a linear relation (Friedrich et al., 1998). Figures 3.1 to 3.6 demonstrate this typical behaviour, with some departures which are discussed further in the later chapters.

Apart from the basic features of the observations, in some months (e.g., June, July and August), it can be seen that there is evidence of ionization occuring, well below 68 km during the dawn or sunrise periods of 0600 to 0800 (note the region below 64 km is not shown in the Figures 3.1 to 3.6). For example, in June 1997, N_e values 64, 66, 68 km were found to be 204, 470, 383 cm^{-3}, respectively at 0600 local solar time (LST). Similarly, in 2000 June at 0600 (LST), 744, 398, 118 cm^{-3} are observed at these heights.

Several possible reasons for this ionization are considered. Although, the method of estimating DAE electron densities is well established (self consistence is one of the evidence), some uncertainty still exists concerning the degree to which these electron densities can be considered reliable at the lower most region of the ionosphere. However, it was shown by (Siskind et al., 1997; Siskind and Russell, 1996) that, NO produced in lower thermosphere can be transported deep into the winter polar middle atmosphere (due to vertical transport). It was demonstrated that in the winter season, vigorous horizontal mixing occuring in the lower mesosphere can bring enhanced NO out of the polar reservoir to latitudes as far equatorward as 30° - 40°.

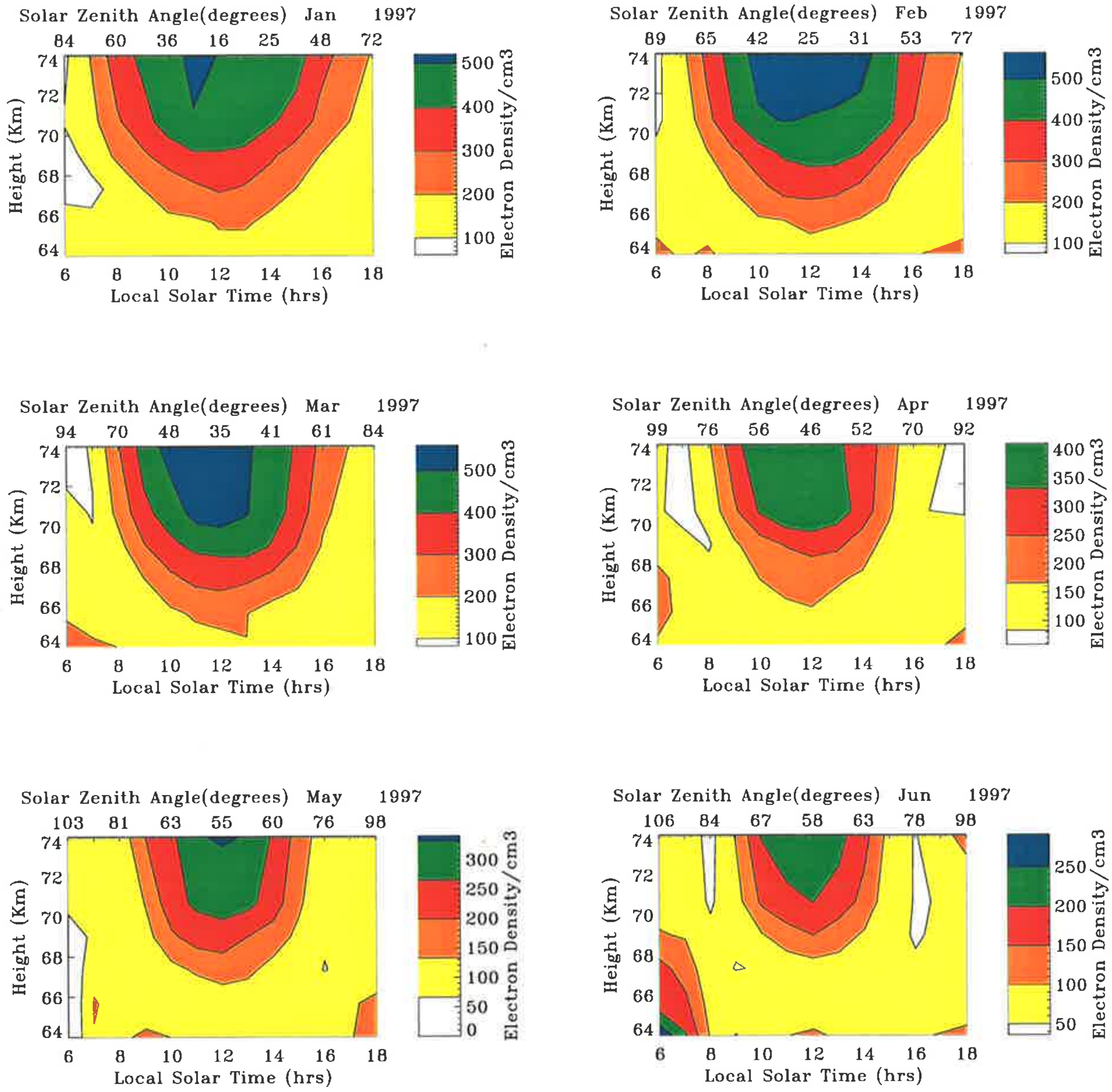

Figure 3.1: Diurnal variation of electron density at Adelaide from January to June (low solar activity period)

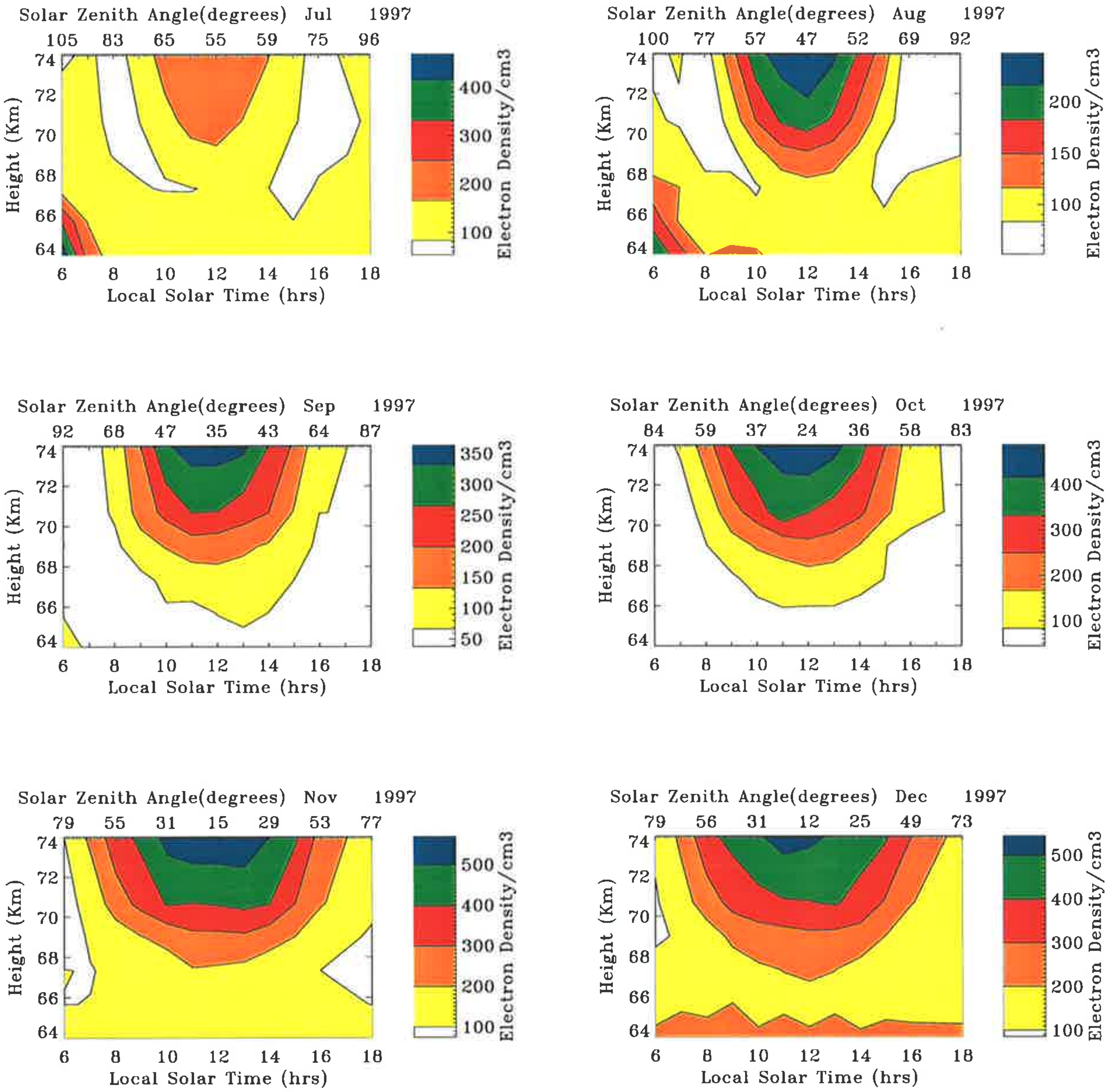

Figure 3.2: As for Figure 3.1, but for July to December months

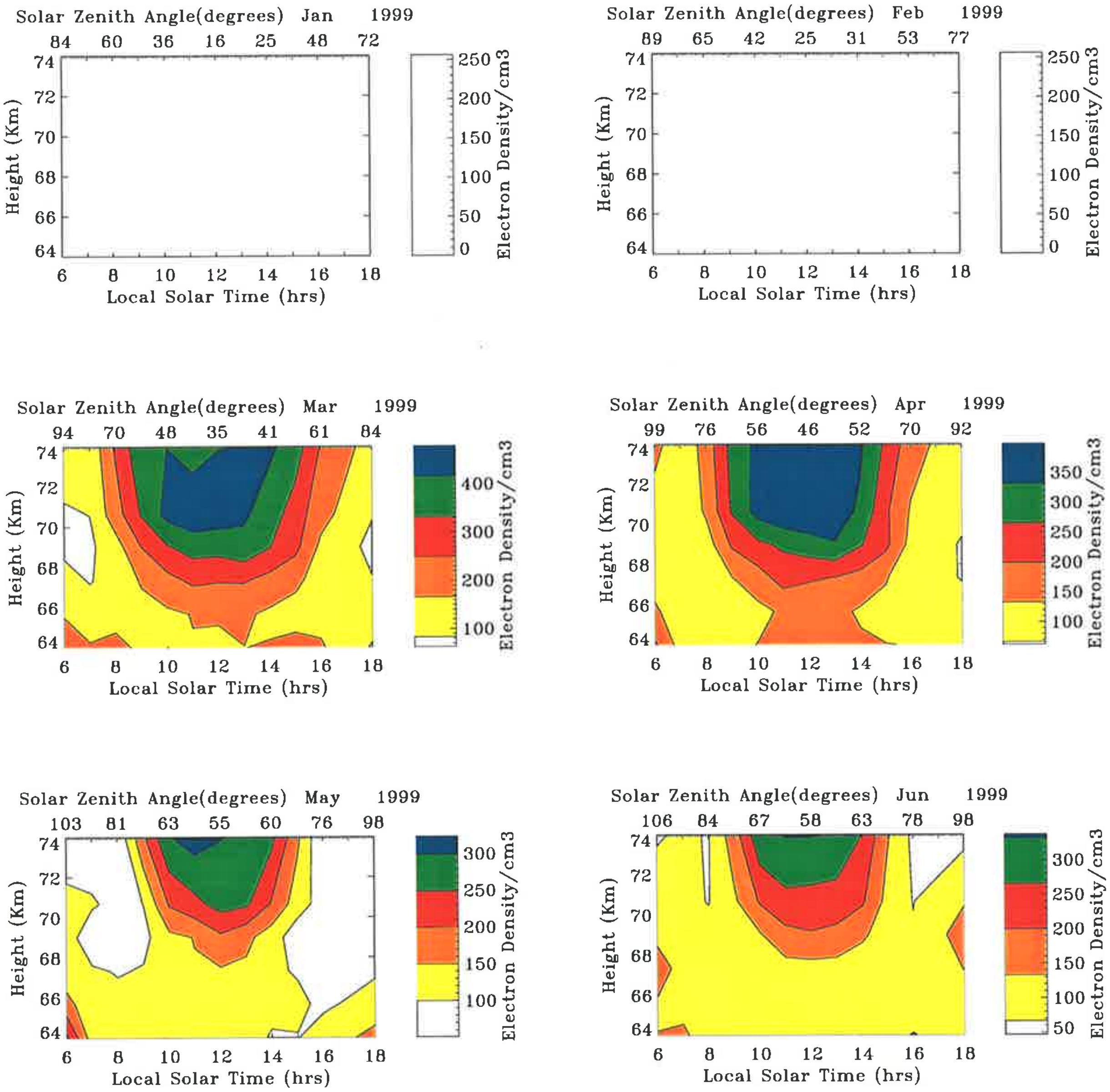

Figure 3.3: As for Figure 3.1, but for January to June 1999 (medium solar activity period), Note that no data available in January and February

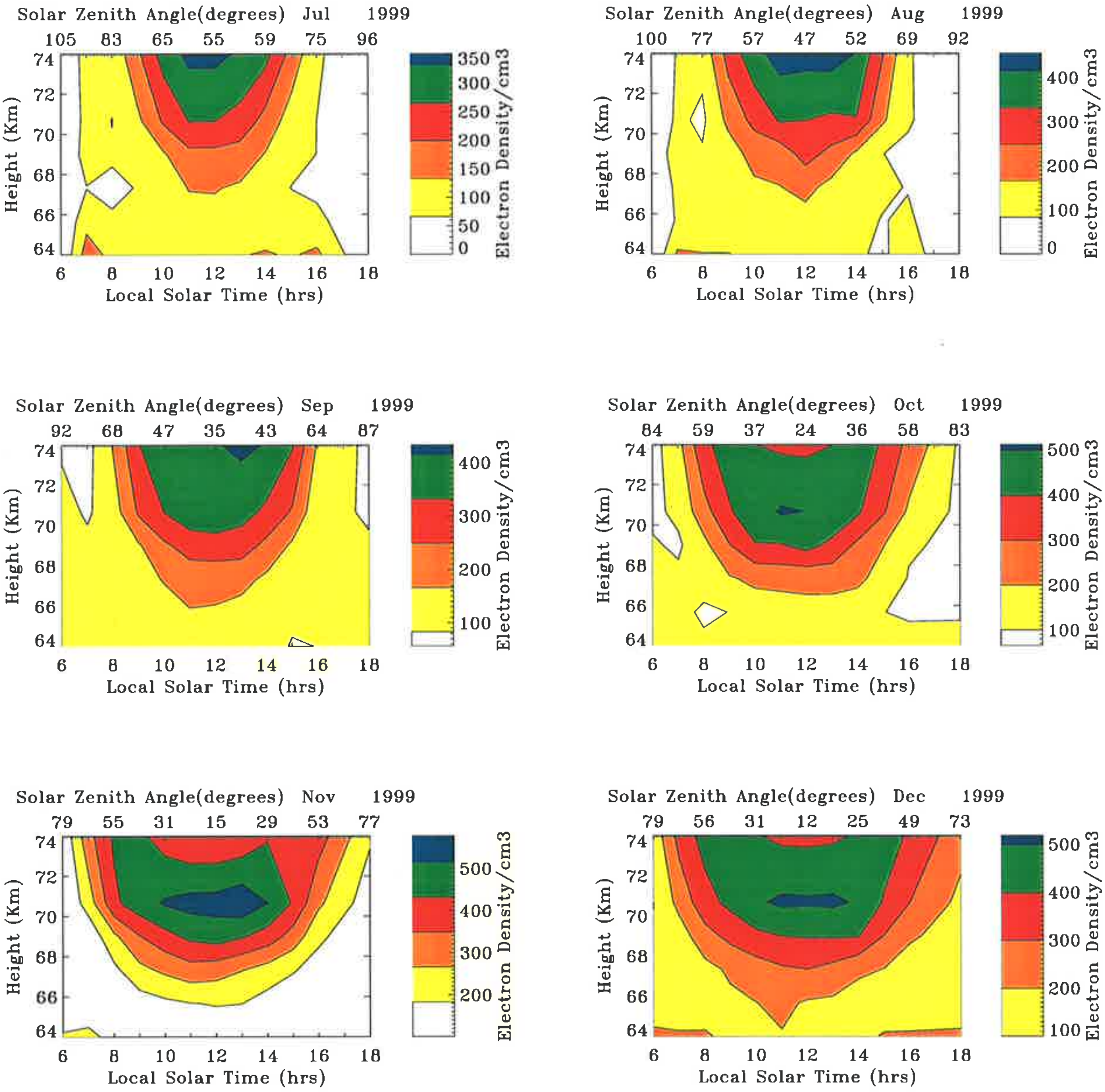

Figure 3.4: As for Figure 3.1, but for July to December 1999 (medium solar activity period)

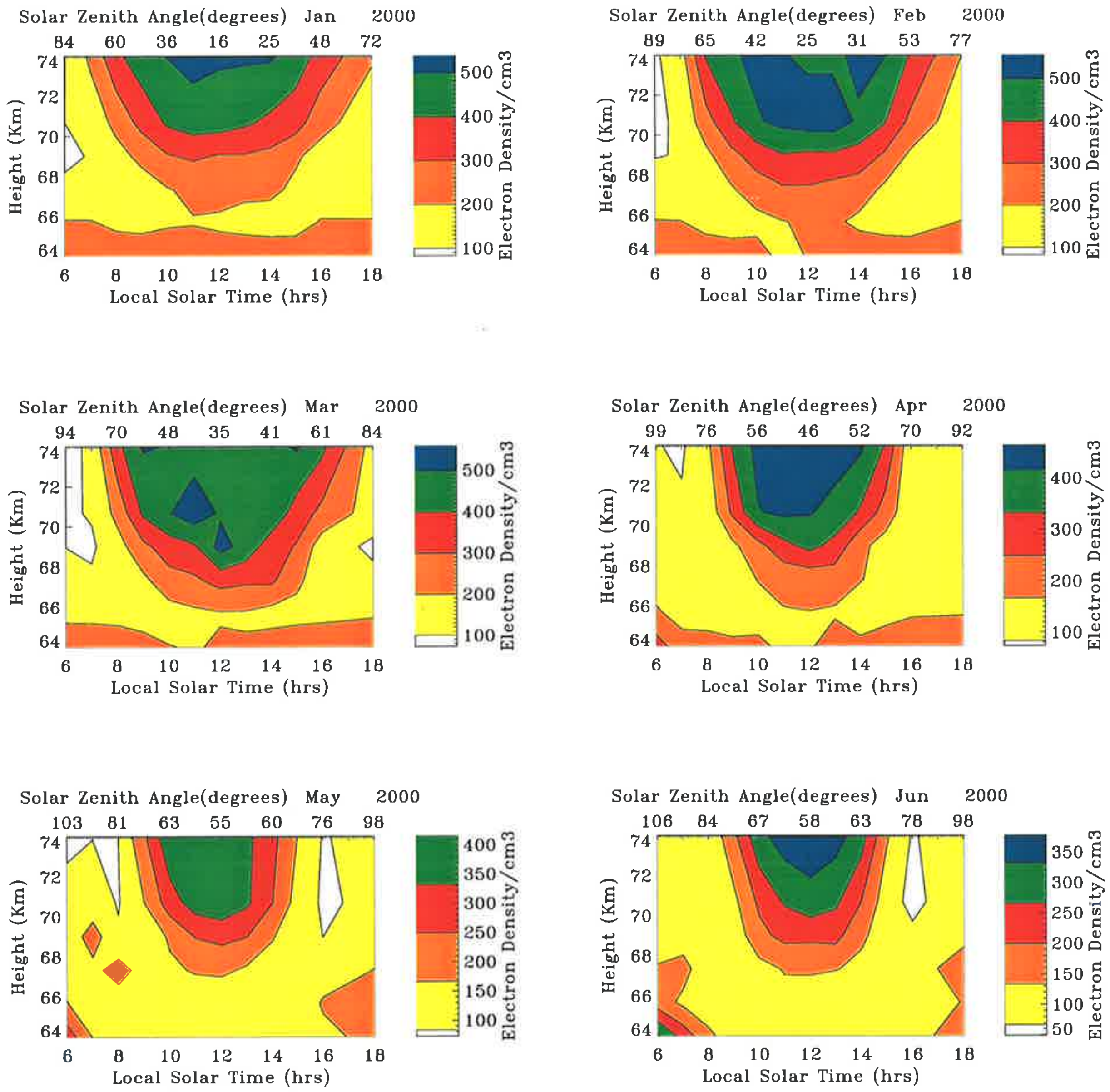

Figure 3.5: As for Figure 3.1, but for January to June 2000 (high solar activity period)

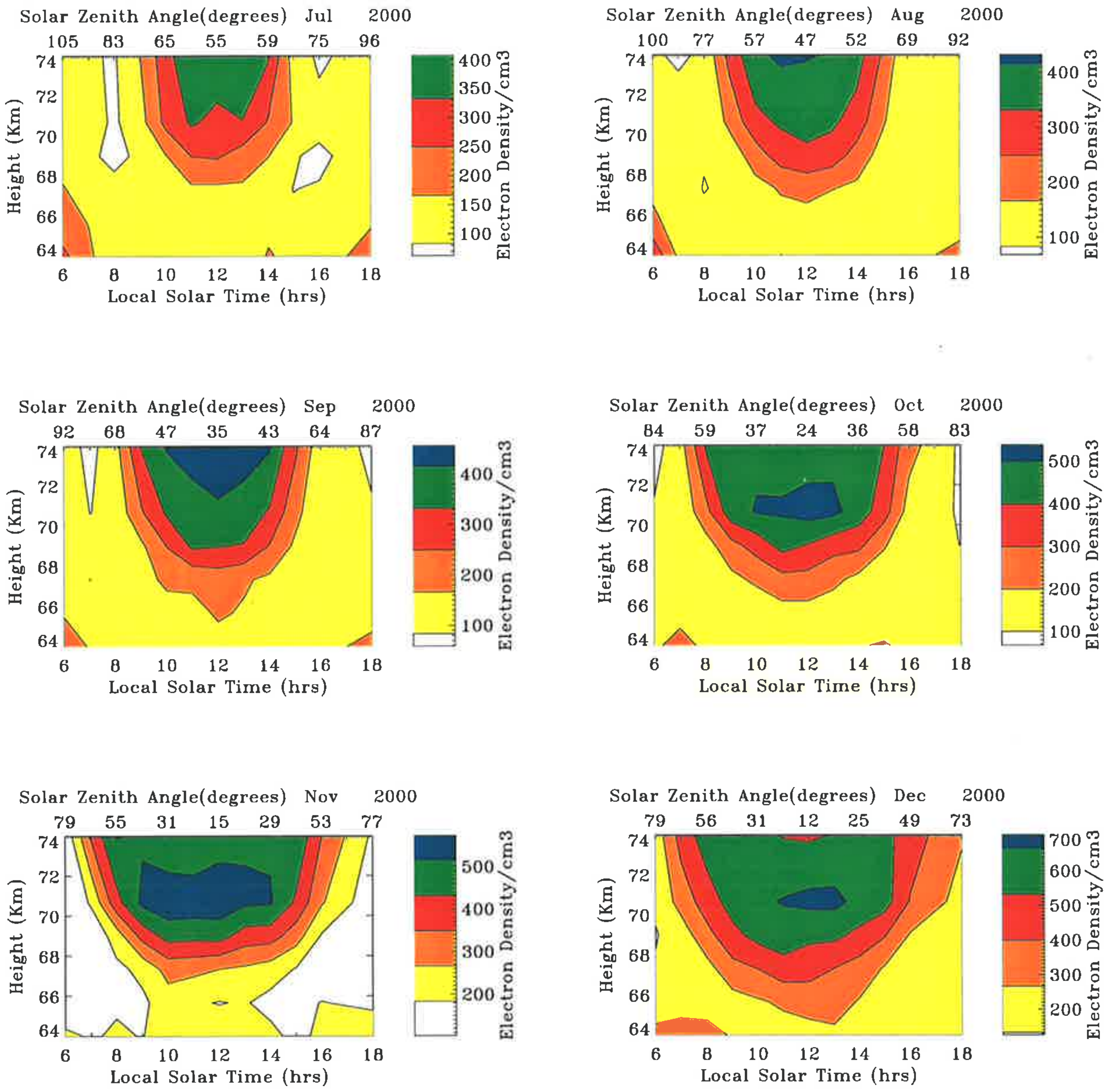

Figure 3.6: As for Figure 3.1, but for July to December 2000 (high solar activity period)

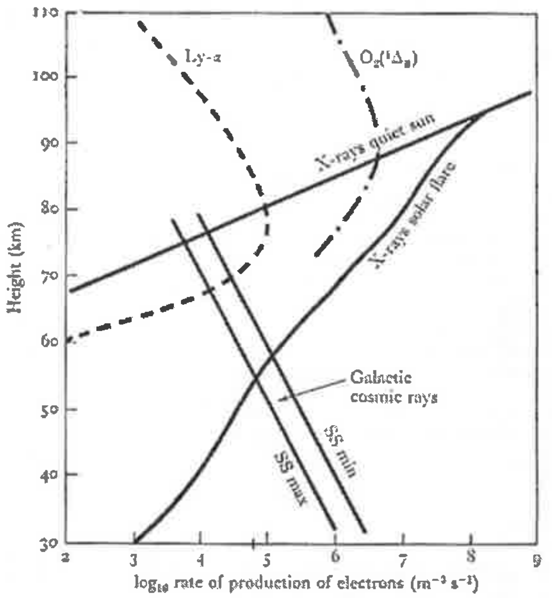

Figure 3.7: The rates at which electrons are produced in the atmosphere below 110 km. The different curves refer to Lyman-alpha ionizing nitric oxide; $X-$rays ionizing all gases at times of quiet sun and at times of solar flare; the wavelength 102.7-111.8 nm ionizing $O_2(1\triangle_g)$ and galactic cosmic rays at maximum and minimum of the sunspot cycle [After Ratcliffe (1972)]

The influence of another source of radiation to be considered is galactic cosmic radiation. Since the strength of the solar field increases with the sunspot number the intensity of the cosmic radiation reaching the earth is weakest at sunspot maximum and strongest at sunspot minimum. The rate is shown, for sunspot maximum and sunspot minimum in the Figure 3.7. Only the electron densities at 66 and 68 km for 1997 are larger than the values in 2000 at corresponding heights, suggesting a correlation with galactic cosmic radiation. These results also indicate that electron density increases with decreasing height. Nicolet and Aiken (1960) have also considered

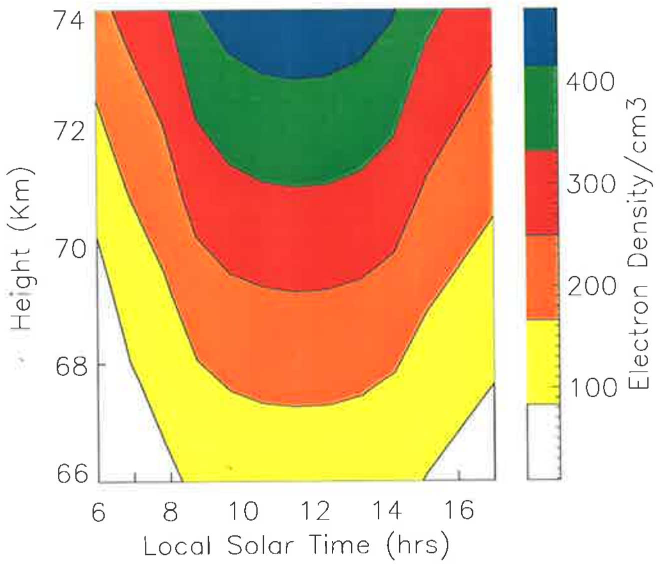

Figure 3.8: Diurnal variation of electron density from IRI95 model data, for 15 January 1997 and 35°S latitude

electron production by cosmic rays below 75 km, and have predicted a similar variation. Observed electron densities below 65 km are almost independent of the zenith angle supporting the fact that at these altitudes cosmic rays are providing main source of ionization.

3.3.1.1 Comparisons with IRI and FIRI

The diurnal variation of electron density results from the IRI model are shown in Figure 3.8. The results shown are for a single day (middle of the month) 15 January 1997. However, no day to day variation was seen in the model results for the entire month. Therefore these single day results can be treated as average values for that month and illustrate the average behaviour of the D-region.These results show a gradual increase of $D-$region electron densities from early morning to near local noon, with a subsequent decrease in the afternoon at all heights covered by the daytime measurements, i.e. from 66 to 74 km. The same general behaviour was observed all through the year.

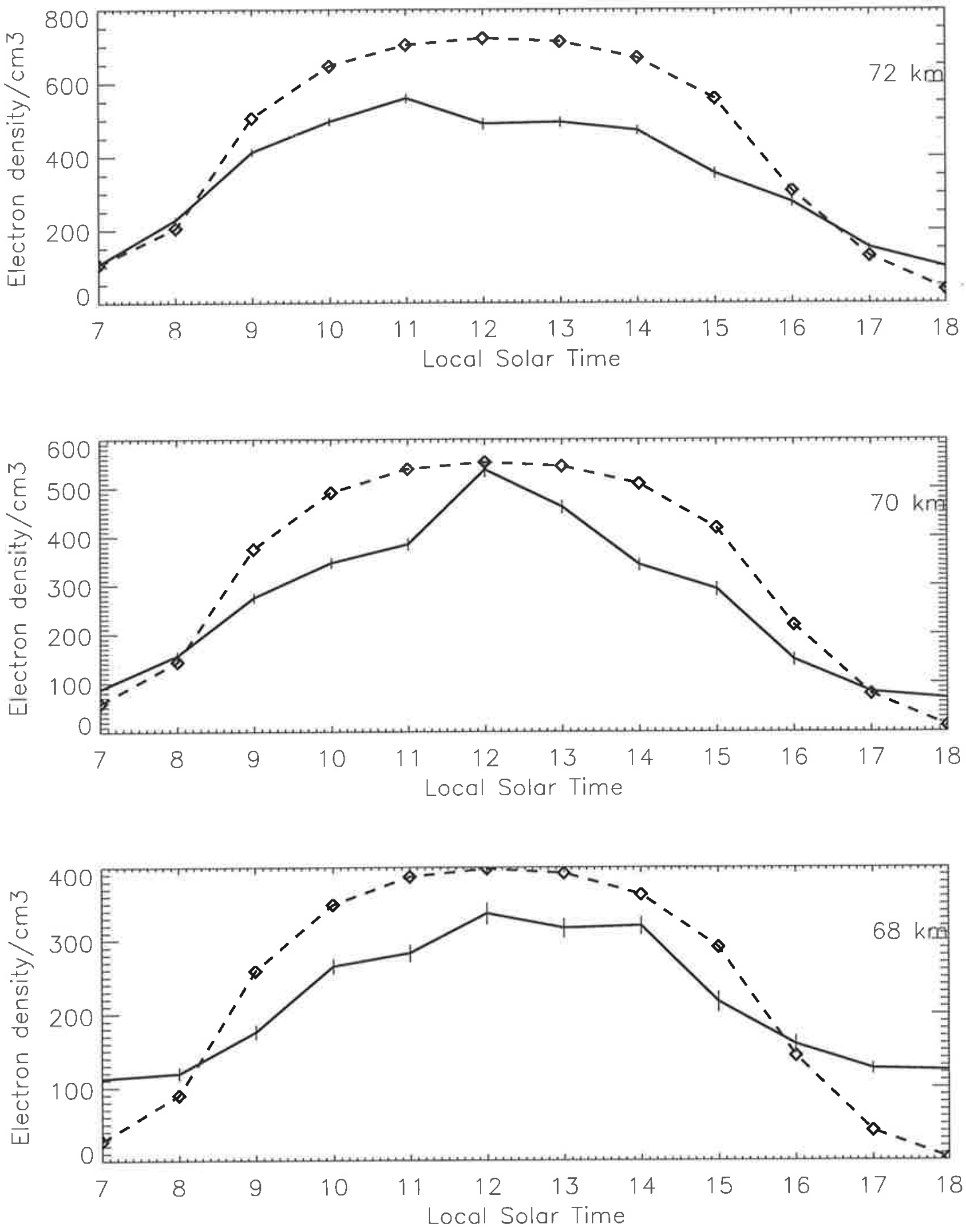

Figure 3.9: Comparison of diurnal variation of observed (solid) and IRI-95 electron density (dashed), 35°S latitude, March 2000.

Table 3.1: Diurnal variation of N_e at Adelaide, March 2000, 70 km.

Local Time	0700/1800	0800/1700	0900/1600	1000/1500	1100/1400	1200/1300
Morning χ	81.7°	69.6°	57.8°	47.07°	38.23°	33.04°
Afternoon χ	82.9°	70.7°	58.9°	48.04°	38.95°	33.32°
Morning N_e	87	156	275	346	384	537
Afternoon N_e	68	81	147	292	342	461
Ratio	1.28	1.92	1.87	1.185	1.122	1.16

Table 3.2: Diurnal variation of N_e due to IRI95 model, March 2000, 70 km.

Local Time	0700/1800	0800/1700	0900/1600	1000/1500	1100/1400	1200/1300
Morning χ	81.7°	69.6°	57.8°	47.07°	38.23°	33.04°
Afternoon χ	82.9°	70.7°	58.9°	48.04°	38.95°	33.32°
Morning N_e	58	143	375	491	539	553
Afternoon N_e	12	77	218	418	509	545
Ratio	4.8	1.85	1.72	1.17	1.05	1.01

Comparison of diurnal variation of N_e due to experimental results from Buckland Park MF radar and IRI-95 model results for 68, 70 and 72 km (March 2000) are shown in the Figure 3.9. Except for sunrise and sunset times, the IRI-95 model data are about 1.2 - 1.4 times larger than the observed N_e due to partial reflection observations.

A key feature, which is of prime interest to us in this study is the diurnal asymmetry of N_e about the local noon. The results presented in the Figure 3.9 are tabulated for comparison. Table 3.1 and 3.2 reveal similar asymmetry during the daytime except for the sunrise/sunset time of 0700/1800. The ratio of morning to afternoon electron densities are presented in the last row of the table. Corresponding zenith angles (χ) and observed and model electron densities are presented for comparison. Maximum asymmetry is found to be between 58° and 70° zenith angles, both due to observed and model data. Although, 0700/1800 ratio in the model data show maximum asymmetry, the ratio may be questionable due to very small values of N_e (12 electrons cm^{-3}). This aspect is considered in detail later in Chapter 5.

Next, Figures 3.10 and 3.11 depicts a comparison between observed (MF radar), IRI and FIRI theoretical electron densities at mid-latitude, high solar activity period. For comparison, FIRI model results also are taken for a single day (middle of the month).

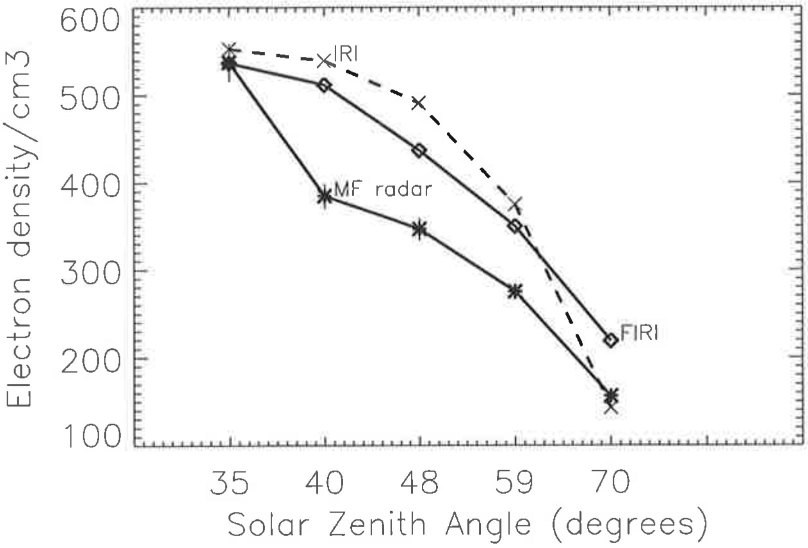

Figure 3.10: Comparison of diurnal variation of observed (solid,$*$) and IRI-95(dashed), FIRI(solid,$\diamond$) electron density (dashed), at 70 km, 35°S latitude, March 2000, N_e variation before noon

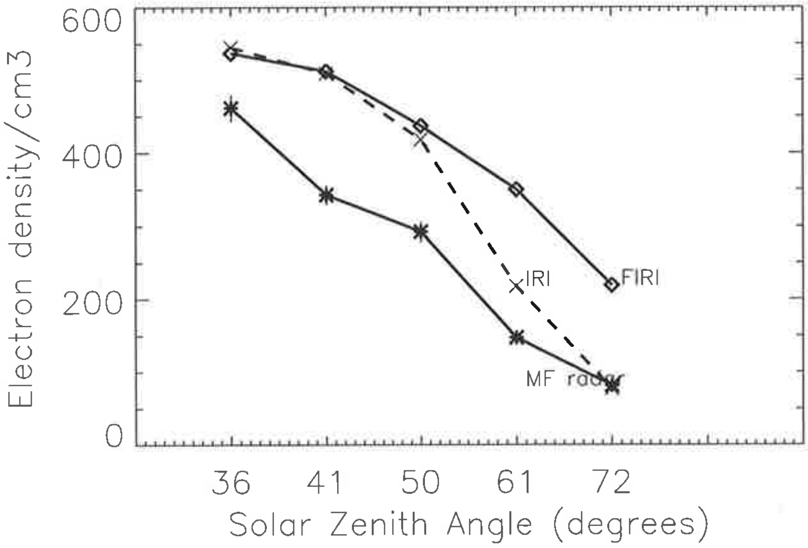

Figure 3.11: As for Figure 3.10, but for after noon hours

The zenith angles equivalent to morning hours (0800 - 1200 LST) and afternoon hours (1300 - 1700 LST) are shown on the X-axis. Except for the steep gradient in IRI N_e after 50° zenith angle, all of the above three results follow the same variation demonstrating solar control. However, morning electron densities due to MF radar are in better agreement with FIRI results than the corresponding afternoon N_e between 35 and 70° zenith angles. FIRI electron densities are about 1.3 - 1.4 times larger than our observed morning electron densities and 1.2 - 2.7 times larger than that of observed afternoon electron densities.

3.3.2 Seasonal Variations

The focus of this section is on the seasonal variation of noon electron densities at lower heights of mid-latitude $D-$region. A feature of these results is the existence of relatively larger mean values of electron densities in fall and reduced values of N_e in spring than in winter and summer over the range of altitudes between 60 and 75 km. Figure 3.12 makes this comparison more directly. Right panel of this figure shows the electron density at constant solar zenith angle (equivalent to winter minimum of 58°). It can be seen that fall electron densities are still larger than winter and spring values lower than summer.

Since the effect of change in solar zenith angle has been removed (by taking the values at constant zenith angle), the variation shown on the right side of Figure 3.12 is representative of variability due to phenomena, such as dynamical effects and transport of minor constituents (e.g., NO). The existence of this equinoctial asymmetry is further illustrated by time series of values throughout the three year period. In order to reduce the amount of detail, the mean concentration of electrons has been presented only for heights between 68 and 72 km. Below 80 km, an essentially annual component is dominant.

The electron density at noon in the $D-$region clearly changes with season. This change is largely because of the decreasing values of solar zenith angles from 58° in June to 12° in December at Adelaide. Observational results given in the Figure 3.12 also

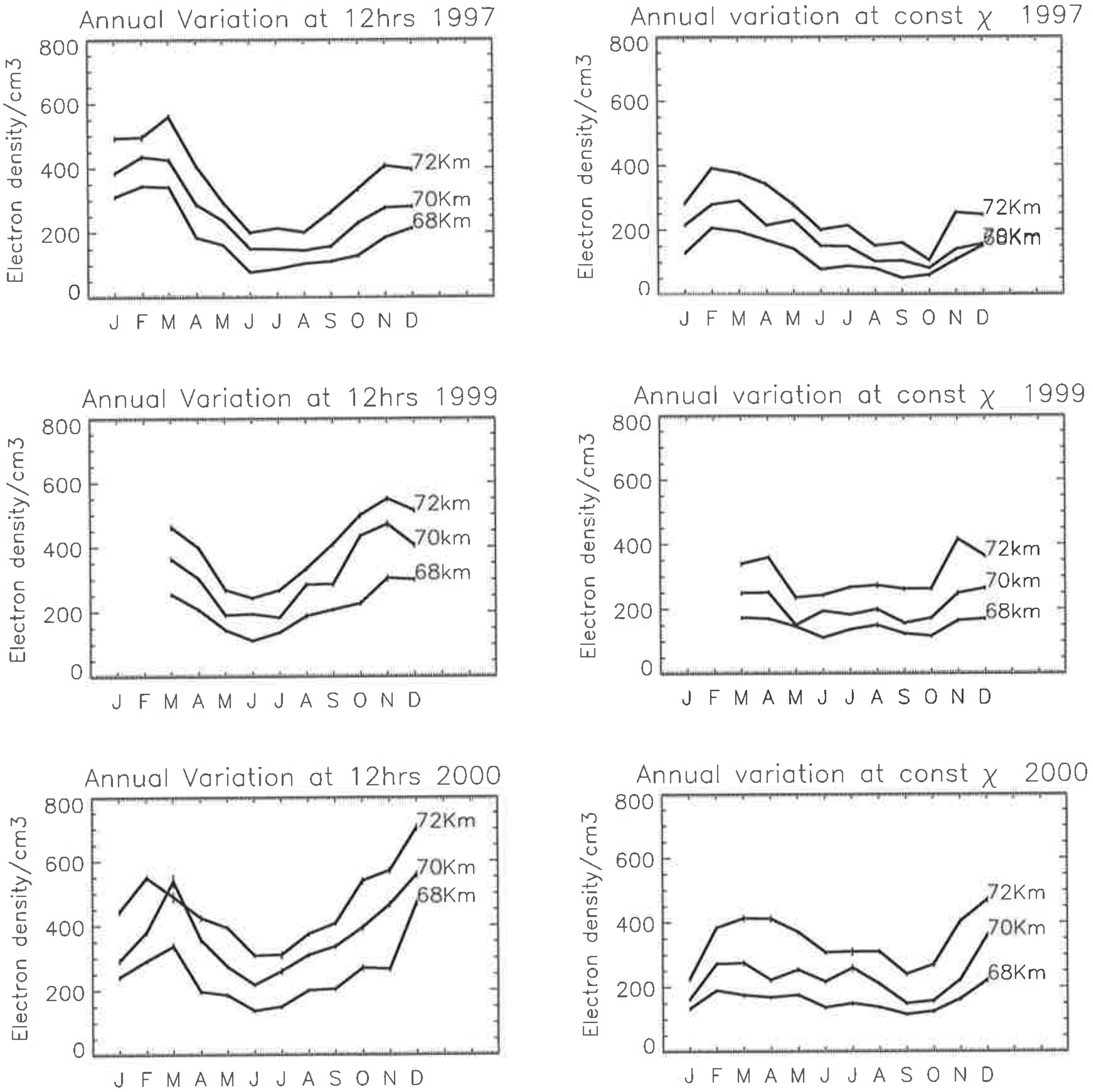

Figure 3.12: Seasonal variation of electron densities at various altitudes. Left: at noon and Right: at constant χ of 58° for all three years.

show that there is a marked seasonal variation which is not proportionately connected with the change in solar zenith angle. The electron density values for March noon and September noon are quite different even though the solar zenith angles are the same at these times (about 34°). This change, which does not accord with the solar zenith angle, is thought to be due to NO density enhancement possibly associated with dynamical effects or to changes in electron loss rate.

Seasonal variation of N_e at noon in comparison with IRI-95 model values at 70 km,

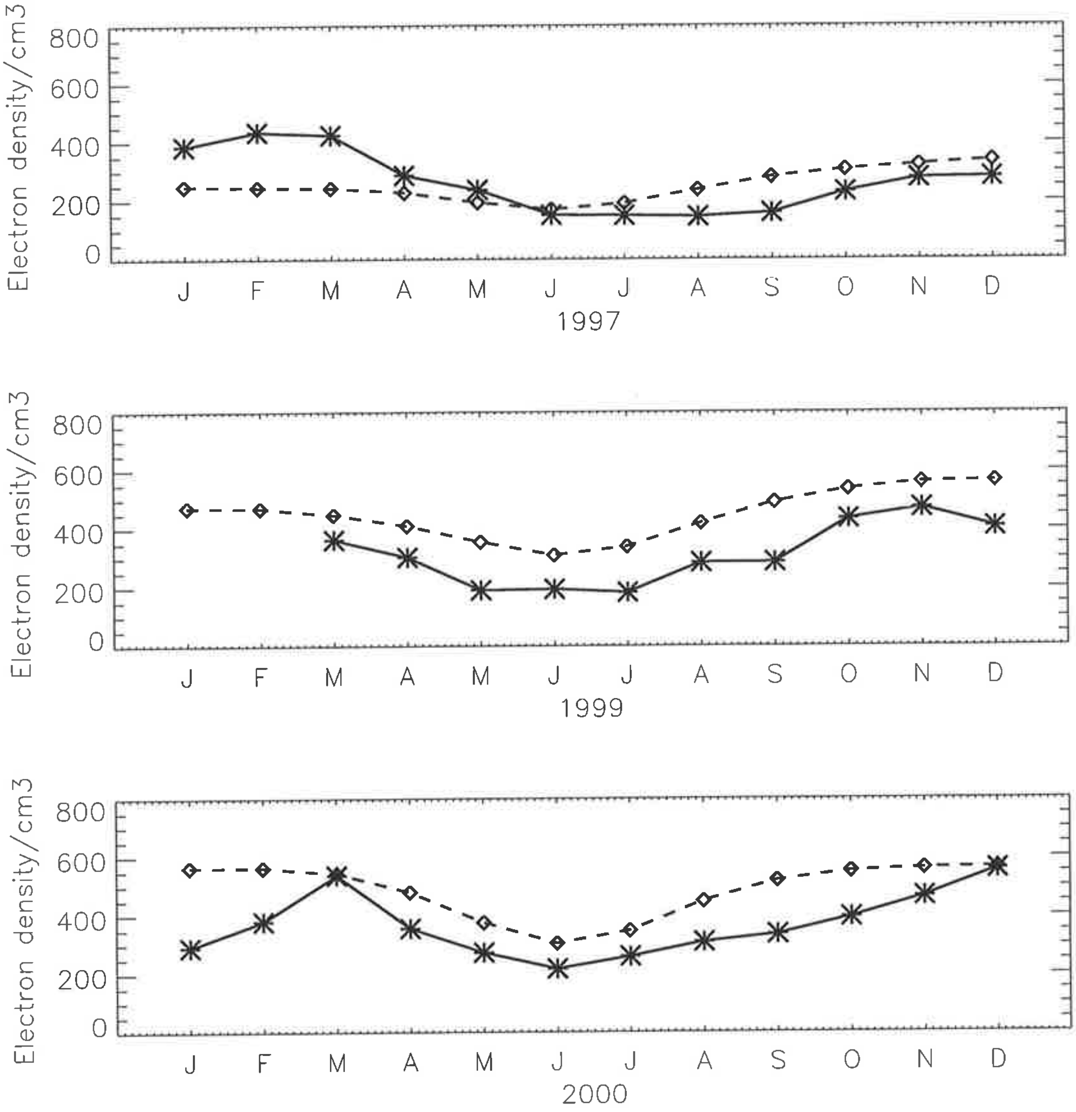

Figure 3.13: Seasonal variation of electron densities at 70 km, from 1997 to 2000 in comparison with electron density variation from IRI95 model (dashed line). Note that data from January 1998 to February 1999 are not available.

for the period of observation (1997-2000) are shown in Figure 3.13. Except for the first half of 1997, model results are systematically larger than the observed electron densities at Adelaide by a factor of 1.5 to 1.9. However, observed electron densities from January through May for 1997 are larger than model results by a factor of 1.25 to 1.7.

Similarly seasonal variation due to FIRI and MF radar results (Figures 3.14 to 3.16) agree quite well in the low solar active period ($F_{10.7}$=50) in comparison to high

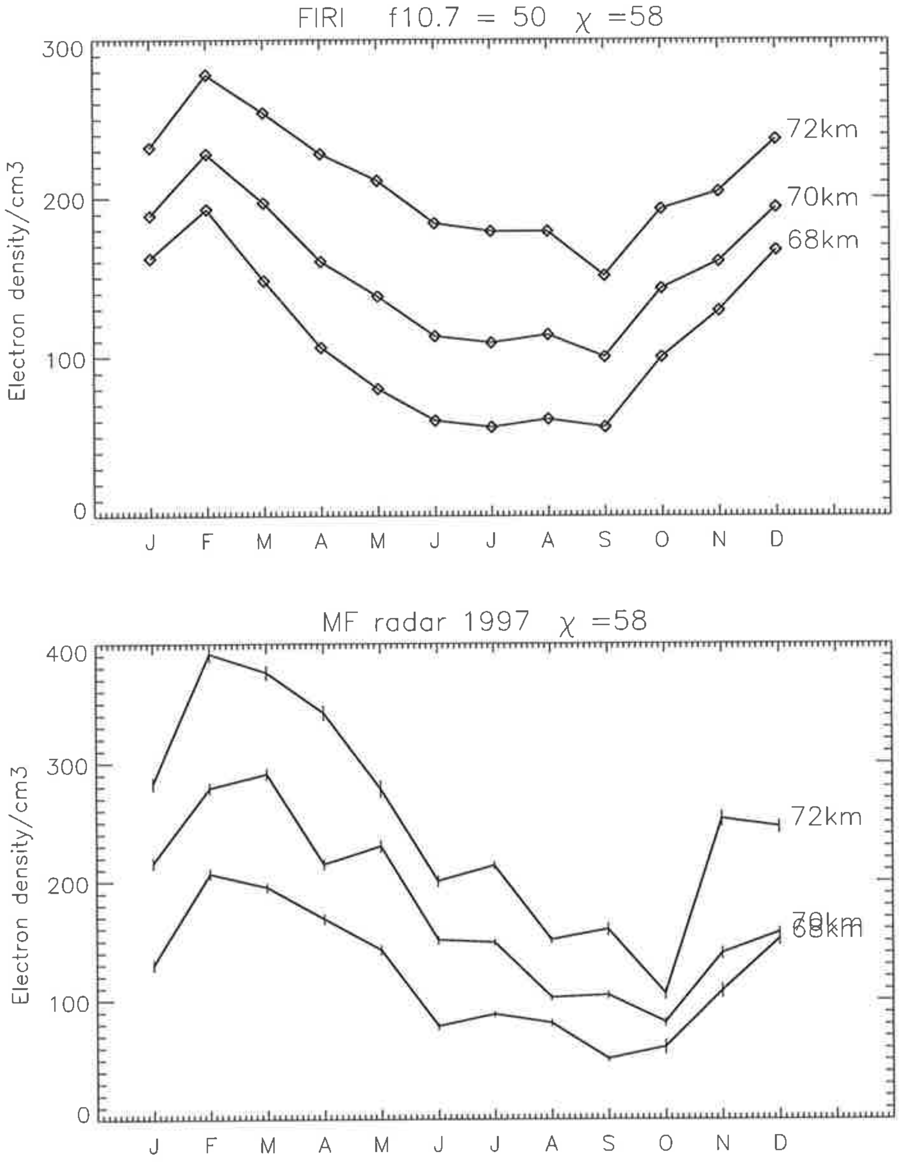

Figure 3.14: Seasonal variation of electron densities at Adelaide (bottom plot) in comparison with electron density variation from FIRI model (top plot), for low solar active period.

solar active period ($F_{10.7}$=180). More direct comparison can be seen in Figure 3.16, at 70 km altitude. All results are at constant $\chi = 58°$ as indicated in the figures. In 1997 the minimum electron density was observed in the month of October, compared to September minimum shown in the FIRI theoretical model results. Observed N_e from January to June are larger than FIRI model results (1.3 times larger in March and May). From July through to December FIRI model results are larger than observed

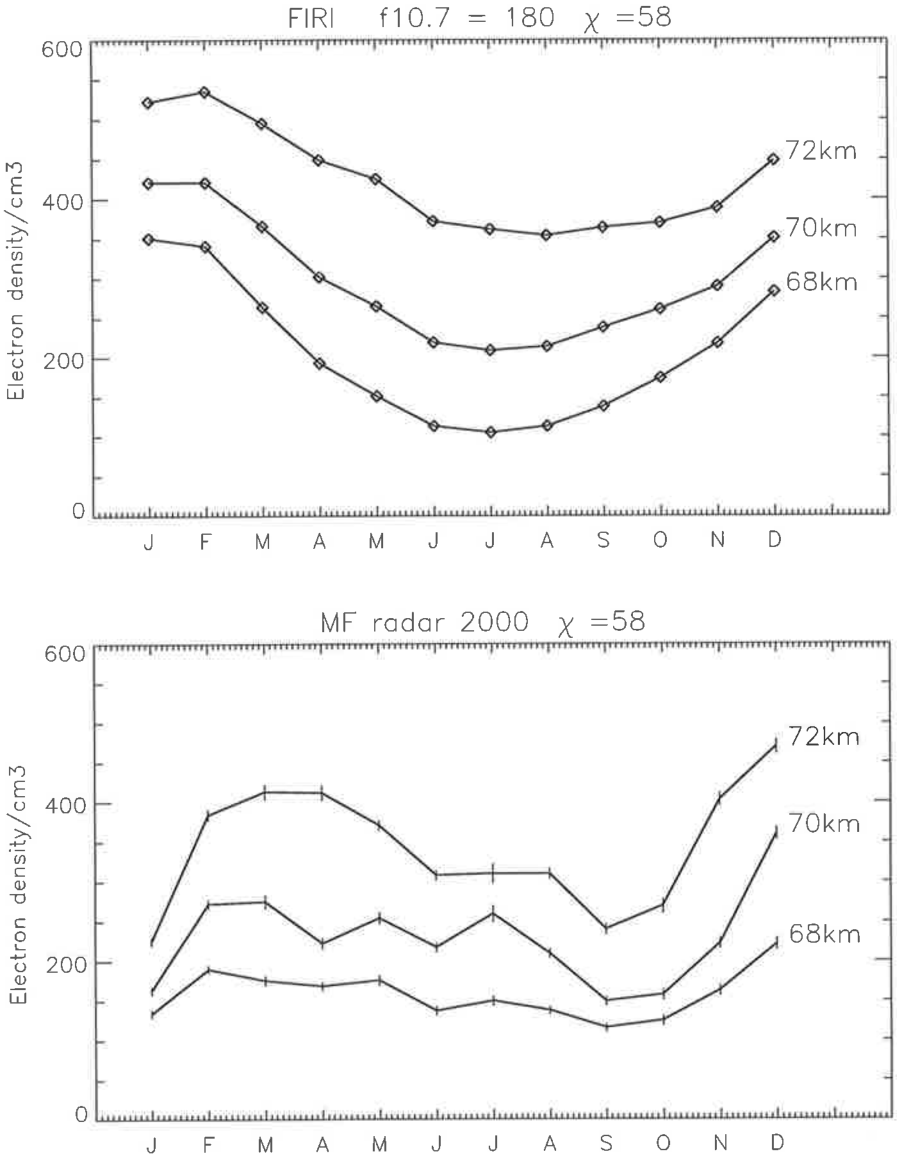

Figure 3.15: As for Figure 3.14, but for a high solar active period of year 2000.

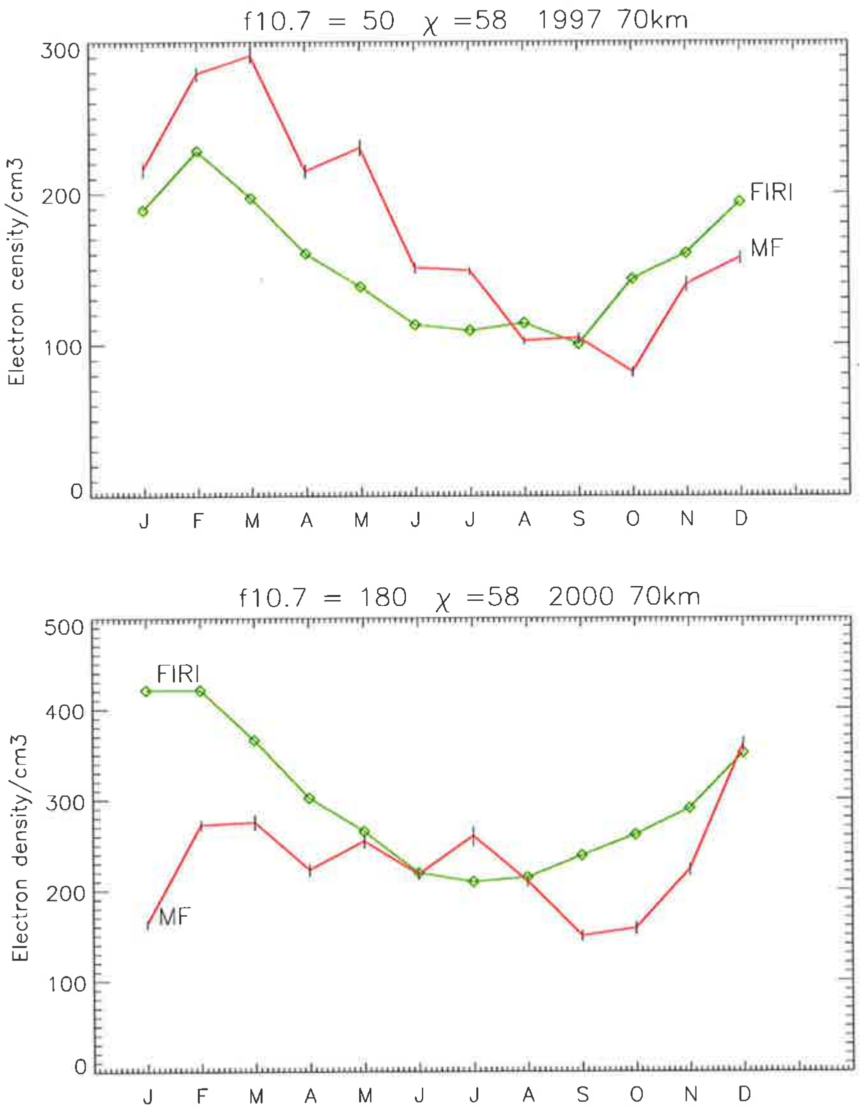

Figure 3.16: Results of Figures 3.14 and 3.15 are combined to show differences in variation at 70 km.

N_e, maximum difference shown is in October (1.99 times larger). The bottom panel of Figure 3.16 shows the difference between FIRI and observed N_e at 70 km for high solar active period. Except for Jun, July and August, FIRI values are 1.3 -2.6 times larger. In this period, the FIRI electron density variation follow the variation of observed noon variation than the constant solar zenith angle variation.

The height structure of observed and model (both for IRI and FIRI) electron densities in 1997 and 2000 are shown in Figures 3.17 and 3.18. Observed N_e are in reasonably good agreement with the model values in the low solar active period (except with August through December IRI model results are comparatively larger). Whereas, in the high solar active period, the observed N_e are generally smaller than both the model results.

The ratios of N_e values in high and low solar active periods, both for FIRI and observed N_e as shown in Figures 3.19 and 3.20. varied between 1.5 and 2.0 (except from January through May of observed N_e, where the ratio was between 0.5 to 1.2). This ratio (1.5 to 2.0) coinciding with the change in the strength of solar Ly-α radiation with respect to solar activity, demonstrates the strong influence of solar control. However, marked difference in the spring equinox months (September and October, Figures 3.19 and 3.20) points to the influence of dynamic changes in the atmosphere on the electron densities.

Next, inter hemispheric latitudinal structure of mid-latitude electron densities at noon are investigated with the help of IRI-95 model results along with Wakkanai data. Figure 3.21 depicts a cross section at solstice from $-60°$ to $+60°$ for various heights. The square line is from IRI95 model data. BP and Wakkanai data are over plotted for comparison. Note the increase in electron density toward the summer hemisphere. The IRI model data matches quite well with the DAE experimental results at BP and WK. Since the comparison of seasonal variation of IRI detailed earlier revealed, anomalous increase during the first half of 1997 (in observed N_e, possibly due to changes in equipment parameters see Table 1.2) compared to other periods, the December 1997 data are over plotted as a representation of summer value.

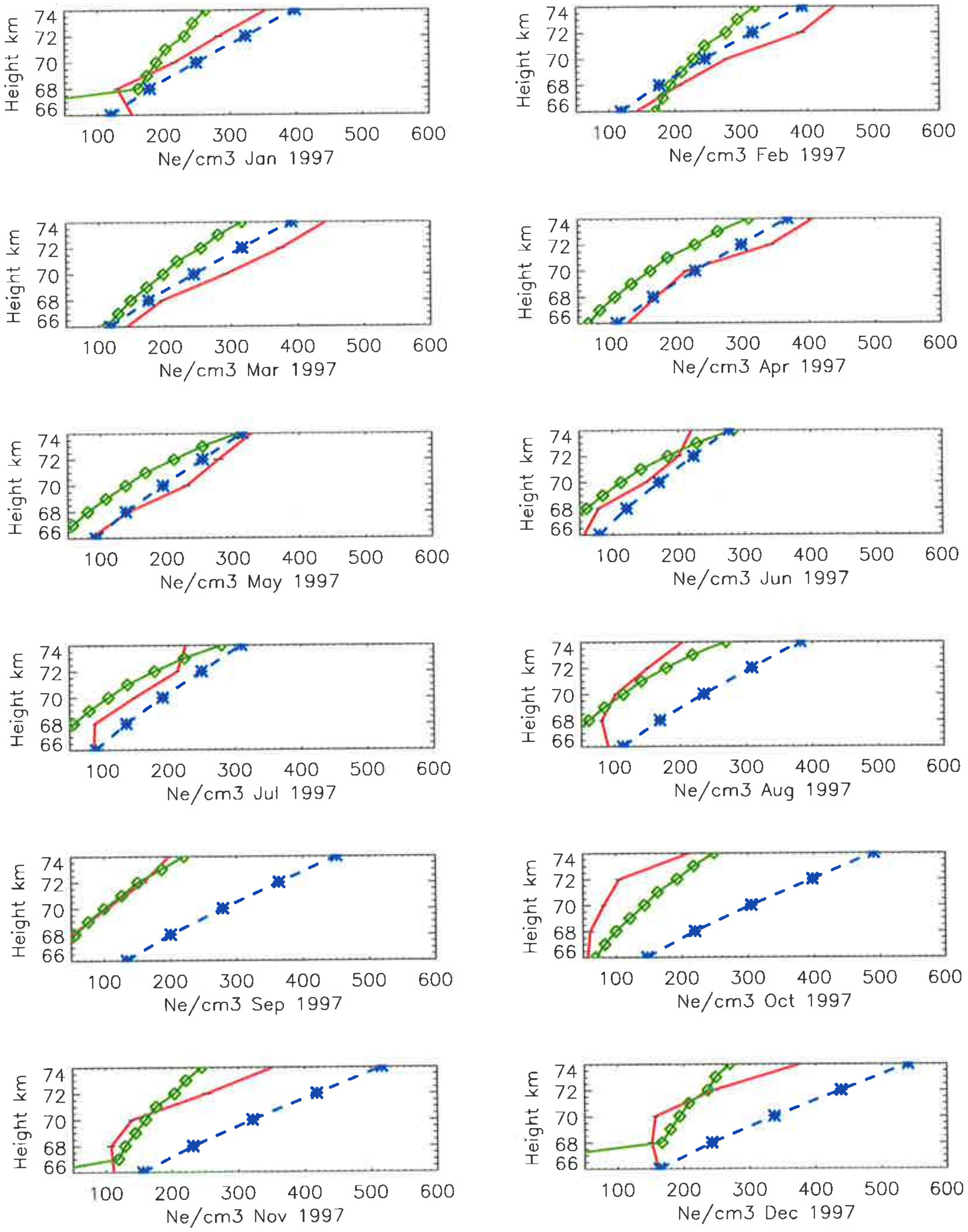

Figure 3.17: Vertical profiles of observed N_e (red) compared with FIRI (green,□) and IRI (blue,$*$) model results , low solar active period. All data at $\chi = 58°$ except that IRI data at noon.

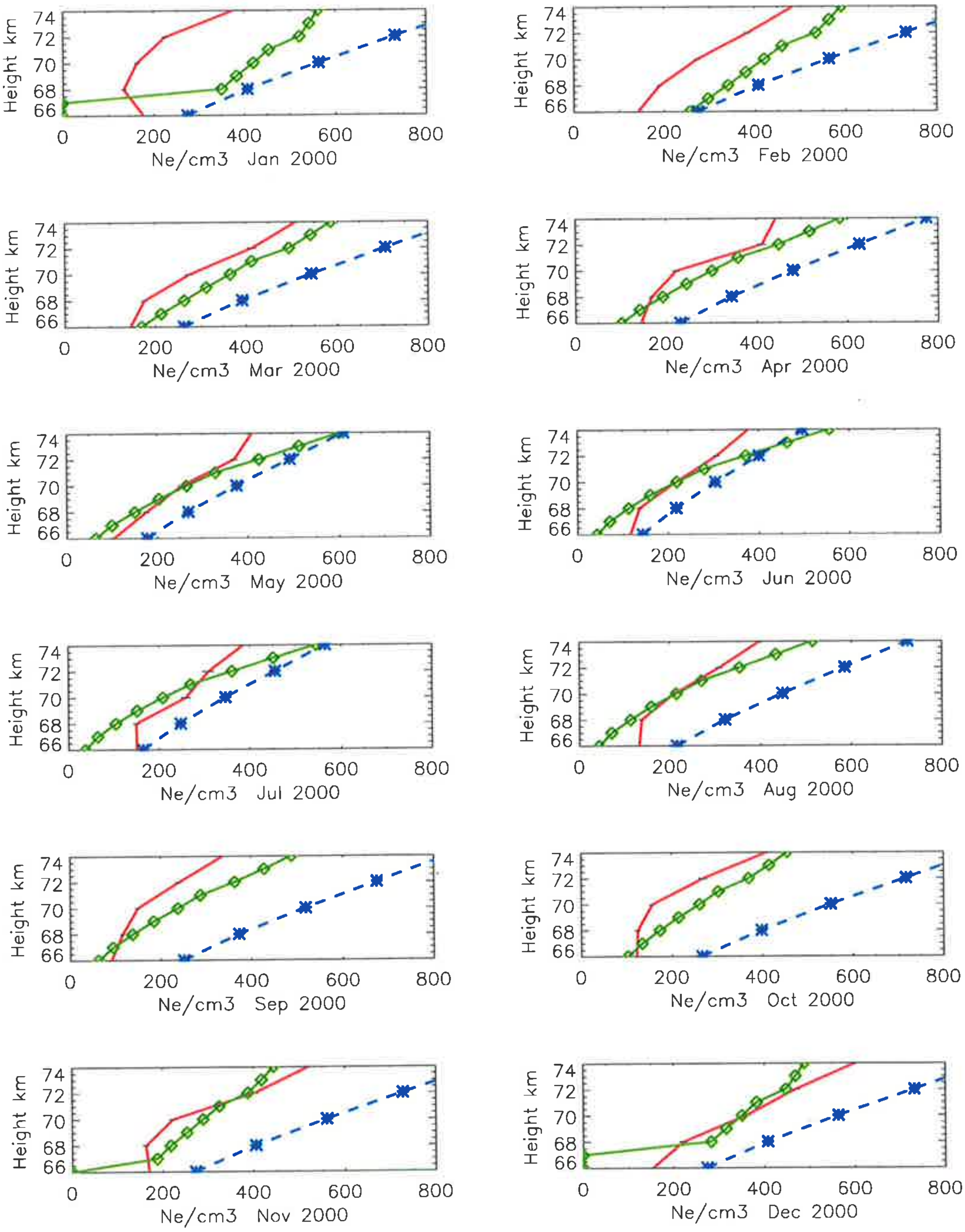

Figure 3.18: As for Figure 3.17, but for high solar activity period.

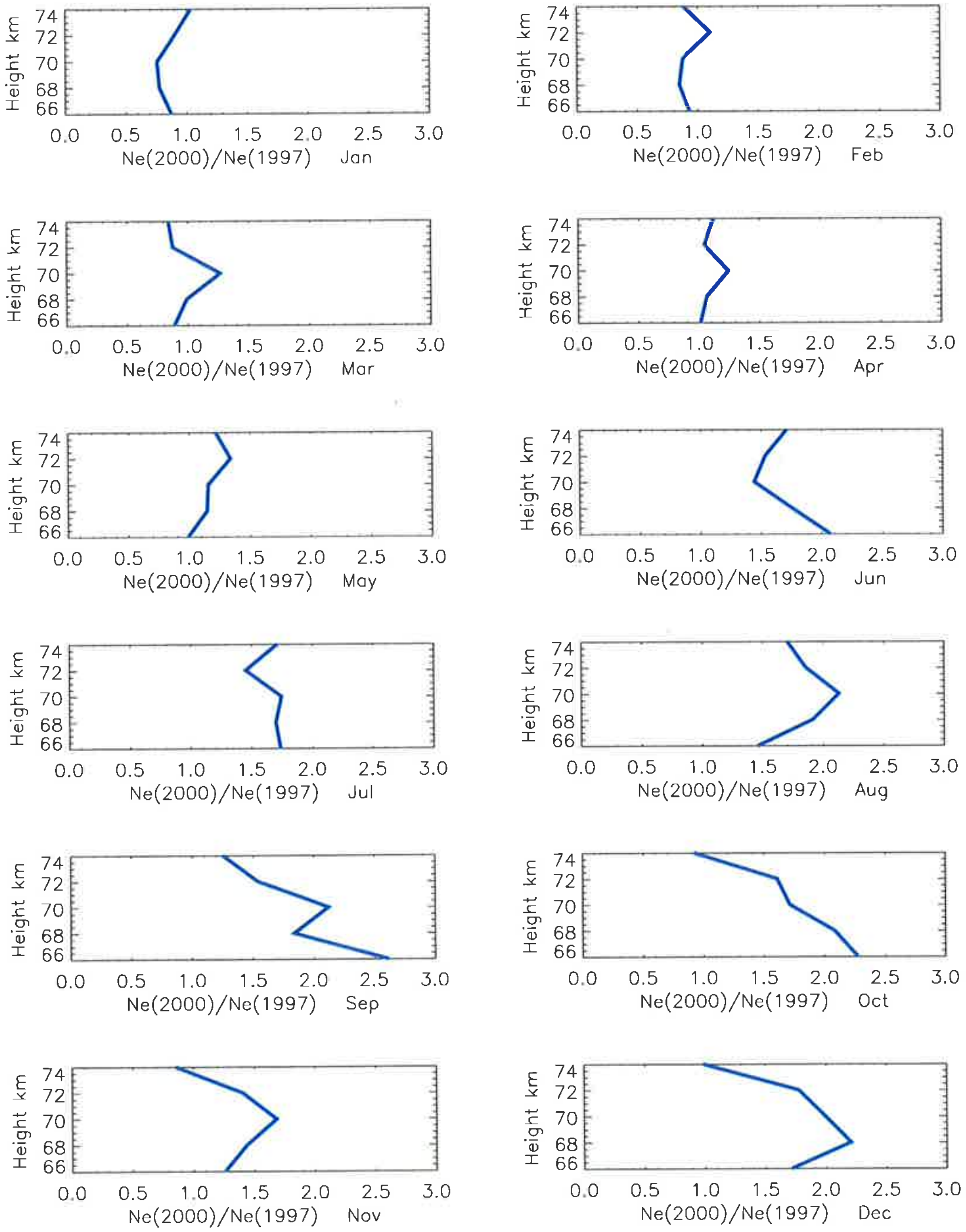

Figure 3.19: Ratio of solar maximum to minimum observed electron density, $\chi = 58°$.

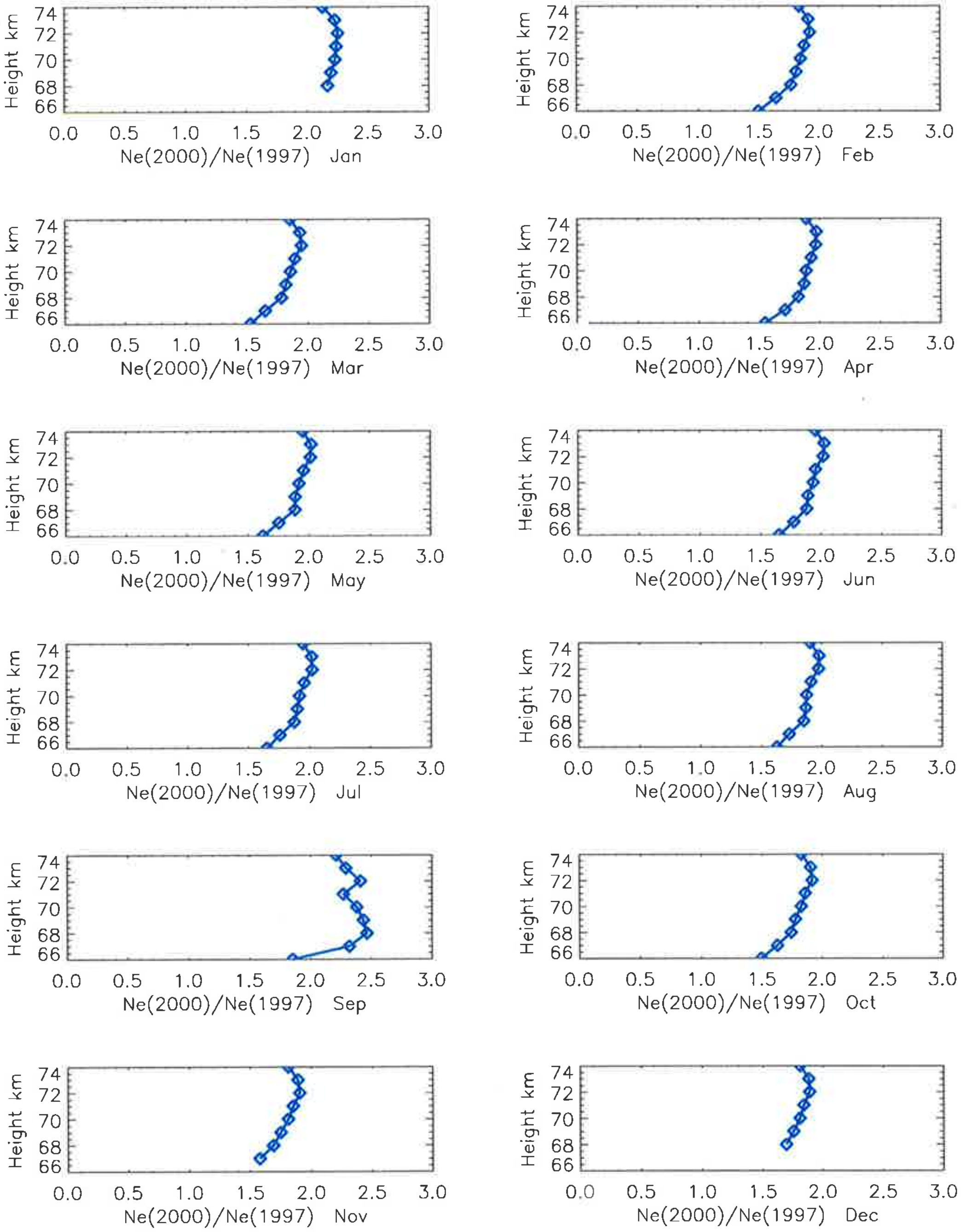

Figure 3.20: As for Figure 3.19, but for FIRI N_e.

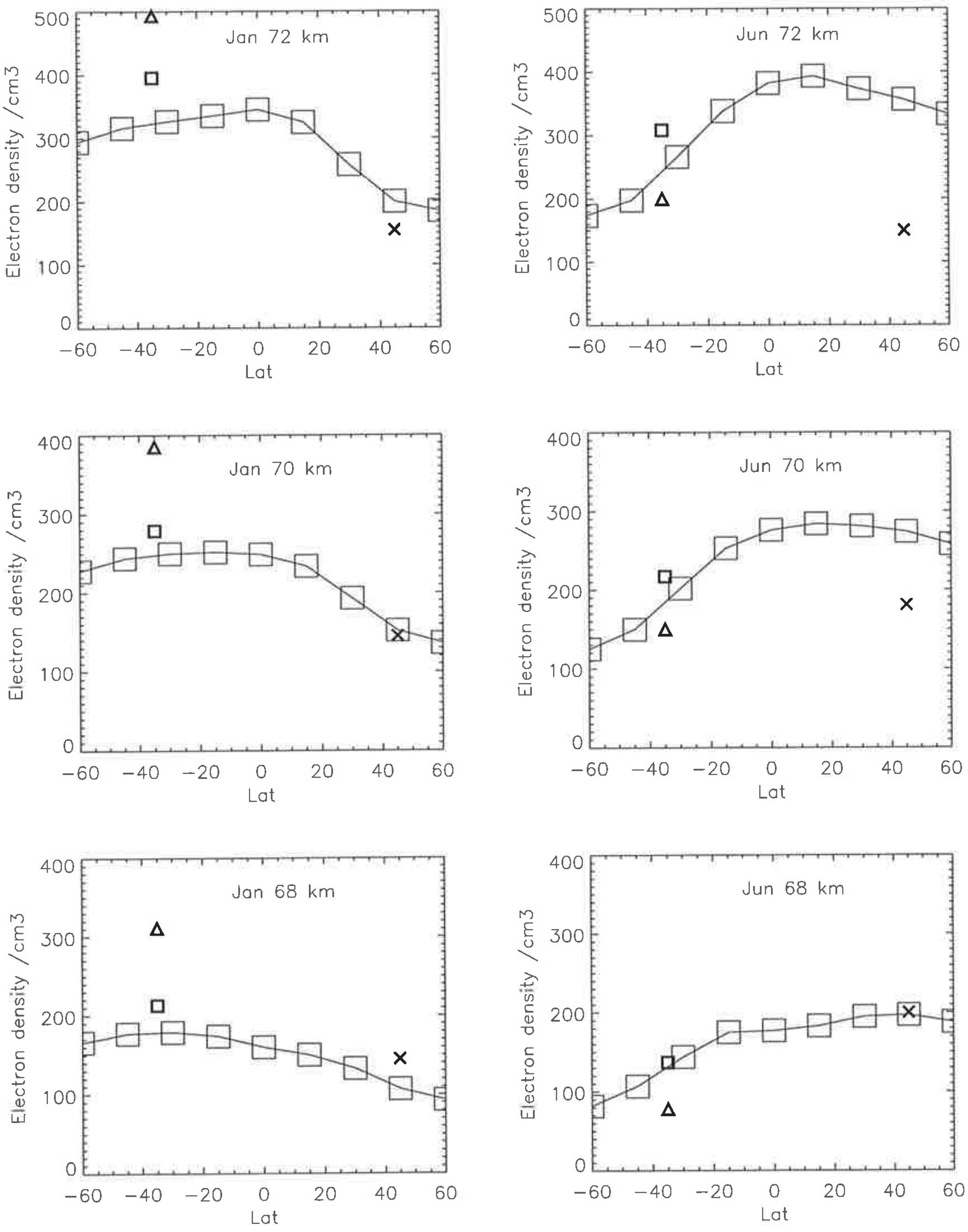

Figure 3.21: Latitudinal variation of electron densities at noon for three different altitudes and 1997, solstice. Left: from summer to winter and Right: from winter to summer hemisphere. The square line is from IRI95 model data. BP(△ (January),□ (December)) and Wakkanai (×) data are over plotted for comparison.

Similar variations were noted by McPeters (1989) in the nitric oxide column densities. The latitudinal distribution of NO is relatively flat at about $5-6\times10^{14}$ molecules cm^{-2}, but with $20-30\%$ more NO at summer mid-latitude than at winter mid-latitude near solstice. In comparison electron densities estimated in this study are about 50% larger in summer than winter mid-latitude. Electron densities at various solar zenith angles were also published by Friedrich and Torkar (2001). In their findings, similar variation was reported at 70 km but above that an inverse relation was found (i.e., increase in electron density toward the winter hemisphere in the altitude range from 80 km to 100 km).

Finally, IRI and FIRI model results are used to back calculate amplitude ratios with help of Sen Wyller magneto-ionic theory, Figure 3.22 (See Section, 2.2 and Equation 2.2 for appropriate theory). These calculated amplitude ratios are compared to the MF radar observed amplitude ratios, to get some understanding of the variation of model ratios. However, since the slope of the amplitude ratio profiles and integrated differential absorption are used to determine the electron densities, no direct predictions can be made regarding the estimation of electron densities, except that, due to larger model densities, the differential absorption is to be larger. Hence the reduction in the model amplitude ratios compared to observed values.

The electron densities used to estimate model amplitude ratios are shown in the Figure 3.23. The total differential absorption at 70 km due to FIRI, IRI and MF radar electron densities are estimated as 2.29, 3.1 and 1.69 dB respectively. As expected, the differential absorption is proportional to the electron densities shown in the Figure 3.23.

3.3.2.1 Effect of solar cycle variations

The purpose of this section is to study how the lower ionospheric daytime electron densities vary with the sunspot cycle (Cycle 23). Hence, the electron density variation from 66 to 74 km (daytime) heights along with the measured sunspot number is shown in Figure 3.24. Regression curves (minimum to maximum activity period) for 66

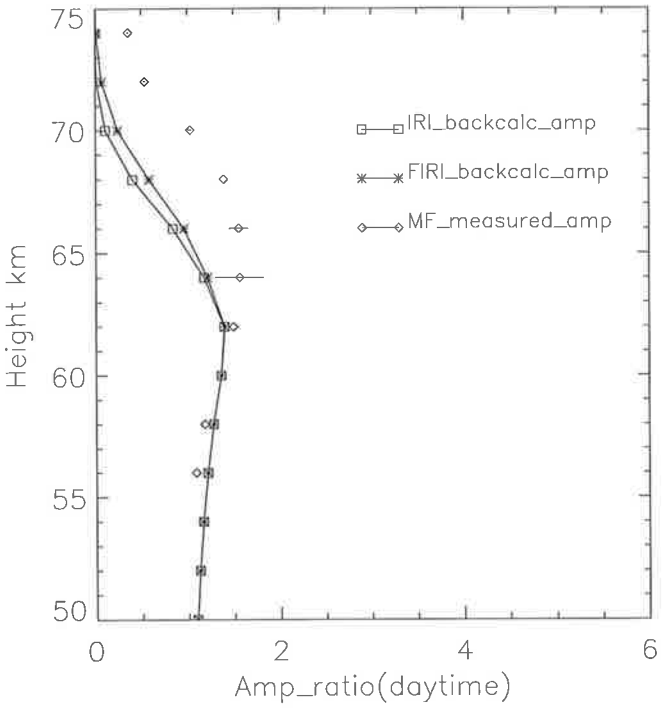

Figure 3.22: Amplitude ratios back calculated using IRI electron density profiles (□, IRI-95) and (◇, MF-measured), the data shown are for February 2000.

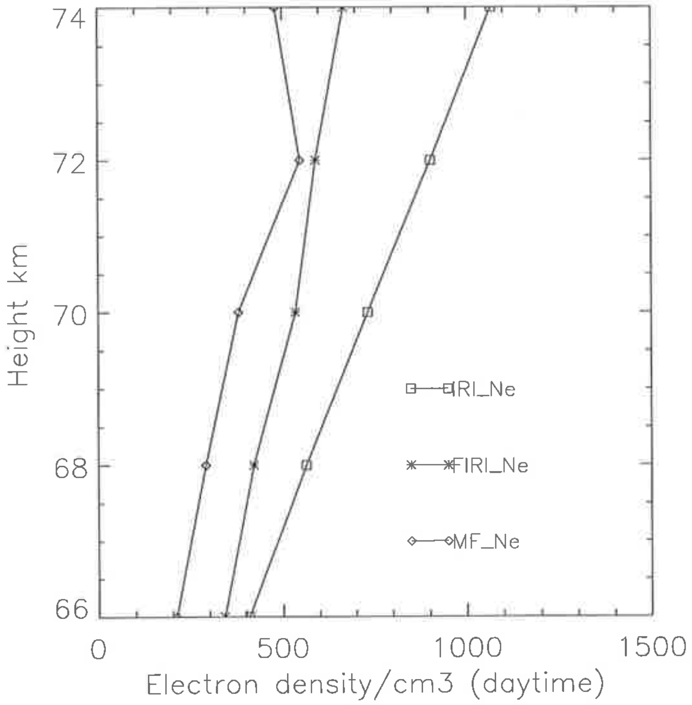

Figure 3.23: Electron densities used to back calculated IRI(□) and FIRI(∗) and estimated electron density(◇) for February 2000, using measured amplitude ratio.

Table 3.3: Regression coefficients for daytime heights.

Height (km)	overall
66	0.29
68	0.24
70	0.26
72	0.35
74	0.46
76	-0.22
SS range	(0-180)

- 74 km altitudes are shown in Figure 3.25. Overall regression coefficients for the observation period are shown in the Table 3.3

For values of SS number less than 50 (1997), the electron density at low altitudes (66 - 74 km) decreases with increasing SS number, at least by a factor of 2. In the following years (1999 and 2000), when the SS number varied between 60 and 180, no correlation is evident between electron density and SS number at these altitudes. This indicates the relative importance of different sources of ionization with solar activity. Galactic cosmic radiation could be one of the sources. A distinct feature to be noted is the electron density enhancement in the months of February and March and the reduction of N_e in September, corresponding to the seasonal variation still persist.

The changes in electron density in quiet and active sun periods reported by Mechtly and Bowhill (1972) for 35°N latitude and 60° solar zenith angle, are comparable to our above observations (Figures 3.26 and 3.27). The envelope of quiet sun profiles have been marked by the horizontal hatch marks, and the envelope of active sun profiles are indicated by the vertical hatch marks. The two envelopes are completely separated from 50 to 60 km. They cross over at about 62 km, and again are completely separated in the other sense between about 65 and 80 km. These variations are similar to our findings as shown in Figure 3.26. Solar activity dependence of FIRI model electron densities at 35° latitude, spring equinox, at 75° zenith angle demonstrated similar variations Friedrich and Torkar (2001).

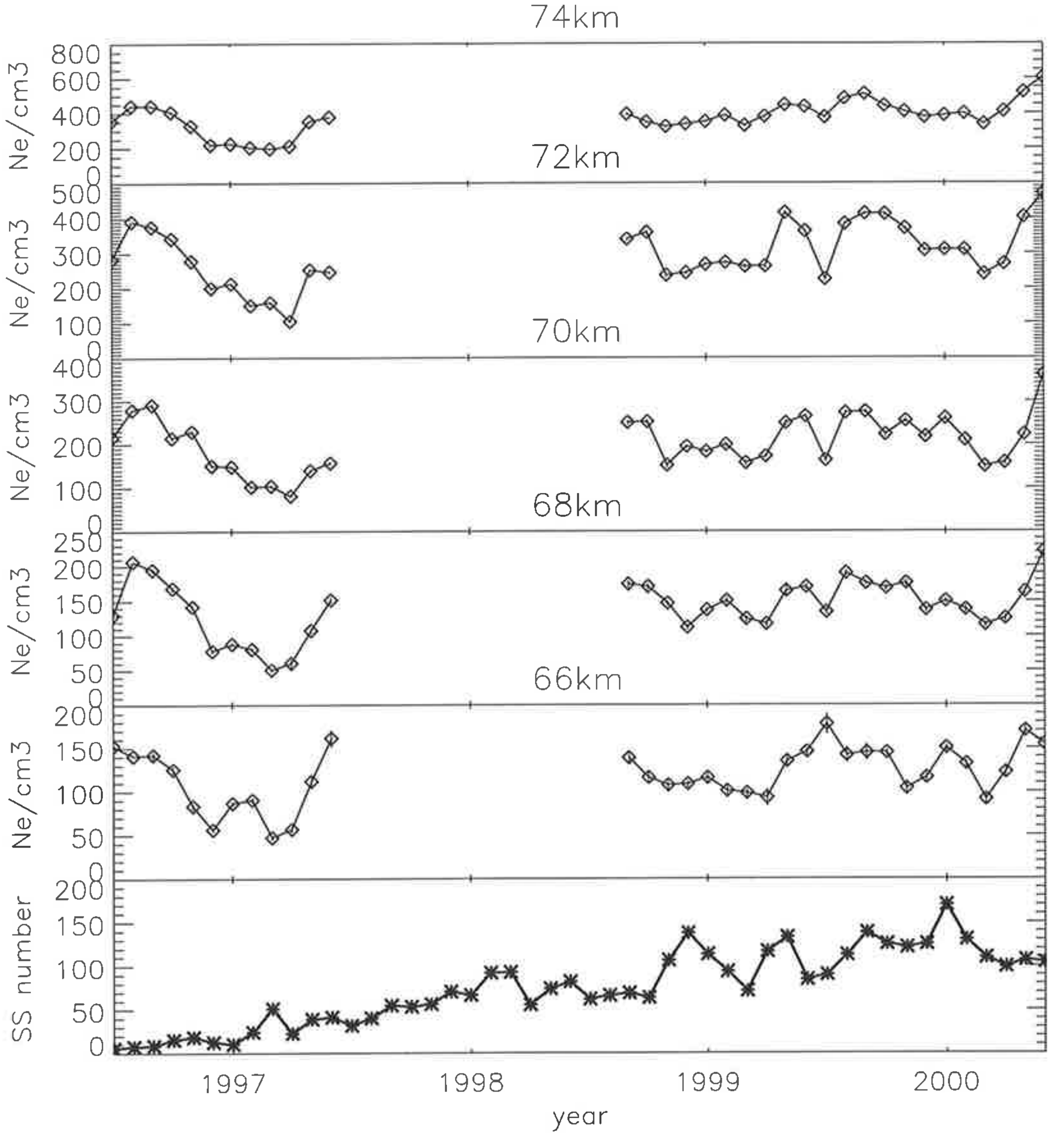

Figure 3.24: As for Figure 4.21, but for $\chi = 58°$ and 66-74 km

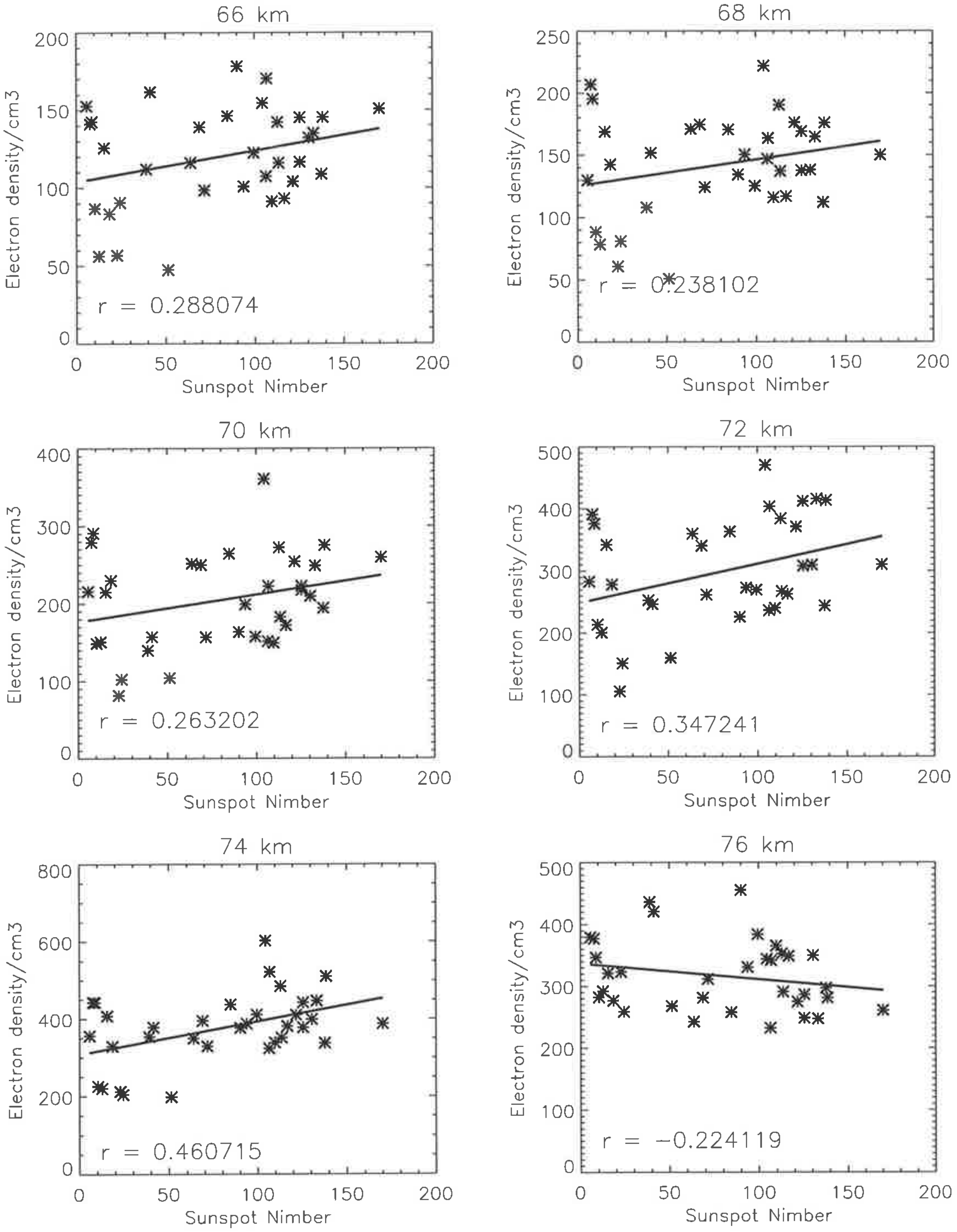

Figure 3.25: Regression curves for low to high solar activity period (1997-2000).

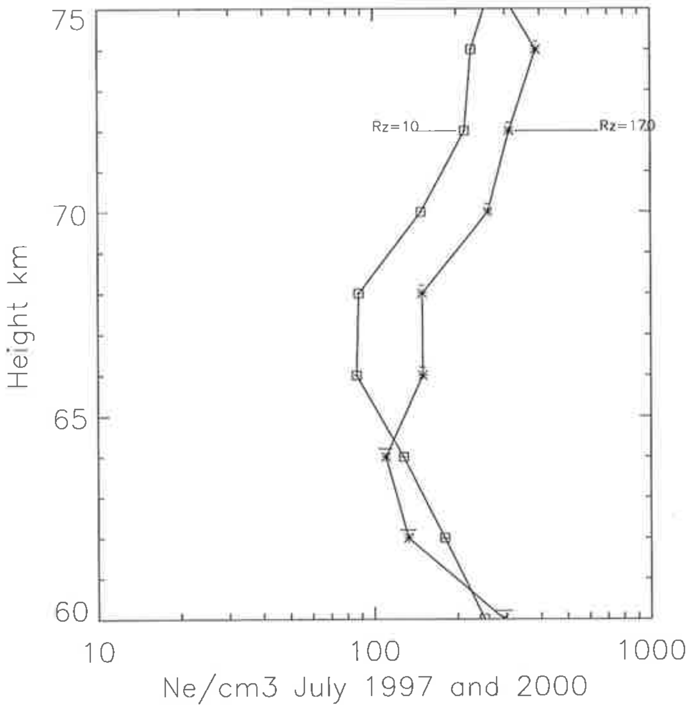

Figure 3.26: Mean electron density profiles measured at Buckland Park(noon) under conditions of low (◇,1997) and high (∗, 2000) solar activity (winter)and Rz=10 and Rz=170, respectively. The horizontal lines are standard error (raised by 0.2 km for clarity)

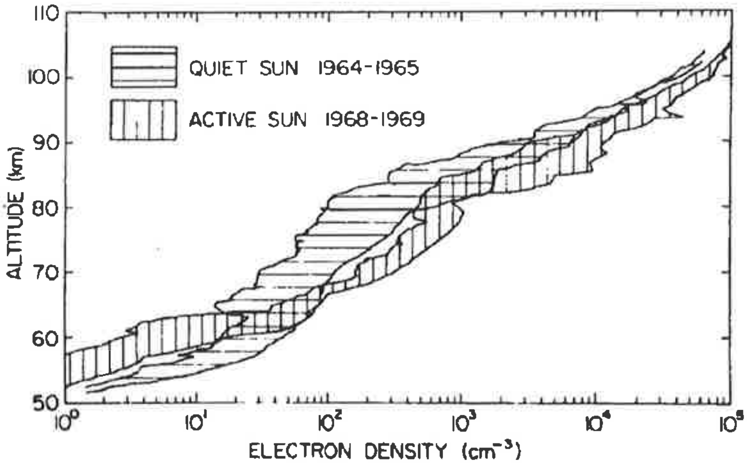

Figure 3.27: Electron density profiles from Mechtly and Bowhill (1972) showing the envelope of quiet and active sun profiles.

Table 3.4: Solar X-ray Flare data for November 1997 obtained from World Data Center A. Times shown are in Universal Time (UT)

Month	Day	Start Time	End Time	Time of Maximum	Class	Multiplier
11	03	0906	0923	0909	M	1.4
11	03	1018	1034	1029	M	4.2
11	03	1955	2109	2008	M	1.0
11	04	0128	0201	0132	M	1.3
11	04	0303	0500	0328	M	4.1
11	04	0554	0713	0559	X	2.1
11	06	1122B	1244	1156	X	9.4
11	15	2237	2338	2242	M	1.0
11	24	1930	2010	1950	M	1.6
11	26	1828	1844	1835	M	2.0
11	27	1302	1338	1317	X	2.6
11	28	0456	0633	0506	M	6.8
11	28	1954	2017	2009	M	1.1
11	29	2233	2358	2242	M	6.4

3.3.2.2 Disturbances

Sometimes disturbances occur on the sun accompanied by the emission of one or more of the following radiations, each of which can produce its own type of disturbance in the ionosphere. For example, if there is a sudden increase in the strength of visible H-alpha line, *solar flare* are produced and if there is an increase in the strength of the X-radiation, $X - ray$ *flares* are produced. X-ray flares, plasma events, and proton events often accompany solar flares. The frequencies of all types of disturbance follow the 11-year solar cycle (Ratcliffe, 1972).

Variations of the electron densities in the day and/or night due to these phenomenon are noted in this study. Some examples of effect of solar flares during the period of 1996-2000 are given below.

November 1997 is considered for analysis, as the number of flares observed in that month are more than any other month in that year. For comparison purposes November 2000 (a high solar activity period) is also considered. Table 3.4 gives the observed flares during November 1997. The start and end times of the maximum are given in UT (Where UT stands for Universal Time), and the type of flare and multiplication factor gives the flux in wm^{-2}. The classification and meaning of X-ray flares are detailed in Chapter 1. The first value in the table (class M and multiplier 1.4) indicates that the flux is 1.4×10^{-5} Watts/m^2.

Two important factors matter in considering flare effects, (i) the time of the day and (ii) the type of flares which can influence the $D-$region ionization. Another factor to be considered is the location of the observing site. The first half of November 1997 was characterized by a significant increase of solar geomagnetic activity, including strong Solar Proton Events (SPE), geomagnetic storms, and Forbush effects. The time of the first 3 flares listed in Table 3.4 coincided with night hours (ACST = UT + 9.5). Hence the effect is not seen in the observed electron density. Following that, there were flares observed on November 4, coinciding with the time of local noon. These flares were accompanied by enhanced proton fluxes with the energy higher than 2 Mev and maximum fluxes reached at 0132 and 0328UT on 4 November. The maximum enhancement of X rays was registered at this time. The accompanying variations in the (A_p) magnetic index are presented in Figure 3.28 showing that a strong magnetic storm accompanied the SPE. However, the effect of proton fluxes and magnetic storms is not expected to be shown at our latitude and in the mesospheric altitude ranges. Significant disturbances still continued on November 5 and 6.

Figure 3.29 shows the plots of N_e which exhibit a significant enhancement on November 4th during daytime hours. The enhancement can either be related to the the SPE event or to the flares before the event. As mentioned above, X-ray flares, plasma events, and proton events often accompany solar flares. It is worth noting that strong ionization seems to have taken place even at altitudes much lower than normal D-region.

Flares were observed on November 8, November 9, November 23 and November 24 (Table 3.5). Enhancement of the electron density on November 9 and sharp increases in N_e at lower altitudes can be seen in the bottom plot of Figure 3.29. Similar

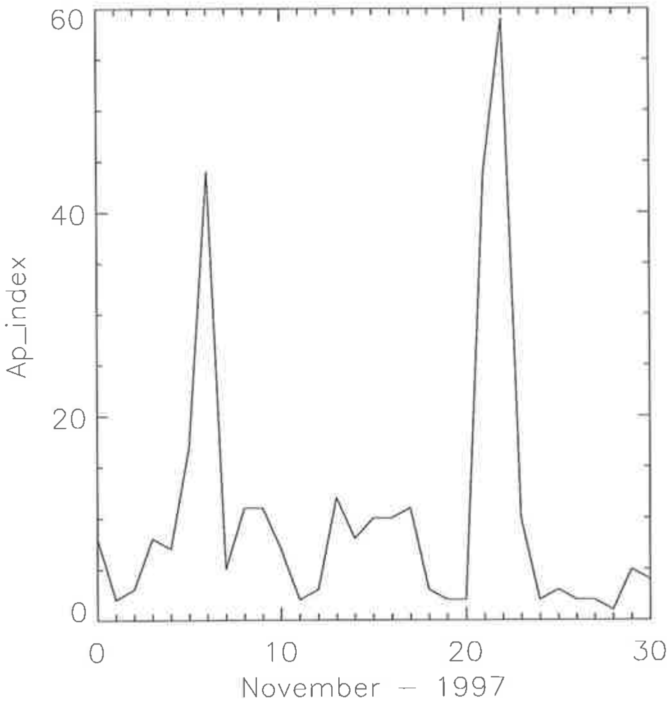

Figure 3.28: November 1997 Ap magnetic index showing the increase in magnetic activity after the flares(on Nov 6 and Nov 23)

observations were reviewed by Danilov (1989). A sharp increase of electron density, N_e, above 50 km and lowering of the $D-$region boundary down to 40 km were also reported by Vanina et al. (1995). These measurements were however carried out at a high latitude station (Molodezhnaia 67.7°S, 45.9°E) in October 1989 and therefore may not be totally acceptable for comparison. A possible contribution was thought due to hard X rays (0.1 -2 nm) and of the solar cosmic rays in the observed effects. The fact that ionization is produced at lower heights than usual shows that the ionizing radiation possesses a smaller absorption cross section than the radiation responsible for the normal D layer.

Examples shown in Figures 3.30 state the fact that ionospheric effects begin at the time of visual sighting of the flare, implying that they are due to electromagnetic, rather than corpuscular, radiation. The electron density reached as high as 1700 cm^{-3} between 66 and 70 km height range. With the availability of ionization rates (q) during the flare conditions, it is possible to estimate the relaxation time (using $\alpha = q/{N_e}^2$).

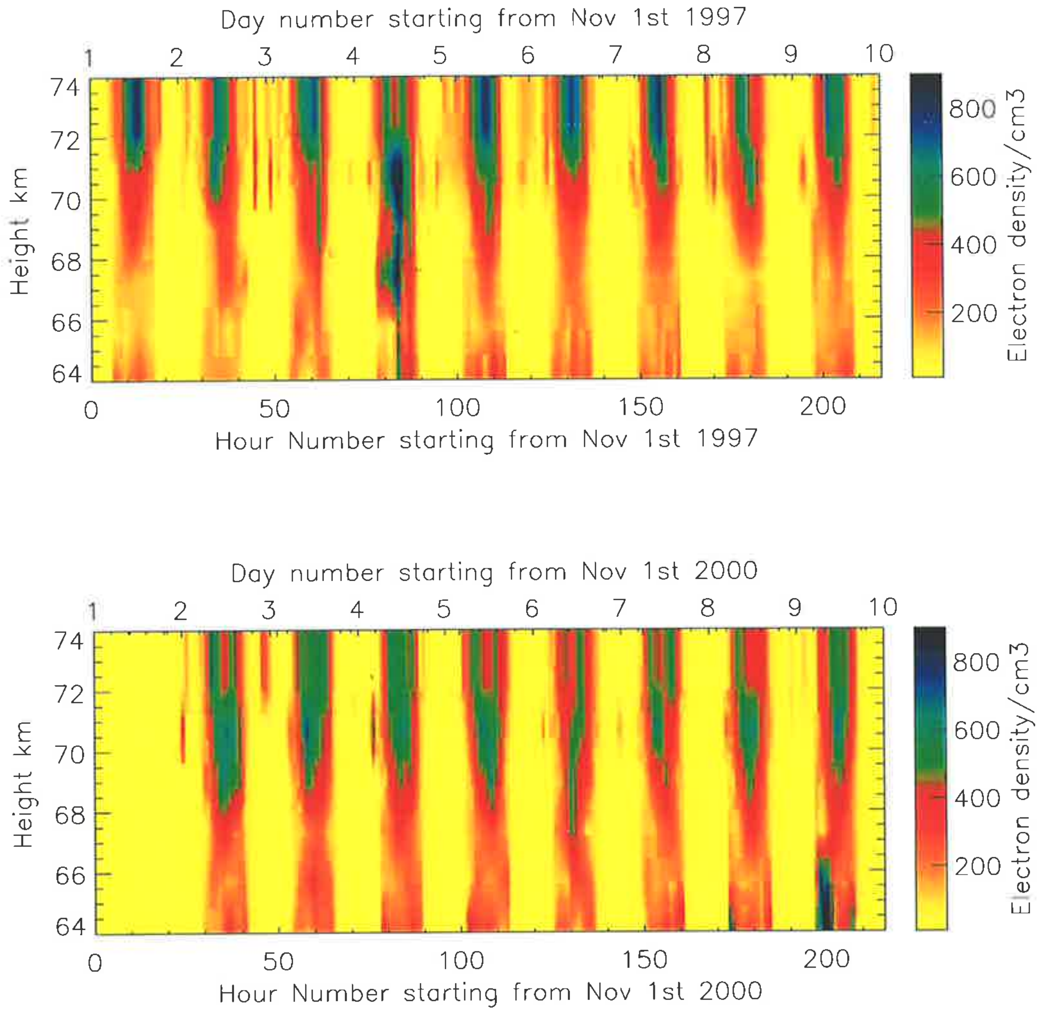

Figure 3.29: Examples of flare effect upon DAE electron density estimates - enhancement occurred on November 4, 1997 and November 9, 2000

Table 3.5: As for Table 3.4, but for 2000.

Month	Day	Start Time	End Time	Maximum Time	Class	Multiplier
11	07	1155	1220	1207	M	16
11	08	0948	1005	0958	M	15
11	08	1622	1646	1636	M	29
11	08	2242	0005	2328	M	74
11	09	0303	0339	0314	M	12
11	09	0601	0621	0610	M	12
11	09	1545	1620	1613	M	10
11	14	1619	1653	1634	M	10
11	18	1051	1109	1100	M	15
11	18	1302	1350	1325	M	15
11	21	1913	1927	1921	M	16
11	23	2318	2337	2328	M	10
11	24	0455	0508	0502	X	20
11	24	1451	1521	1513	X	23
11	24	2143	2212	2159	X	18
11	25	0059	0201	0131	M	82
11	25	0906	0940	0920	M	35
11	25	1833	1855	1844	X	19
11	26	0247	0320	0308	M	22
11	26	1634	1656	1648	X	40
11	30	0900	0944	0925	M	10
11	30	2027	2044	2038	M	13

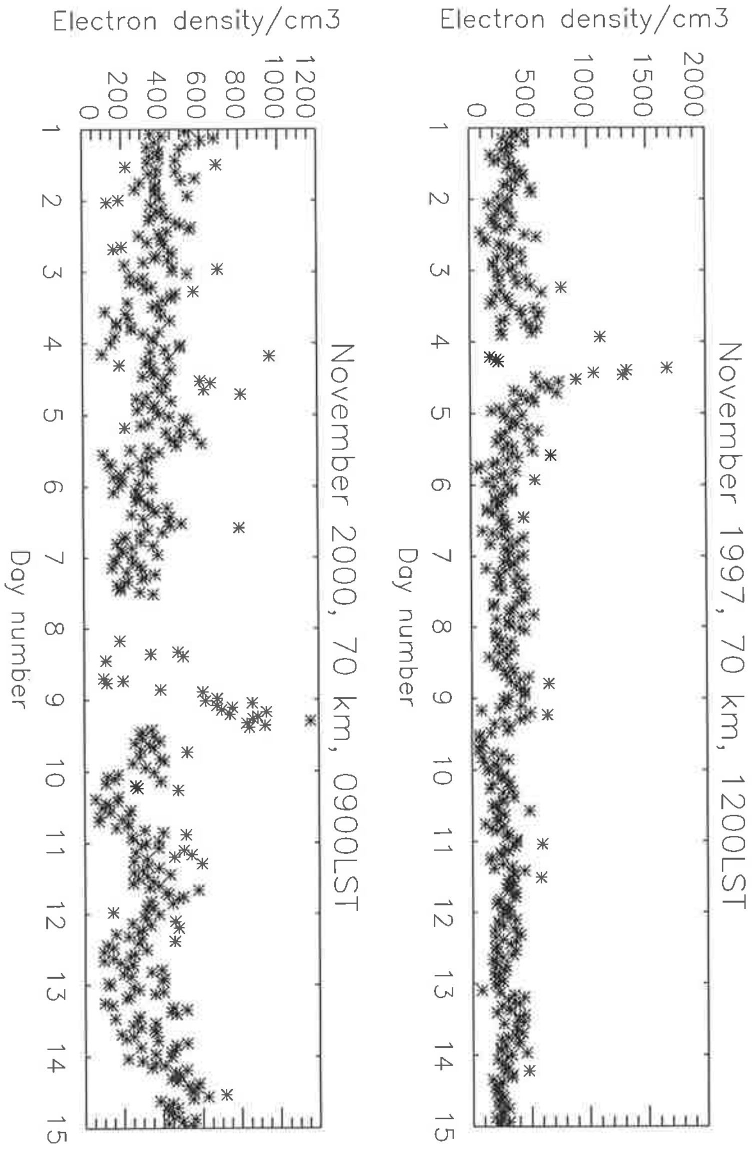

Figure 3.30: Time series of electron density (two minute data) between 1200 -1300 LST for each day in November 1997 and between 0900 - 1000 LST for November 2000

Although such estimation is not undertaken in the present work, previous researchers findings are considered as given below.

A reduction of α_{eff} at 65 km than at 70 km during the recovery phase of Solar X-ray events (SXR) can lead to the increase in electron density at lower heights (65 km) (Montbriand and Belrose, 1972). It was thought that the principal ion produced immediately following ionization by either $X-$rays, energetic electrons or protons is O_2^+ (Narcisi, 1971). Thus during moderately disturbed conditions ${O_2}^+$ is the major ion in the entire $D-$region. It is known that during undisturbed conditions the water cluster ions occur predominant below 83 km. During a solar proton event these ions can dominate below 73 km and can produce excess electron densities in comparison to normal electron concentrations. From Mitra and Rowe (1972), it can be pointed out that the decrease in loss rate is apparently due to the effect of negative ions at 70 km region.

3.3.3 Comparison with other observations

Although many profiles of electron densities have been reported in the literature since 1953, only a few of these are useful for comparison purposes. It is necessary to reject those data which are influenced by, or due to, corpuscular influx at high latitudes, and to confine attention to mid-latitude data. For present purposes "mid-latitude" will be assumed to be equatorward (50°) geographic latitude, such that an eastward atmospheric circulation is the normal condition in winter in the mesosphere.

Results from the partial reflection measurements at Wakkanai in 1997 are given in Figure 3.31. The profiles are calculated from similar experimental setup as BP except that at Wakkanai circularly polarized signals were transmitted, whereas a linear polarisation was used at BP.

It should be noted that different collision frequencies (ν) used by different workers and the latitude of the measurements, can change the magnitude of the electron density values, but the nature of the variation either diurnal or seasonal should remain the same. Since ν for each day remains the same, the diurnal variation effectively is independent of the collision frequency used. Hence, the results at Adelaide and Wakkanai are consistent with the diurnal variation expected at these latitudes. The calculated latitudinal dependencies of the electron densities were already discussed in the previous section (Figure 3.21) for local noon.

Some points to be noted from Figure 3.31 are: turnover heights appears to be around 72 km except during summer months. A relatively larger asymmetry is evident about noon in all the seasons. At lower altitudes around 60 - 64 km (not shown in

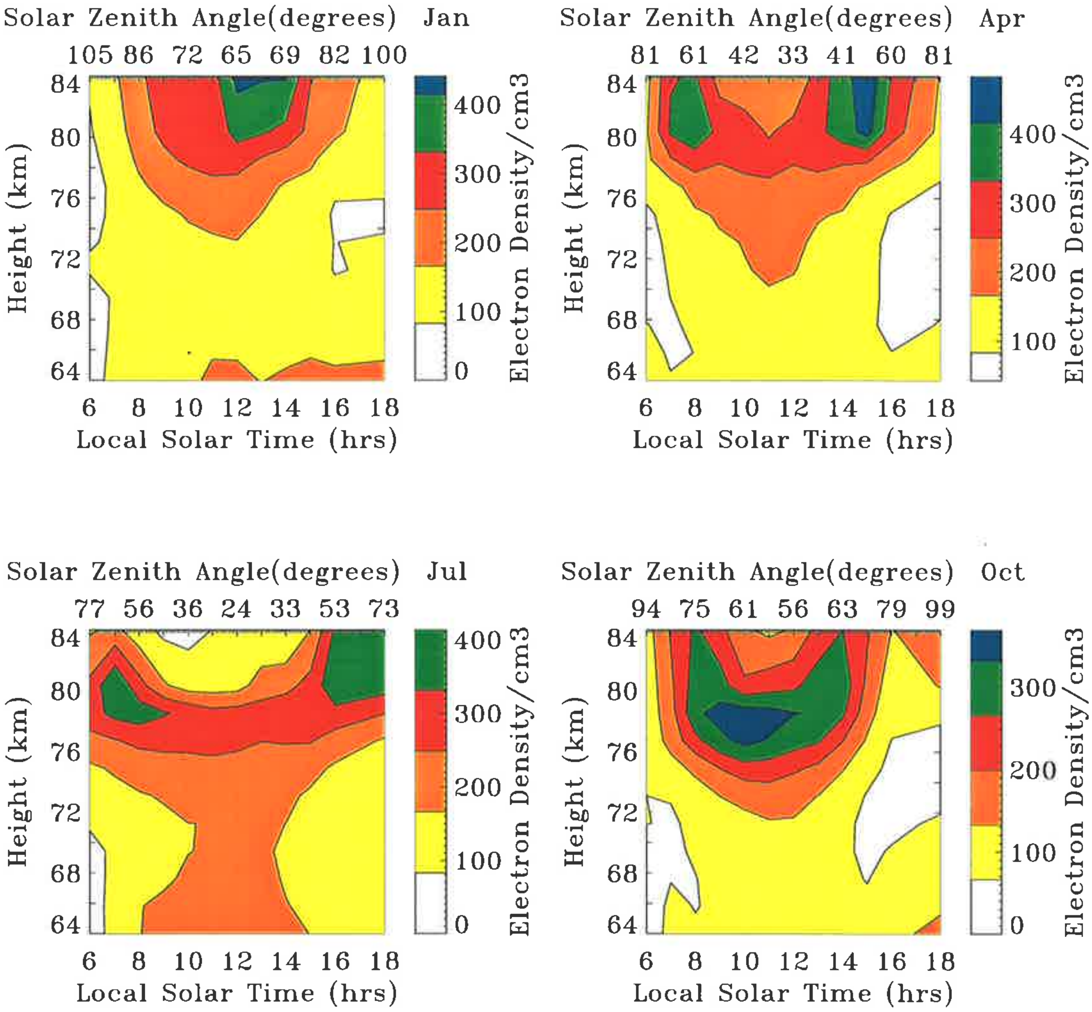

Figure 3.31: Diurnal variation of electron density at Wakkanai winter, summer and equinoctial months, 1997 (low solar activity period)

the figure), an increase in ionization in winter (January, 1600-1800 LST) is observed, similar to Adelaide observations.

A detailed comparison can be made between data published by Belrose and Burke (1964), for Ottawa, by Gregory et al. (1969) for Christchurch, by Igarashi et al. (1999) for Wakkanai, and our data. It should be noted that the Ottawa data refer to a period about 2 years before solar minimum, Christchurch data are for solar minimum and three subsequent years. Buckland Park and Wakkanai data are for the solar minimum.

Table 3.6: Comparison of four partial reflection installations.

Location	Geographic	Geomagnetic	L shell value
Adelaide	35°S,138°E	46°	2.06
Christchurch	44°S,170°E	51°	2.5
Ottawa	45°N,76°W	54°	3.18
Wakkanai	45°N,142°E	38°	1.55

Table 3.7: A comparison of N_e data, Adelaide 35°S, Christchurch 44°S, Ottawa 45°N and Wakkanai 45°S. Columns show electron densities per cm^3, (a) as measured (b) amended for winter minimum $\chi = 58°$ (all data for 70 km).

Season	Location and period	(a)	(b)
Winter	Adelaide 1997	94 (150)	94 (150)
	Christchurch 1963-1967	100	150
	Ottawa 1961	80	130
	Wakkanai 1997	145	145
Summer	Adelaide 1997	213 (325)	116 (200)
	Christchurch 1963-1967	360	380
	Ottawa 1997	320	330
	Wakkanai 1997	175	148

All data sets are derived from the same technique, but the collision frequencies assumed in each investigation can be different. The values quoted in the table are due to old standard collision frequencies at all locations, except for the values shown in brackets for Adelaide, which are derived using the latest laboratory collision frequencies.

A height of 70 km is selected for comparison. The Ottawa data are for five magnetically quiet days in each season; the Buckland Park, Christchurch and Wakkanai data are for not less than 57 days in each season for a period of solar minimum conditions. The sets of values are presented in Table 3.7. In columns marked (*a*), measured values at local noon are listed; while in those marked (*b*), the same values have been amended for winter minimum (close to $\chi = 58°$). The data shown in brackets for Adelaide are due to new collision frequencies at Buckland Park. Table 3.7 shows fair agreement between the values at these locations at winter and summer seasons and at 70 km. Enhancement of electron density going from winter to summer, as χ decreases, is evident at all four locations.

3.4 Summary and Conclusions

Solar control is the dominant influence in determining the seasonal variation of noon electron densities in the mesosphere and lower thermosphere (65-78 km) at mid-latitudes. In general, as the solar zenith angle increases, the electron density decreases. In contrast to the predicted behaviour of a static atmosphere, mean noon electron densities, in the region 60-75 km and at constant solar zenith angle, are found to be larger in autumn months than in any other month at 35°S.

Comparison of altitude variations of N_e in each month with IRI95 and FIRI model results are investigated. Experimentally determined electron density at Buckland Park are relatively in good agreement with model values in the low solar active period. Whereas, in the high solar active period, the observed N_e are generally smaller than both the model results. Seasonal variation of N_e due to IRI95 model did not show any enhancement in fall months in comparison to the experimentally measured data. However, seasonal variation of FIRI model results agree well with our observations.

Amplitude ratios back calculated from the model electron density profiles are found to be smaller than MF radar measurements due to increased model N_e values. The inter latitudinal dependencies of electron densities from IRI model are compared with the observed electron densities at Adelaide 35°S and Wakkanai 45°N. In this study an increase in electron density toward the summer hemisphere was noted. Electron density variation with respect to sunspot number is considered. Examples of N_e during disturbed conditions showed enhancement including electron density enhancement below 66 km.

Chapter 4

Nighttime Electron Density

4.1 Introduction

At present there are few techniques capable of producing observations of lower ionospheric $D-$region electron densities at night. Incoherent scatter radars are capable of estimating electron densities above 80 km (Mathews, 1986), whereas ionosondes are capable of estimating electron density above 100 km (Huang and Reinisch, 1986). However, the inversion of ionosonde data requires several assumptions, and a unique electron density profile often cannot be calculated. Rocket measurements are capable of producing highly accurate measurements, but their expense means they are usually used only on a campaign basis.

The partial reflection differential absorption experiment (DAE) as used here is capable of measuring nighttime electron densities on a continuous basis. This is one of the first largest databases of mesospheric ionization and can be used to define the basic seasonal and diurnal climatology of the nightly variation of ionization. Before analyzing the results, a brief description of the limitations of MF radar measurements for the nighttime ionization are presented. General trends and concepts adopted from suitable models and theoretical studies are illustrated below.

The final distribution of electron density at any altitude depends mainly on two factors. Chemical processes involving ionization rates and recombination coefficients and physical processes like the transport of ionizable elements in that altitude region. Since the data considered in this study are at higher zenith angles (larger than 90° due to night hours), and at upper $D-$region heights it is appropriate to assume that NO dominates the ion pair production (Friedrich et al., 1998). Two important elements responsible for ionization in this altitude region are nitric oxide (NO) with its ionization threshold low enough to be ionized by the prominent and stable solar Ly-α line, and $O_2(1_\triangle g)$ ionized by radiation with wavelengths in the range of 102.7-111.8 nm. Hence, the climatology of this trace element (NO) (Siskind et al., 1998; McPeters, 1989; Siskind et al., 1997) is of prime importance in analyzing our results of electron density variation.

The nighttime sources consist principally of scattered Ly$-\alpha$ and Ly$-\beta$, but the contribution of cosmic X-rays in the production of ionization in the nighttime $D-$region may amount to a sizable fraction of all nighttime sources (see section 1.2.2.1). Above 95 km the Ly$-\beta$ contribution is generally far in excess of the production due to cosmic $X-$rays, but at and around 90 km, the relative importance of cosmic $X-$ray and scattered Ly$-\alpha$ depends on the variation of the scattered Ly$-\alpha$ flux, its variation with time and on the nighttime concentrations of nitric oxide, and also on the variations in the flux from the source regions. Since some of these are uncertain, exact contributions are difficult to establish. But on the basis of diurnal and seasonal variation of measured electron densities, possible sources of ionization are investigated.

The aim of this work is to review the salient characteristics of mid-latitude nighttime electron density profiles in the region 80-100 km and the associated mechanisms required for maintaining the nighttime D-region ionization and structure. For such an analysis proper consideration must be given to the effects of transport, production, recombination and diffusion. Sample electron density profiles are used to illustrate the variation with respect to time, altitude, and solar activity. Also the winter anomaly is investigated in brief. Next the dynamics and average ionization rates in the region are investigated.

4.2 Nighttime Observations and Limitations

Mid-latitude MF-HF radar nighttime observations can only be made above approximately 80 km. The nighttime electron densities observed at these heights can be significantly larger than those observed below 80 km during the day (Holdsworth et al., 2002). This suggests that the assumptions that underly the DAE may be less valid as detailed in the section 2.5.2.

Also, both the magnitude and seasonal variation of the electron density are dependent on the collision frequencies used to estimate the electron density. The electron density profiles shown here are calculated using the latest laboratory measurements (Equation 2.11). As described in section 2.3, the basis of using these new ν values is that the corrected collision frequencies using the measurements of the lowest part of the ionosphere (60-66 km) match these new collision frequencies. The same method could not be used for the nighttime results (i.e. estimating the correction factors using the base of the nighttime ionization at 80-85 km range) as the signal returns from these heights are statistically insignificant. Despite the restrictions evident in night time data, we believe that results can be very useful.

The use of 2.11 resulted in the reduction of N_e values (almost by a factor of 2) in comparison with N_e values estimated using old standard collision frequencies (2.9). Figure 4.1 is an example of change in electron density variation due to different collision frequencies. See section 2.3 for change in height structure of N_e, due to these two ν profiles.

Separate collision frequency profiles were used for each month, using pressure values from suitable model, such as CIRA-86, the COSPAR International Reference Atmosphere (Fleming et al., 1990). Electron density values used for the purpose of obtaining a mean night electron density profile have been taken for each hour. For example the midnight electron density refers to values obtained between 2300 and 0000 Local standard time (LST). The main database was obtained during $1997-2000$ covering periods of both low and high solar activity. The data were grouped by season:

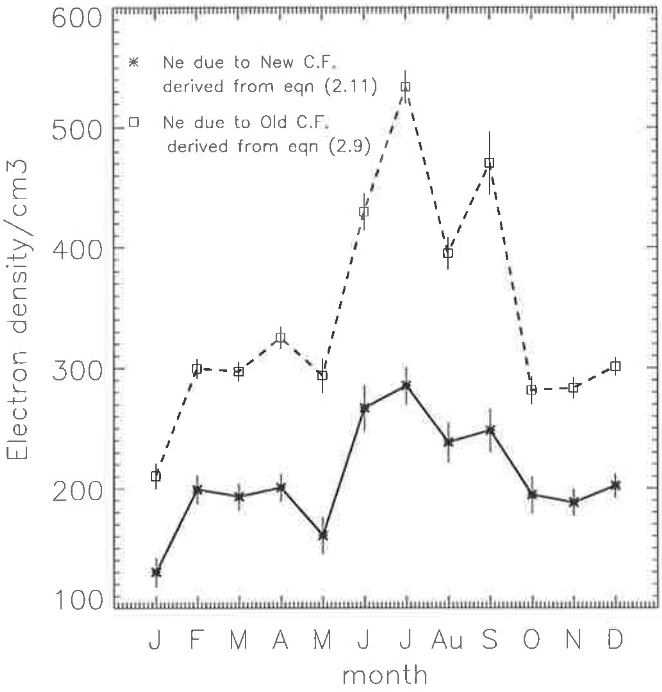

Figure 4.1: Electron density variation at 92 km at night, showing the change in electron density due to the use of different collision frequencies (ν). Dashed line N_e due to old standard ν, derived from Equation (2.9). Solid line N_e due to latest laboratory ν, derived from Equation (2.11)

winter (May-July), summer (November-February), spring (August-October) and fall (March-April). Solar minimum and maximum periods (1997 and 2000 respectively) are considered mainly.

Electron density profiles during nighttime conditions are calculated using the same scheme as used for daytime conditions, with some modifications appropriate to nighttime conditions. The nighttime results correspond to after 1800 (between 1800 and 0600 LST) and greater than 90° zenith angles. Comparison of our results with those of earlier workers and with IRI and FIRI model results are presented in the following sections.

4.3 Results and Discussion

4.3.1 Seasonal variation

Monthly mean vertical profiles of the electron density in the nighttime lower ionosphere are shown in Figure 4.2 for all the months for 1997 and 2000. It is evident from Figure 4.2 that the electron density increases systematically as the altitude increases, plausibly explicable by a corresponding structure in the NO profiles (Friedrich et al., 1998). Electron densities for 2000, solar maximum period, are approximately 1.5 - 3.0 times larger than that for 1997 solar minimum period (Figure 4.3). This change in N_e is comparable to the change of approximately 50% in the strength of Ly-α radiation from solar minimum to maximum conditions (Ratcliffe, 1972).

The seasonal variation of electron densities over the range of altitudes between 84 and 98 km at Adelaide is brought on more clearly in Figure 4.4. A feature of these profiles is the existence of relatively larger mean values of electron densities in winter than in summer. There is no marked difference between the spring and fall equinoctial periods (Figure 4.5).

At 90 km winter (M, J, J average) electron densities are at least 25% larger than summer (N, D, J, F average) values. Above that height, up to about 96 km, the difference generally increases up to 35%. The statistical significance of data below 88 km is very low and no marked seasonal variation is observed at these altitudes. These seasonal variations reflect the competition between photo-dissociation and transport.

As the NO is the major element responsible for the ionization in the $D-$region heights, these seasonal variations are compared with the reference NO model presented by Siskind et al. (1998) (Figure 4.6). This model is based upon the two datasets (namely, HALOE-Halogen Occultation Experiment and SME-Solar Mesosphere Explorer). The model covers a wide range of solar, geomagnetic and seasonal conditions. Only the observations made by HALOE are of interest to us in our present study due to the altitude range covered by our results (80-100 km). However, the HALOE observations are average sunrise (SR) and sunset (SS) data, and here we are assuming

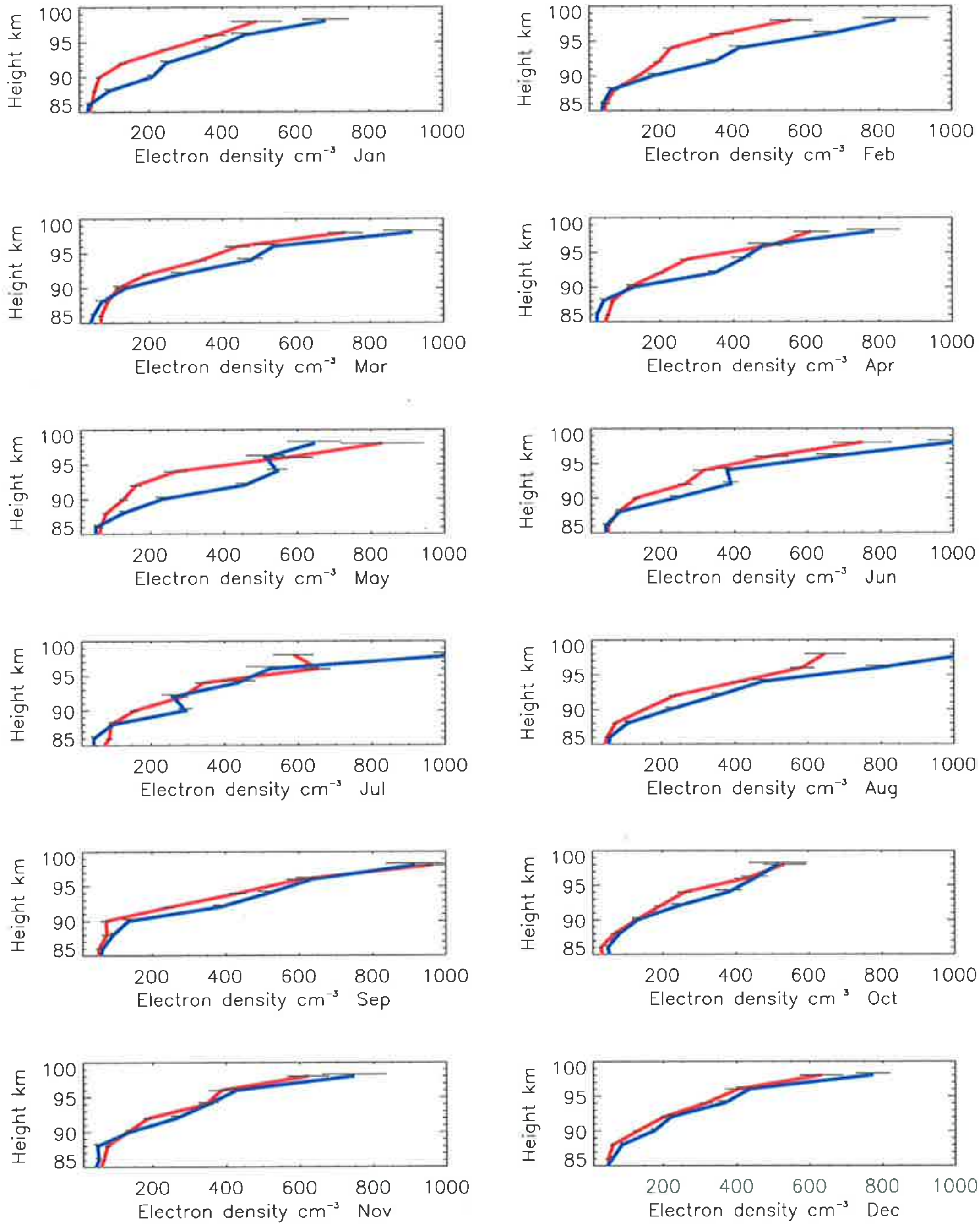

Figure 4.2: Monthly mean nighttime profiles at 2300 LST 1997 (red), 2000 (blue).

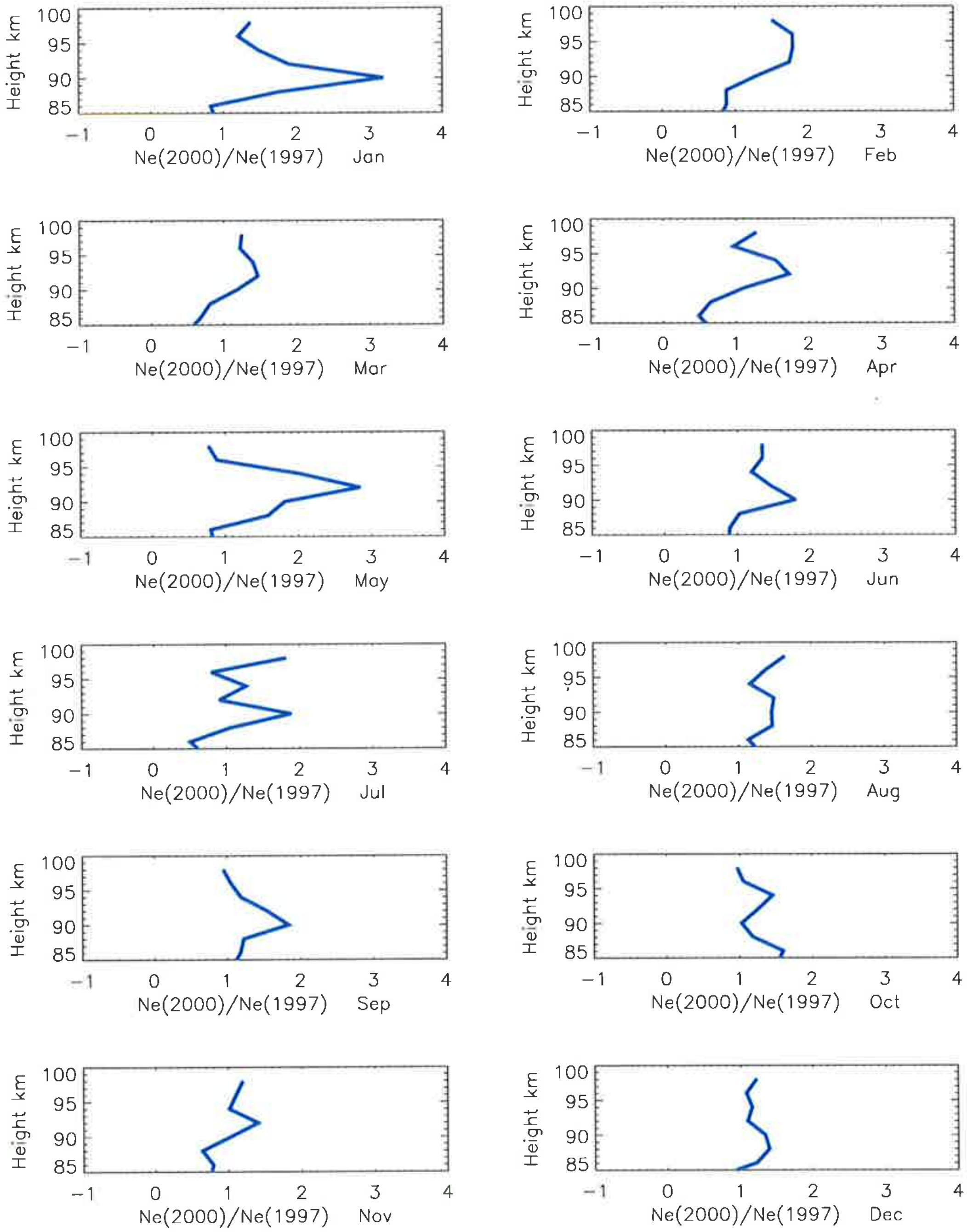

Figure 4.3: Ratio of solar maximum and minimum electron densities for each month

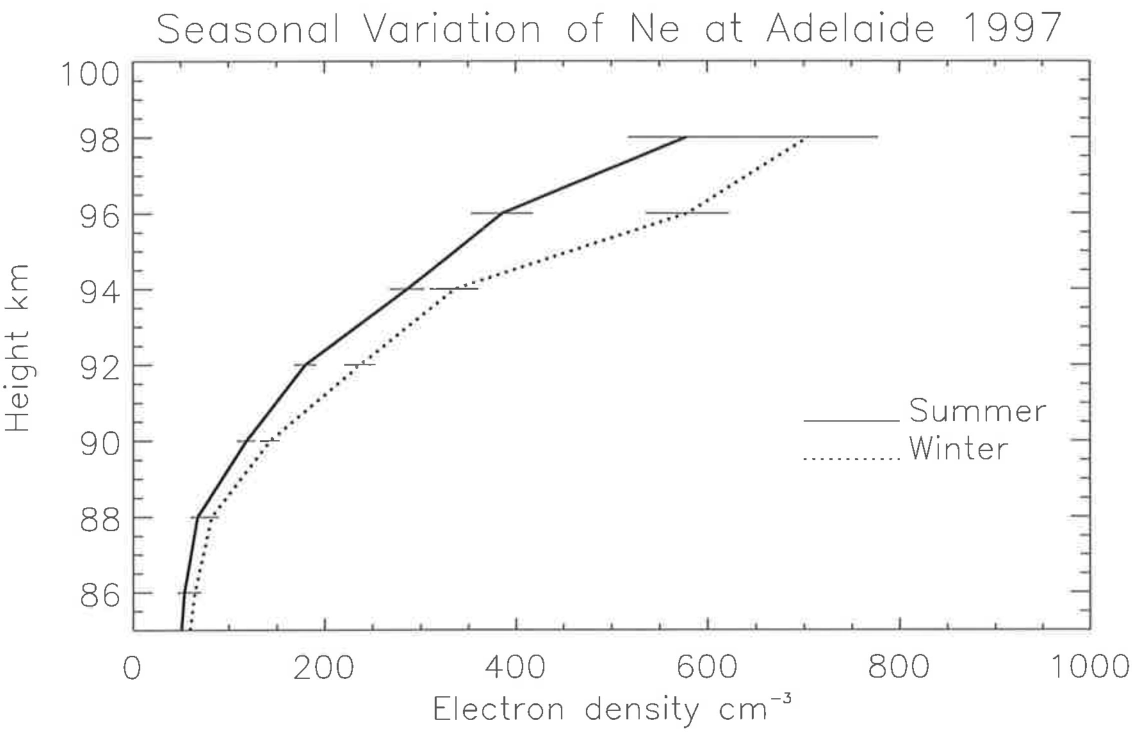

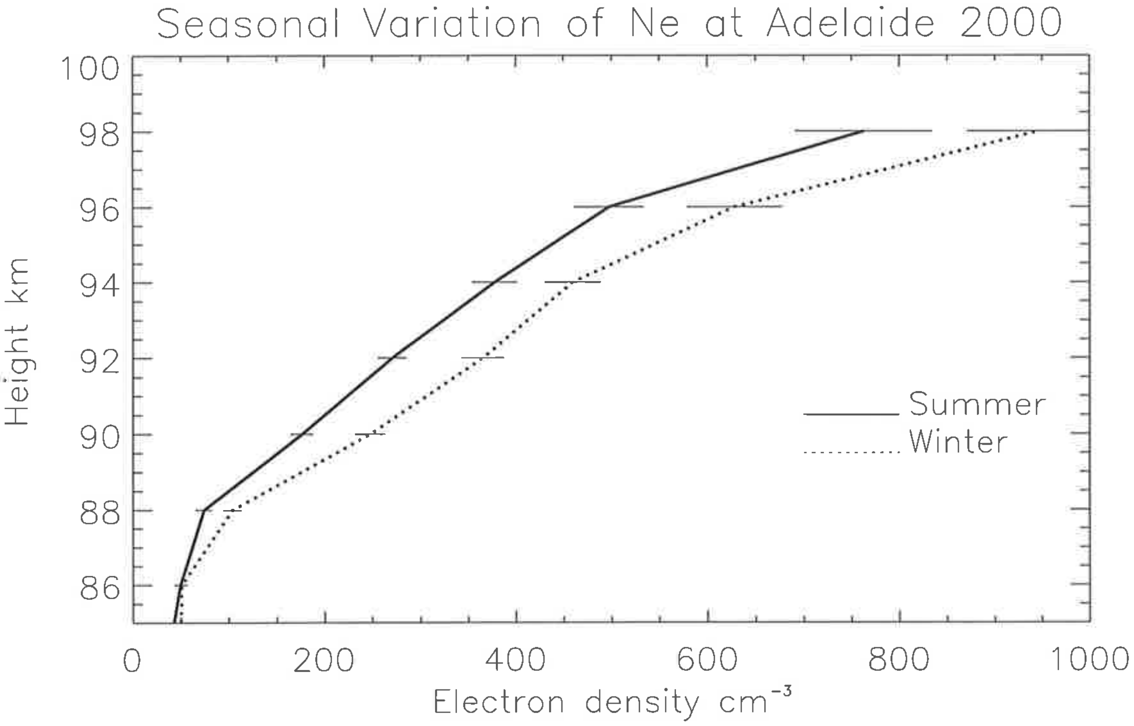

Figure 4.4: Seasonal variation of electron density at 2300 LST. Summer (solid) and winter (dotted). Horizontal lines are the standard error at 95% confidence level

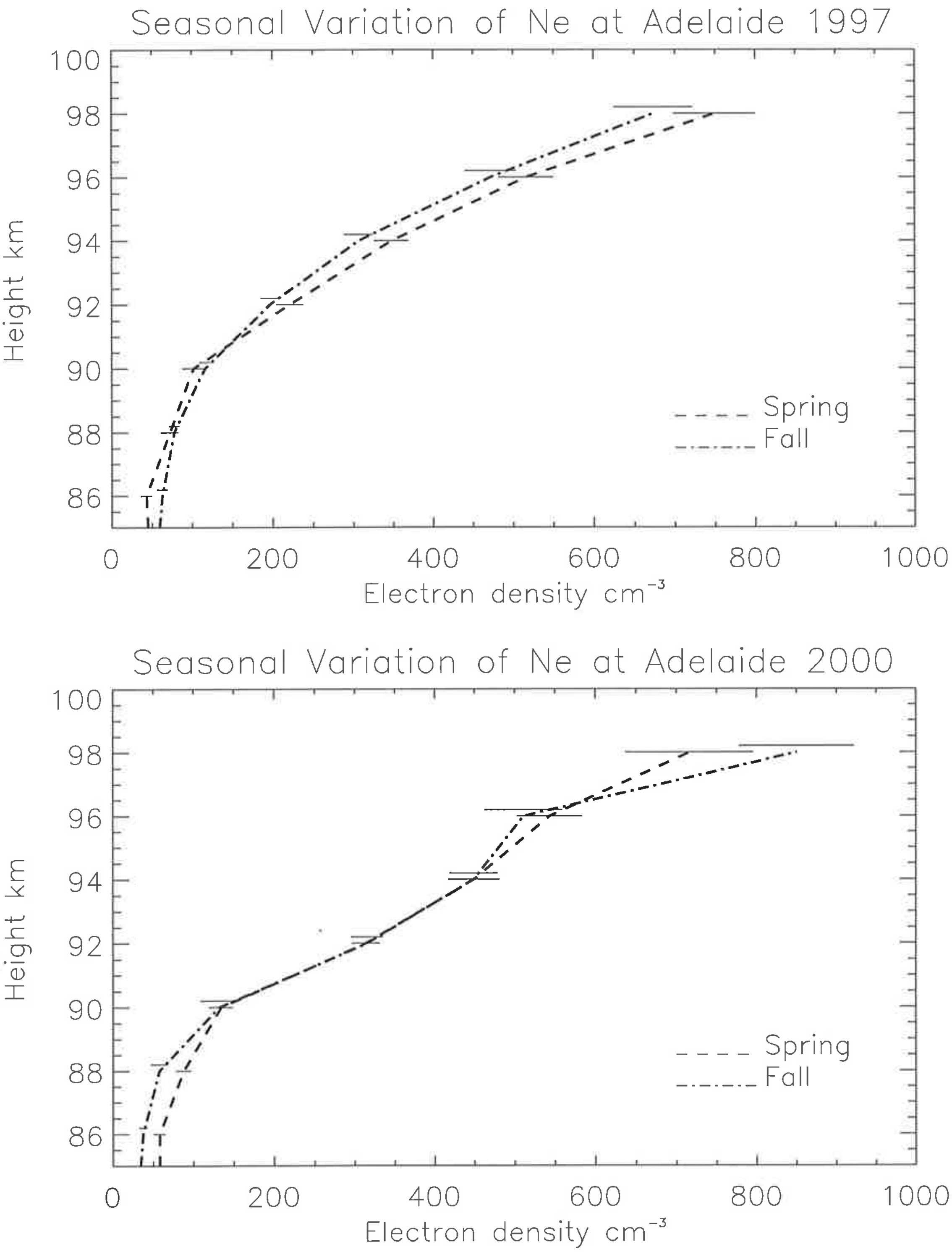

Figure 4.5: As for Figure 4.4, but for spring (dashed) and fall (dash-dot)

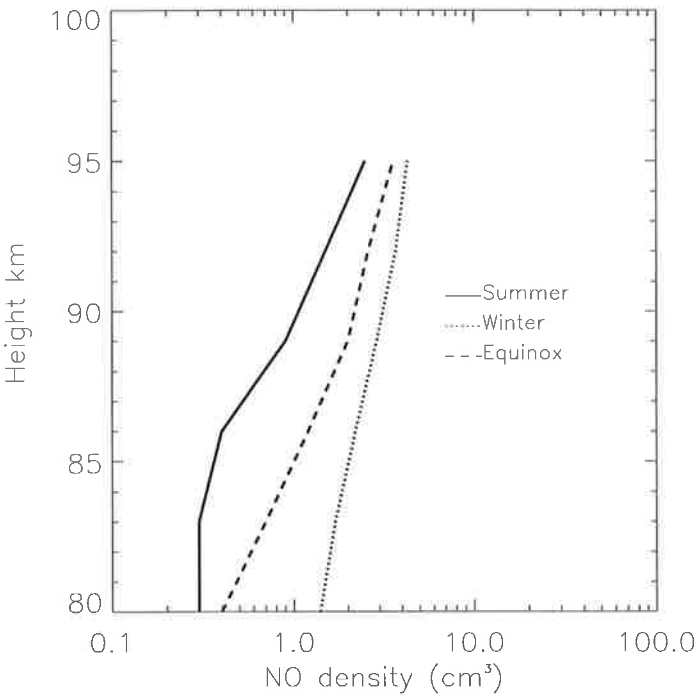

Figure 4.6: Seasonal variation of zonal average mesospheric NO densities (× 10^7 cm^3). Summer (solid line), winter (dotted line) and equinox (dashed line) at 40°S (averaged from 1992 - 1995, i.e. averaged over all levels of solar activity). Data extracted from [(Siskind et al., 1998)]

that it is close to diurnal-nighttime average, as the chemical lifetime of NO below 90 km is in the order of many days (Siskind, 1994).

It was noted that densities less than approximately 0.5×10^7 are of low signal to noise. The comparison reveals a similar increase in winter mesosphere in both the results (HALOE and MF radar). For example, HALOE NO densities in winter, at 89 km are 3.2 times larger than the corresponding summer values. In comparison, winter to summer observed N_e at 90 km is approximately 1.5. The vertical structure of both NO and electron density have a similar variation.

To investigate further the annual and solar cycle variations, monthly mean electron densities at 2300 LST and at constant $\chi = 120°$ (evening hours) are presented in the Figures 4.7 to 4.10. It is apparent that, the observed electron densities in winter (M, J, J) are 1.2 - 1.5 times larger than the summer values. Figures 4.9 and 4.10 are N_e observed at constant χ. These figures show similar enhancement in winter.

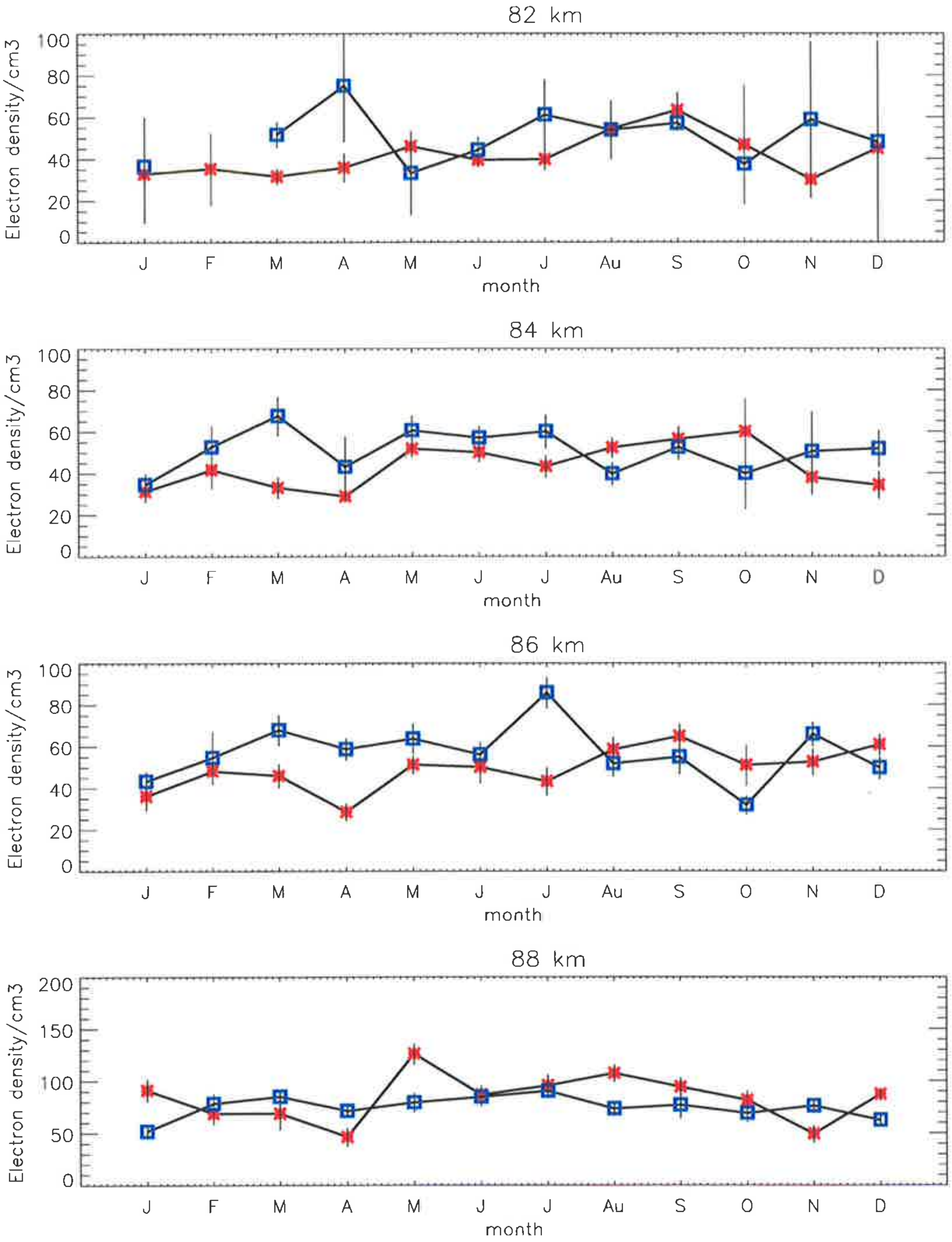

Figure 4.7: Seasonal variation of electron densities at various altitudes between 2300 and 0000 LST and for solar maximum 2000 (red, □) and solar minimum 1997 (blue, $*$) conditions. Vertical bars are standard errors at 95% confidence level

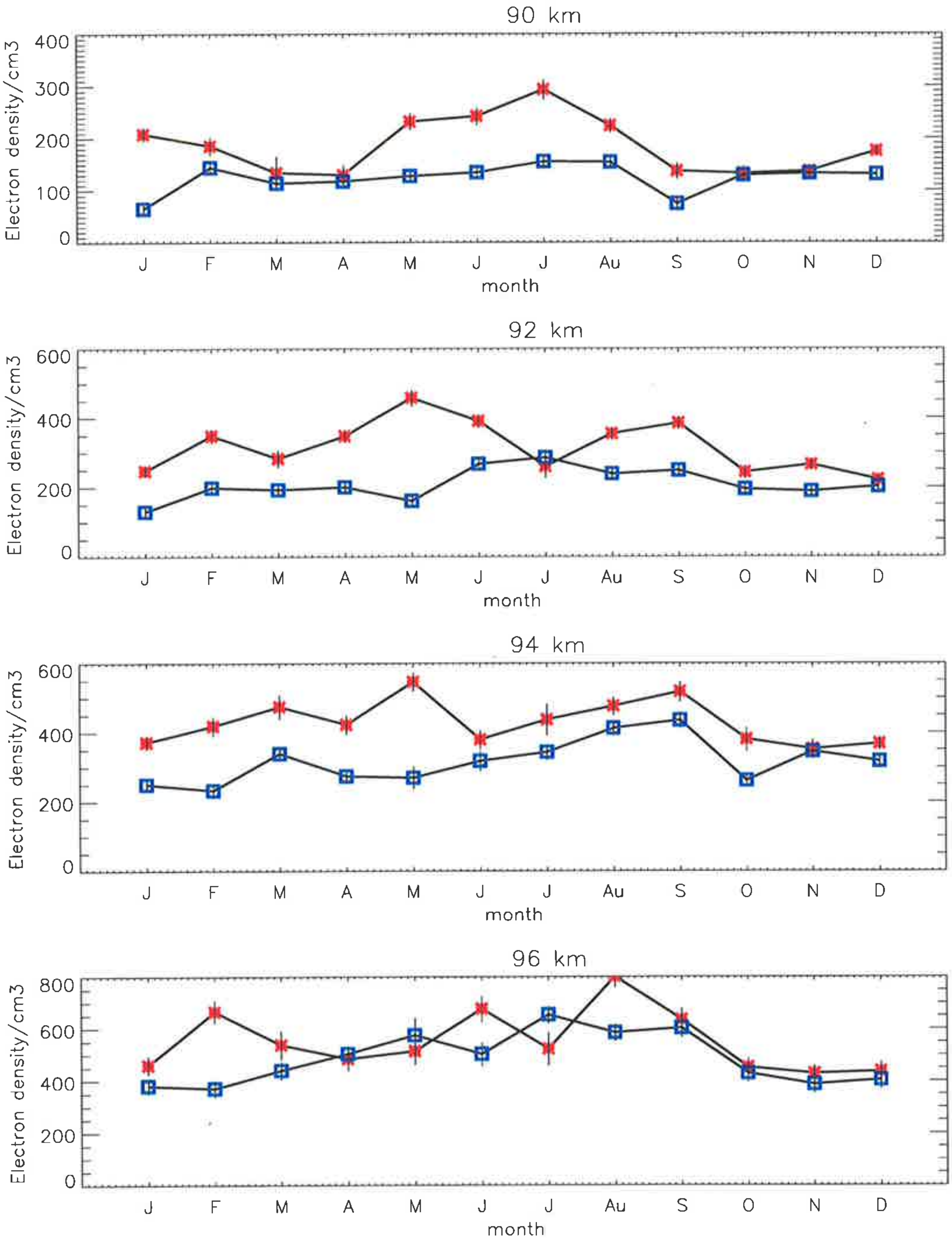

Figure 4.8: As for Figure 4.7, but for 90 to 96 km altitude range

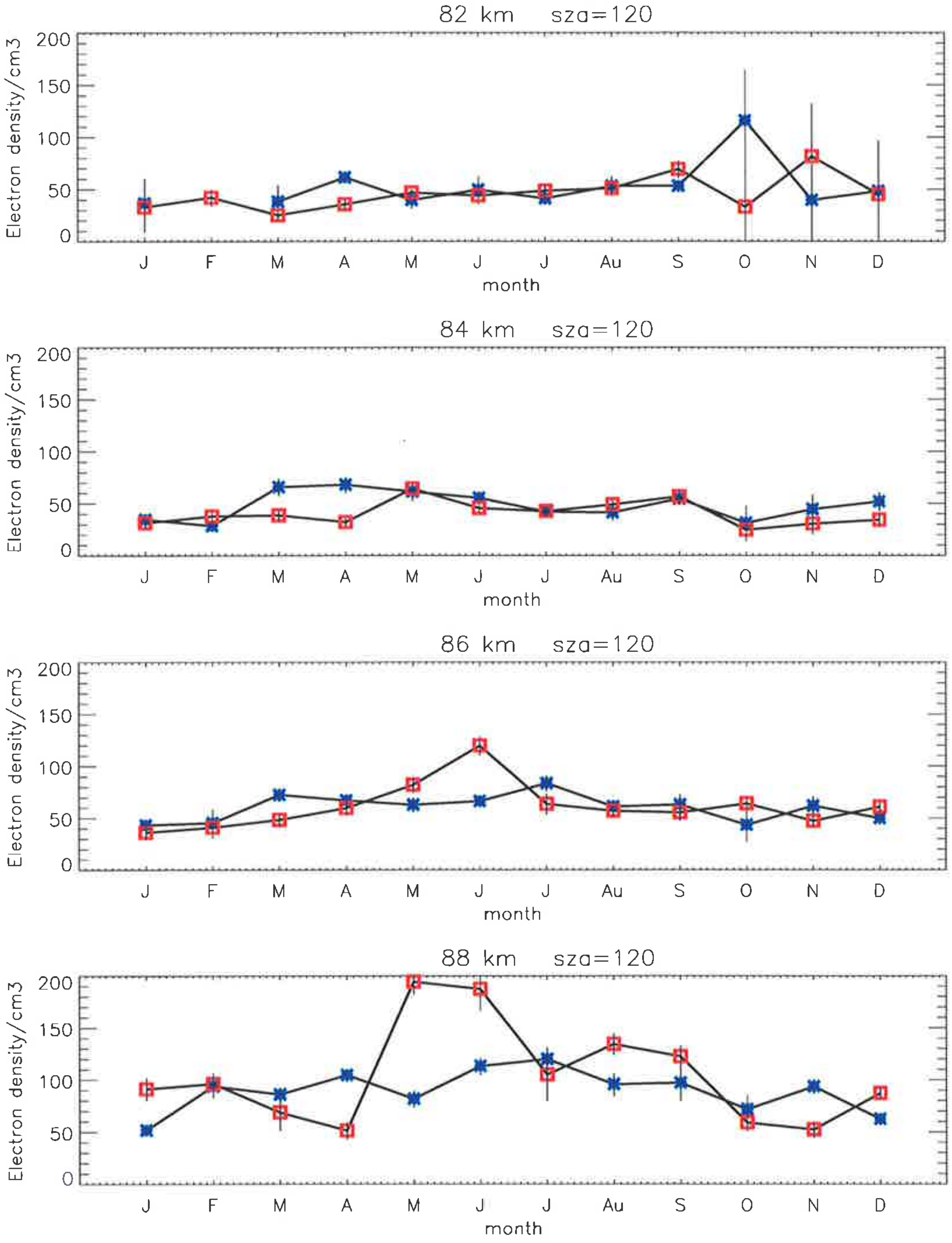

Figure 4.9: Seasonal variation of electron densities at constant solar zenith angle of 120 degrees and for solar maximum 2000 (red) and solar minimum 1997 (blue) conditions

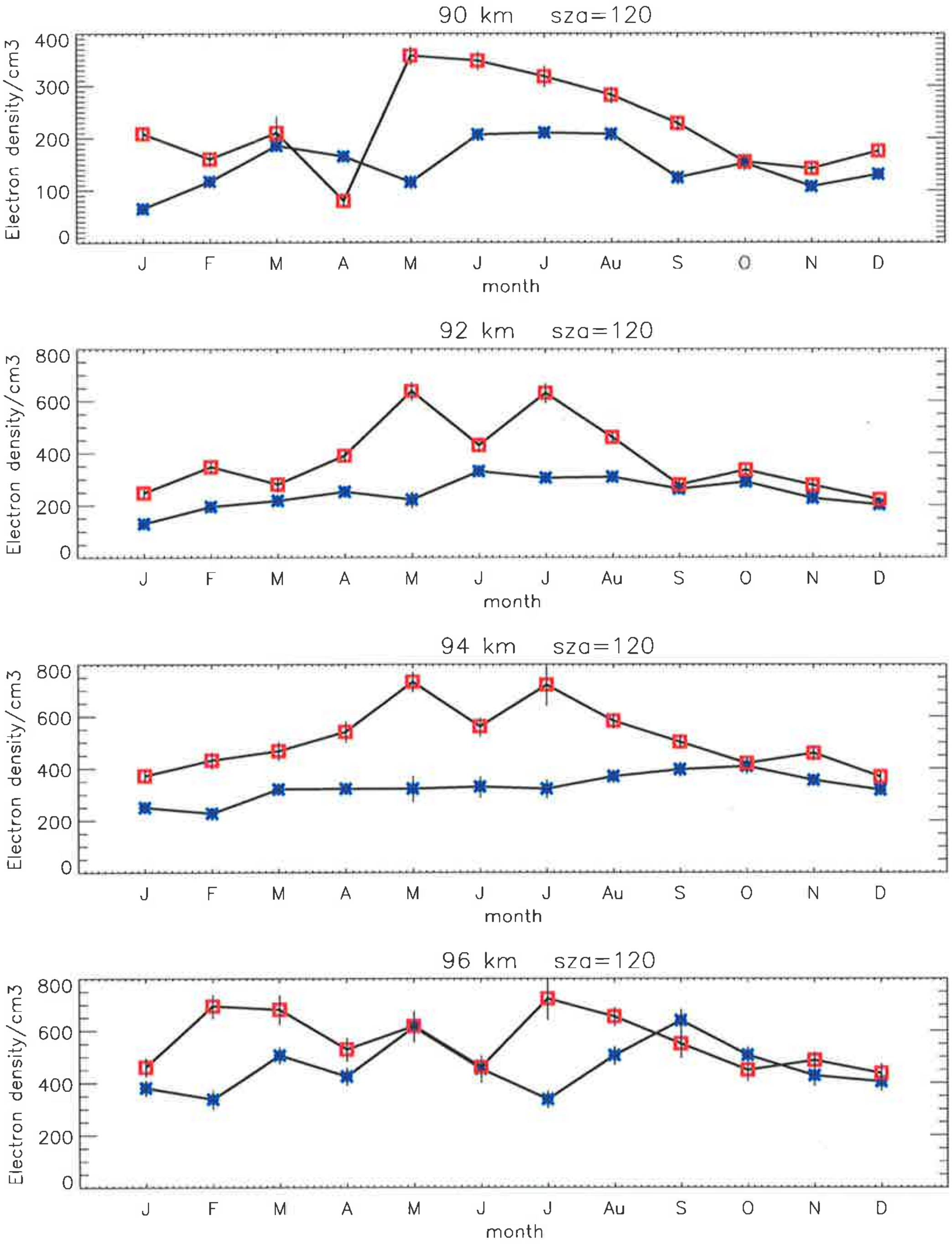

Figure 4.10: As for Figure 4.9, but for 90 to 96 km altitude range

Higher electron densities in winter than summer at constant χ is sometimes termed as a "normal winter anomaly" (Schwentek, 1965). From the two-dimensional model calculation of nitric oxide transport by Siskind et al. (1998), enhanced NO in the wintertime mesosphere is seen to be transported equatorward as far as $30^\circ - 40^\circ$ when planetary wave mixing was included.

4.3.1.1 Comparisons with IRI, FIRI and Wakkanai

Our results are compared with i) IRI95, ii) FIRI, and also iii) with electron densities at Wakkanai in this section. A description of IRI and FIRI models is given in Chapter 1. Above 80 km, the IRI model results do not show any inter-annual variability, unlike the IRI daytime results. Hence, only 1997 IRI data are shown, which is representative of all the years.

Figure 4.11 shows comparison of observed and IRI model altitude variations. It is found that the MF radar nighttime N_e values at 2300 LST are 2 - 7 times smaller than IRI model values above 84 km depending on the month and height. Figure 4.12 shows the comparison made between IRI and MF annual N_e variation at 90 km. At this altitude model densities are approximately 4.5 times larger than 1997 values and 2 - 4 times larger than that of 2000 densities. Since, IRI model data above 80 km remained constant from year to year, any difference shown is due to change in N_e in different years. These constant values of IRI annual electron densities above 80 km, as shown in Figure 4.12 are unrealistic showing no seasonal variations.

As a new contribution to IRI, electron density data based on Faraday rotation experiment (FIRI) was presented by Friedrich and Torkar (2001). Following these reports, comparisons between observed and FIRI model results are presented in the Figures 4.16 - 4.18. Both low ($F_{10.7}$=50) and high ($F_{10.7}$=180) solar active periods at constant $\chi = 120^\circ$ are considered. It can be seen from the figures that, FIRI data are about a factor of 10 higher than observed N_e in the low solar activity period and a factor of 2 higher in the high solar activity period. It is possible that our MF radar electron densities are under estimated by a factor of 2 due to the assumption of new

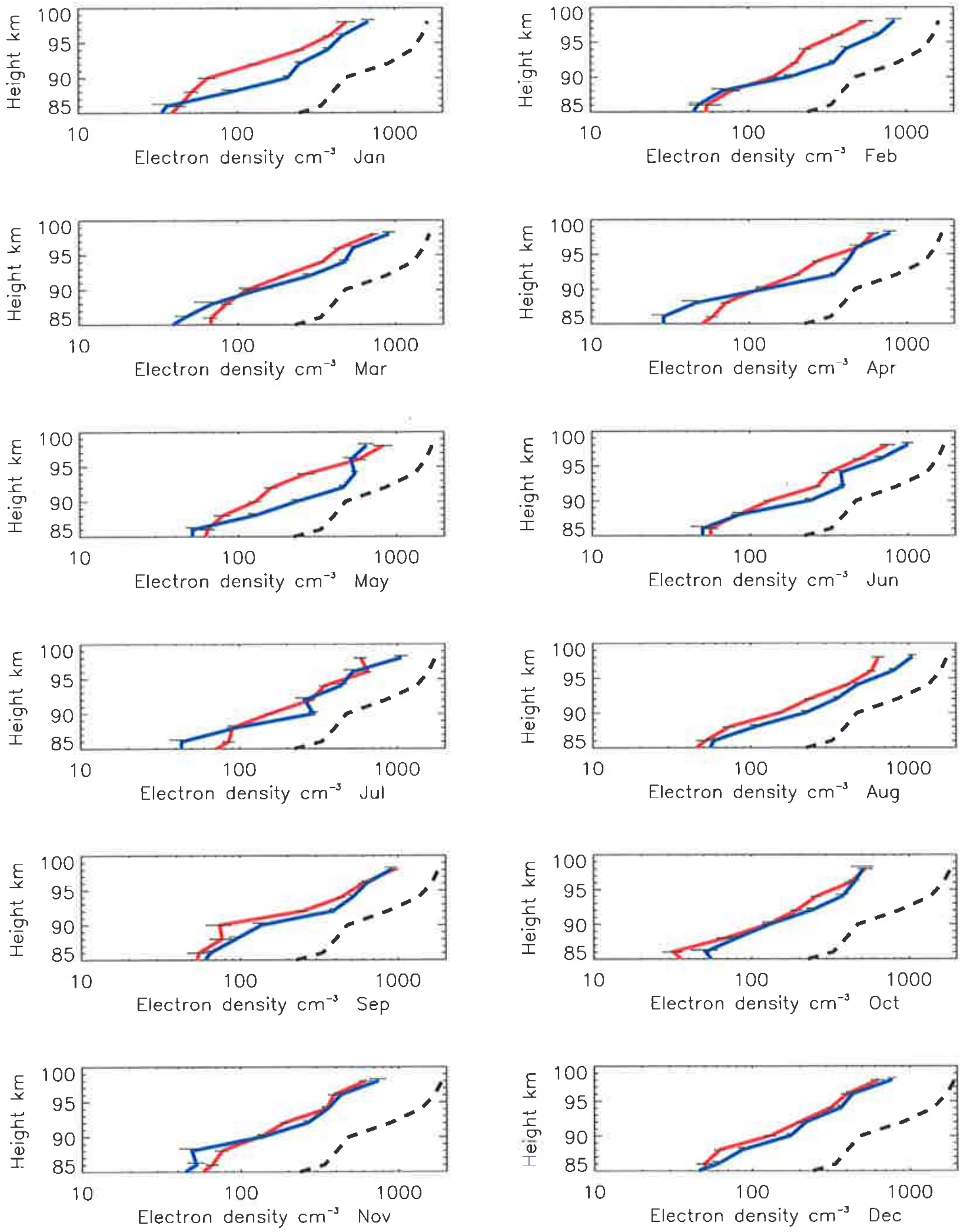

Figure 4.11: Monthly mean nighttime profiles at 2300 LST 1997(red), 2000(blue) in comparison with IRI95-model(dashed) results.

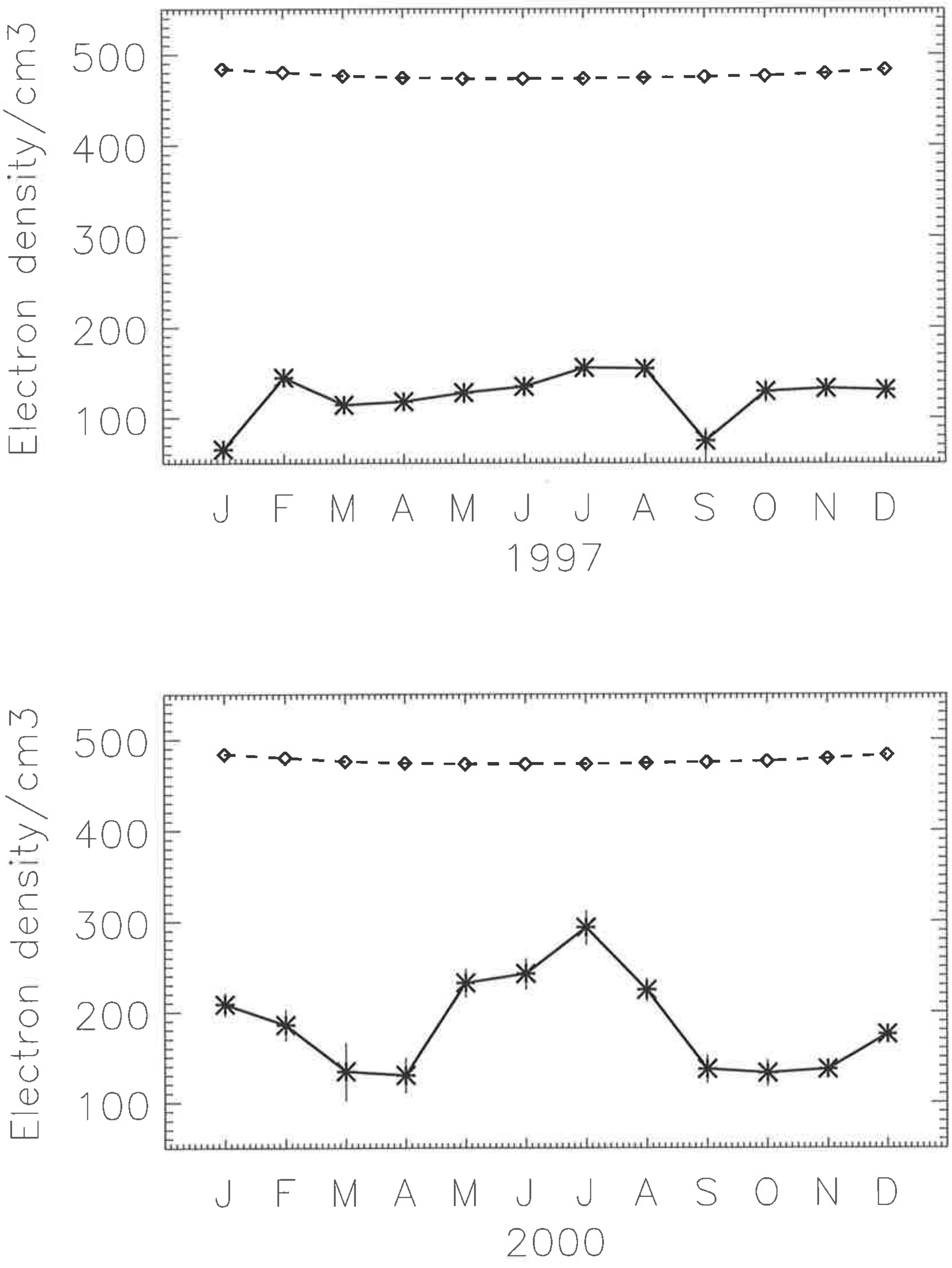

Figure 4.12: Comparison of observed (solid line) and IRI95 model (dashed line) N_e annual variation. All data for 90 km, (35°S) and 2300 LST

collision frequencies (section 4.2). Also, limitations in FIRI night estimates (Friedrich and Torkar, 2001) needs to be considered before deriving any conclusions regarding these nighttime N_e values.

However, comparison of seasonal variation in both the results (FIRI and MF radar) indicate similar increases in winter mesosphere, which also coincides with the HALOE NO density seasonal variations as detailed earlier. In addition to transport effects arising from wave motion, this increase in winter N_e can be ascribed partly to temperature changes occur in the dynamic atmosphere. Higher temperatures at these altitudes may impede the formation of water cluster ions and similar view was also expressed by Friedrich and Torkar (2001). Therefore, mean values of temperature at 85 and 90 km, from Cospar International Reference Atmosphere (CIRA-86), are plotted to indicate the expected trend of temperatures throughout one complete year (Figure 4.15).

The photo-chemistry of the 'disturbed' winter mesosphere has been investigated by Sechrist (1967). He demonstrated that since several temperature-dependent reactions may be involved, changes in temperature in the mesosphere could modify the calculated electron densities in the mesosphere above 80 km. However, Geisler and Dickinson (1968) have shown that although temperature fluctuations alter the concentration of nitric oxide, the variation is less than that due to transport effects and occurs more slowly. The time scale is likely to be several weeks. These alternative views suggest a competition between transport and ion chemistry in the lower ionosphere.

As a comparison between IRI, FIRI model results and MF radar measurements, vertical profiles of electron densities are presented in Figures 4.16 and 4.17, for low and high solar activity periods of 1997 and 2000. As stated earlier, observed N_e are smaller than model values.

In order to see whether our values are inaccurate or not the IRI electron density profile for February 2000, at 2300 LST are used to back-calculate the amplitude ratios using Sen Wyller magneto ionic theory. These amplitude ratios are compared with MF measured values as shown in Figure 4.18. Unlike the daytime results, observed

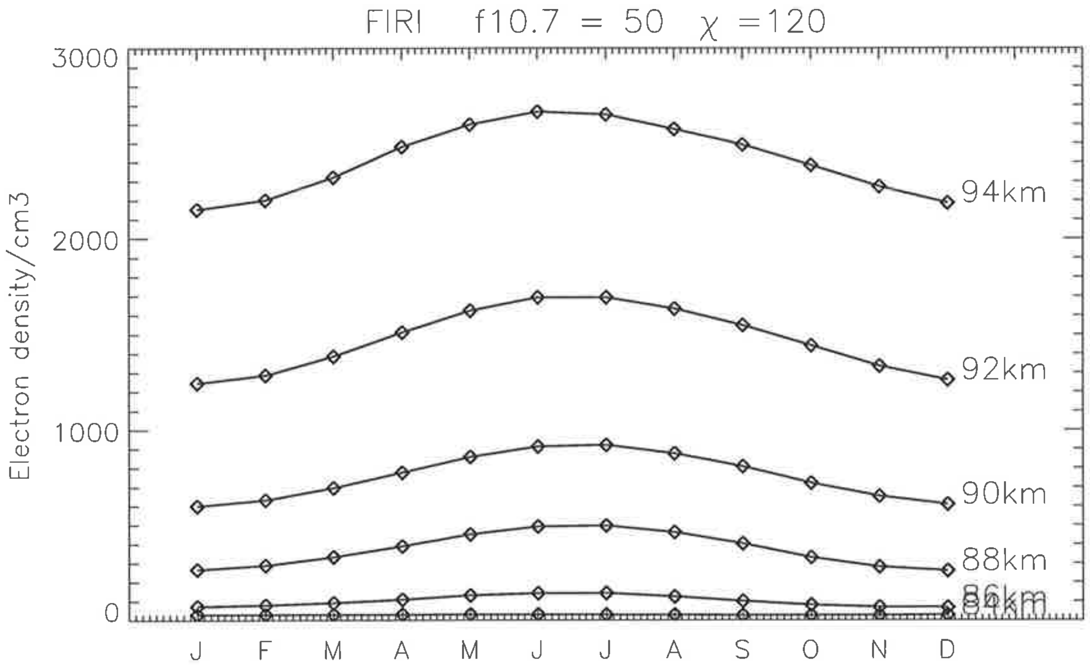

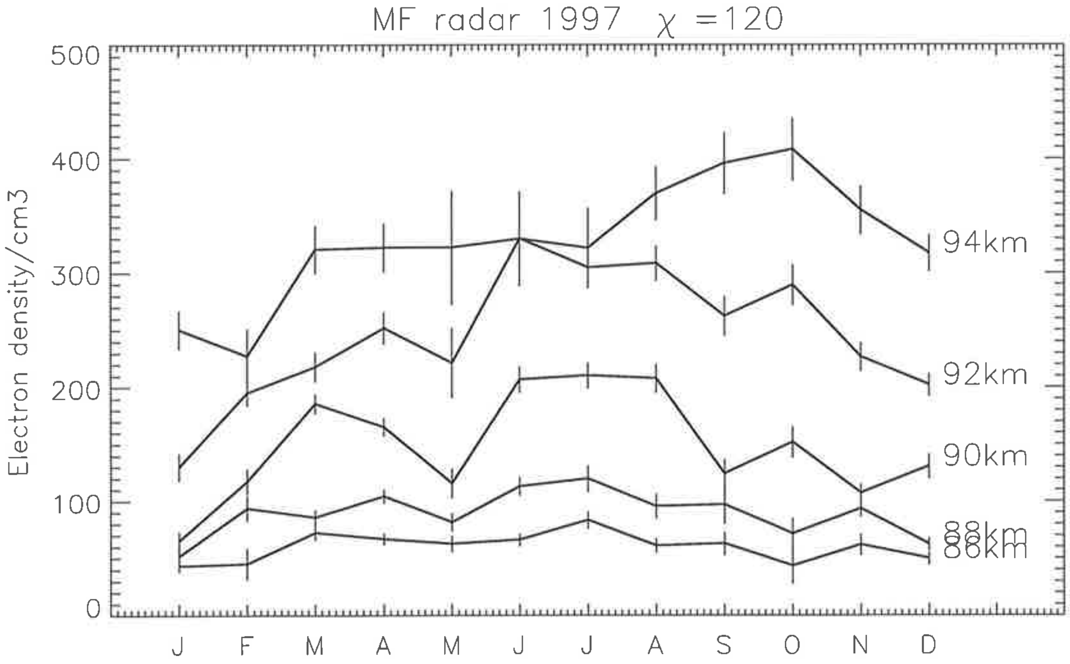

Figure 4.13: Comparison of seasonal variation, (top) FIRI model data, (bottom) DAE observed, low solar activity.

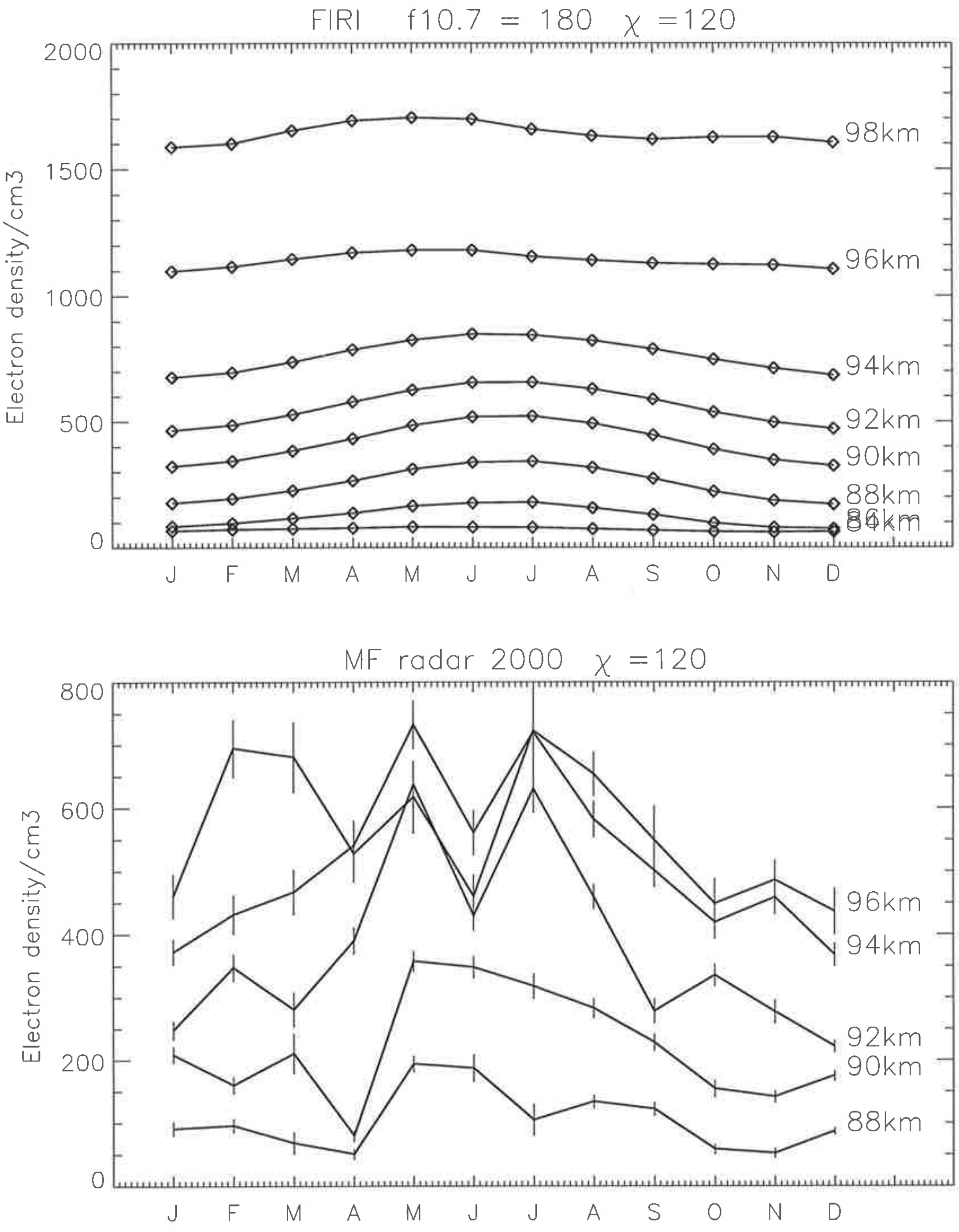

Figure 4.14: As for Figure 4.13, but for high solar activity.

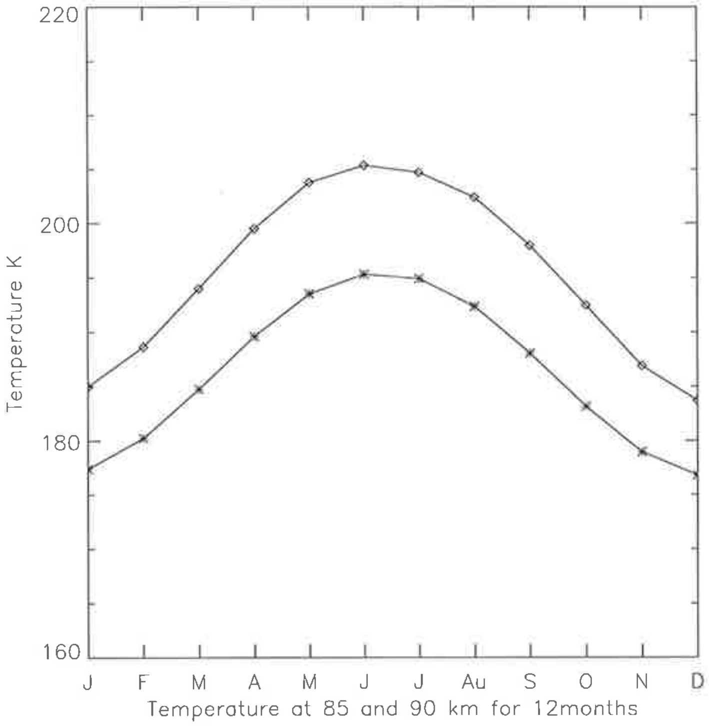

Figure 4.15: Seasonal variation of temperatures (top) at 70 km (⋆), at 75 km (⋄) and (bottom) at 85 km (⋄) and at 90 km (⋆) from CIRA-86 model

and (calculated) model amplitude ratios are significantly different at night. The key feature which is noticeable here is the turnover heights for the model results are at 82 km indicating maximum differential absorption at this altitude, which is debatable at this latitude. However, as suggested in section 2.5.2, further work is required to improve and interpret the nighttime DAE results, both with respect to measuring the amplitude ratios and estimating collision frequencies.

Figure 4.19 and 4.20 show seasonal variation of N_e at Adelaide and Wakkanai (45°N). The electron densities shown for Adelaide in this instance are calculated using old standard collision frequency (Equation 2.9), to match with Wakkanai estimates. In contrast to Adelaide, the observed electron densities at Wakkanai in summer are larger than in winter and spring values. These higher N_e in summer (for Wakkanai) can be attributed to either downward transport from the auroral zones above 90 km or result from in-situ production by high energy (10-100 kev) electrons. It is difficult to separate out these two effects without more information on either particle precipitation

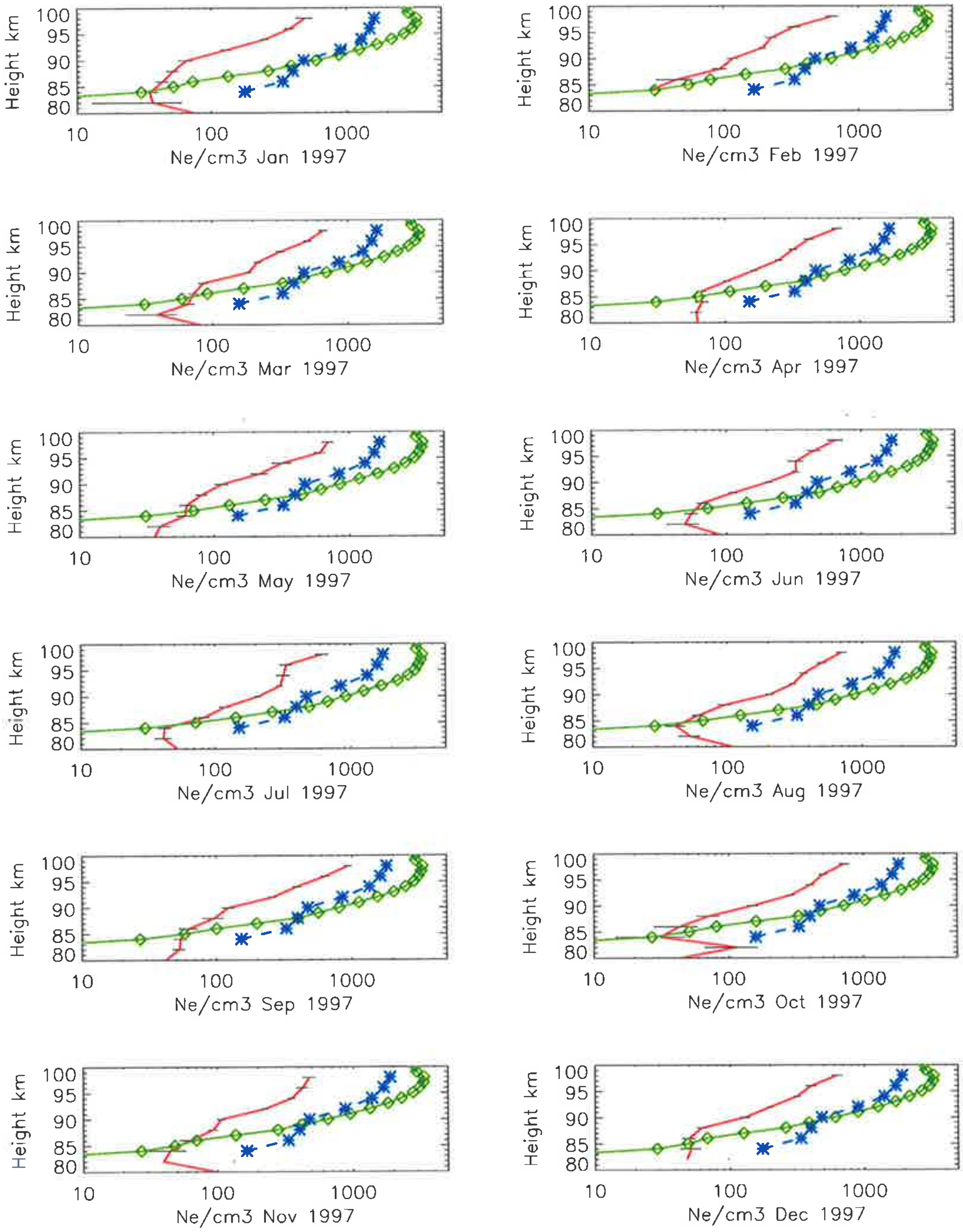

Figure 4.16: Vertical profiles of MF (solid,red), IRI (*,blue) and FIRI (□,green), low solar activity.

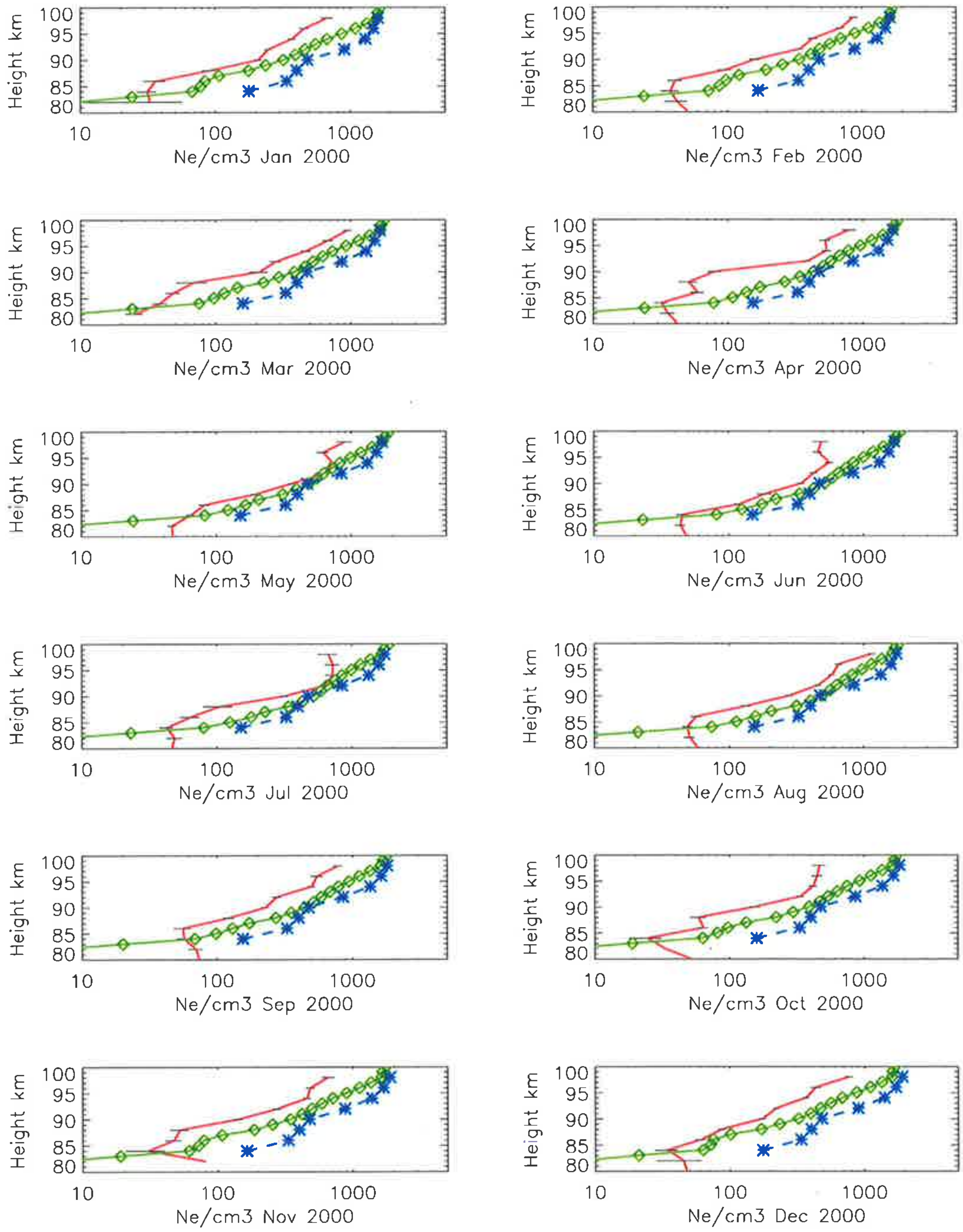

Figure 4.17: As for Figure 4.16, but for high solar activity.

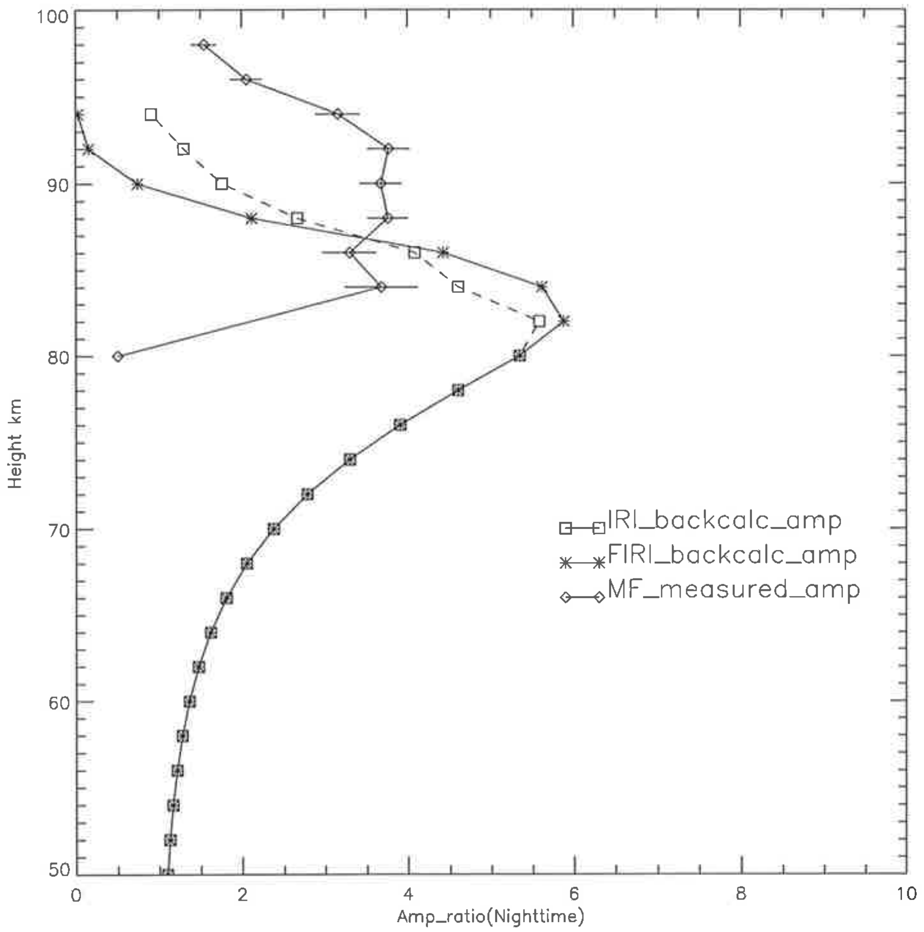

Figure 4.18: Amplitude ratios back calculated using IRI and FIRI electron density profiles (□, IRI-95), (∗, FIRI) and (◇, MF-measured), the data shown are for February 2000.

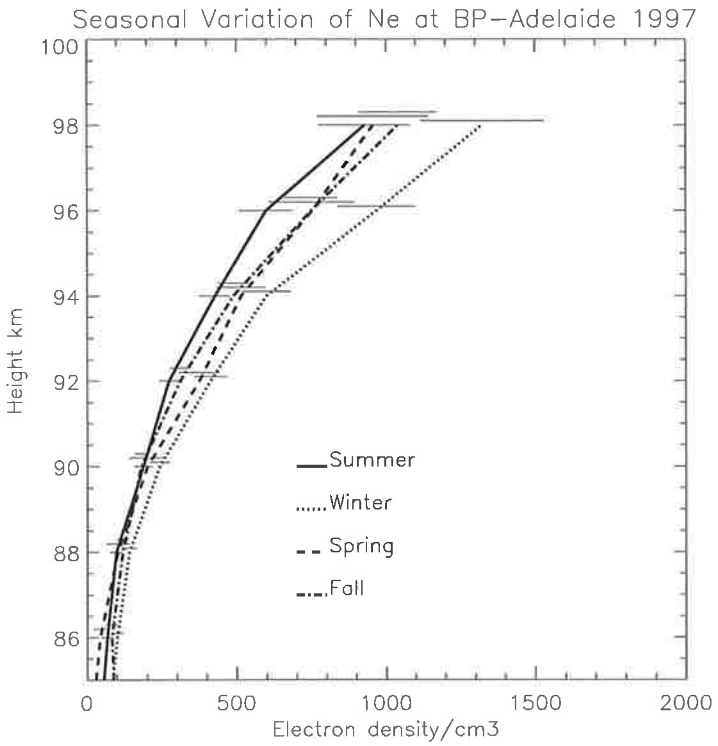

Figure 4.19: Seasonal variation of electron density at Adelaide (35°S. (N_e due to old standard collision frequency Equation 2.9) for comparison

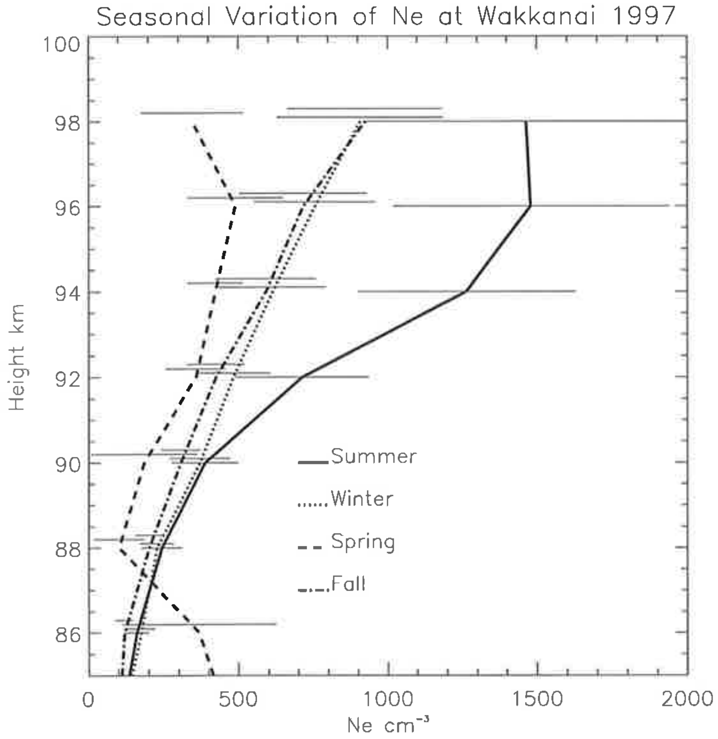

Figure 4.20: Seasonal variation of electron density at Wakkanai(45°N)

Table 4.1: Regression coefficients for nighttime.

Height (km)	overall
86	0.30
88	0.52
90	0.61
92	0.68
94	0.76
96	0.66
SS range	(0-180)

or vertical transport rates (Siskind et al., 1997).

4.3.1.2 Effect of solar cycle variation

The purpose of this section is to study how the lower ionosphere electron densities vary with the sunspot cycle (Cycle 23). To isolate the seasonal influences from the dominant dependence of ionization on solar zenith angle, all data are considered at smallest midnight solar zenith angle which can be observed every day of the year at Adelaide (namely, 120°). Figure 4.21 shows electron density variation from 86 to 94 km (at $\chi = 120°$) in comparison to the measured sunspot number. The sunspot number data were obtained from the Ionospheric Prediction Services (IPS) web site (www.ips.gov.au). The labels on the X-axis are marked for every 12 months at July each year. Regression curves (minimum to maximum activity period) for 86 - 96 km altitudes are shown in Figure 4.22. Table 4.1 lists the coefficients for comparison.

From Table 4.1 it can be inferred that the data shows a positive correlation with sunspot number (all the coefficients except for 86 km are greater than 0.5). However, an important feature to note in these figures is that there is still the influence of seasonal variability (e.g., sharp peaks shown in the months of June and July in each year).

To investigate the possible causes for the above detailed variation in N_e, an NO density variation is considered. The source of NO is important because thermospheric

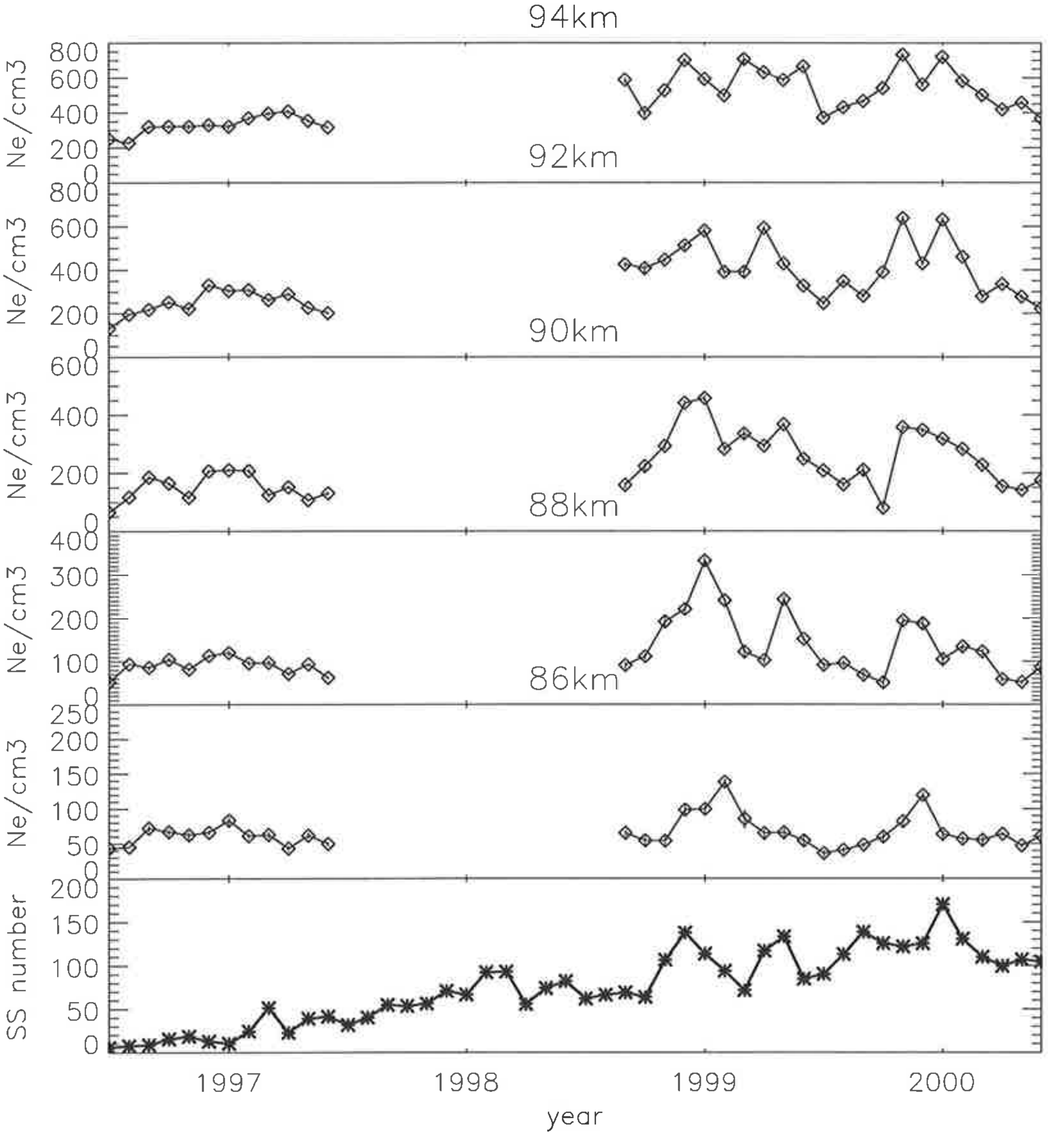

Figure 4.21: Electron density (1997 to 2000) at a constant $\chi = 120°$. Gaps shown are due to non-availability of data (January 1998 - February 1999) The thick line (bottom plot) shows the sunspot number variation in the same period.

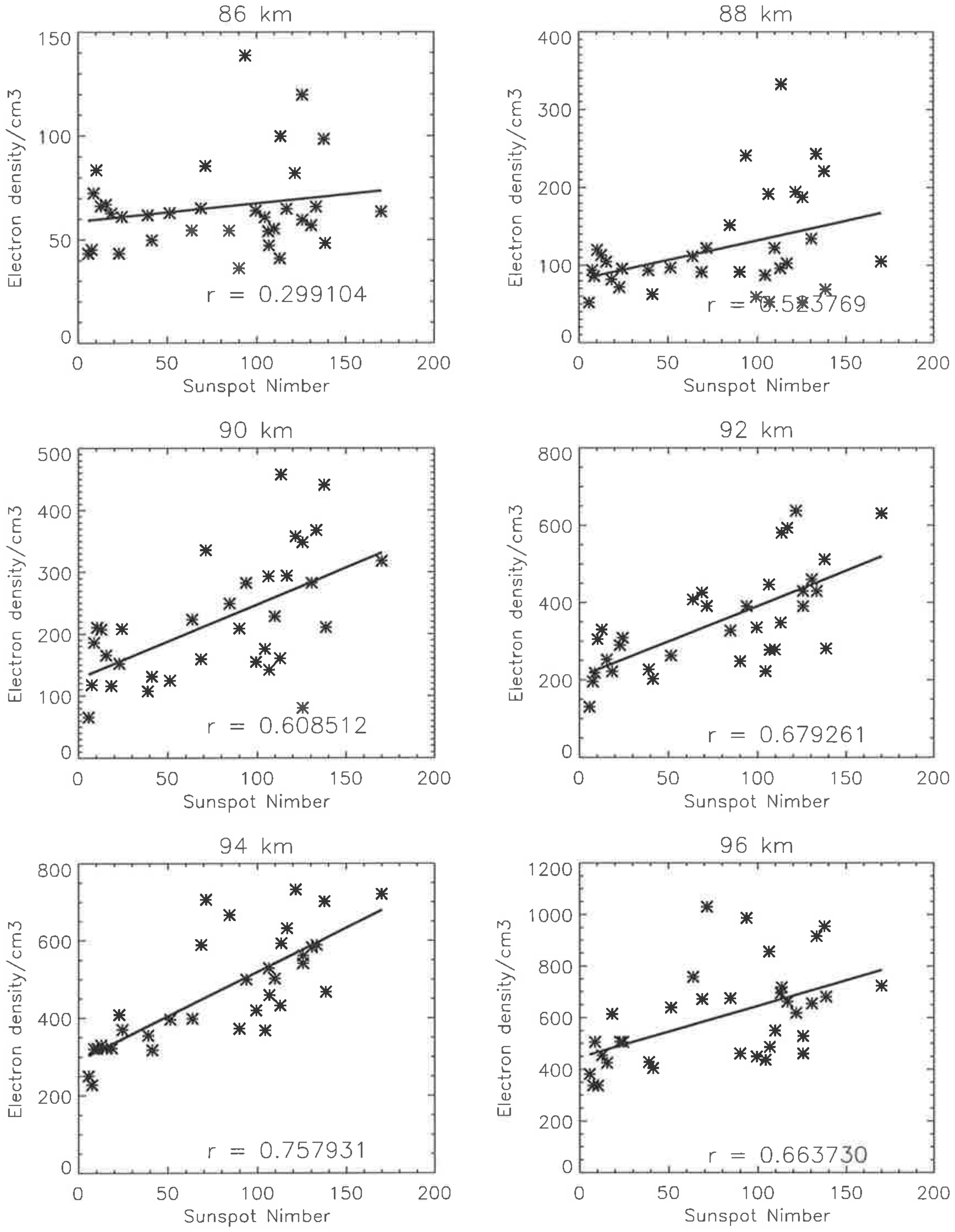

Figure 4.22: Regression curves for low to high solar activity period

NO production varies strongly over a solar cycle and the downward transport of this trace element determines the distribution of N_e in the lower thermosphere and mesosphere.

Investigations carried out by previous researcher (Solomon et al., 1982; McPeters, 1989; Siskind et al., 1997) are useful in evaluating NO variation in high and low solar active periods. Long-term trends in cumulative NO presented by McPeters (1989) indicate that NO variation follows the solar cycle, with NO being largest and nearly constant near solar maximum and smallest and nearly constant near solar minimum (1985-1986). This variation was shown to be more pronounced in equatorial nitric oxide (~50%) than mid-latitudes. A similar trend in equatorial NO was observed by Barth et al. (1988). The observed electron density variation (overall variation from 1997 -2000) reported here are in good agreement with the above mentioned studies of McPeters (1989).

4.3.2 Diurnal variation and decay

In this section, the temporal variation of the nighttime electron densities is discussed, and an attempt is made to investigate possible sources of electron production using these time series (Figures 4.23 to 4.26) . Although the nighttime data considered here are prone to large uncertainties in their absolute values, general trends and variations can be deduced from the measured sets of data.

Most of the model results to date are studies related to $E-$region or lower ionosphere (Titheridge, 2001; Friedrich and Torkar, 2001; Gough, 1975; Strobel et al., 1980; Strobel et al., 1974; Harris and Tohmatsu, 1972; Tohmatsu and Wakai, 1970), part of which falls into the upper $D-$region and more specifically the region of nighttime measurements made by the MF radar at Adelaide. The electron densities measured here are interpreted, with the help of those previous studies and other investigations related to precipitating energetic electrons as an ionizing source in the mid-latitude nighttime $D-$region (Nicolet, 1979; Manson and Merry, 1970; Manson and Merry, 1971; Potemra and Zmuda, 1970).

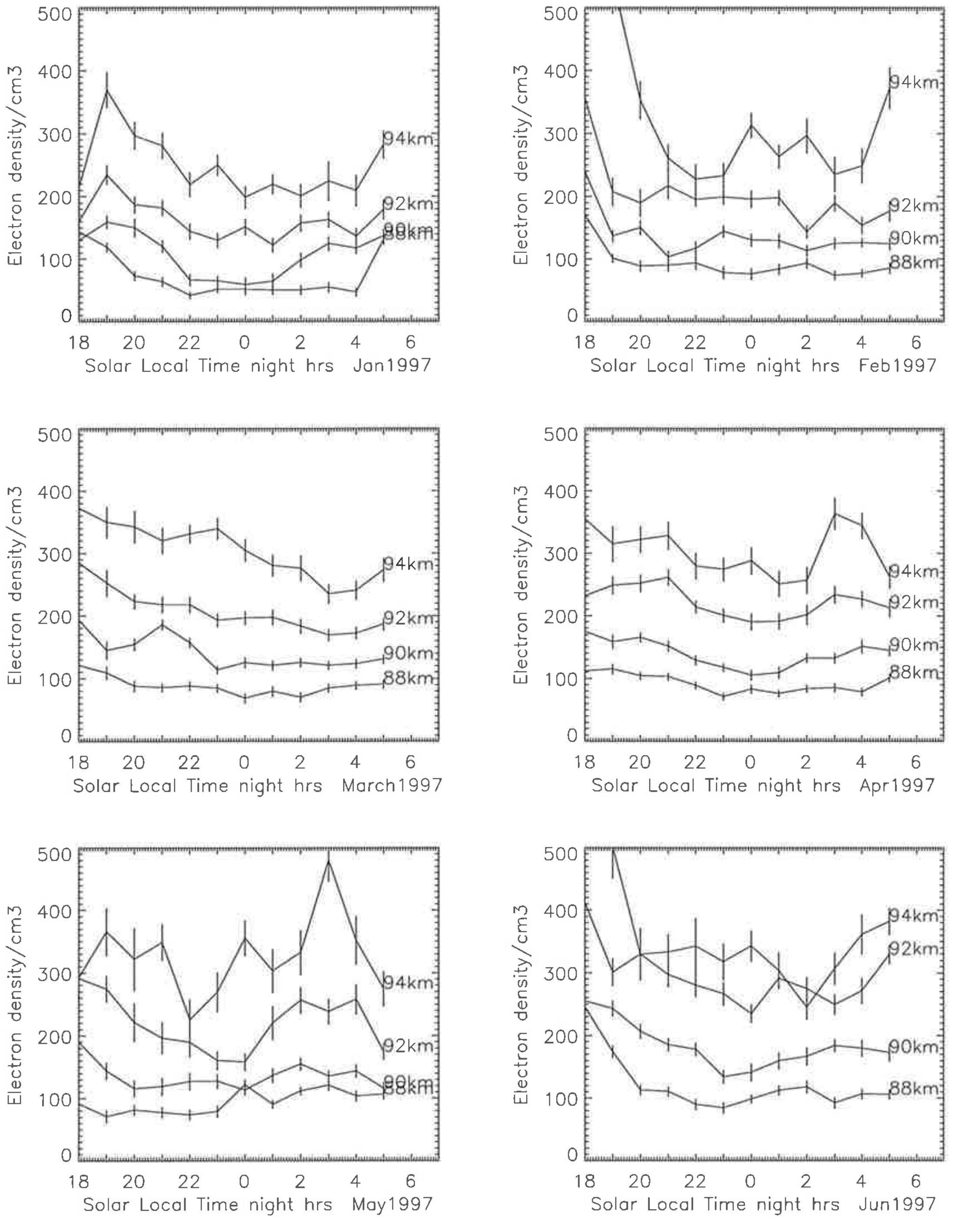

Figure 4.23: Electron density decay in night hours (low solar activity period, 1997) January to June. The vertical bars are standard errors at 95% confidence level.

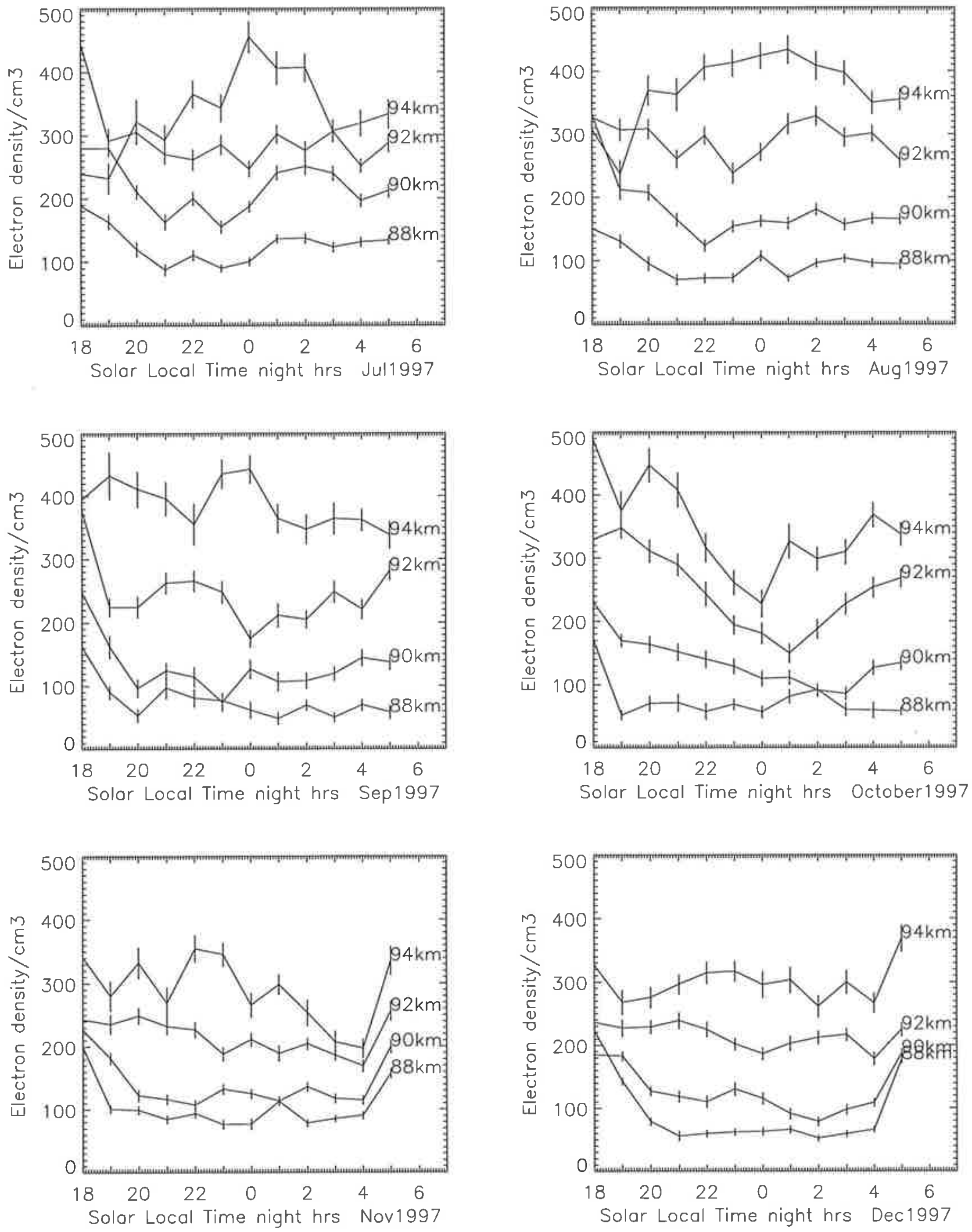

Figure 4.24: As for Figure 4.23, but for July to December 1997

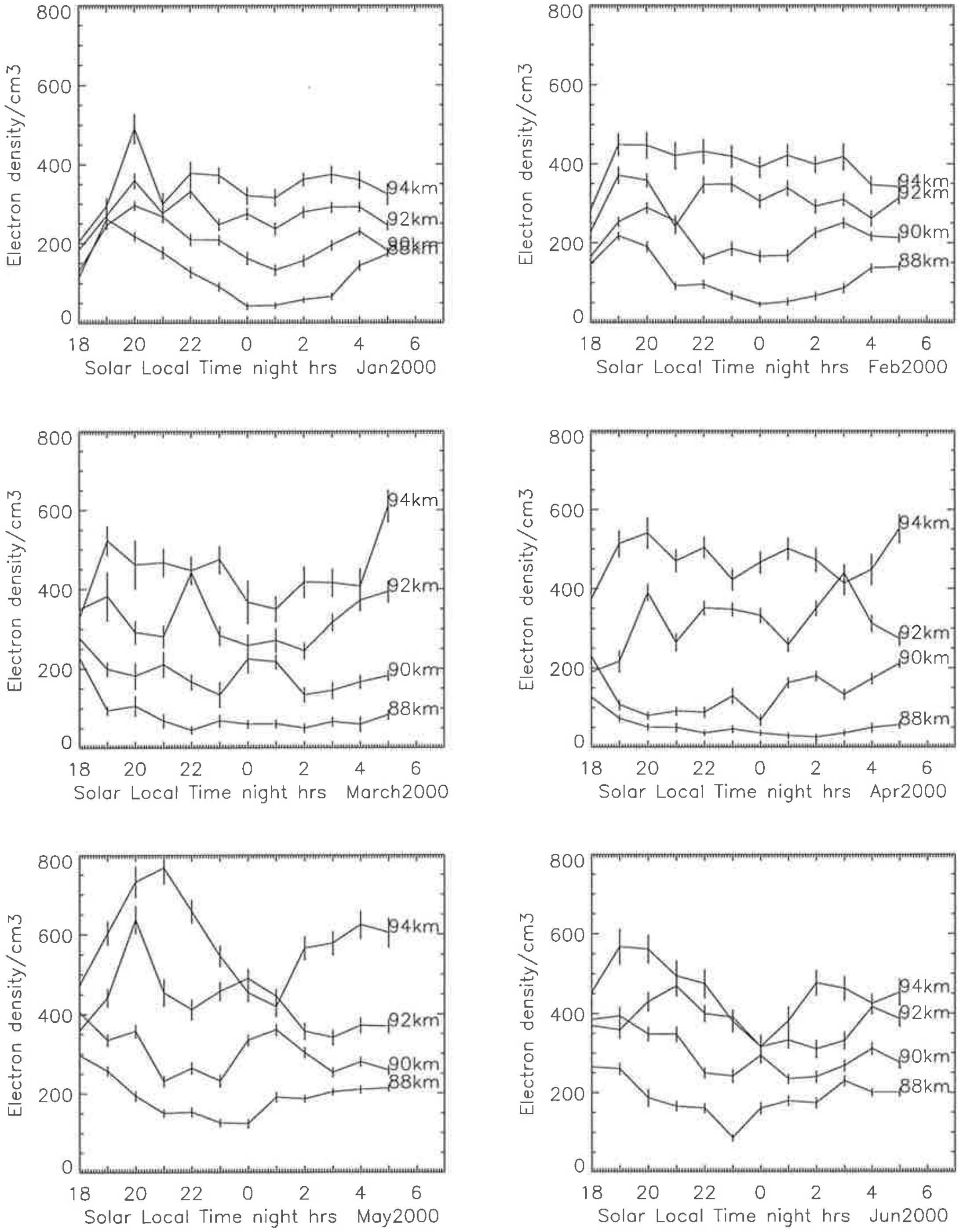

Figure 4.25: As for Figure 4.23, but for high solar activity period 2000

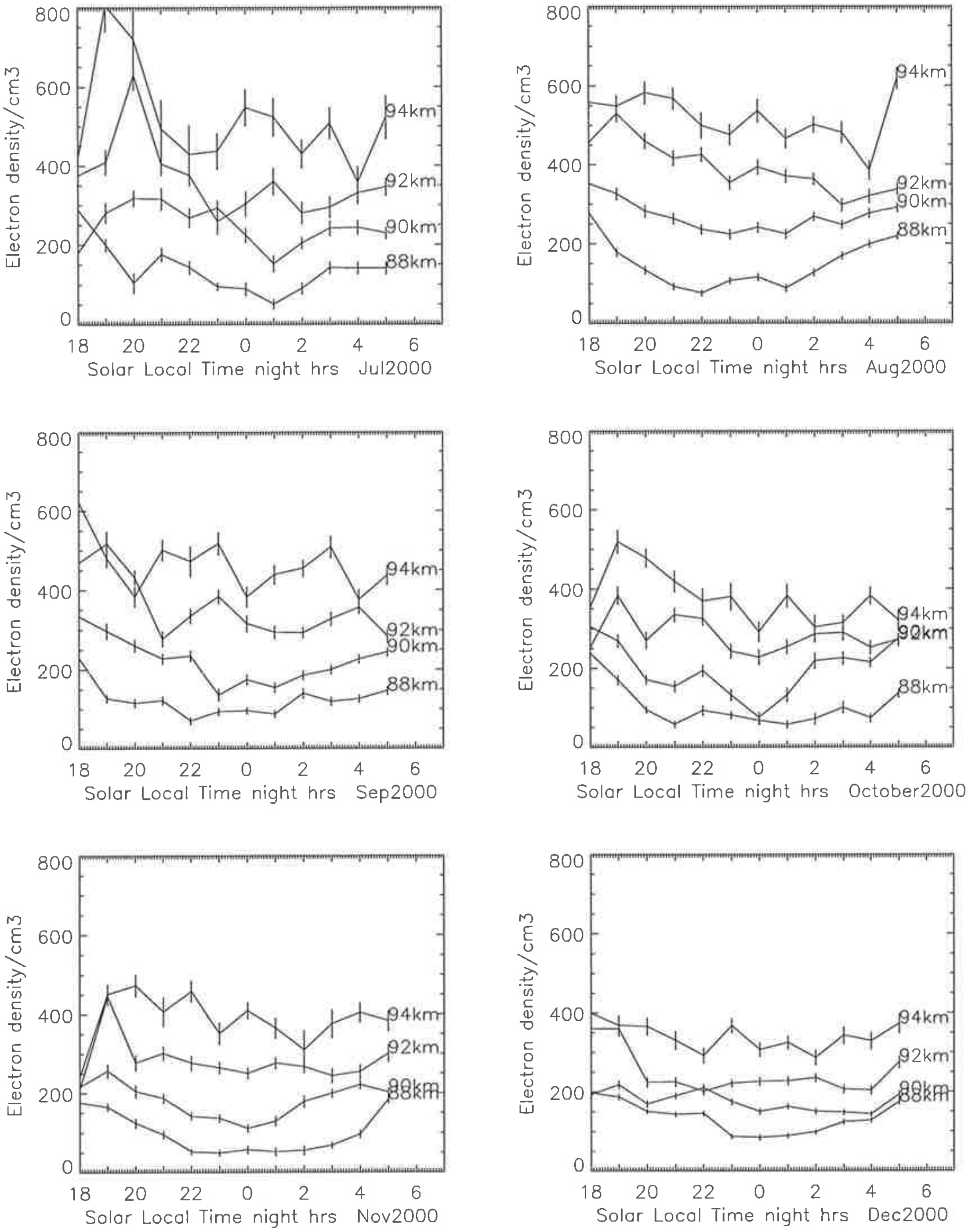

Figure 4.26: As for Figure 4.25, but for July to December 2000

Swider (1972) and Aikin (1972) Strobel et al. (1974) showed that the intensities of Ly$-\alpha$ and Ly$-\beta$ radiation fields from terrestrial and extraterrestrial sources are sufficient to maintain the nighttime lower ionosphere at observed electron density levels. Ogawa and Tohmatsu (1966) showed that hydrogen Ly$-\beta$ played the major important role in the ionization process above 100 km. At night one can assume that photo-detachment of negative ions is not effective. Present electron density data are investigated on the basis of such established concepts regarding the formation of nighttime ionization.

First, the general structure of these series are considered and compared to the variation of possible sources mentioned in the introduction section above. The temporal behaviour of the electron-density profiles during night in each month are shown in Figures 4.23 to 4.26 for 88 to 94 km; the electron density below 88 km showed little change with time (not shown in the figure). It can be seen that there generally exists a slight decay in the electron density after sunset (for Sunrise (SR) and Sunset (SS) local times at ground level see Table 4.2). The decay is more evident for sunspot minimum and in the equinoctial months. For example, see results for March 1997 in Figure 4.23 and October 1997 in Figure 4.24.

For comparison, diurnal variations of N_e due to IRI model results are shown in Figure 4.27. Comparison of these results with the experimentally measured electron densities indicate several differences. The IRI model results show significant decay below 86 km and minimum N_e is reached at local midnight, whereas above 86 km, the minimum is reached around 2100 LST and remains constant until 0400 LST and from then N_e increases up to 0600 LST. In contrast, the observed N_e did not show such smooth variations. In most of the months the minimum N_e was found to occur at local midnight. Also, the IRI model values are larger than the observed values by a factor of 4 - 10 as discussed previously.

Table 4.2: Sunrise and Sunset times (LST) for each month (1997) at Adelaide (middle of the month)

Month	Sunrise (SS)	Sunset (SS)
1	0556	2002
2	0627	1935
3	0652	1858
4	0616	1717
5	0640	1649
6	0656	1644
7	0650	1658
8	0622	1721
9	0540	1743
10	0459	1807
11	0531	1937
12	0531	2001

4.3.2.1 Recombination coefficient

A calculation of the recombination coefficient (Figure 4.28) can be made from the nighttime electron density decay after sunset for each season. Assuming that solar radiation scattered from geocorona is the only source of electrons $(P << L)$ and that there is no vertical transport ($w = 0$) at night, then the electron concentration decays as

$$\frac{dN}{dt} = -L(N) \tag{4.1}$$

In some situations the loss rate L(N) is proportional to the concentration, and in other situations the electrons are lost by recombining with positive ions so that

$$L(N) = \alpha N(e)N(i) \tag{4.2}$$

where N_e and N_i are the concentrations of electrons and ions and α is a recombinations constant. Under most circumstances the two concentrations are equal (charge neutrality), so the 4.2 may be rewritten as

$$N = N_e = N_i \tag{4.3}$$

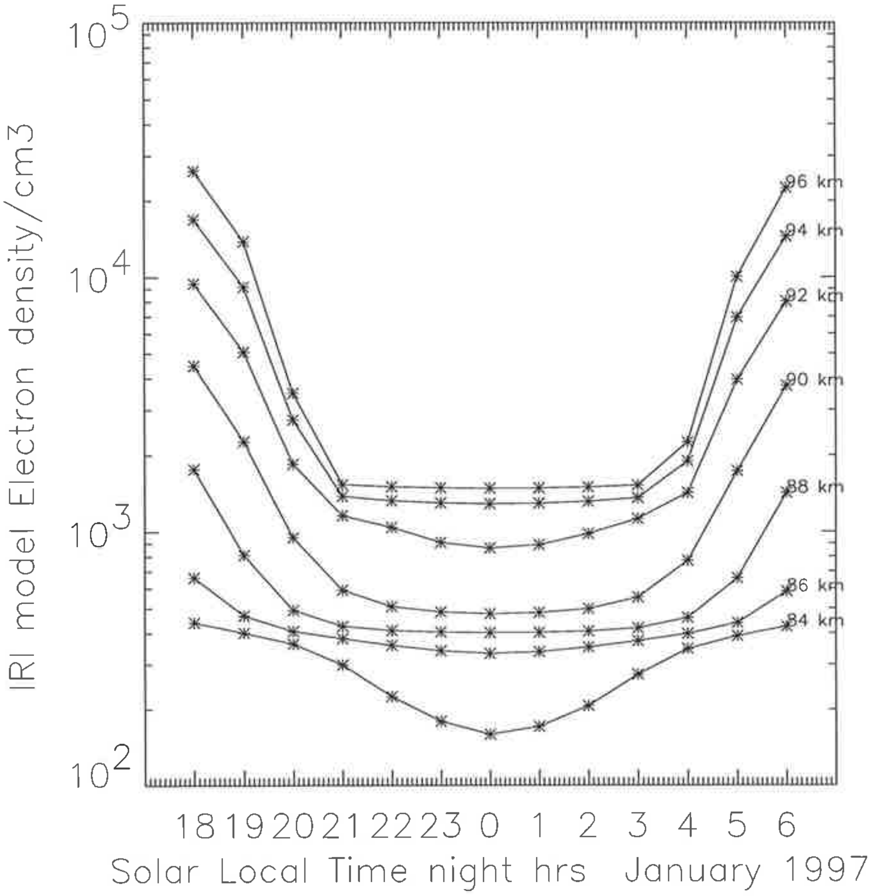

Figure 4.27: IRI model electron density decay in night hours (low solar activity period) January 1997, for 35°S

and

$$L(N_e) = \alpha {N_e}^2 \tag{4.4}$$

The decay then proceeds according to the equation

$$\frac{dN_e}{dt} = -\alpha {N_e}^2 \tag{4.5}$$

Using the above equation and the nighttime electron densities observed here the average recombination coefficients can be estimated. Since the time interval dt taken here (one hour) is large, the values estimated can only be approximations. Also, only the equilibrium electron density N_e due to photo-ionization was considered (particle ionization was neglected). The assumption of the absence of nighttime sources may not be correct (see below). However, many authors have found it satisfactory to assume

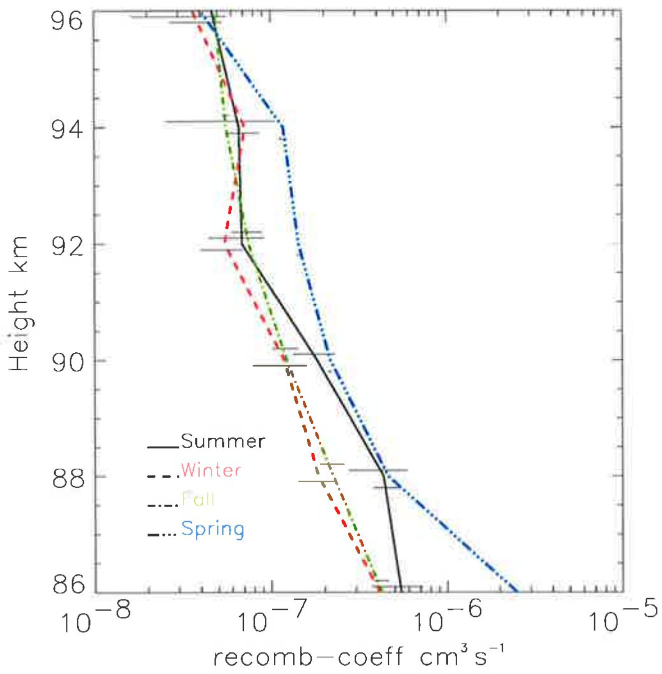

Figure 4.28: Recombination coefficient calculated using Figures 4.23 and 4.24 for 1997 (low solar activity period). The horizontal lines are standard error at 95% confidence levels. For clarity, the error bars are raised or lower by 0.1 to 0.2 km

that the net result of the complex processes involved can be approximated by the simple law represented by (4.5) (Gledhill, 1986; Swider, 1988). These average recombination coefficients are used to discuss the type and magnitude of possible ionization sources.

Figure 4.28 shows the derived recombination coefficients for all the seasons. The error bars are simply the standard error of the means for each season and do not represent the total uncertainties in estimating the absolute values due to the errors in the measured electron densities. Also, since the recombination coefficient is a function of solar zenith angle as well as height, values differ at each hour after sunset. The values presented here are at 2300 local time for each season. The fact that the local sunset times change in each season is not taken into account.

Effective electron recombination coefficients were deduced by Torkar et al. (1998) from measured ion production rates and plasma densities using twenty nine $D-$region

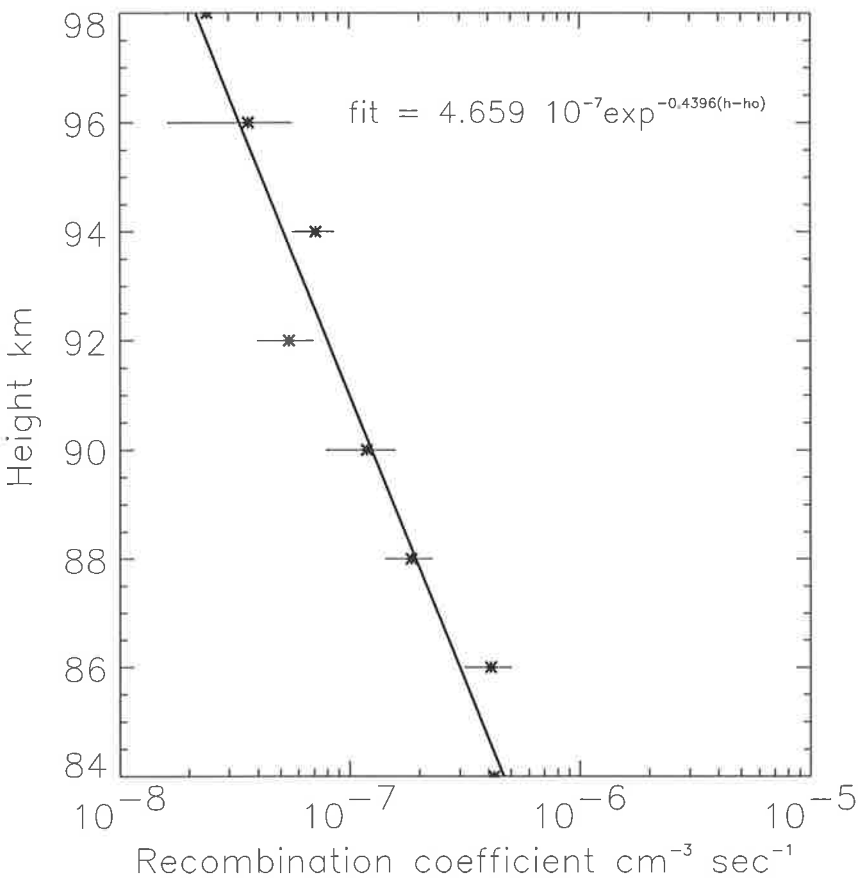

Figure 4.29: Vertical profile of recombination coefficient (winter average) represented by $*$ and the straight line shown is a fit corresponding to the equation shown at the top right hand corner

rocket flights. They were grouped according to day and night conditions. Most rockets were launched from high latitudes and only two flights took place from a mid-latitude site and one from the equatorial region. However, nighttime effective recombination coefficients of positive ions from their study compare well with our calculated recombination coefficients. The coefficients ranged between 5×10^{-6} - 10^{-7} cm^3 s^{-1} for the altitude range of 60 - 120 km.

The examination of the effective recombination coefficient derived here shows that it is too large (i.e., $\sim 10^{-7}$ cm^{-3} sec^{-1}) to explain the existence of observed nighttime electron density in the absence of a source or sources of ionization. It was pointed out by Torkar and Friedrich (1983) that theoretical model predicts a much stronger dependence of the electron loss rate on ion production at night than day time conditions. This is primarily due to the reduced formation of negative ions by attachment at times of large ion production. The straight line shown in the Figure 4.29, has been fitted to the heights below 98 km and corresponds to the equation

$$\alpha = 4.66 \times e^{-0.4396(h-ho)} \tag{4.6}$$

where ho is 84 km and h is the height. It should be noted that the concept of an effective recombination coefficient and its variation with height should be used with care and that the results of its application should not be given too much weight. Nevertheless, it might prove to be useful in the future for the study of $D-$region nighttime ionization.

4.3.2.2 Discussion

In the absence of transport, a source of ionization is required to explain the nighttime electron density profile. This conclusion was pointed out by Ferguson et al. (1965) and Donahue (1966). Furthermore, if smaller recombination rates are assumed ($\alpha \leq 10^{-8} cm^{-3} sec^{-1}$) there would be an inconsistency with too high an electron density during the daytime. Solar radiation in the extreme ultra-violet and $X-$ray regions of the spectrum is deposited between 60 and 200 km, producing free electrons and ions (Aikin, 1972). At night, scattered solar Ly$-\alpha$ and Ly$-\beta$ as well as HeI and HeII are present. These and other lesser known sources, for example cosmic $X-$rays and extreme ultraviolet radiation, contribute to the formation of the nocturnal D and E regions.

Figure 4.30 is an extract from Potemra and Zmuda (1970) for comparison purposes. The height profiles of ion-pair production rates due to precipitating electron spectrum are labeled A, B and C. The ionization due to galactic cosmic rays from Webber (1962) and scattered H Ly$-\alpha$ are shown in this figure, where the curve labeled (1) was computed from the Barth (1966) NO profile and curve (2) from the Nicolet (1965) profile. The figure also depicts the ionization expected from the $X-$ray source, Sco

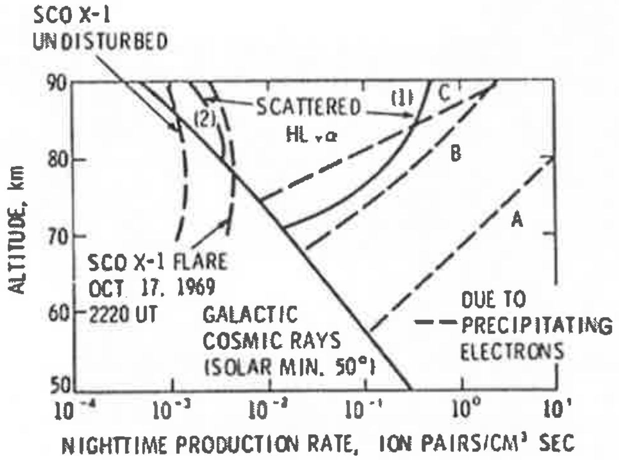

Figure 4.30: Ionization rates in the nighttime D region [After Ogawa and Tohmatsu (1966)].

X-1 during undisturbed conditions and during flares observed on October 17, 1969.

A quantitative description of the relative importance of the various sources of ionization however is difficult, since there are uncertainties in quantities both in the estimated ionization rates from the observed data and the presence or absence of fluxes of energetic electrons at this site. The vertical distribution of NO also plays an important role, as this is the only species ionizable by hydrogen(H) Ly$-\alpha$.

The mere fact that any ionization rate is comparable to or larger than production rates from other sources is, however, no guarantee that its effect will show in N_e. If one computes the residual N_e at $\sim 10^4$s after sunset at heights of 80 to 100 km, one finds that it makes little difference whether one includes any source or not, even without considering $q\ (Ly-\alpha)$. This is because $\alpha {N_e}^2$ is the dominant term for several hours after sunset, and q, which is of order of $10^{-2} cm^3 s^{-1}$ or less (see Figure 4.30) begins to become effective only when $\alpha {N_e}^2$ is reduced to this value late at night. With $\alpha \sim 1 \times 10^{-6} cm^3 s^{-1}$ at 90 km at night, this value is reached only when N_e has been reduced to a value of about $10^2\ cm^{-3}$ (α at this point about three orders of magnitude larger than the total q at 90 km).

For comparison, at 92 km, estimated recombination coefficient (approximately 1×10^{-7}–$3 \times 10^{-7}\ cm^3 s^{-1}$) along with the measured electron density values (150-300 cm^{-3}) from our data suggests that the possible ionization rates (neglecting transport effects) could range from $2.25 \times 10^{-3}\ cm^{-3}$ to $2.7 \times 10^{-3}\ cm^{-3}$. Comparison of these rates with those of previous researchers (Mitra and Ramanamurthy, 1972) and the values shown in Figure 4.30 points to the possible sources as Ly$-\alpha$, Ly$-\beta$ and SC XR-1. The more crucial, and for the purpose of this work, the deciding role, is that of nitric oxide. If nitric oxide has the same concentration at night as during the day in these height ranges, then, as shown in the calculations of Poppoff and Whitten (1969), $q_{Ly-\alpha}$ is the dominant production rate at night and there is no chance that the effect of cosmic $X-$ray sources is even marginally significant.

Theoretical calculations by Strobel (1971) shows no diurnal variation of NO concentration at heights of 80-100 km. Nevertheless, there is some experimental evidence that at heights around 90 and 95 km the NO concentration is about an order of magnitude lower than during the day (Narcisi et al., 1969; Friedrich et al., 1998). This evidence comes from the post-sunset (SS) and pre-sunset (SR) measurements of NO concentrations and ion compositions by Narcisi et al. (1969) and Friedrich et al. (1998), respectively.

There has been considerable discussion concerning the importance of celestial $X-$ray sources in the formation of nighttime lower ionosphere, (see Aikin (1972) and further references therein). The diffuse $X-$ray background is greater than the cosmic-ray ionization at the equator between 80 and 90 km and becomes equal to the cosmic-ray contribution between 35° and 45° geomagnetic latitude. SC XR-1 is the most important single source of cosmic $X-$ray ionization. It exhibits a time variation and its relative importance depends on the variation of nitric oxide, and also on the variations in the flux from the sources (Mitra and Ramanamurthy, 1972)

As can be seen in the Figure 4.30 the contribution due to cosmic $X-$rays is normally less than 10^{-2} cm^3 sec^{-1} and that due to scattered Ly$-\alpha$ can vary from 5×10^{-2} to 10^0 cm^3 sec^{-1}. Ionization rates due to that of energetic electrons are greater than 10^{-1} cm^3 sec^{-1}. Similar height variation in nighttime ionization rates of lower ionosphere was shown by Aikin (1972). Calculation of electron production rates due to photo-ionization and particle precipitation for the mid-latitude ionosphere from 70-140 km during periods of quiet solar activity were performed by Manson and Merry (1971). Comparison of these ionization rates with the variation and magnitude of the ionization rates estimated using Adelaide data (example shown at 92 km in earlier part of this section) suggests that the possible nighttime ionization sources are nighttime ultraviolet radiation (Ly$-\alpha$) and SC XR-1 (denoted in the Figure 4.30 as SCO X-1).

Among different sources of photo-ionization analyzed by Strobel et al. (1980), scattered sunlight (air-glow) (consisting of hydrogen and helium lines resonantly scattered around the Earth by hydrogen and helium in the Earth‘s geocorona) has least effect at midnight and increases markedly toward sunrise and sunset. A similar trend in observed N_e can be seen in most of the months and at altitudes below 92 km (Figure 4.23). (The electron density at 94 km generally showed large variations from month to month.) This is consistent with the fact that the minimum ionisation occurs at or an hour after midnight. This seems to be quite consistent with a nocturnal production related to the sun (scattered sunlight as described in the previous paragraph). Hence, these figures provide an indication that the source of electron production in the $D-$region below 92 km at night is related to scattered Ly-α or Ly-β radiation. Also, the ratio of solar maximum to solar minimum N_e is found to be 1.5 - 3.0, coinciding with the variation of Ly-α radiation intensity from solar maximum to minimum conditions.

In summary, the intensities of the nighttime ultraviolet radiation from the geocorona and extraterrestrial are able to produce the electron densities in the region 80 to 100 km. However, it must be emphasized that the same electron density variations can also be due to the redistribution of the density due to wind variation in this region.

4.4 Summary and Conclusions

General characteristics of mid-latitude nighttime electron densities in the region 80 − 100 km are reviewed with the help of Buckland Park MF radar observations. Monthly mean vertical profiles of electron density in the nighttime $D-$region showed that the electron density increases systematically with altitude, plausibly explicable by a corresponding structure in the nitric oxide (NO) profiles. Comparison of our results with IRI and FIRI model results showed that, at 23 hours local time the electron densities are much lower than model results.

Seasonal variation of electron densities at BP showed a moderately greater N_e values in winter and spring than summer values, especially in the height range of 88−96 km. Similar winter enhancement was reported by Friedrich and Torkar (2001) due to FIRI model results. Mean values of temperatures at 85 and 90 km from CIRA-86 model are compared with the annual variation of electron densities, since several temperature dependent reactions may be involved in the process of electron density production. These mean values of temperatures (CIRA-86) showed similar enhancement in the winter months indicating some effect on the seasonal variation of electron density at mid-laitude. Investigations of effect of solar cycle variation revealed that, above 80 km altitude, the electron density increases almost linearly with sunspot number.

Average recombination rates were estimated and these estimated values compare well with the earlier studies. Diurnal variation of electron density generally exhibited decay after sunset. For the sunspot minimum period, in the equinoctial months, the electron density decay is more prominent than other other months. But after local midnight, the electron density generally increased. Since the scattered sunlight has least effect at midnight and increases markedly towards sunrise and sunset consistent with the variation of diurnal electron density at Adelaide, it was concluded that this is an indication that the source of electron production in the $D-$region at night is related to the sun. An alternative explanation was thought to be the result of electron redistribution by the tidal winds of the solar diurnal tide.

In summary, the electron density variations in the nighttime $D-$region at Adelaide, indicate the possibility of several sources of ionization, namely, UV and transport due to wind variations and possibly precipitated energetic electrons . The use of partial reflection technique, on a network basis, to study the synoptic structure and energetics of the region in the $D-$region are advocated.

Chapter 5

Implications of Dynamic Atmosphere

5.1 Introduction

In this chapter the central features of observations that deviate from the classic Chapman model of a static atmosphere are examined as consequences of a dynamic atmosphere. It is shown that an asymmetry in the diurnal variation of electron density exists in all seasons in the height range 64-96 km. Possible mechanisms that may cause this asymmetry are investigated. In particular, tidal effects on the diurnal variation of electron density are considered. Measurements of $D-$region electron concentrations between 65 and 90 km generally exhibit strong solar control as indicated by the previous chapters. However, a common feature observed by many workers and as well as from our measurements is a diurnal asymmetry in N_e.

It was pointed out by Gregory et al. (1969) that mesospheric meteorology plays an important role in determining the structure and distributions of electron density in the D-region. Chakrabarty et al. (1983) also showed that, to satisfy the noon time electron density profiles in different seasons at Saskatoon, a seasonal variation in NO is necessary. Mid-latitude observations at Ottawa (45°N) reported by Coyne and Belrose

(1972) indicate higher N_e after noon, whereas at Tsumeb (19°S), higher electron densities were often observed before noon (Thrane et al., 1968). Pronounced asymmetries in N_e have also been observed between 95 and 120 km at mid-latitudes with higher electron densities occuring in the morning hours (Monro et al., 1976). Long-period measurements of ionospheric absorption in central Europe show that there is a considerable seasonal variation in the asymmetry of the diurnal variation of absorption at certain frequencies (Lastovicka, 1977).

Recently, Siskind et al. (1998) published a climatology of NO in the mesosphere and thermosphere (50-160 km) based on SME and HALOE/UARS satellite measurements, while Friedrich et al. (1998) published the results of comparisons of HALOE/UARS nitric oxide density measurements with other ionospheric data. In their study, diurnal asymmetry of NO densities was reported to be observed. The existence of a diurnal asymmetry of the NO density was confirmed by Lastovicka (2001), through the analysis of multi-frequency radio wave absorption measurements in the lower ionosphere over Central Europe. Marsh et al. (2000) explained the SR/SS anomaly in the NO observations in terms of tidal induced perturbations, which indicates a need to investigate the tidal influence on the electron density.

To date, no satisfactory explanation of the occurrence of asymmetry in the diurnal variation in electron density has been given. The findings from the present study can provide additional support to the previous workers findings, including the results of Friedrich et al. (1998). Another objective is to extend the knowledge of the diurnal asymmetry from near noon to the entire day. The possibility that time-varying effects, due to particle influx, were encountered is considered remote. The study has been made for all seasons and in the altitude regions of 66-72km (daytime) and 86-96km (nighttime) where we feel the data are most reliable.

Two different mechanisms causing this asymmetry are addressed including, i) tidal variations in density and temperature affecting electron recombination rates and ii) tidal variations in NO (caused by vertical advection) affecting production rates. It is likely a combination of both have an effect, and perhaps the dominant process may change with altitude or solar zenith angle. The tidal effect in recombination rates should show up at a maximum or minimum in the temperature perturbation, while the advection effect will maximize at the point in time where the wind reverses direction (Private Communication, Dr. D. R. Marsh, 2001).

Two aspects appear significant. First, the diurnal asymmetry in the time series of electron densities in the height range of 64 to 94 km, which show variation, not in accord with any smoothly varying function of solar zenith angle. Second, the existence of large electron densities, in winter above 80 km (as shown in nighttime observations, in Chapter 4) and equinoctial asymmetry (fall values larger than spring) in the lower height range of 66 -76 km (as detailed in the day time results, in Chapter 3).

The second feature detailed above was thought to be due to downward advection of NO, by the mean meridonial circulation in the wintertime mesosphere and the effects of planetary wave mixing on the latitudinal gradient of NO (Siskind et al., 1997). This was explained in brief in the previous chapters. The focus of this chapter is on the diurnal asymmetry, thus the diurnal variation is considered in detail as below.

5.2 Results and Discussion

5.2.1 Diurnal Asymmetry

The asymmetry exists in almost all the months. As examples asymmetry at 72 km, 84 km and 90 km are shown in Figures 5.1 to 5.9. Careful examination of the height variation of electron density reveals that the sense of asymmetry changes according to the time of the day and altitude region. Also the magnitude of the asymmetry is different in each month. For example, in May 1997 above $\chi = 80°$, afternoon N_e are larger than before noon N_e (Figure 5.1), in contrast to asymmetry below $\chi = 80°$.

Similarly, a seasonal asymmetry at $\chi = 65°$ is different from the asymmetric variation at $\chi = 58°$ (Figure 5.1) and the difference between asymmetry at $\chi = 85°$ and at $\chi = 90°$ can be seen in Figure 5.5, where vertical line is passing through the electron

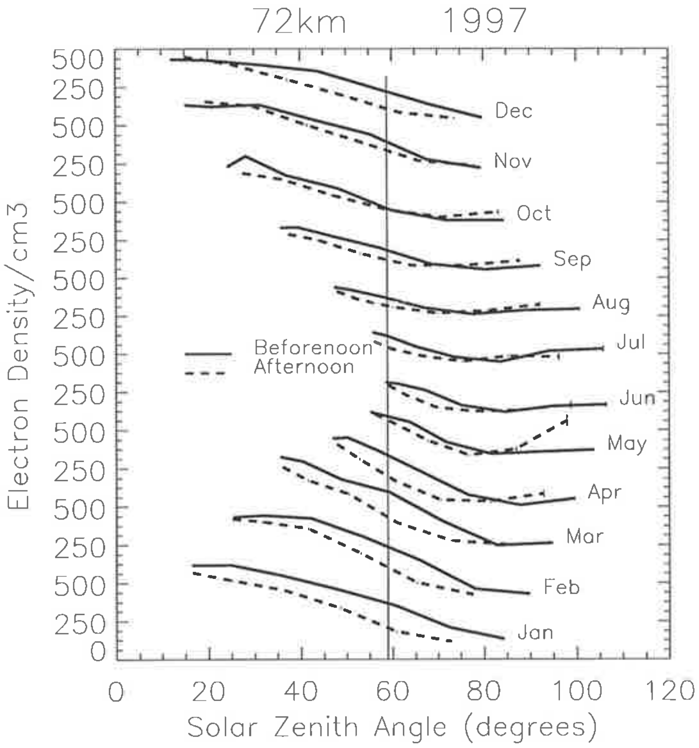

Figure 5.1: Electron density with respect to solar zenith angle at 72 km for the low solar activity period of 1997

density values in each month.

Although, the asymmetry exists at most zenith angles, only asymmetry at 58° Sza (before noon to after noon equivalent to winter minimum) and 90° Sza (Sunrise to Sunset) in all the three years are considered for comparison (Figure 5.1 to 5.15). Figure 5.16 summarizes all these profiles. Incidentally, observations made at these zenith angles coincide with the altitudes where NO is the source of dominant ion production (see example Figures 5.17 and 5.18).

Significant asymmetry is observed during equinox periods below 88 km, at $\chi = 90°$ (Tables 5.4, 5.5 and 5.6). At lower altitudes, around 66 – 76km, a larger asymmetry is observed in summer and equinox months and no significant asymmetry is observed in winter months (Tables 5.1, 5.2 and 5.3). Similar features can be seen in all three years (namely, 1997, 1999 and 2000), except that the January to February 1999 data are not shown due to equipment problems.

The maximum asymmetry observed is about 2.5 during December, in the 70-74

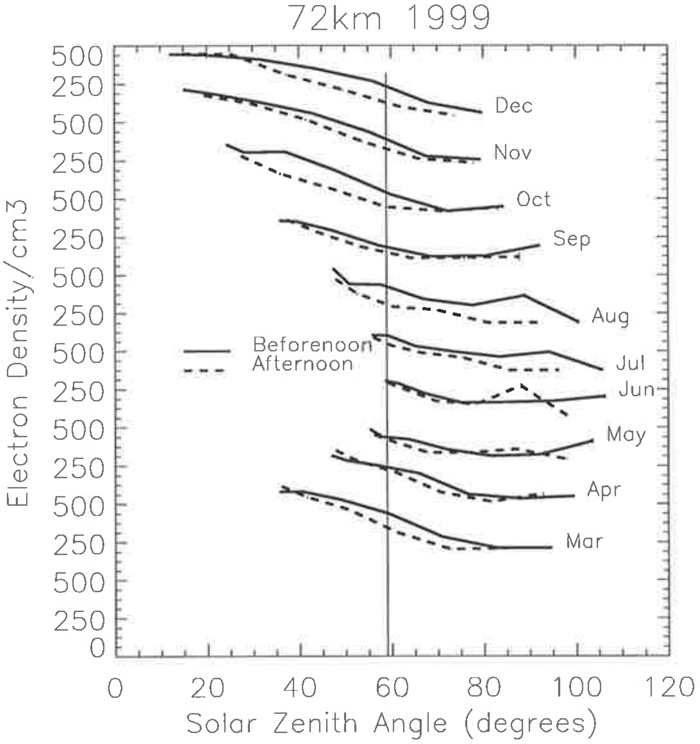

Figure 5.2: As for Figure 5.1, but for 1999

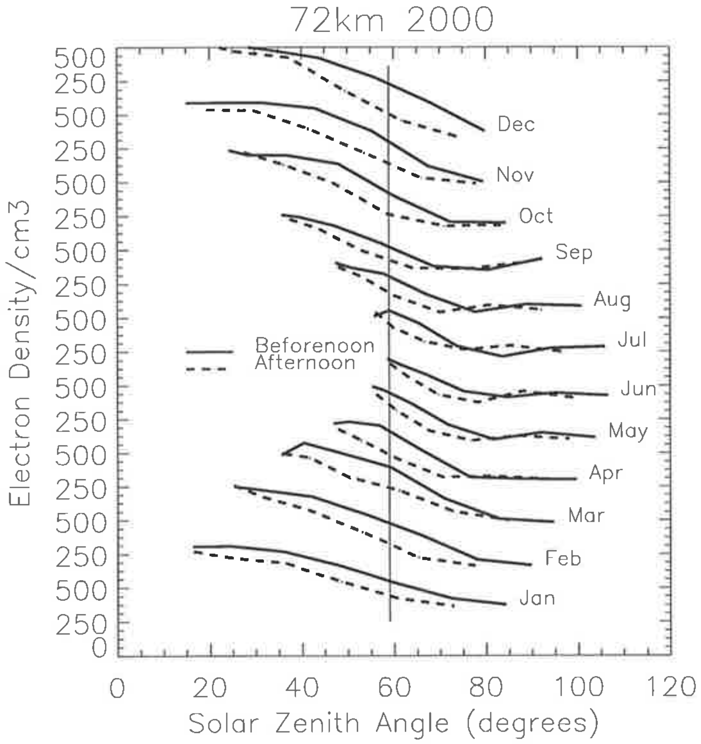

Figure 5.3: As for Figure 5.1, but for 2000 (high solar activity period)

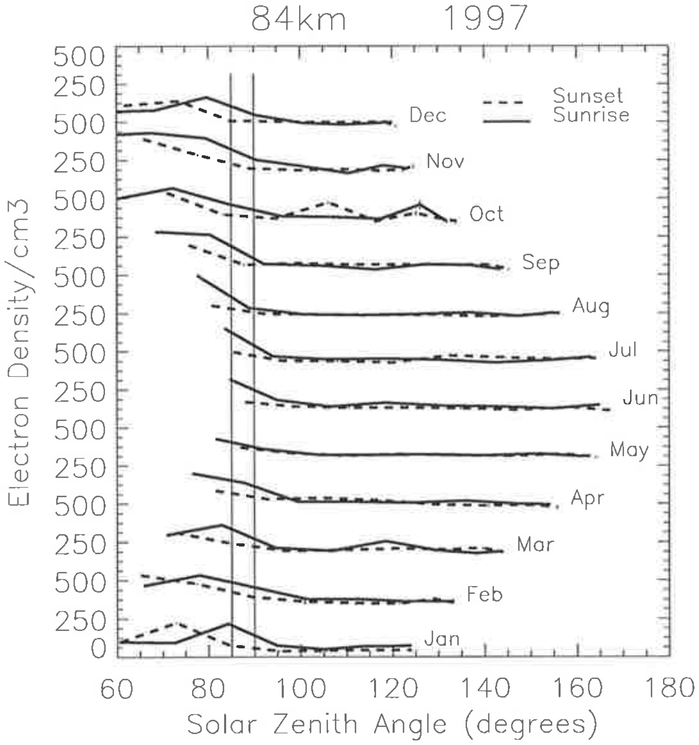

Figure 5.4: Electron density with respect to solar zenith angle at 84 km and for 1997

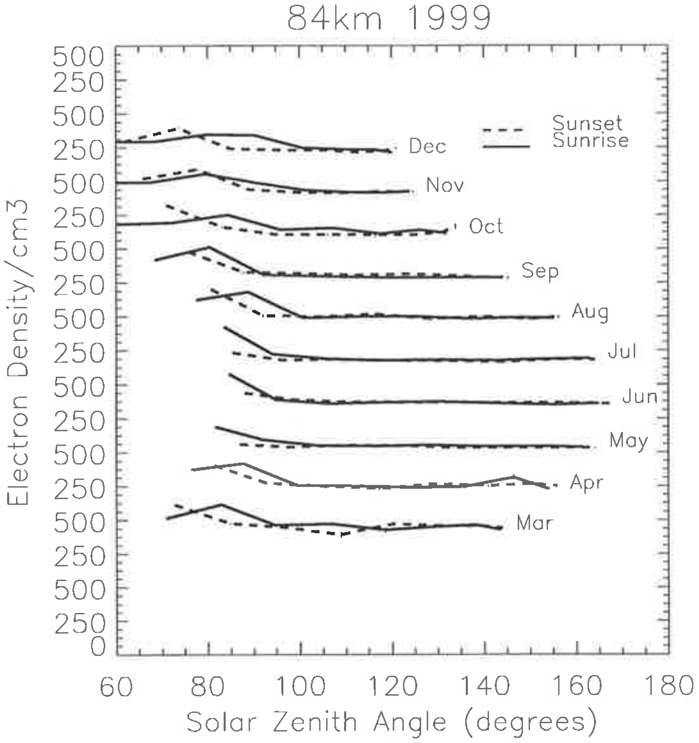

Figure 5.5: As for Figure 5.4, but for 1999

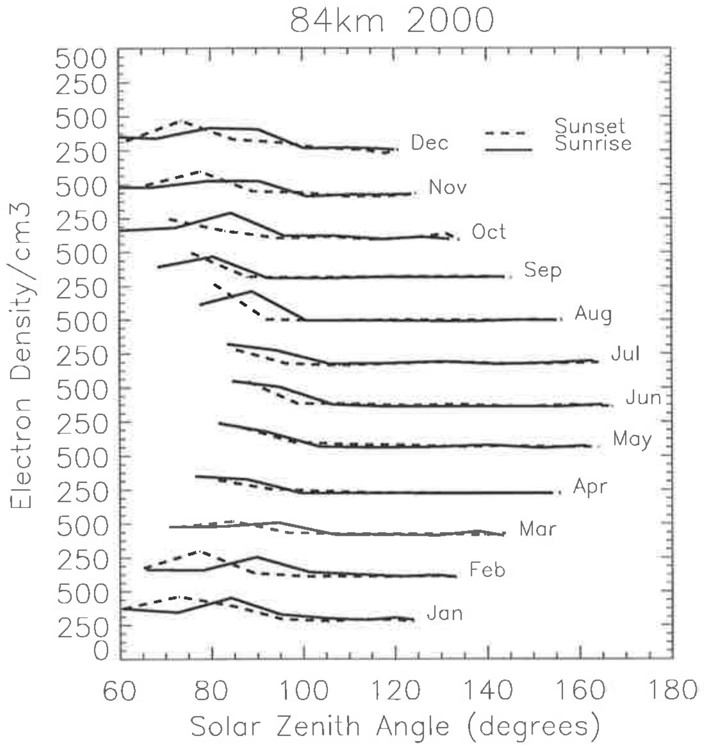

Figure 5.6: As for Figure 5.4, but for 2000

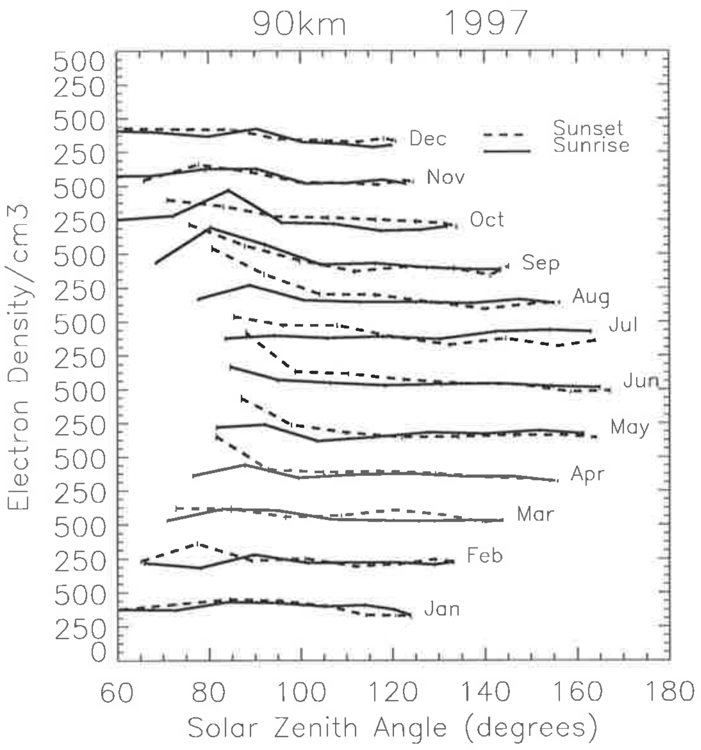

Figure 5.7: Electron density with respect to solar zenith angle at 90 km and for 1997

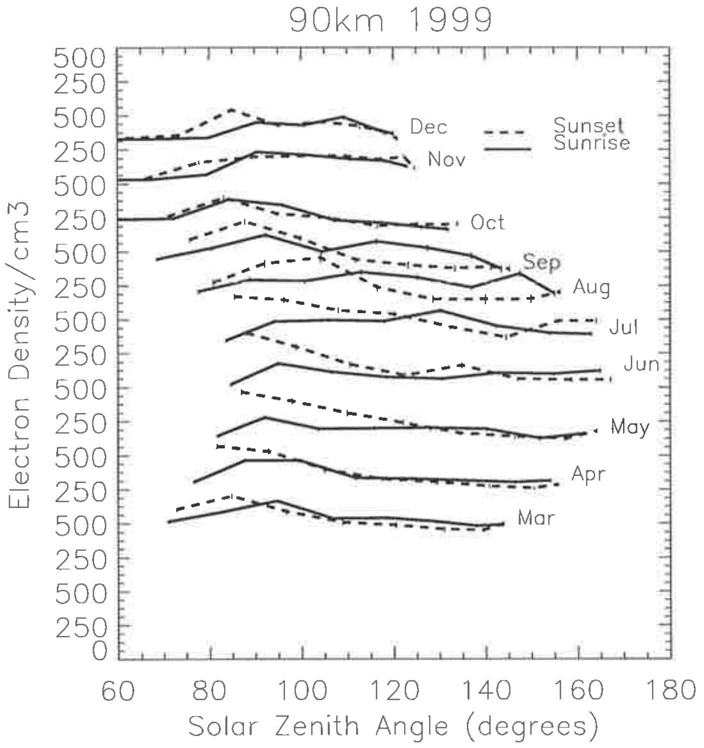

Figure 5.8: As for Figure 5.7, but for 1999

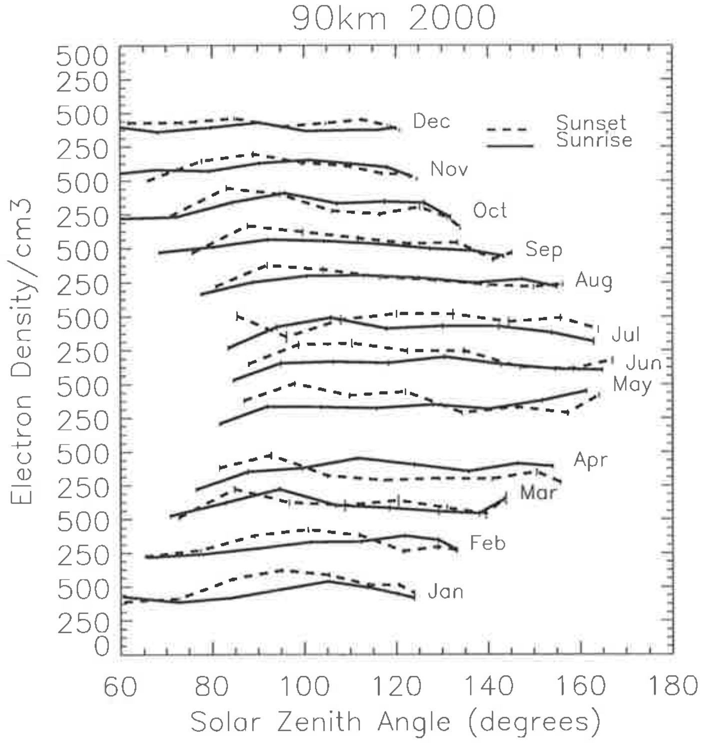

Figure 5.9: As for Figure 5.7, but for 2000

km height range. Between 84 and 88 km a maximum ratios of 3.9 - 5.2 is found in the month of October. Siskind et al. (1998) discussed the latitudinal variation of the SR/SS ratio and showed that it is largest at the equator, i.e., in excess of one order of magnitude, compared to less than a factor of two at 57° latitude. Accordingly, from the Figure 5.16 electron density measurements made at Buckland Park (35° latitude) reveal that the magnitude of this ratio is generally around 2.5.

Generally, morning N_e are larger than afternoon N_e and sunrise values (N_{SR}) are larger than sunset values (N_{SS}), except for the winter months (M,J,J), below 90 km. Above 90 km sunset values (N_{SS}) are larger than sunrise values (N_{SR}) in almost all the months. These N_e variations (presented as vertical profiles) are compared to the NO variations. The NO zonal averages, for all seasons are reported as sunset values (SS) larger than sunrise values (SR) up to approximately 92 km and above that height sunrise values are reported to be larger than sunset values (Friedrich et al., 1998). This is in opposite sense to the observed asymmetry at Adelaide.

It was also pointed out by Friedrich et al. (1998) that the HALOE team cannot rule out an uncertainty in modelling the instrument spectral response as the possible cause. To validate the possibility of existence of asymmetry in the electron density variation as well as the NO density measurements, another set of measurements at a different latitude(Wakkanai) are considered. Electron density observations at Wakkanai 45°N revealed similar asymmetric features as Adelaide in the daytime height range, as shown in the Figures 5.19 to 5.21.

For comparison a zenith angle of 65° is chosen for Wakkanai (summer minimum). The amount of asymmetry is comparatively less than that at Adelaide, consistent with an increase with decreasing latitude. As we are uncertain about the measurements during February, March and also the night observations, no comparison is made during these times. But, the similarity in the available daytime results at Wakkanai and Adelaide, matches the findings of (Lastovicka, 2001), pointing out that the asymmetry is most pronounced in summer in comparison to winter (at 66 - 76 km range). Also, it is important to note that both at Adelaide and Wakkanai morning electron density

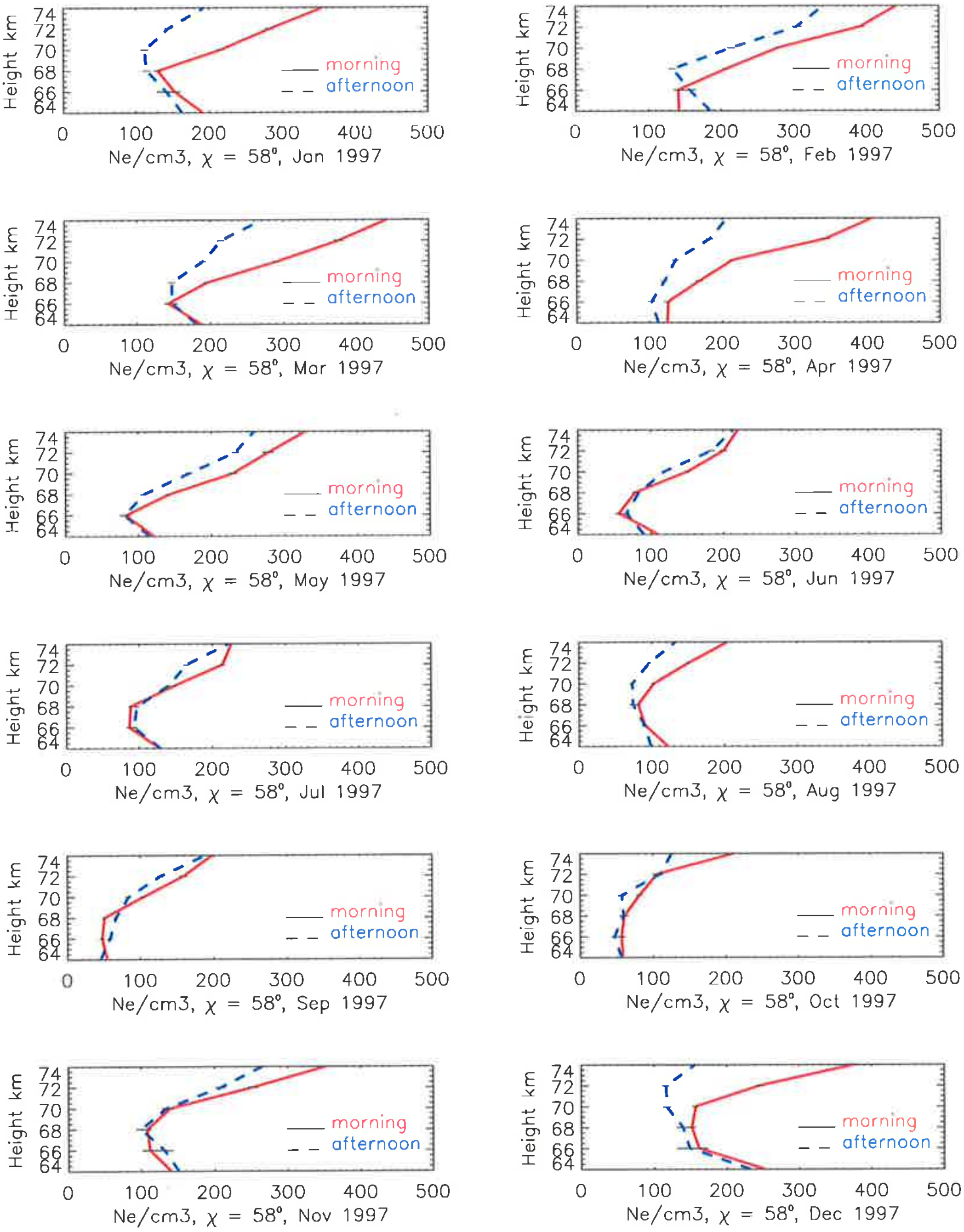

Figure 5.10: Altitude variation of asymmetry in each month at 58° zenith angle and for 1997

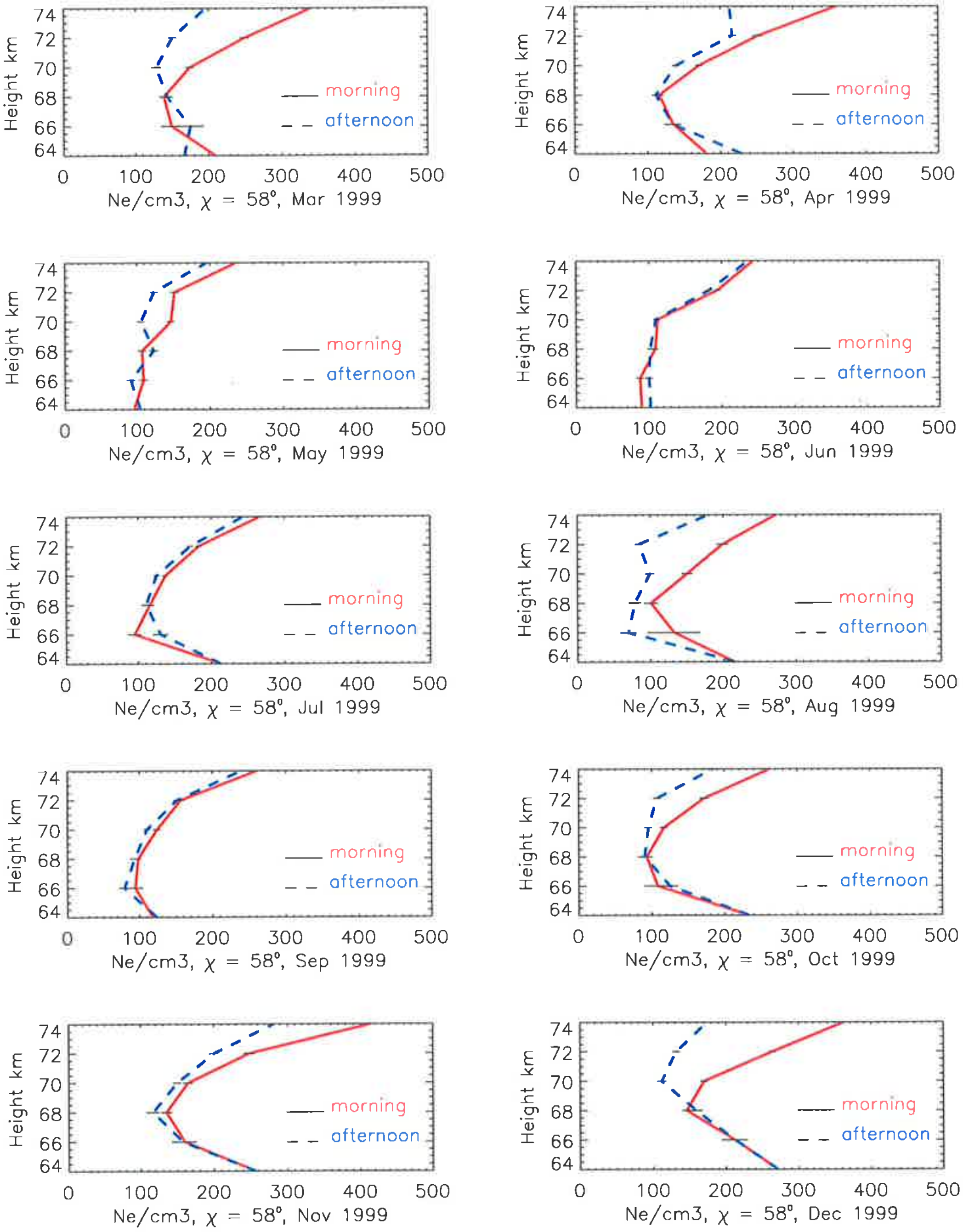

Figure 5.11: As for Figure 5.10, but for 1999

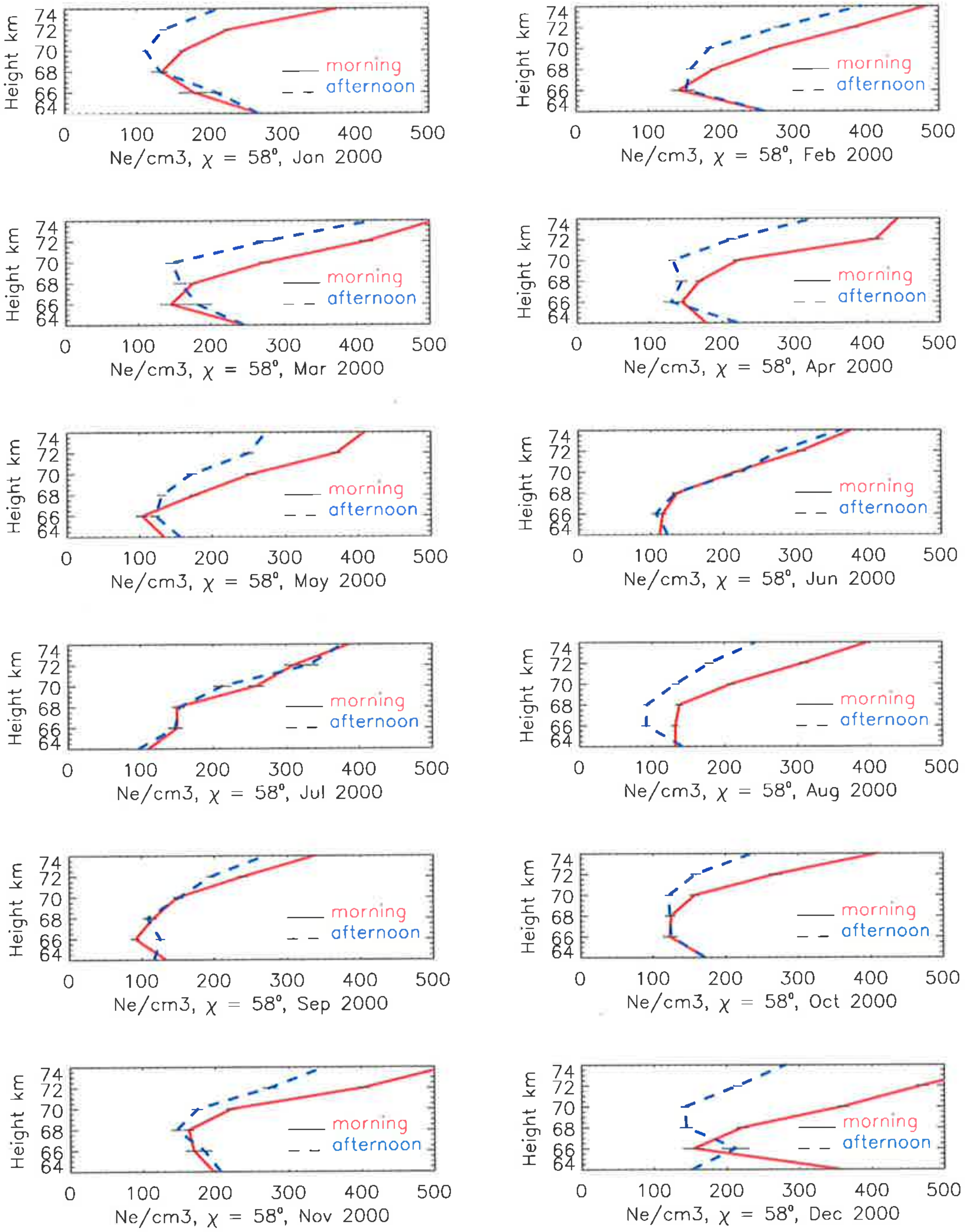

Figure 5.12: As for Figure 5.10, but for 2000

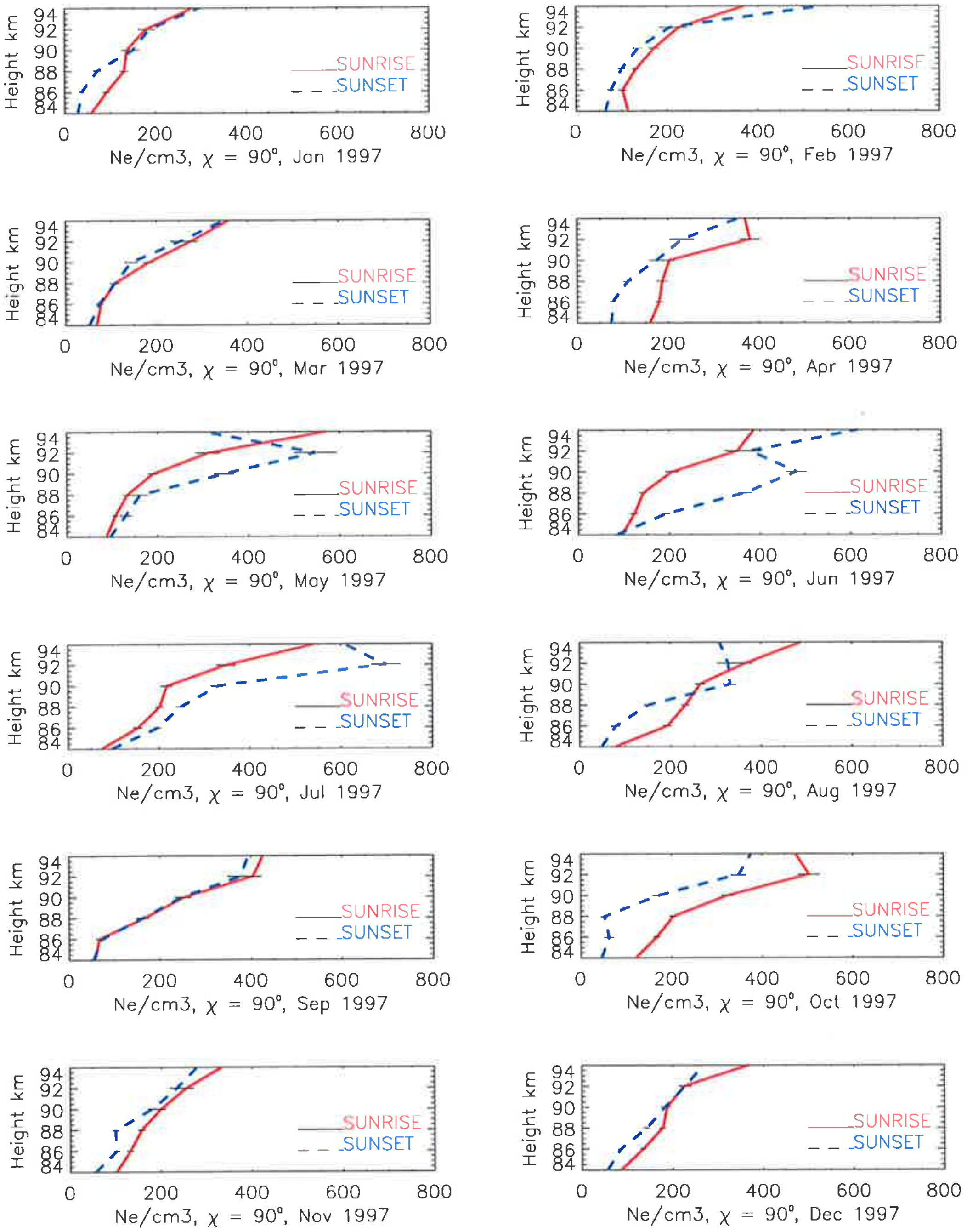

Figure 5.13: Altitude variation of asymmetry in each month at 90° zenith angle and for 1997

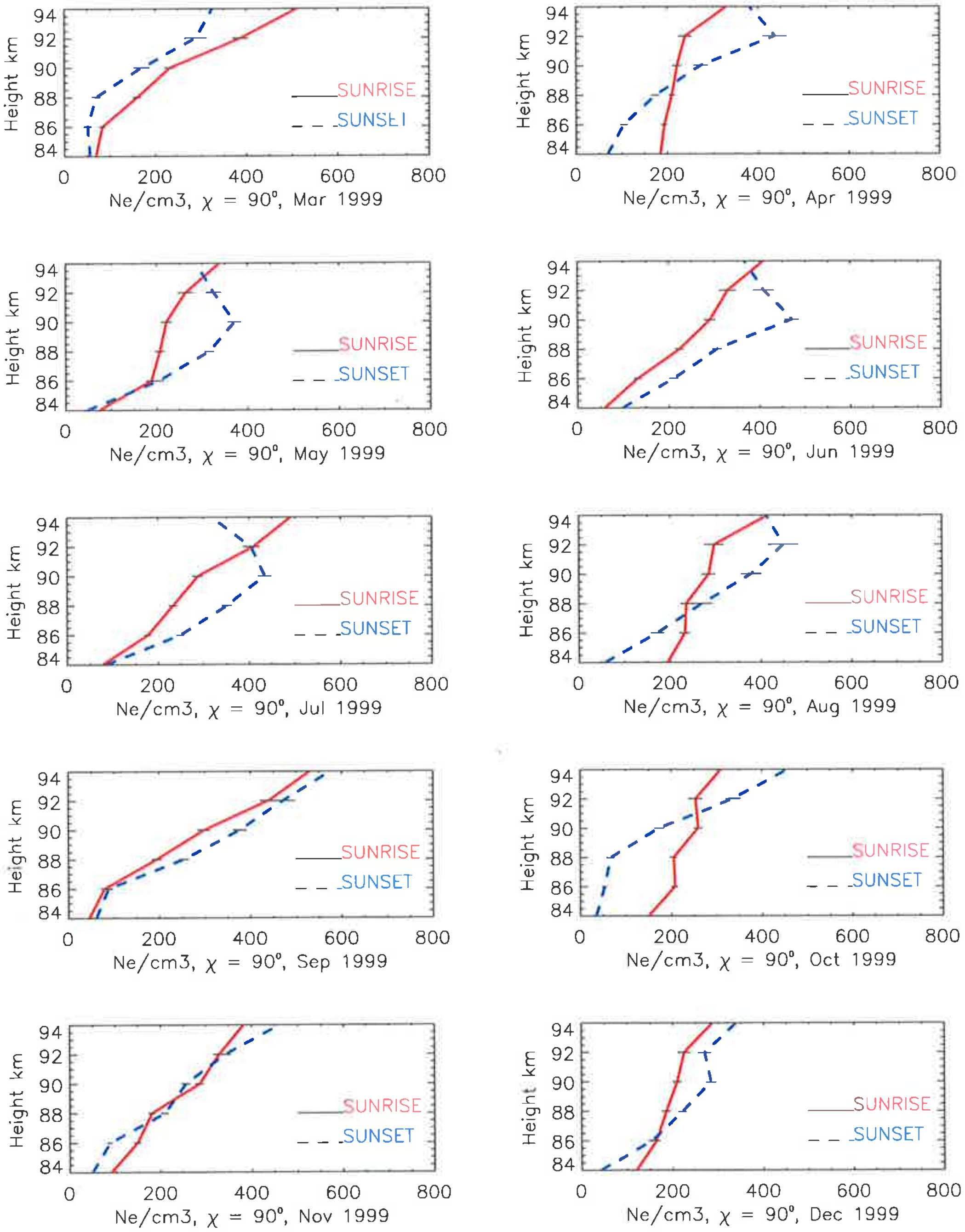

Figure 5.14: As for Figure 5.10, but for 1999

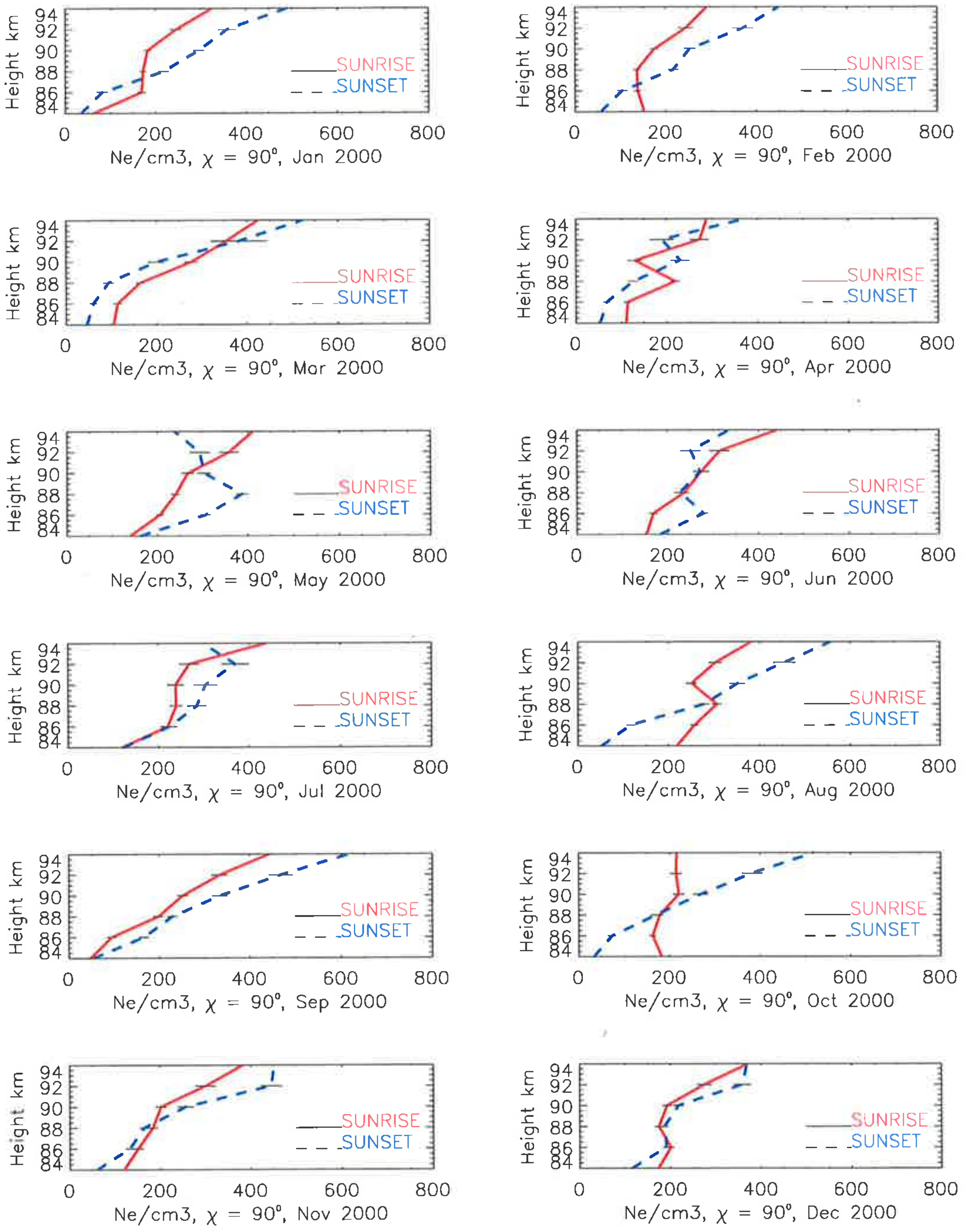

Figure 5.15: As for Figure 5.10, but for 2000

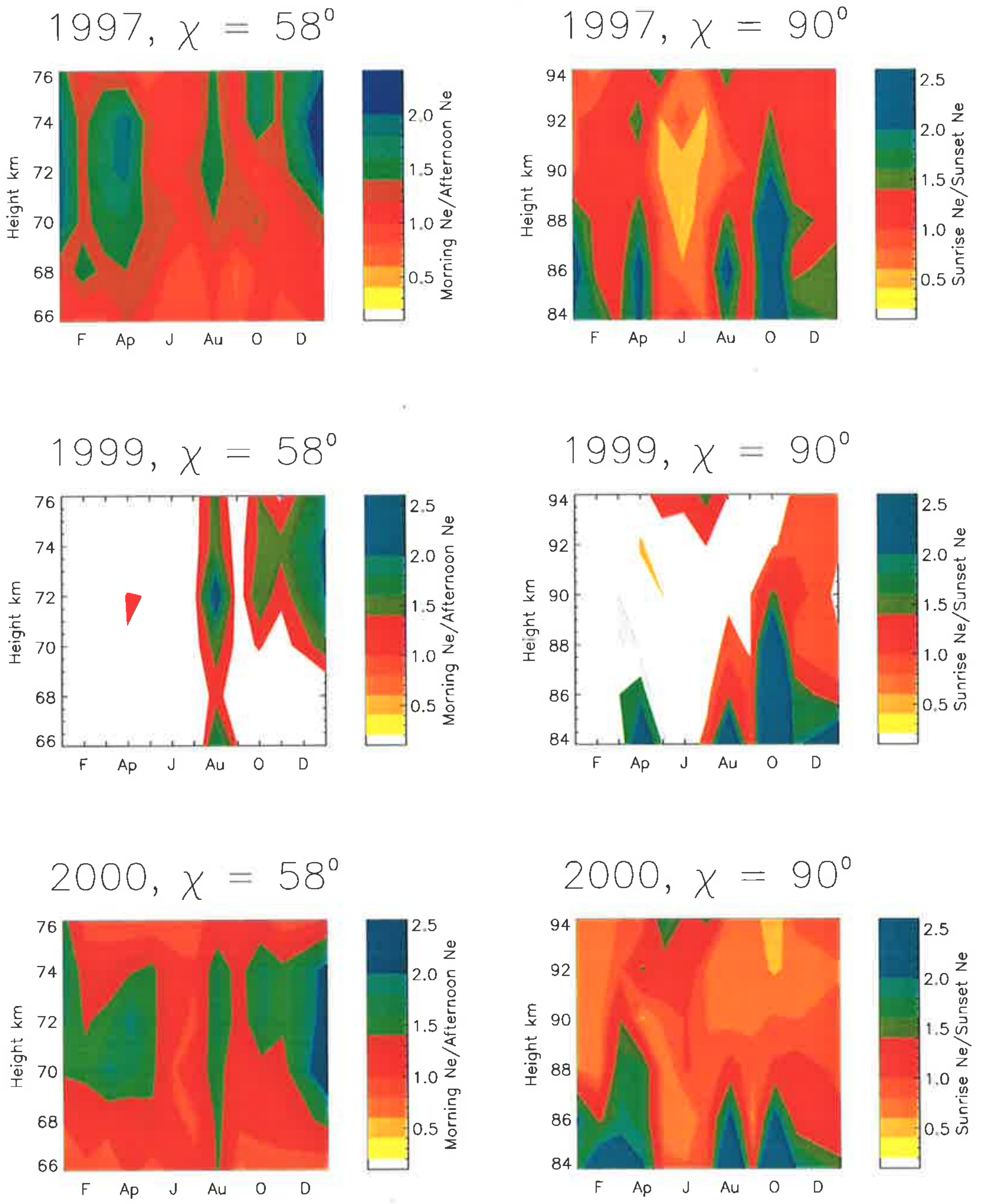

Figure 5.16: Observed asymmetry in each month at $\chi = 58°$ (66 - 76 km) and at $\chi = 90°$ (84 - 94 km).

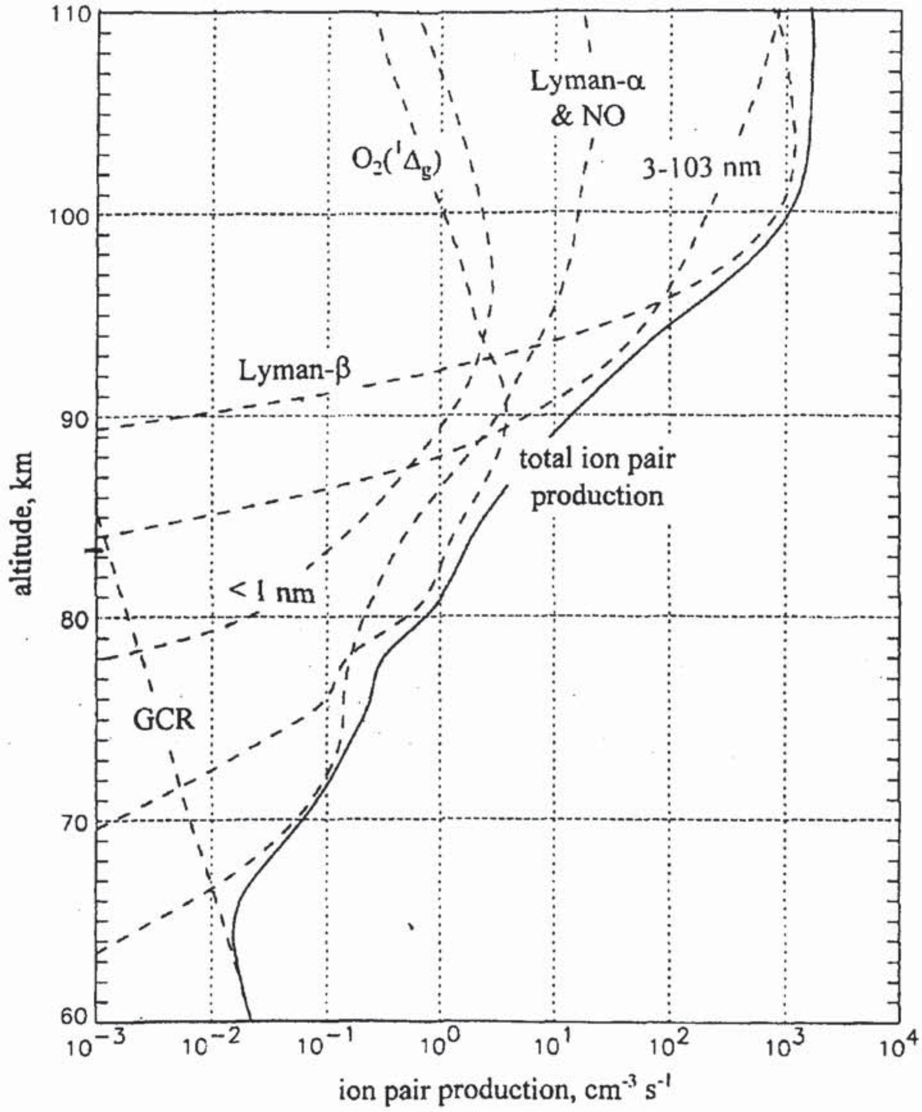

Figure 5.17: Ionization processes at the equator for low solar activity conditions ($F_{10.7} = 75Jy$), a solar zenith angle of 45° and the mean [NO] profile from HALOE. At this zenith angle the concentration of the trace constituents NO and $O_2(1\triangle_g)$ dominate between 66 and 88 km, whereas at other altitudes only the intensity of the ionizing flux and not the atmosphere's composition matters [After Friedrich et al. (1998)].

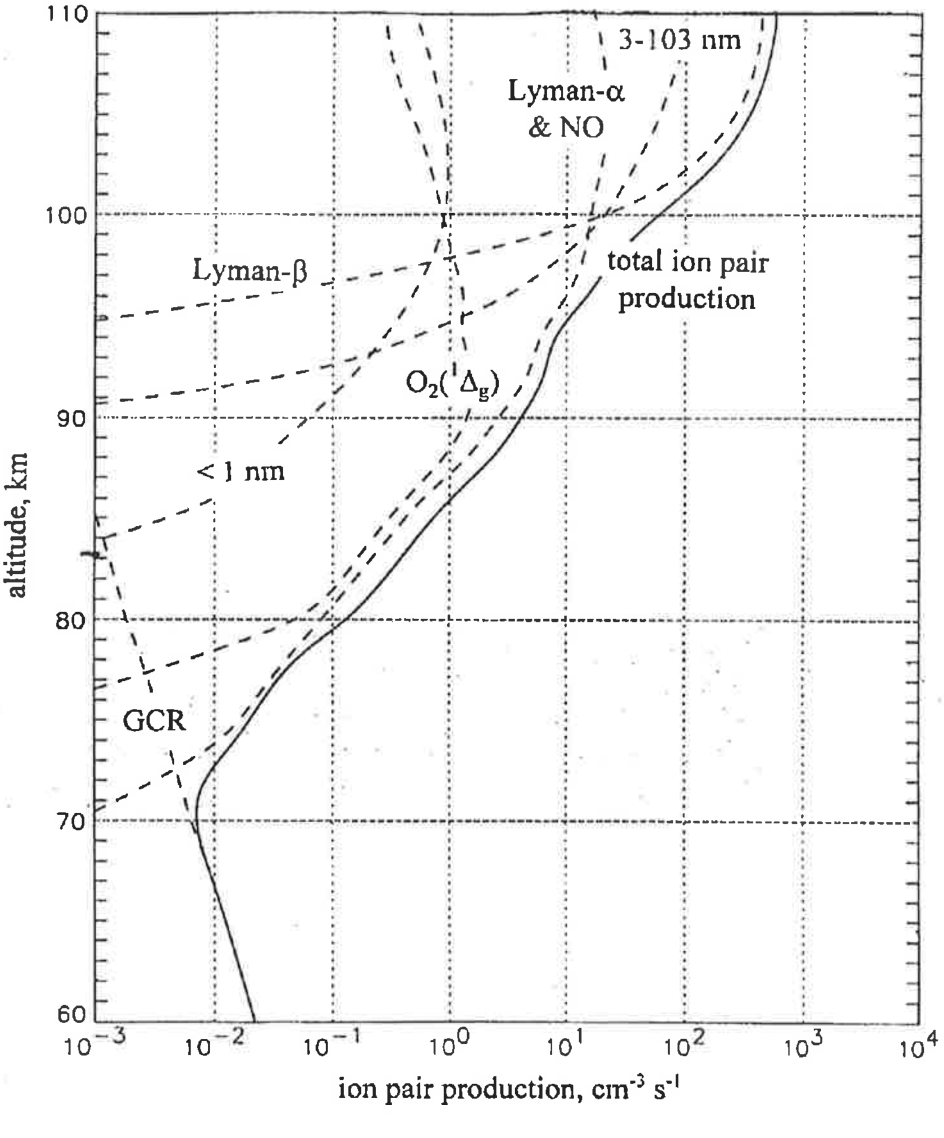

Figure 5.18: As per Figure 5.17 but for zenith angles of 75°

Table 5.1: Ratio of Morning to afternoon N_e at $\chi = 58°$ 1997.

Height	Jan	Feb	Mar	Apr	May	Jun	Jul	Aug	Sep	Oct	Nov	Dec
66 km	1.07	0.93	0.96	1.22	1.02	0.84	0.93	1.00	0.81	1.20	0.85	1.08
68 km	1.12	1.54	1.32	1.39	1.31	0.93	0.91	1.11	0.76	1.01	1.08	1.09
70 km	1.92	1.30	1.52	1.57	1.35	1.27	1.05	1.40	1.23	1.41	1.04	1.33
72 km	1.94	1.28	1.75	1.86	1.19	1.08	1.29	1.56	1.24	0.95	1.20	2.11
74 km	1.84	1.29	1.63	1.97	1.27	1.03	1.01	1.53	1.04	1.69	1.32	2.40
76 km	1.57	1.06	1.26	1.09	0.81	1.05	1.06	1.47	1.05	1.71	1.34	1.95

Table 5.2: Ratio of Morning to afternoon N_e at $\chi = 58°$ 1999.

Height	Jan	Feb	Mar	Apr	May	Jun	Jul	Aug	Sep	Oct	Nov	Dec
66 km	-	-	0.85	1.00	1.18	0.87	0.72	1.88	1.187	0.86	1.016	1.00
68 km	-	-	0.96	1.04	0.87	1.06	1.04	1.27	1.04	1.03	1.15	0.91
70 km	-	-	1.35	1.22	1.38	1.02	1.09	1.50	1.12	1.21	1.09	1.52
72 km	-	-	1.65	1.16	1.22	1.06	1.06	2.34	1.03	1.60	1.24	2.00
74 km	-	-	1.73	1.69	1.20	1.02	1.09	1.51	1.08	1.42	1.47	2.08
76 km	-	-	1.58	1.36	1.22	1.03	1.07	1.49	0.96	1.4	1.15	1.84

Table 5.3: Ratio of Morning to afternoon N_e at $\chi = 58°$, 2000.

Height	Jan	Feb	Mar	Apr	May	Jun	Jul	Aug	Sep	Oct	Nov	Dec
66 km	0.85	0.93	0.80	1.11	0.85	1.08	1.02	1.43	0.72	0.97	0.92	0.72
68 km	1.01	1.19	1.10	1.16	1.34	1.01	0.97	1.47	1.07	1.01	1.11	1.52
70 km	1.45	1.47	1.86	1.67	1.47	0.97	1.22	1.57	0.98	1.28	1.26	2.52
72 km	1.64	1.36	1.50	1.92	1.47	1.10	0.93	1.72	1.22	1.68	1.46	2.18
74 km	1.76	1.22	1.19	1.34	1.49	1.04	1.02	1.63	1.24	1.73	1.48	2.13
76 km	1.53	0.85	0.84	0.77	0.79	0.93	0.90	1.12	0.97	1.11	0.81	1.00

Table 5.4: Ratio of Sunrise to Sunset N_e at $\chi = 90°$, 1997.

Height	Jan	Feb	Mar	Apr	May	Jun	Jul	Aug	Sep	Oct	Nov	Dec
84 km	1.96	1.77	1.28	2.14	0.91	1.12	0.76	1.63	1.07	2.67	1.8	1.54
86 km	2.35	1.32	1.05	2.28	0.82	0.64	0.77	2.41	0.91	2.65	1.28	1.57
88 km	1.78	1.30	0.99	1.67	0.82	0.38	0.81	1.54	1.02	3.92	1.55	1.24
90 km	0.91	1.25	1.26	1.15	0.54	0.42	0.65	0.80	1.02	1.91	1.10	1.02
92 km	0.95	1.09	1.09	1.64	0.56	0.92	0.49	1.11	1.07	1.44	1.08	0.99
94 km	0.95	0.68	1.02	1.04	1.86	0.62	0.89	1.58	1.08	1.26	1.19	1.37

Table 5.5: Ratio of Sunrise to Sunset N_e at $\chi = 90°$, 1999.

Height	Jan	Feb	Mar	Apr	May	Jun	Jul	Aug	Sep	Oct	Nov	Dec
84 km	-	-	1.23	2.68	1.57	0.59	0.90	3.38	0.74	4.31	1.81	2.85
86 km	-	-	1.59	1.82	0.91	0.62	0.71	1.34	0.90	3.90	1.68	1.05
88 km	-	-	2.26	1.20	0.65	0.72	0.66	0.87	0.76	3.08	0.85	0.84
90 km	-	-	1.36	0.81	0.59	0.61	0.66	0.74	0.79	1.48	1.11	0.73
92 km	-	-	1.33	0.54	0.81	0.80	1.01	0.65	0.93	0.75	0.96	0.83
94 km	-	-	1.56	0.86	1.17	1.11	1.53	1.01	0.92	0.67	0.82	0.84

Table 5.6: Ratio of Sunrise to Sunset N_e at $\chi = 90°$, 2000.

Height	Jan	Feb	Mar	Apr	May	Jun	Jul	Aug	Sep	Oct	Nov	Dec
84 km	1.76	2.66	2.27	2.05	0.86	0.83	0.97	4.15	0.87	5.38	1.99	1.50
86 km	2.03	1.31	1.87	1.65	0.66	0.60	0.98	2.20	0.57	2.20	1.13	1.05
88 km	0.79	0.62	1.72	1.72	0.62	1.04	0.83	1.10	0.86	1.04	1.11	0.93
90 km	0.61	0.69	1.38	0.56	0.88	1.00	0.78	0.71	0.75	0.81	0.78	0.88
92 km	0.68	0.65	0.92	1.43	1.21	1.25	0.72	0.66	0.71	0.56	0.67	0.76
94 km	0.66	0.64	0.81	0.77	1.72	1.31	1.48	0.68	0.71	0.41	0.84	1.01

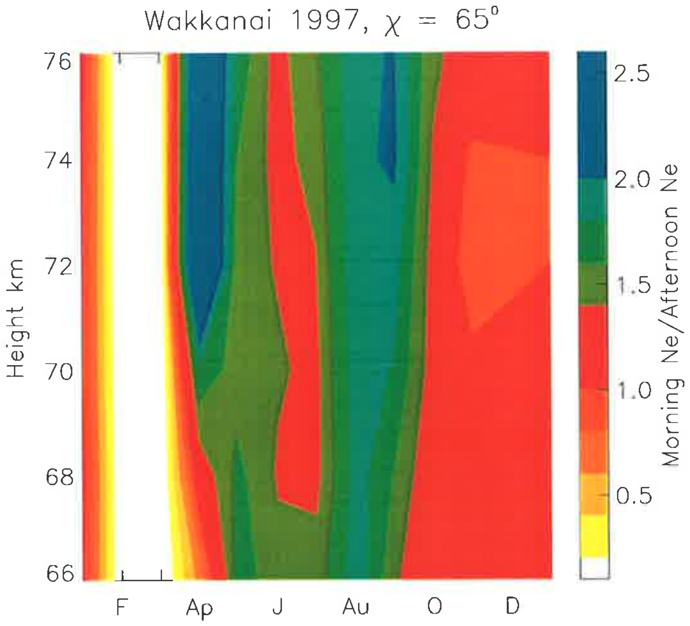

Figure 5.19: As for Figure 5.16, but for Wakkanai 1997

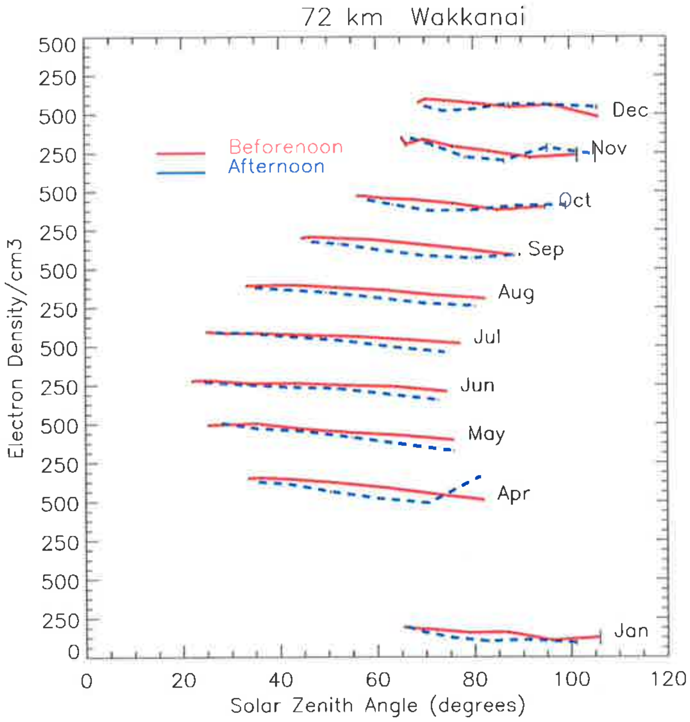

Figure 5.20: As for Figure 5.1, but for Wakkanai 1997

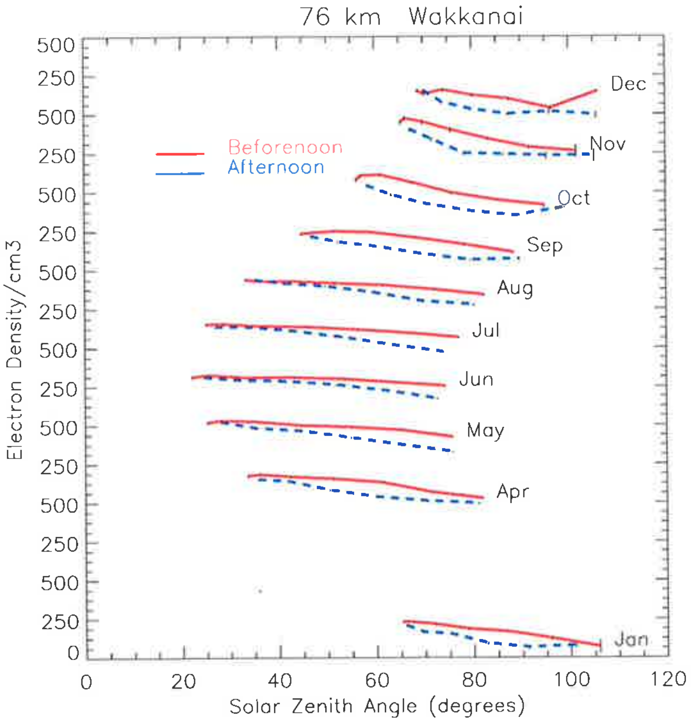

Figure 5.21: As for Figure 5.1, but for Wakkanai 1997

values are larger than afternoon values.

5.2.2 Signatures of tidal influence - Temperature effects

Firstly, temperature and density tidal oscillations are considered. Lower (higher) temperatures enhance (inhibit) the formation of clusters and inhibit (enhance) their thermal breakup, thus reducing (increasing) the electron concentration, since the recombination coefficients of cluster ions increase with cluster size and are all large in comparison with that of NO^+ (Forbes, 1981).

Based on Forbes (1981) studies, further investigations are carried out here using Adelaide MF radar data. Temperatures at 86 km and 72 km under equinox conditions (March) at 35° latitude are plotted versus local time (Figure 5.22 and 5.23) using data from the Global Scale Wave Model (GSWM) (Hagan et al., 1999). These temperatures are derived from the GSWM after using the Adelaide tidal winds to "calibrate" the amplitudes and phases of GSWM results.

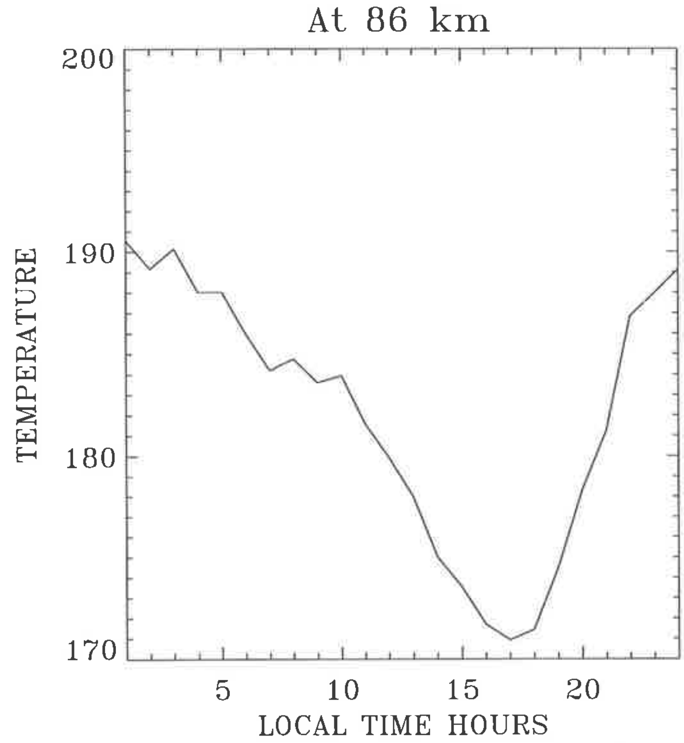

Figure 5.22: Neutral temperature versus local solar time at 86 km and 35°S latitude under equinox(March) conditions, using the GSWM model data

The temperature variation at 86 km, which represents a superposition of diurnal and semi-diurnal components, exhibits a minimum of 171°K at about 1600 LST and a maximum of about 185°K in the early morning hours. For this particular case the diurnal and semi-diurnal components add to give a peak to peak variation of 15°K. Similar values were presented in the study of Forbes (1981), except that in his study the afternoon temperatures were larger than morning temperatures, hence changing the sense of asymmetry. As an effect of variations in ambient temperature, changes in the effective recombination coefficient (α_{eff}) might take place. This change is estimated, assuming NO^+ as the precursor ion, from the following equation (Weller and Biondi, 1968), where T is the neutral temperature.

$$\alpha = 4.1 \times 10^{-7} \times (\frac{300}{T})^{1.5} \tag{5.1}$$

The higher morning temperatures enhance the thermal breakup of cluster ions,

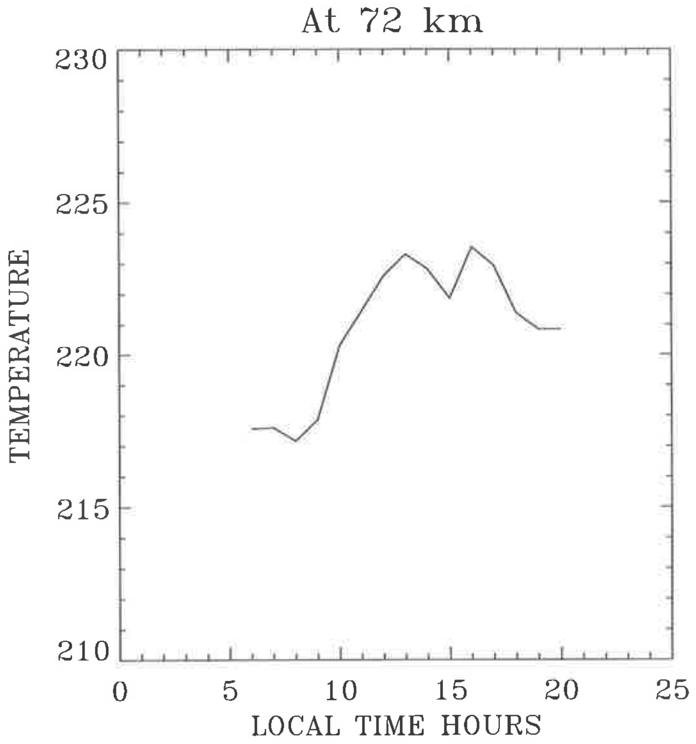

Figure 5.23: As for Figure 5.22, but for 72 km

which increases the relative abundance of NO^+ and reduces the effective recombination coefficient to roughly $\alpha_{mor} = 0.848 \times 10^{-6} cm^{-3} s^{-1}$ at 0900 hours (with 185K temperature and using equation 5.1) as compared to a post-noon value of $\alpha_{aft} = 0.955 \times 10^{-6} cm^{-3} s^{-1}$ at 1600 hours (with temperature 171K). Thus the ratio of electron densities at 0900 to 1600 LST is of order $(\alpha_{aft}/\alpha_{mor})^{1/2} = 1.06$.

At 72 km, no pronounced oscillations (either diurnal or semi-diurnal) were observed in the neutral temperatures, which makes it difficult to explain the asymmetry in terms of temperature differences at this altitude range for our location. However, it is possible that, the asymmetry at lower altitudes can be due to electron density advection from upper mesosphere. Also, from the above calculations, it can be concluded that, the diurnal asymmetry due to the effect of change of electron loss rate caused by diurnal asymmetric neutral temperatures is very less. Hence, the possibility of the asymmetry due to other phenomena such as advection is investigated in the following section.

Since the tidal oscillations of temperature vary with latitude and height, the asymmetric behavior of electron concentrations in the $D-$region would be expected to have a dependence on latitude as well. It was pointed out by Forbes (1981) that the electron concentration at 79 km plotted versus local time for 0°, 30°, and 60° latitude showed that the electron concentrations at 0° are enhanced in the morning hours, whereas the reverse is true at 30° and 60°. This behavior, which is simply a consequence of the change in sign of the Hough mode functions which describe the temperature oscillation, is consistent with our observations and as well as the observations of Coyne and Belrose (1972) and Thrane et al. (1968).

5.2.3 Signatures of tidal influence - Advection effects

In this section, partial reflection wind data at Adelaide are analyzed to investigate qualitatively and quantitatively the effect of winds, including the effects of transport due to vertical wind of diurnal tide. Diurnal tidal components are deduced using harmonic fits of the horizontal wind components as shown in the Figures 5.24.

The ionospheric electron density profiles revealed signatures of both the solar zenith angle control and the effects of tidal variations in the asymmetry. As shown in the Figure 5.16, the asymmetry at $\chi = 58°$ and 90° revealed that it is maximum during April, August and all through the summer months at 64 - 74 km. However, in the 84 - 94 km range, the largest asymmetry is in October and April (Figures 5.4 to 5.6). Qualitatively, this asymmetry is consistent with the seasonal variation of diurnal tidal amplitudes as shown in Figures 5.24. Accordingly, at Adelaide, maximum amplitudes are attained in March and subsidiary maxima are observed in July/August and October (Vincent et al., 1998). The seasonal variation of asymmetry in electron density in the altitude range of 84 – 94 km also supports a tidal explanation for the anomaly in HALOE low-latitude NO density. However, in the altitude range of 66-76 km, apart from equinoctial asymmetry, there is asymmetry during summer months, which points to the need for other explanations.

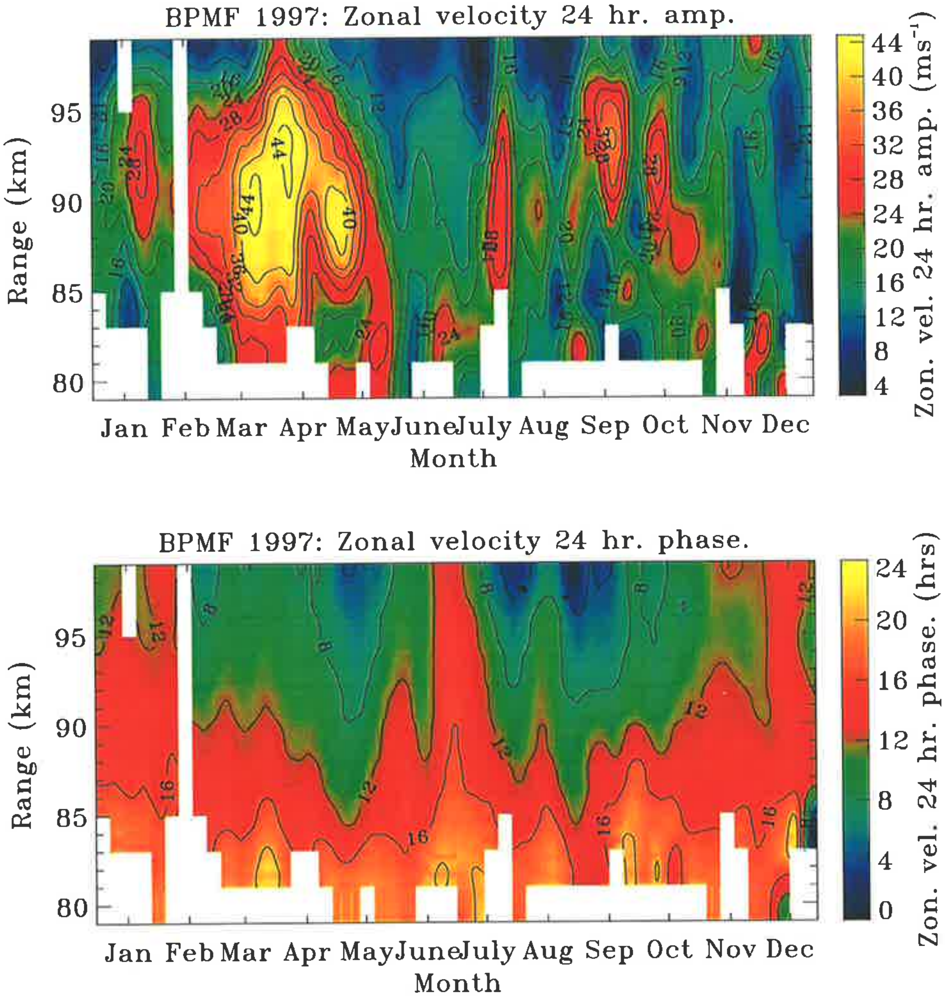

Figure 5.24: Tidal components of diurnal tide using harmonic fits for 1997

Next, the perturbation induced by vertical advection of the diurnal tide is considered for a quantitative analysis. The distribution of electrons, or the dissociation products (such as NO), formed by solar radiation are likely to be affected by vertical motions. After having been produced they may disappear by chemical or ionic reactions, or they may be transported to other heights, so that the shape of the final distribution may differ considerably from that of the simple production layer.

Since NO is thought to be the prime constituent influencing the electron concentration in $D-$region, this minor constituent is considered for investigating the tidal effects on electron densities using information on tides obtained at Adelaide. NO will

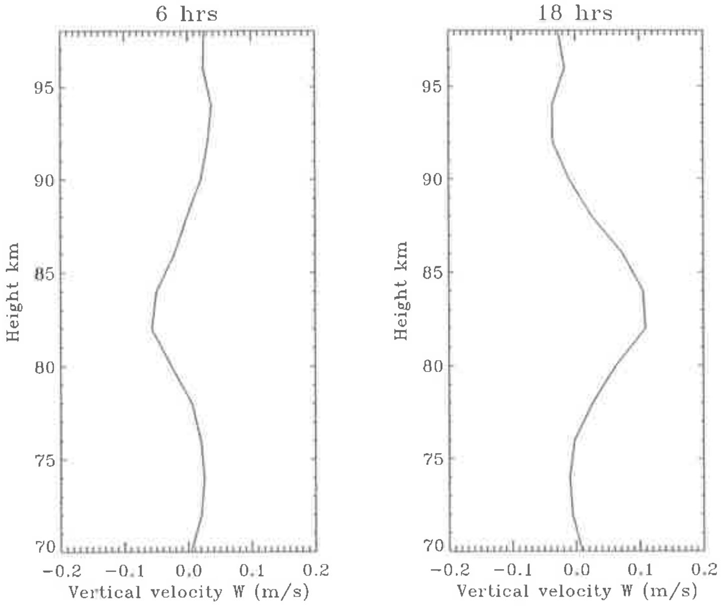

Figure 5.25: GSWM diurnal tide vertical winds (m/s) at 0600 hrs local time and 1800 hrs local time at 35°S

be affected by tidal motions if the dynamical lifetime is less than or equal to the chemical lifetime. For much of MLT the chemical lifetime for NO exceeds the dynamical lifetime, and so tides will affect the distribution of NO (Marsh et al., 2000), and hence the electron densities as well. It is expected that a downwelling wind will advect air richer in nitric oxide into regions that have relatively smaller NO.

A dynamical lifetime for vertical advection due to the diurnal tide can be defined as :$\tau_w = \frac{H}{\bar{W}}$, where H is the (neutral) scale height, and $\bar{W}$ is the mean magnitude of the vertical velocity over half the diurnal cycle. Estimates of $\bar{W}$ are taken from the Global Scale Wave Model (GSWM) (Hagan et al., 1999) using the Adelaide horizontal winds to calibrate the amplitudes and phases.

Figure 5.25 show vertical wind fields of diurnal tide calculated by GSWM at two local times for southern hemisphere fall equinox conditions. Using these vertical velocities, and assuming drift equilibrium, an estimate of the magnitude of the tidal NO perturbation can be made by considering the vertical advective term in the continuity equation written in terms of concentration (n) as given below.

$$\frac{dn}{dt} = -W\frac{dn}{dz} = \frac{Wn}{H} \tag{5.2}$$

The SR to SS (morning to afternoon) ratio is then simply $e^{\frac{\triangle t\bar{W}}{H}}$, where $\triangle t$ and $\bar{W}$ are elapsed time and mean vertical wind between maximum (1800 or 1900 LST) and minimum (0600 LST) amplitudes respectively. The following calculations carried out for Adelaide vertical wind variations show that tidally-induced variations are comparable to those observed, and it is likely that the dominant perturbing mechanism is direct tidal advection.

Example of the magnitude of the tidally-induced variations at 84 km are given below. The maximum amplitude reached at 1800 LST is 0.105 ms^{-1}. The magnitude of minimum amplitude reached at 0600 LST is -0.0496 ms^{-1}. Therefore $\triangle t$ = 12hrs, mean vertical amplitude between these hours is 0.16 ms^{-1}. Hence the ratio of NO (pointing to electron density ratio) between 0600 and 1800 using Equation 5.2 is found to be 2.37 (neutral scale height H is taken as 8 km).

The observed asymmetry in N_e for the 2000 March at 84 km is between 2.27, which is in good agreement with the theoretical ratio calculated above. Also it can be seen that the wind direction reverses around this altitude (82-84 km). However, a word of caution is that the statistical significance of electron density data below 85 km can be very less. In conclusion comparison of tidally induced variation due to neutral temperature oscillations and vertical advection indicate that, it is likely that the dominant perturbing mechanism is direct tidal advection.

There are number of other mechanisms which could produce diurnal variations in temperature and even constituents. Walterscheid (1998) has shown theoretically that gravity waves may induce accelerations of mean flows and also the diurnal wind amplitude. Such a process could affect temperatures and also NO at our location in the presence of horizontal gradients of that constituent. Finally, there is the possibility of production of heat by photochemical reactions, particularly due to the recombination of oxygen atoms (Torkar et al., 1998) at higher altitudes (above 90km).

5.3 Conclusions

An asymmetry in the diurnal variation of electron density N_e has been observed at Adelaide. The asymmetry is larger in summer than in winter and mostly morning electron densities are larger than the corresponding afternoon values in the range of 66-76 km. These findings match with the findings reported earlier (Lastovicka, 2001; Lastovicka, 1977). At higher altitudes $80 - 100$ km region (nighttime), sunrise values are larger than sunset values and the asymmetry is largest during equinoctial months indicating the correlation with diurnal wind variations. Comparison of asymmetry in different years revealed very little inter-annual variations.

The sense of the asymmetry changes according to the time of the day, season and altitude region. The magnitude of the asymmetry observed in each month is different and generally the observed asymmetry is around 2.5 consistent with the study of Siskind et al. (1998). Comparisons with Wakkanai(45°N) revealed that, both at Adelaide and Wakkanai morning electron density values are larger than afternoon values.

An explanation of this asymmetry is given in terms of diurnal asymmetry in the variation of NO which was reported to be consistent with a perturbation induced by the migrating diurnal tide (Marsh et al., 2000). Also, effect of temperature and density tidal oscillations are considered, affecting the electron density rearrangement. In particular, the ratio of prenoon to postnoon recombination coefficient due to temperature oscillations (α_1/α_2) is found to be around 1.06, in comparison to the N_{SR}/N_{SS} ratio due to diurnal tidal wind variations of 2.37. This indicates that the dominant perturbing mechanism is direct tidal advection.

Chapter 6

Summary

This thesis has concentrated on the study of structure and formation of lower ionospheric ionization ($D-$region in particular) by means of improved MF radar electron density observations at Adelaide. Summary of important objectives achieved are as follows.

In Chapter 2, the key finding was that the collision frequencies derived using the DAE method were found to be in good agreement with the latest laboratory measurements of the momentum transfer collision frequencies (Robertson et al., 1997). Adoption of this latest laboratory collision frequency profile resulted in a change in magnitude of computed electron densities compared to the use of old standard collision frequencies. The electron density in 66 - 76 km range was increased by a factor of 1.5 to 1.7 and above 80 km the electron density was reduced by a factor of 2.

In Chapter 3, data from daytime radar observations are used to study mid-latitude $D-$region characteristics. The basic characteristics, such as dominant influence of solar control in determining the seasonal and diurnal variation of electron densities were established. The observed diurnal asymmetry led to further investigations as this asymmetry was found to be in line with recently reported NO sunrise sunset asymmetry. Also, at noon and at constant solar zenith angle, mean electron densities were found to be enhanced in autumn months and reduced in spring months in contrast to the predicted behaviour of a static atmosphere. These departures are thought to be due to the influence of dynamic atmosphere on electron density variation.

Comparisons of diurnal and seasonal variation of observed electron densities with the theoretical values from FIRI and IRI models are found to be in good agreement. Comparison of back calculated radio wave absorption due to these model profiles with our measurements established the fact that, as the electron density increases wave absorption increases. Inter hemispheric latitudinal dependencies of the electron densities from IRI model are compared with the observed electron densities at 35°S (Adelaide) and 45°N (Wakkanai). Increase in electron density towards the summer hemisphere was noted.

One of the important consequences of improved MF radar is the measurements of nighttime electron densities in the height range of 80-100 km. Although, some uncertainties exists in the assumption of collision frequencies and hence estimated electron densities, these data were very useful in studying the general characteristics as detailed in Chapter 4. Different mechanisms required to maintain the night $D-$region ionization and structure are investigated. It was pointed out that the intensities of nighttime ultraviolet radiation from the geocorona and extraterrestrial should be able to produce the electron densities in the region of our interest.

Average recombination rates were estimated and these estimated values compared well with the earlier studies. Diurnal variation of electron density generally exhibited decay after sunset. A comparison of seasonal variation of these nighttime electron densities at Adelaide with that of IRI, FIRI and HALOE NO densities showed several common features between them. One such common feature is an increase of N_e values in winter than in summer. Similarly, vertical profiles exhibited the same structure.

Investigations of solar activity effects suggested that, above 80 km although the electron density increases with SS, strong influences of seasonal variations appear to persist. Similarly, daytime observations of electron densities on flare days revealed increase in the electron concentration.

In Chapter 5, observed asymmetry in the diurnal variation of electron density N_e was considered and the reasons for the same were investigated. In 66-76 km altitude range, the observed asymmetry is found to be larger in summer than in winter and mostly morning electron densities are larger than the corresponding afternoon values, coinciding with the findings of Lastovicka (2001). Observed asymmetry above 80 km was found to be in agreement with the asymmetry in NO densities reported by Friedrich et al. (1998), except that the sense of asymmetry is in the opposite direction.

Asymmetry observed in each month was on an average around 2.5 consistent with the study of Siskind et al. (1998) (suggesting the asymmetry found in NO densities is largest at the equator, i.e., in excess of one order of magnitude, compared to less than a factor of two at 57° latitude). Comparisons with electron density estimates for Wakkanai(45°N) revealed that, both at Adelaide and Wakkanai morning electron density values are larger than afternoon values. An explanation of this asymmetry is given in terms of diurnal asymmetry in the variation of NO which was reported to be consistent with a perturbation induced by the migrating diurnal tide (Marsh et al., 2000). Comparison of the calculated tidally induced variations due to temperature and advection indicated that, the dominant perturbing mechanism is direct tidal advection.

In summary, the thesis work has endeavoured to understand the lower ionospheric ionization with help of estimated electron densities from MF radar sited at Adelaide. This work supports the fact that NO densities play a major role in the formation of lower ionospheric ionization and complements the efforts in forming the NO climatology with the use of global measurements of nitric oxide in the Earth's upper atmosphere by satellite experiments. Comparisons of theoretical model results such as IRI and FIRI with our observations demonstrated the fact that, long records of radar observations in future can contribute in evaluating the reliability of different techniques and models of ionospheric $D-$region.

Common features observed between nighttime observations due to our MF radar and IRI, FIRI results and HALOE NO densities encourages the fact that with further improvements both in radar measurements and model calculations, it is possible to facilitate enhanced understanding of the nighttime $D-$region. Since the region of these nighttime observations coincides with mesospheric dynamic regime, the results can be of use in evaluating models such as TIME-GCM. Investigations for the cause of diurnal and seasonal asymmetry observed, demonstrated the effect of planetary waves on the electron density rearrangement. The observational results are consistent with the theoretical studies indicating that the Ly-α radiation has the strongest influence in the formation of both daytime and nighttime $D-$region. In other words, again the NO plays a major role in the formation and maintenance of lower ionospheric ionization.

6.1 Future Research

As reported by Friedrich et al. (1998), the nitric oxide densities obtained by the HALOE instrument aboard the UARS present a unique set of measurements which can practically only be checked against the results of theoretical models or, indirectly, by comparison to ionospheric data. More measurements from MF radar on a continuous basis will get invaluable insights into the dynamical coupling of the atmosphere. Further work on the nighttime measurements including accurate estimation of collision frequencies above 80 km will be very useful in understanding the aeronomy of nighttime ionization. The ongoing measurements creating long data bases can be useful in investigating the periodicity and solar cycle changes with higher statistical significance.

The study of diurnal asymmetry was carried out due to tidal perturbations in the present work, however, influence of gravity waves on electron density rearrangement will be a very useful study. Further work can be aimed at correlative data analysis from identical DAE implementations at several locations such as Wakkanai and Yamagawa in Japan, the Poker Flat MF radar in Alaska (Igarashi et al., 1999), and Andesnes MF radar in Norway providing measurements on a network basis, to formulate climatology of $D-$region ionization.

Appendix A

Collision frequencies in the D–region

This is a reprint of the paper,

R. Vuthaluru, R. A. Vincent, D. A. Holdsworth, I. M. Reid (2002), 'Collision frequencies in the D–region', *Journal of Atmospheric and Solar Terrestrial Physics* **64**, 2043–2054.

Vuthaluru, R., Vincent, R.A., Holdsworth, D.A., and Reid, I.M., (2002) Collision frequencies in the D-region.
Journal of Atmospheric and Solar-Terrestrial Physics, v. 64 (18), pp. 2043-2054.

http://dx.doi.org/10.1016/S1364-6826(02)00220-1

Appendix B

Differential absorption measurements

This is a reprint of the paper,

D. A. Holdsworth, Rupa Vuthaluru, I. M. Reid, R. A. Vincent (2002), 'Differential absorption measurements of mesospheric and lower thermospheric electron densities using the Buckland Park MF radar', *Journal of Atmospheric and Solar Terrestrial Physics* **64**, 2029–2042.

Holdsworth, D.A., Vuthaluru, R., Reid, I.M., and Vincent, R.A., (2002) Differential absorption measurements of mesospheric and lower thermospheric electron densities using the Buckland Park MF radar.
Journal of Atmospheric and Solar-Terrestrial Physics, v. 64 (18), pp. 2029-2042.

References

Aikin, A. C. (1972), 'Ionization sources of the ionospheric D and E regions', *Aeronomy report (University of Illinois)* **48**, 96–103.

Balsley, B. B. and Gage, K. S. (1980), 'The MST radar technique: Potential for middle atmospheric studies', *Pure and Applied Geophysics* **118**, 452–493.

Barth, C. A. (1966), 'Rocket measurements of nitric oxide in the upper atmosphere', *Planetary and Space Science* **14**, 623–630.

Barth, C. A., Tobiska, W. K. and Siskind, D. E. (1988), 'Solar-terrestrial coupling: Low-latitude thermospheric nitric oxide', *Geophysical Research Letters* **15**, 92–94.

Belrose, J. S. (1970), 'Radio wave probing of the ionosphere by the partial reflection of radio waves (from heights below 100 km)', *Journal of Atmospheric and Terrestrial Physics* **32**, 567–596.

Belrose, J. S. and Burke, M. J. (1964), 'Study of lower ionospere using paritial reflections, 1, Experimental technique and method of analysis', *Journal of Geophysical Research* **69**, 2799–1818.

Belrose, J. S., Burke, M. J. and Coyne, T. (1972), 'D-region measurements with the differential absorption, differential phase partial reflection experiments', *Journal of Geophysical Research* **77**(25), 4829–4838.

Bilitza, D. (1990), 'International Reference Ionosphere, 1990, National Space Science Data Center, Greenbelt Maryland', *Aeronomy report (University of Illinois)* **90**(22).

Bilitza, D. (1998), 'The E- and D- region in IRI', *Advances in Space Research* **21**(6), 871–874.

Briggs, B. H., Elford, W. G., Felgate, D. G., Golley, M. G., Rossiter, D. E. and Smith, J. W. (1969), 'Buckland Park aerial array', *Nature* **223**, 1321–1325.

Budden, K. G. (1985), *The propagation of radio waves*, Cambridge University Press.

Chakrabarty, D. K., Meek, C. E. and Manson, A. H. (1983), 'Asymetry in the diurnal variation of temperature and electron loss coefficient in the mesosphere', *Journal of Atmospheric and Terrestrial Physics* **45**, 309–314.

Cohen, D. J. and Ferraro, A. J. (1973), 'Modeling the D-region partial-reflection experiment', *Radio Science* **8**(5), 459–465.

Coyne, T. N. R. and Belrose, J. S. (1972), 'The diurnal and seasonal variation of electron densities in the midlatitiue D-region under quiet conditions', *Radio Science* **7**, 163–174.

Coyne, T. N. R. and Belrose, J. S. (1974), 'An investigation into the effects of limited height resolution in the differential-absorption paritial reflection experiment', *Journal of Geophysical Research* **78**(34), 8276–8288.

Danilov, A. D. (1989), 'General overview of the solar activity effects on the lower ionosphere', *Handbook for the Middle Atmosphere Program* **29**, 183–191.

Danilov, A. D. (1990), 'Achievements in the D-region studies during MAP', *Advances in Space Research* **10**, 133–149.

Danilov, A. D. (1998), 'Review of long-term trends in the upper mesosphere, thermosphere and ionosphere', *Advances in Space Research* **22**(6), 907–918.

Donahue, T. M. (1966), 'Ionospheric reaction rates in light of recent measurements in the ionosphere and the laboratory', *Planetary and Space Science* **14**, 33–48.

Ferguson, E. E., Fehsenfeld, F. C., Goldan, P. D., and Schmeltekopf, A. L. (1965), 'Positive ion-neutral rections in the ionosphere', *Journal of Geophysical Research* **70**, 4323–4329.

Fleming, E. L., Chandra, S., Barnett, J. J. and Corney, M. (1990), 'Zonal temperature,pressure,zonal wind and geophysical height as a function of latitude', *Advances in Space Research* **10**, 11–59.

Flood, W. A. (1968), 'Revised theory for partial reflection D-region measurements', *Journal of Geophysical Research* **73**(15), 5585–5598.

Forbes, J. M. (1981), 'Tidal effects on D and E region ion chemistries', *Journal of Geophysical Research* **60**(A3), 1551–1563.

Friedrich, M., Syskind, D. E. and Torkar, K. M. (1998), 'HALOE nitric oxide measurements in view of ionospheric data', *Journal of Atmospheric and Terrestrial Physics* **60**, 1445–1457.

Friedrich, M. and Torkar, K. M. (2001), 'FIRI: a semiempirical model of the lower ionosphere', *Journal of Geophysical Research* **106**, 21409–21418.

Gage, K. S. and Balsley, B. B. (1984), 'MST radar studies of wind and turbulence in the middle atmosphere', *Journal of Atmospheric and Terrestrial Physics* **46**, 739–753.

Geisler, J. E. and Dickinson, R. E. (1968), 'Vertical motions and nitric oxide in the upper mesosphere', *Journal of Atmospheric and Terrestrial Physics* **30**, 1501–1521.

Gledhill, J. A. (1986), 'The effective recombination coefficient of electrons in the ionosphere between 50 and 150 km', *Radio Science* **21**(3), 399–408.

Gough, M. P. (1975), 'On the U. V. source of nighttime E region', *Planetary and Space Science* **23**, 1236–1237.

Gregory, J. B., , and Manson, A. H. (1967), 'Mesospheric electron number densities at 35 degree latitude', *Journal of Geophysical Research* **72**(3), 1073–1080.

Gregory, J. B., , and Manson, A. H. (1969), 'Seasonal variation of electron densities below 100 km at mid-latitudes - II, Electron densities and atmospheric circulation', *Journal of Atmospheric and Terrestrial Physics* **31**, 703–729.

Hagan, M. E., Burrage, M. D., Forbes, J. M., Hackney, J., Randel, W. J. and Zhang, X. (1999), 'GSWM-98 results for Migrating Solar Tides', *Journal of Geophysical Research* **104**, 6813–6827.

Harris, R. D. and Tohmatsu, T. (1972), 'A nighttime ionospheric E-region model', *Aeronomy report (University of Illinois)* **48**, 199–210.

Hines, C. O. (1965), *Physics of the earth's upper atmosphere*, Englewood Cliffs, N. J.. : Prentice-Hall.

Holdsworth, D. A. and Reid, I. M. (2003), 'The Buckland park MF radar, Submitted for Publication', *Radio Science* pp. –.

Holdsworth, D. A., Vuthaluru, R., Reid, I. M. and Vincent, R. A. (2002), 'Differential absorption measurements of mesospheric and lower thermospheric electron densities using the buckland park MF radar', *Journal of Atmospheric and Solar Terrestrial Physics* **64**(18), 2029–2042.

Huang, X. and Reinisch, B. W. (1986), 'Vertical electron density profiles from the digisonde network', *Advances in Space Research* **18**(6), 121–129.

Igarashi, K., Murayama, Y., Nagayama, M. and Kawana, S. (1999), 'D-region electron density measurements by MF radar in the middle and high latitudes', *Advances in Space Research* **5**, 19–42.

JATP (1987), 'Special issue', *Journal of Atmospheric and Terrestrial Physics* **49**, 1–149.

Kelley, M. C. (1989), *The Earth's ionosphere*, Academic Press, Inc., San Diego, CA.

Lastovicka, J. (1977), 'Seasonal variation in the asymmetry of diurnal variation of absorption in the lower ionosphere.', *Journal of Atmospheric and Terrestrial Physics* **39**(8), 891–894.

Lastovicka, J. (2001), 'Nitric oxide densities and their diurnal asymmetry in the upper middle atmosphere as revealed by ionospheric measurements', *Journal of Atmospheric and Solar Terrestrial Physics* **63**, 21–28.

Manson, A. H. and Meek, C. E. (1984), 'Partial reflection D-region electron densities', *Handbook for the Middle Atmosphere Program* **13**, 113–123.

Manson, A. H. and Merry, M. W. J. (1970), 'Particle influx and the 'winter anomaly' in the mid-latitude (L = 2.5 - 3.5) lower ionosphere', *Journal of Atmospheric and Terrestrial Physics* **32**, 1169–1181.

Manson, A. H. and Merry, M. W. J. (1971), 'Sesonal variations of electron densities below 100 km at mid-latitudes-IV Preliminary model calculations', *Journal of Atmospheric and Terrestrial Physics* **33**, 413–428.

Marsh, D. R., and III, J. M. R. (2000), 'A tidal explanation for the sunrise/sunset anomaly in HALOE low-latitude nitric oxide observations', *Geophysical Research Letters* **27**(19), 3197–3200.

Mathews, J. D. (1986), 'Incoherent scatter radar probing of the 60-100km atmosphere and ionosphere', *Proceedings of the IEEE* **24**(5), 765–778.

McPeters, R. D. (1989), 'Climatology of nitric oxide in the upper stratosphere, mesosphere, and thermosphere : 1979 through 1986', *Journal of Geophysical Research* **94**(D3), 3461–3472.

Mechtly, E. A. (1974), 'Accuracy of rocket measurements of lower ionosphere electron concentrations', *Radio Science* **9**, 373–384.

Mechtly, E. A. and Bowhill, S. A. (1972), 'Changes of lower ionosphere electron concentrations with solar activity', *Journal of Atmospheric and Terrestrial Physics* **34**, 1899–1907.

Meek, C. E. and Manson, A. H. (1981), 'Use of full polarisation measurement in the partial reflection experiment', *Journal of Atmospheric and Terrestrial Physics* **43**(1), 1267–1274.

Meier, R. R. and Mange, P. (1973), 'Spatial and temporal variations of the lyman-alpha airglow and related atomic hydrogen distributions', *Planetary and Space Science* **21**, 309–327.

Mitra, A. P. and Ramanamurthy, Y. V. (1972), 'Ionization contribution by cosmic X-rays', *Aeronomy report (University of Illinois)* **48**, 120–126.

Mitra, A. P. and Rowe, J. N. (1972), 'D-region chemistry during solar flares', *Aeronomy report (University of Illinois)* **48**, 281–298.

Mitra, A. and Rowe, J. N. (1974), 'Ionospheric constraints of mesospheric nitric oxide', *Journal of Atmospheric and Terrestrial Physics* **36**, 1797–1808.

Monro, P. E., Nisbet, J. S. and Stick, T. L. (1976), 'Effect of tidal oscillations in the neutral atmoshphere on electron densities in the E-region', *Journal of Atmospheric and Terrestrial Physics* **38**, 523–528.

Montbriand, L. E. and Belrose, J. S. (1972), 'Ionization contribution by cosmic X-rays', *Aeronomy report (University of Illinois)* **48**, 290–297.

Narcisi, R. S. (1971), 'O_2^+ as a source of water cluster ions in the D region', *Aeronomy report (University of Illinois)* **48**, 182–186.

Narcisi, R. S., Philbrick, C. R., Bailey, A. D. and Della, L. (1969), 'Review of daytime, sunrise, and sunset ion composition of the D region, in Meteorological and Chemical Factors in D-region Aeronomy', *Aeronomy report (University of Illinois)* **32**, 355–363.

Neyaber, R. H., Marino, L. L., Rothe, E. W. and Trajillo, S. M. (1961), 'Low-energy electron scattering from atomic oxygen', *Phys. Rev* **123**, 148–152.

Nicolet, M. (1965), 'Nitrogen oxides in the chemosphere', *Journal of Geophysical Research* **70**(3), 679–685.

Nicolet, M. (1979), 'Photodissociation of nitric oxide in the mesosphere and stratosphere: Simple numerical relations for atmospheric model calculations', *Geophysical Research Letters* **6**(11), 866–868.

Nicolet, M. and Aiken, A. C. (1960), 'The formation of the D–region of the ionosphere', *Journal of Geophysical Research* **65**, 1469–1483.

Ogawa, T. and Tohmatsu, T. (1966), 'Photoelectric processes in the upper atmosphere, 2, the hydrogen and helium ultraviolet glow as an origin of the nighttime ionosphere', *Rep. Ionos. Space Res. Japan* **20**(4), 395–417.

Phelps, A. V. and Pack, J. L. (1959), 'Electron collision frequencies in nitrogen and in the lower ionosphere', *Phs. Rev. Letters* **3**, 340–342.

Piggott, W. R. and Thrane, E. V. (1966), 'The effect of irregularities in collision frequency on the amplitude of weak partial reflections', *Journal of Atmospheric and Terrestrial Physics* **28**, 311–314.

Poppoff, I. G. and Whitten, R. C. (1969), 'Ionospheric effect of X-rays from scorpius XR-1', *Nature* **224**, 1187–1188.

Potemra, T. A. and Zmuda, A. J. (1970), 'Precipitating energetic electrons as an ionization source in the mid-latitude nighttime D- region', *Journal of Geophysical Research* **75**, 7161–7167.

Ratcliffe, J. A. (1972), *An introduction to the ionosphere and magnetosphere*, Cambridge University Press.

Reid, I. M., Vandepeer, B. G. W., Dillon, S. C. and Fuller, B. M. (1995), 'The new Adelaide medium frequency Doppler radar', *Radio Science* **30**(4), 1177–1189.

Rishbeth, H. and Garriott, O. K. (1969), *Introduction to Ionospheric Physics*, Academic Press, New York.

Robertson, A. G., Elford, M., Cromption, R., Sun, M. A. W. and Trail, W. K. (1997), 'Rotational and vibrational excitation of nitrogen by electron impact', *Australian Journal of Physics* **50**, 441–472.

Schwentek, H. (1965), 'Regular and irregular behavior of the winter anomaly in ionospheric absorption', *Journal of Geophysical Research* **70**, 4323–4329.

Sechrist, C. F. (1967), 'A theory of the winter absorption anomaly at middle latitudes', *Journal of Atmospheric and Terrestrial Physics* **29**, 113–136.

Sen, H. K. and Wyller, A. A. (1960), 'On the generalization of the appleton-hartree magnetoionic formulas', *Journal of Geophysical Research* **65**, 3931–3953.

Siskind, D. E. (1994), 'On the radiative coupling between mesospheric and thermospheric nitric oxide', *Journal of Geophysical Research* **99**, 22757–22766.

Siskind, D. E., Bacmeister, J. T., Summers, M. E. and III, J. M. R. (1997), 'Two dimensional model calculations of nitric oxide transport in the middle atmosphere and comparison with Halogen Occultation Experiment data', *Journal of Geophysical Research* **102**(D3), 3527–3545.

Siskind, D. E., Barth, C. A. and Russell, J. M. (1998), 'A climatology of nitric oxide in the mesosphere and thermosphere', *Advances in Space Research* **21**(10), 1353–1362.

Siskind, D. E. and Russell, J. M. (1996), 'Coupling between middle and upper atmosheric NO: Constraints from HALOE observations', *Geophysical Research Letters* **23**(2), 137–140.

Solomon, S., Crutzen, P. J. and Roble, R. G. (1982), 'Photochemical coupling between the thermosphere and the lower atmosphere,1,Odd nitrogen from 50 to 120 km', *Journal of Geophysical Research* **87**, 7206–7220.

Strobel, D. F. (1971), 'Diurnal variation of nitric oxide in the upper atmosphere', *Journal of Geophysical Research* **76**(10), 2441–2452.

Strobel, D. F., Opal, C. B. and Meier, R. R. (1980), 'Photoionization rates in the nighttime E- and F- region ionosphere', *Planetary and Space Science* **28**, 1027–1033.

Strobel, D. F., Young, T. R., Meier, R. R., Coffey, T. P., and Ali, A. W. (1974), 'The nighttime ionosphere: E region and lower F region', *Journal of Geophysical Research* **79**(22), 3171–3177.

Swider, W. (1972), 'E-region model parameters', *Journal of Atmospheric and Terrestrial Physics* **34**, 1615–1621.

Swider, W. (1988), 'Electron loss and the determination of electron concentration in the D-region', *Pure and Applied Geophysics* **127**(2/3), 403–414.

Thrane, E. V., Haug, A., Bjell, B., Anastassiades, M. and Tsagakis, E. (1968), 'Measurements of D region electron densities during the international quiet sun years', *Journal of Atmospheric and Terrestrial Physics* **30**, 135–150.

Titheridge, J. E. (2001), 'Production of the low-latitude night E layer', *Journal of Geophysical Research* **106**(7), 12781–12786.

Tohmatsu, T. N. and Wakai, N. (1970), 'An investigation of nighttime ionising sources in low- and mid-latitudes', *Advances in Geophysics* **26**, 209–211.

Torkar, K. M., and Friedrich, M. (1998), 'Empirical electron recombination coefficients in the D- and E-region', *Journal of Atmospheric and Terrestrial Physics* **50**(8), 749–761.

Torkar, K. M. and Friedrich, M. (1983), 'Tests of an ion-chemical model of the D- and the E-region', *Journal of Atmospheric and Terrestrial Physics* **45**(6), 369–385.

Vandepeer, B. G. W. and Reid, I. M. (1995), 'On the spaced antenna and Imaging Doppler Interferometer techniques', *Radio Science* . Accepted, 1995.

Vanina, L. B., Kokin, G. A. and Kniazev, A. K. (1995), 'Electron concentration and meteorological parameter vriations in the ionospheric D region at molodezhnaia station during the proton events in october 1989', *Geomagnetism and Aeronomy* **35**(4), 137–140.

Vincent, R. A. (1984), 'Gravity-wave motions in the mesosphere', *Journal of Atmospheric and Terrestrial Physics* **46**, 119–128.

Vincent, R. A., Kovalam, S., Fritts, D. C. and Isler, J. (1998), 'Long-term MF radar observations of solar tides in the low-latitude mesosphere: Interannual variability and comparison with GSWM', *Journal of Geophysical Research* **103**, 8667–8683.

Volland, H. (1988), *Atmospheric Tidal and Planetary Waves*, Kluwer Academic Publishers.

VonBiel, H. A. and Flood, W. A. (1970), 'Differential phase partial - reflection technique for the determination of $d-$region electron densities', *Journal of Geophysical Research* **75**(25), 4863–4870.

Walterscheid (1998), 'Aerospace rept. no. atr-81(9553)-4', *Journal of Atmospheric and Terrestrial Physics* **60**, 1234–1234.

Webber, W. (1962), 'The production of free electrons in the ionospheric D layer by solar and galactic cosmic rays and the resultant absorption of radio waves', *Journal of Geophysical Research* **67**, 5091–5106.

Weller, C. S. and Biondi, M. A. (1968), 'Recombination, attachment, and ambipolar diffusion of electrons in photo-ionized NO afterglows', *Phys. Rev* **172**, 198–206.

Weller, C. S. and Carruthers, G. R. (1972), 'High altitude observations of far and extreme UV radiation at night', *EOS* **53**, 1066–1072.